Boiling of water at low pressure : The role of subcooling and thermophysical properties on the bubble dynamics and heat transfer

Karolina Wojtasik

To cite this version:

Karolina Wojtasik. Boiling of water at low pressure : The role of subcooling and thermophysical properties on the bubble dynamics and heat transfer. Thermics [physics.class-ph]. Université de Lyon; Wroclaw University of Science and Technology, 2021. English. NNT : 2021LYSEI045 . tel-03433365v1

HAL Id: tel-03433365
https://theses.hal.science/tel-03433365v1

Submitted on 17 Nov 2021 (v1), last revised 24 Nov 2021 (v2)

N°d’ordre NNT : 2021LYSEI045

THESE de DOCTORAT DE L’UNIVERSITE DE LYON
opérée au sein de
INSA Lyon
En cotutelle internationale avec
Wroclaw University of Science and Technology

Ecole Doctorale N° 162
Mécanique, Énergétique, Génie Civil et Acoustique

Spécialité de doctorat : Thermique et Énergétique

Soutenue publiquement le 02/07/2021, par :
Karolina WOJTASIK

Boiling of water at low pressure: the role of subcooling and thermophysical properties on the bubble dynamics and heat transfer

---

Devant le jury composé de :

BUTRYMOWICZ Dariusz	Professeur (Politechnika Bialostocka)	Président
ROBINSON Anthony	Professeur (Trinity College, Dublin)	Rapporteur
PIASECKA Magdalena	Docteur habilité (Politechnika Swietokrzyska)	Rapporteure
GIRAUD Florine	Maître de conférences (CNAM, Paris)	Examinatrice
CHOROWSKI Maciej	Proffesseur (Politechnika Wroclawska)	Examinateur
RULLIÈRE Romuald	Maître de conférences (INSA Lyon)	Co-encandrat
BONJOUR Jocelyn	Professeur (INSA LYON)	Directeur de thèse
ZAJĄCZKOWSKI Bartosz	Docteur habilité (Politechnika Wroclawska)	Directeur de thèse

Département FEDORA – INSA Lyon - Ecoles Doctorales – Quinquennal 2016-2020

SIGLE	ECOLE DOCTORALE	NOM ET COORDONNEES DU RESPONSABLE
CHIMIE	**CHIMIE DE LYON** **http://www.edchimie-lyon.fr** Sec. : Renée EL MELHEM Bât. Blaise PASCAL, 3e étage **secretariat@edchimie-lyon.fr** INSA : R. GOURDON	**M. Stéphane DANIELE** Institut de recherches sur la catalyse et l'environnement de Lyon IRCELYON-UMR 5256 Équipe CDFA 2 Avenue Albert EINSTEIN 69 626 Villeurbanne CEDEX **directeur@edchimie-lyon.fr**
E.E.A.	**ÉLECTRONIQUE, ÉLECTROTECHNIQUE, AUTOMATIQUE** **http://edeea.ec-lyon.fr** Sec. : M.C. HAVGOUDOUKIAN **ecole-doctorale.eea@ec-lyon.fr**	**M. Gérard SCORLETTI** École Centrale de Lyon 36 Avenue Guy DE COLLONGUE 69 134 Écully Tél : 04.72.18.60.97 Fax 04.78.43.37.17 **gerard.scorletti@ec-lyon.fr**
E2M2	**ÉVOLUTION, ÉCOSYSTÈME, MICROBIOLOGIE, MODÉLISATION** **http://e2m2.universite-lyon.fr** Sec. : Sylvie ROBERJOT Bât. Atrium, UCB Lyon 1 Tél : 04.72.44.83.62 INSA : H. CHARLES **secretariat.e2m2@univ-lyon1.fr**	**M. Philippe NORMAND** UMR 5557 Lab. d'Ecologie Microbienne Université Claude Bernard Lyon 1 Bâtiment Mendel 43, boulevard du 11 Novembre 1918 69 622 Villeurbanne CEDEX **philippe.normand@univ-lyon1.fr**
EDISS	**INTERDISCIPLINAIRE SCIENCES-SANTÉ** **http://www.ediss-lyon.fr** Sec. : Sylvie ROBERJOT Bât. Atrium, UCB Lyon 1 Tél : 04.72.44.83.62 INSA : M. LAGARDE **secretariat.ediss@univ-lyon1.fr**	**Mme Sylvie RICARD-BLUM** Institut de Chimie et Biochimie Moléculaires et Supramoléculaires (ICBMS) - UMR 5246 CNRS - Université Lyon 1 Bâtiment Curien - 3ème étage Nord 43 Boulevard du 11 novembre 1918 69622 Villeurbanne Cedex Tel : +33(0)4 72 44 82 32 **sylvie.ricard-blum@univ-lyon1.fr**
INFOMATHS	**INFORMATIQUE ET MATHÉMATIQUES** **http://edinfomaths.universite-lyon.fr** Sec. : Renée EL MELHEM Bât. Blaise PASCAL, 3e étage Tél : 04.72.43.80.46 **infomaths@univ-lyon1.fr**	**M. Hamamache KHEDDOUCI** Bât. Nautibus 43, Boulevard du 11 novembre 1918 69 622 Villeurbanne Cedex France Tel : 04.72.44.83.69 **hamamache.kheddouci@univ-lyon1.fr**
Matériaux	**MATÉRIAUX DE LYON** **http://ed34.universite-lyon.fr** Sec. : Stéphanie CAUVIN Tél : 04.72.43.71.70 Bât. Direction **ed.materiaux@insa-lyon.fr**	**M. Jean-Yves BUFFIÈRE** INSA de Lyon MATEIS - Bât. Saint-Exupéry 7 Avenue Jean CAPELLE 69 621 Villeurbanne CEDEX Tél : 04.72.43.71.70 Fax : 04.72.43.85.28 **jean-yves.buffiere@insa-lyon.fr**
MEGA	**MÉCANIQUE, ÉNERGÉTIQUE, GÉNIE CIVIL, ACOUSTIQUE** **http://edmega.universite-lyon.fr** Sec. : Stéphanie CAUVIN Tél : 04.72.43.71.70 Bât. Direction **mega@insa-lyon.fr**	**M. Jocelyn BONJOUR** INSA de Lyon Laboratoire CETHIL Bâtiment Sadi-Carnot 9, rue de la Physique 69 621 Villeurbanne CEDEX **jocelyn.bonjour@insa-lyon.fr**
ScSo	**ScSo*** **http://ed483.univ-lyon2.fr** Sec. : Véronique GUICHARD INSA : J.Y. TOUSSAINT Tél : 04.78.69.72.76 **veronique.cervantes@univ-lyon2.fr**	**M. Christian MONTES** Université Lyon 2 86 Rue Pasteur 69 365 Lyon CEDEX 07 **christian.montes@univ-lyon2.fr**

*ScSo : Histoire, Géographie, Aménagement, Urbanisme, Archéologie, Science politique, Sociologie, Anthropologie

Acknowledgments

This work was carried out as a part of jointly supervised PhD thesis (french-polish cotutelle) and was partly financed by French Governemnt (Bourse du Gouvernement Francais). The research presented in this thesis is the output of the effort and support of several people to whom I am extremely grateful.

Firstly, I would like to express my sincere gratitude to all my supervisors. From Polish side: prof. Bartosz Zajaczkowski and dr Tomasz Halon, from French side: prof. Jocelyn Bonjour and dr Romuald Rullière. Their advice and guidance during the whole PhD studies helped me to successfully finish this manuscript. I am grateful for their patience during checking subsequent versions of this thesis and all publications along the way. Their constructive and helpful suggestions allowed me to improve the presentation of obtained results and brought my work to a higher level. I could not have imagined having a better advisors and mentors during this PhD journey. Additional thank you for my French supervisor for helping me to adjust in a new culture during these months spent in France. I would like to also acknowlegde prof. Zbigniew Krolicki who also supervised me during my first two years of my PhD. Eventhoug, I could always get the advice and help, any time I needed it.

I thank my colleagues that I meet during those last few years. I would like especially acknowledge Angnieszka Kujawska, Stanislawa Halon and Zbigniew Rogala from WUST and Moomal Quereshi, Naveed Ahmad, Sonya Rodichkina, Nicolas Cardin, Damien Gloriod, Adrien Abbate, Hazem Ben Aissia, Longkai Guo from INSA Lyon. I am grateful for the stimulating discussions and ideas that appeared during our conversations, but also for the fun we have had in the last four years. Special thank you to Sandra Michaïe for her guidance with respect to laboratory work at CETHIL and really big help during my first stay in France.

I would also like to thank Marta Brzezinska and Martyna Militowska (from WUST) and Nazaré Marques and Marilyne Galindo (from INSA Lyon) for their help with the documents and formal matters.

I would like to acknowledge Alexandra Apostoluk and Alicja Bailly. I am very grateful for the opportunity to participate in the meetings of polish community living in Lyon (you always knew new Poles arriving to the city).

Finally, I would like to express my gratitude to my family. Special thank you go to my fiancé Maciej, who has always cheered me up during those sometimes difficult moments. I thank my mom, my sister and Blanka for their love and support over the years and the fact that they always believed in me.

Abstract

Boiling is a common heat transfer mode used in many commercial and industrial applications, e.g. evaporators of air-conditioning and refrigeration units. Recently, there is a renewed interest in the development of efficient cooling technologies which utilize environmentally-friendly refrigerants. Some of those mediums, e.g. water, need to evaporate at low pressure to achieve cooling: for instance, a saturation temperature of 10°C corresponds to a saturation pressure of 1.2 kPa.

Close to the triple point, the physics of boiling is significantly different in comparison to atmospheric pressure. This statement concerns both thermal features (larger wall superheat required to initiate boiling, smaller values of heat transfer coefficient) and bubble dynamics (larger bubble size, smaller frequency of bubble detachment). Although the knowledge on subatmospheric boiling is slowly growing, many of its aspects remain unknown or vaguely theoretical. For that purpose, there is still a need to contribute the knowledge concerning boiling phenomena from a fundamental point of view. To do so, extensive experimental studies should be performed.

The initial analysis provided in this thesis was focused on isolated bubbles. A novel heat flux sensor was used to measure the instantaneous heat flux independently in seven concentrical zones of a heated surface on which boiling was taking place. Its utilization was especially beneficial at low pressure as larger bubble size simplified the observation of the bubble foot. Such analysis allowed the discovery of three types of low pressure bubbles and confirms the existance of associated thermal phenomena, such as microlayer evaporation and movement of the liquid pool during bubble growth.

In order to gain insight into boiling phenomena for more practical applications, another test campaign was conducted on a rough surface where multiple nucleation sites were activated simultaneously. The experiments were carried out for a wide range of operating parameters. Special attention was paid to the level of liquid, as it creates a pressure-induced subcooling resulting in the strong effect on the bubble diameter and bubble growth time. Because of the random character of the boiling process, a statistical analysis of the instantaneous heat flux was proposed. Based on this approach, four distinct boiling regimes were distinguished and characterized. To provide a more general description of boiling regimes over wide range of operating conditions, a dimensionless boiling regime map was proposed. Such interpretation is also useful in order to determine the thermo-hydrodynamic features of subatmospheric boiling and to verify what regime is expected under specific working conditions.

An alternative idea for some types of low-pressure evaporators (e.g. shell and tube) can involve the evaporation of small droplets sprayed onto the heated wall. Such approach can be beneficial at low pressure, as large bubbles could form dry patches on the heated surface inhibiting effective heat transfer. In the literature, there is lack of knowledge concerning the evaporation process at subatmospheric conditions. For this reason, the last experiments were focused on the evaporation process of a small drop or thin layer of liquid from a hot horizontal surface. Based on the heat flux measurements and high-speed camera recordings, distinct thermal processes occurring during drop evaporation were distinguished. This demonstrated that the use of this heat flux sensor is a promising measurement technology for the study of drop evaporation and spray cooling at low pressure.

Keywords: Pool boiling, Low pressure, Bubble dynamics, Experimentation, Visualization.

Contents

List of Figures

List of Tables

Nomenclature

Latin

A	Area	m^2
c_{cr}	Constant dependent on the geometry of the heater	-
c_p	Specific heat	$\mathrm{J(kg{\cdot}K)^{-1}}$
c_{sf}	Constant dependent on the surface-fluid combination	-
C	Concentration of solutant	-
d	Diameter	m
D	Diffusion coefficient	$\mathrm{m^2s^{-1}}$
$f(\theta)$	Factor related to the shape of isoconcentration curves	
F	Force	N
$F_{1->2}$	View factor from one surface to another surface	
g	Acceleration of gravity	$\mathrm{m^2s^{-1}}$
h	Heat transfer coefficient	$\mathrm{Wm^{-2}K^{-1}}$
h_{lv}	Latent heat of vaporisation	$\mathrm{J{\cdot}kg^{-1}}$
h_p	Thickness of precursor film	m
H	Height	m
HP	Heating power	W
I	Current	A
l_c	Capillary length	m
L_c	Characteristic length	m
L^*	Dimensionless parameter	-
$\overline{L}, \overline{A}, \overline{B}$	Distances	m
m	Mass	kg
M	Molar mass	$\mathrm{kg{\cdot}mol^{-1}}$
M_x, M_y	Number of points along x and y axes	-
n	Number of picture	-
p	Pressure	Pa
p_{La}	Laplace pressure	Pa
r	Radius	m
R	Universal gas constant	$\mathrm{J{\cdot}mol^{-1}K^{-1}}$

q	Heat flux	$\mathrm{Wm^{-2}}$
Q	Absorbed amount of heat	W
s	Sensitivity of the sensor	$\mathrm{V(Wm^2)^{-1}}$ or $\mathrm{VK^{-1}}$
sp	Spatial step	m
S_q	Root mean square roughness	m
t	Time	s
T	Temperature	K
U	Voltage	V
V	Volume	$\mathrm{m^3}$
x	Distance	m
z	Altitude of the surface	m
$\overline{x}, \overline{y}$	Relative distances	px

Greek

α	Thermal diffusivity	$\mathrm{m^2s^{-1}}$
β	Coefficient of thermal expansion	$\mathrm{K^{-1}}$
γ	Angle	rad
δ	Thickness	m
Δ	Difference	-
ϵ	Emissivity	-
ζ	Coefficient dependent on the contact angle	-
θ	Contact angle	degree
κ	Mean curvature of a drop	m
λ	Thermal conductivity	$\mathrm{Wm^{-1}K^{-1}}$
μ	Dynamic viscosity	Pa·s
ν	Kinematic viscosity	$\mathrm{m^2s^{-1}}$
ρ	Density	$\mathrm{kgm^{-3}}$
σ	Surface tension	$\mathrm{Nm^{-1}}$

Subscripts

0	Initial conditions
$1-10$	Numeration
app	Applied
b	Bubble
B	Buoyancy
$centre$	Centre of the heating surface

co	Connection cable
$convection$	Natural convection
cr	Critical
$drop$	Drop
d	Drag
eff	effective cavity
$film$	Film boiling
$foot$	Bubble foot
$growth$	Bubble growth
$high$	Higher thermocouple
i	Inertia
l	Liquid
lv	Liquid - vapor interface
low	Lower thermocouple
$mean$	Mean value
min	Minimum
n	Number of sensor's zone
$nucleate$	Nucleate boiling
p	Pressure
$pipe$	Pipe for drop generation
rad	Radiation
sat	Saturation conditions
sl	Liquid - liquid interface
sub	Subcooling
sv	Solid - vapor interface
$total$	Total heat transfer
tr	Triple point
v	Vapor
$waiting$	Waiting time
$wall$	Heated surface
ΔT	Temperature difference
σ	Surface tension
∞	Conditions far from the calculation point

Dimensionless numbers

I_R	Robinson and Judd criterion	$I_R = \left(\frac{4}{27}\right)\left(\frac{\sigma}{\rho_l \alpha_l^2}\right)\frac{r_{cr}}{Ja^2}$
Ja	Jakob number	$Ja = \frac{\rho_l c_{p(l)} \delta T_{wall}}{\rho_v \delta h_{lv}}$ or $Ja = \frac{c_{p(l)} \delta T_{wall}}{\delta h_{lv}}$
Ja^*	Modified Jakob number	$Ja^* = \frac{c_{p(l)} L_c q_{app}}{\delta h_{lv} \lambda_l}$
La	Laplace number	$La = \frac{\rho l_c \sigma_{lv}}{\eta^2}$
Ma_T	Thermal Marangoni number	$Ma_T = -\frac{d\sigma_{lv}}{dT}\frac{l_c \Delta T}{\eta \alpha}$
Ma_C	Solutal Marangoni number	$Ma_C = -\frac{d\sigma_{lv}}{dC}\frac{l_c \Delta C}{\eta \alpha}$
Pr	Prandtl number	$Pr = \frac{c_p \mu}{\lambda}$
Ra	Rayleigh number	$Ra = \frac{g\beta}{\nu\alpha}(T_s - T_\infty){l_c}^3$

Abbreviations

CAH	Contact Angle Hysteresis
CCA	Constant Contact Angle
CCR	Constant Contact Radius
CDF	Cumulative Distribution Function
IR	Infrared
ITO	Indium Tin Oxide
MEMS	Microelectromechanical systems
PDF	Probability Density Function
PFV	Photron Fastcam Viewer
TPHL	Triple Phase Contact Line

Introduction

The boiling phenomenon is associated with a liquid transformation into a vapor phase while heating it to the boiling point along with the generation of bubbles in the liquid phase. Boiling is considered to be an effective heat transfer mode, as it is characterized by higher heat transfer coefficient than natural or forced convection [49]. For that reason, it is utilized in many applications, e.g in cooling systems, heat pipes etc.

Boiling process has been extensively investigated by many researchers in the last decades and many studies concerning this phenomenon have been published. Despite that, due to complexity of the phenomena involved in the boiling heat transfer, the whole process is still not fully understood. This is particularly true for less conventional boiling conditions, e.g. at a very low pressure. Recently, the increasing global energy demand led to environmental pollution and the depletion of fossil fuel reserves. This sparked interest in development of highly effective and low-cost cooling systems that can utilize environmentally-friendly refrigerants. Among them, one of the most promising is water.

Water possesses many advantages which make it a very proficient refrigerant. It is widely available, non-toxic, non-flammable, cheap and is characterized by high latent heat of evaporation. However, it also has some limitations. In order to use water for cooling or refrigeration purposes, it has to evaporate at low saturation temperatures and consequently - low pressure (water temperature of 5 - 15 °C corresponds to saturation pressure in a range of 0.9 - 1.7 kPa), which is also close to its triple point (T_{tr} = 0.01°C, p_{tr} = 0.61 kPa).

At such conditions, the boiling characteristics are totally different. The wall superheat required to initiate boiling is larger and often exceeds 10 K. The generated bubbles are large in size and depart with low frequency. Additionally, the heat transfer coefficients are significantly reduced and the traditional correlations available in the literature are no longer valid [131]. This causes low-pressure heat exchangersto be over-designed, and thus less effective and larger than is necessary.

The present manuscript aims at extending the knowledge concerning fundamental aspect of pool boiling (with respect to bubble dynamics and heat transfer) and liquid evaporation at low pressure. For that purpose, several experimental studies were carried out. The boiling process was investigated for a polished surface with a single nucleation site (Chapter 3), as well as, for a rough surface with multiple cavities (Chapter 4).

An alternative idea for some types of low-pressure heat exchangers (e.g. shell and tube) can be the evaporation of small droplets sprayed onto the heated wall. Such approach might be more beneficial at proximity to the triple point, as large bubbles can form dry patches on the heated surface inhibiting the effective heat transfer. In the literature, there is no information concerning drop evaporation at low pressure. This phenomena was investigated at atmospheric conditions, however, due to differences in the thermophysical properties of water, it is necessary to experimentally verify the heat transfer processes involved in the evaporation at sub-atmospheric conditions. The last tests focused on the studies of evaporation of a drop or a thin layer of liquid on a horizontal surface (Chapter 5).

Scientific hypothesis of the dissertation

Based on the literature studies, two main thesis of this dissertation were proposed:

I. The change in the thermophysical properties of water near the triple point has a significant impact on the dynamics of the phase transformation process.

II. The influence of hydrostatic pressure cannot be ignored in the experimental analysis and model studies of the boiling process in sub-atmospheric conditions.

Objectives of the dissertation

The main aim of this manuscript is to present the experimental studies of the processes of boiling and evaporation occurring at low pressure. The main tasks that were performed to elaborate this PhD work were as follows:

- Preparation of an automatized script for the analysis of large series of images - i.e. proper distances calculation including the parallax effect (Chapter 2).
- Analysis of the bubble dynamics for a single nucleation site using novel heat flux sensor; the studies involves bubble foot evolution and estimation of the low-pressure bubble types (Chapter 3).
- Analysis of the influence of the liquid level and resulting subcooling on the bubble dynamics and heat transfer (Chapter 3 and 4).
- Determination of low-pressure boiling regimes for various operating parameters (vapor pressures, applied heat fluxes, liquid levels). Preparation of dimensionless boiling map (Chapter 4).
- Analysis of the heat transfer processes involved in the evaporation of a drop and a thin liquid layer on a hot horizontal surface (Chapter 5).

Thesis structure

The manuscript is divided into five chapters with two appendices:

- **Chapter 1:** This chapter describes the fundamental concepts required to describe the boiling process on a flat surface. The influence of the low pressure on the boiling behavior is also discussed.
- **Chapter 2:** In this chapter, the description of the test-bench used to perform experiments is provided. Additionally, the experimental procedures and data processing techniques are explained.

- **Chapter 3:** This chapter focuses on the analysis of the bubble dynamics at low pressure on a mirror-polished surface with a single, active nucleation site placed at the center. The experiments are conducted with a novel heat flux sensor which measures instantaneous value of heat flux independently in seven zones of the sensor. Such analysis enables to follow the bubble foot growth and analyze associated phenomena related to this process.

- **Chapter 4:** The overall boiling behavior on a rough surface with multiple nucleation sites is described in this chapter. Four distinct boiling regimes observable for various working conditions are characterized. Based on all the results, a boiling regime map is proposed.

- **Chapter 5:** This chapter presents the preliminary studies of evaporation process at low pressure. First part focuses on the literature review of liquid evaporation on a horizontal surface. The further part describes the experimental studies of drop and liquid layer evaporation at low pressure.

Chapter 1

Literature review

Pool boiling has been extensively studied for more than 80 years since the pioneering work of Nukiyama [88]. Over this period of time, many progresses have been made to understand the fundamental processes of boiling (bubble nucleation, growth and detachment) and their relationship with thermal effects that are responsible for the effective heat transmission from the wall to the fluid, which characterizes boiling. Despite the inventiveness of the researchers, despite the accelerating improvement or invention of experimental techniques, despite the increase of computational capacities whose simulation results can help interpret experimental results and build theories, the mechanisms governing the bubble life cycle still remain poorly understood.

Additionally, in order to use water for cooling at the temperature levels normally occurring in refrigeration systems, it must be evaporated at very low-pressures (approx. 1 kPa). Under such conditions, the physics of the boiling process is noticeably different in comparison to atmospheric conditions. Although the knowledge on subatmospheric boiling is slowly growing, many of its aspects remain unknown or vaguely theoretical.

In this chapter, the general background concerning pool boiling process is presented. Section 1.1 introduces fundamental information related to the boiling process at atmospheric conditions. The influence of low pressure on the boiling behavior is described in Section 1.2. The short overview of the measurement techniques used to experimentally study boiling phenomenon is presented in Section 1.3.

1.1 Pool boiling on a flat surface

The pool boiling experiments are often conducted on flat surfaces, as this constitute a good reference case for more complex configurations. Even though, the heated wall in real-life is not always horizontal and flat, this approach is beneficial in order to deeply understand fundamental aspects of the boiling phenomenon, with respect to heat transfer and bubble dynamics. The following sections will cover the most important information concerning boiling process, including nucleation process, bubble dynamics and influence of the subcooling on the boiling behavior.

1.1.1 Boiling curve

Pool boiling curve was plotted based on Nukiyama observations. In 1934, he performed experiments on heating liquids by nichrome and platinum wires [88]. He noticed that the boiling behavior is different depending on the difference between heater temperature and liquid temperature (ΔT_{wall}) named wall superheat. The typical saturated boiling curves, for both imposed temperature and imposed heat flux conditions, are presented in Fig. 1.1. Each point at the curve corresponds to the steady-state value of ΔT_{wall} resulting to the application of a constant heat flux. Four main heat transfer regimes are distinguished on such boiling curve [15, 31, 88]:

- **Natural convection** (to point A in Fig. 1.1 a and b) - when the liquid temperature is above its saturation temperature, there is still no bubbles on the surface if the superheat is too low (for water this is usually between 2-6 K). The motion of liquid is driven by currents of natural convection.

- **Nucleate boiling regime** (between points A' and C in Fig. 1.1 a and b) - the first bubbles start to form at point A' on the boiling curve. The difference between points A and A' in Fig. 1.1 a and b corresponds to the onset of the nucleate boiling. The boiling becomes more intense, more nucleation sites start to be activated with the increase of wall superheat (i.e. moving towards point C).

  The nucleate boiling regime can be divided into two subgroups: in the region A-B, the isolated bubbles are generated, however they collapse slightly after they detach from a heated wall. The movement of the liquid pool due to bubble entrainment is responsible for an increase of heat transfer coefficient and heat flux in this region.

  When the wall temperature reaches certain value (corresponding to point B in Fig. 1.1), the number of active nucleation sites is so large and the bubbles are rising and detaching with such frequency that continuous columns of vapor are formed. Point C in Fig. 1.1 is called the critical (or maximum) heat flux and for water its value exceeds 1 MW·m^{-2}.

- **Transition boiling regime** or unstable film boiling regime (between points C and D in Fig. 1.1 a) - when the wall superheat ΔT_{wall} exceeds value corresponding to point C, the heat flux starts to decrease. In this boiling regime nucleate boiling as well as, film boiling occur alternately.

- **Film boiling regime** (beyond point D in Fig. 1.1 a) - at point D (called Leidenfrost point), nucleate boiling regime completely vanishes. The surface is fully covered by a vapor film. The presence of vapor layer is responsible for lowered heat transfer coefficient at this regime. The increase of heat flux with the rise of wall superheat is the result of heat transfer via radiation to the liquid through the vapor phase, which becomes more important at high temperatures.

The shape of the boiling curves presented in Fig. 1.1 is as a whole the same for various working fluids. The actual form of a boiling curve depends on applied fluid, heated wall properties and operating pressure. It is, however, relatively independent on the geometry of the heated wall.

It is also worth mentioning that at imposed heat flux condition, the pool boiling curve may not fit to the one presented in Fig. 1.1 a beyond point C. When wall temperature exceeds q_{cr} (what corresponds to point C in Fig. 1.1 a and b), the surface temperature might increase to its melting point causing burnout phenomenon. In such a case, the heat flux does not decrease after point C but it remains constant with a sudden jump of wall temperature (see line C - E in Fig. 1.1 b). The surface temperature which corresponds to point E is often above the melting point of the heating materials, that is why point C is often called the burnout point and the heat flux at this point - the burnout heat flux.

When the reverse process is performed, i.e. lowering the heat flux from point E, the intense drop of wall superheat while reaching D in Fig. 1.1 b (thus q_{min}) is observable. In this case, the boiling phenomenon also does not follow the transition part of the boiling curve (i.e. between points C and D in Fig. 1.1 b).

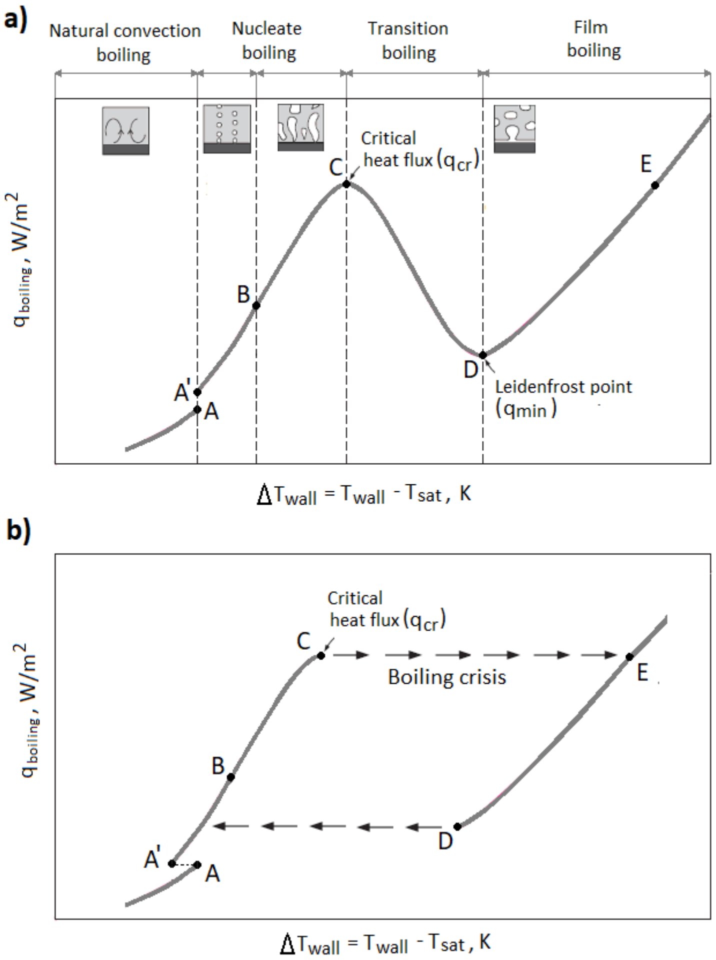

Figure 1.1: Boiling curves: a) at imposed temperature conditions, b) at imposed heat flux conditions.

In practice, most of the heat transfer devices operate below q_{cr} in order to avoid burnout phenomenon. The exception is cryogenic equipment operating with fluids such as oxygen or nitrogen. In this case point E on the boiling curve usually lies below the melting point of most of the heating materials. This allows to operate under steady film boiling conditions without occurrence of the burnout.

In conditions other than cryogenic, most common form of boiling is nucleate boiling regime, as high heat transfer rates are associated with relatively small wall superheat ΔT_{wall} (usually for water $\Delta T_{wall} < 30°C$). For that purpose, the next sections of this Chapter will focus mostly on the description of the nucleate boiling regime.

1.1.2 Heat transfer correlations in pool boiling

Distinct boiling regimes occur during pool boiling, as discussed in Section 1.1.1. They possess unique features, thus different relations are applied to express the heat transfer. In this section, the most common heat transfer correlation for each regime will be shortly described.

1.1.2.1 Natural convection

When the heat flux is too low to initiate boiling and no bubbles is present in the surface, the heat transfer can be accurately determined using relations for natural convection, as the process is governed by the natural convection currents [15, 44, 99].

1.1.2.2 Nucleate boiling

In the nucleate boiling regime, the heat transfer is strongly dependent on the nucleation phenomenon (the numbers of active nucleation sites, bubble frequency etc.). The properties of the heated wall are also important (material, roughness etc.) as they affect the boiling process. This makes the prediction of heat transfer difficult to conduct. The available correlations for nucleate boiling are empirical or semi-empirical. One of the most widely used correlation was proposed by Rohsenow in 1952 and has the following form [15, 119]:

$$q_{nucleate} = \mu_l h_{lv} \left[\frac{g(\rho_l - \rho_v)}{\sigma} \right]^{1/2} \left[\frac{c_{p(l)}(T_{wall} - T_{sat})}{c_{sf} h_{lv} Pr_l^n} \right]^3 \tag{1.1}$$

In the above equation, n is an experimental constant dependent on the fluid and c_{sf} is an experimental constant dependent on the surface-fluid combination. Eq. 1.1 is applicable for clean and relatively smooth surface. It is often considered that it can be used for any geometry of the heated surface, because, up to some extent, the rate of heat transfer during nucleate boiling does not primarily depend much on the geometry or orientation of the wall.

1.1.2.3 Critical heat flux

Another important parameter is estimation of the critical (maximum) heat flux (point C in Fig. 1.1) in order to avoid the possibilities of burnout which would be dangerous for the system. Its value for pool boiling conditions was estimated theoretically by Kutateladze in 1948 and by Zuber in 1958. They used different approaches but obtained similar results. The maximum heat flux is expressed as [15]:

$$q_{cr} = C_{cr} h_{lv} [\sigma g \rho_v^2 (\rho_l - \rho_v)]^{1/4} \tag{1.2}$$

C_{cr} is a constant dependent on the geometry of the heater. For flat horizontal surface it has value [15]:

$$C_{cr} = 0.149 \quad for \quad L^* > 27 \tag{1.3}$$

$$C_{cr} = 18.9 \frac{\sigma}{g(\rho_l - \rho_v) A_{wall}} \quad for \quad 9 < L^* < 20 \tag{1.4}$$

The calculations are made based on the dimensionless parameter L^* which is dependent on the size of the heater (by means of characteristic length l_c which for horizontal surface is equal to the wall width or diameter) and has following form:

$$L^* = l_c \left[\frac{g(\rho_l - \rho_v)}{\sigma} \right]^{1/2} \tag{1.5}$$

Analyzing Eq. 1.2 it is observable that the maximum heat flux is not dependent on the fluid-wall combination and most of the thermophysical properties of the working fluid (such as viscosity, thermal conductivity and specific heat).

Its value is however proportionally dependent on the enthalpy of vaporization, thus a large value can be obtained for fluid with large h_{lv} such as water. Cichelli and Bonilla [19] estimated that the critical heat flux is also strongly related to operating pressure. The value of q_{cr} rises with pressure by about $1/3 \cdot p_{cr}$ and then starts to decrease reaching zero at the critical pressure.

1.1.2.4 Minimum heat flux

Minimum heat flux occurs at the so-called Leidenfrost point. It corresponds to the lowest value of heat flux which can occur during film boiling regime. It can be estimated based on the expression proposed by Zuber [15]:

$$q_{min} = 0.09 \rho_v h_{lv} \left[\frac{\sigma g(\rho_l - \rho_v)}{(\rho_l - \rho_v)^2} \right]^{1/4} \tag{1.6}$$

Eq. 1.6 is applicable for large horizontal planes. The constant 0.09 was proposed by Berenson in 1961, as he replaced the theoretical value of $\pi/24$ for 0.09, as it better suited to experimental data. Nevertheless, still the error of calculating q_{min} can reach 50% or even more.

1.1.2.5 Film boiling

Berenson proposed a correlation for convective heat transfer during film boiling over a large horizontal plane [31]:

$$q_{film} = 0.425 \left[\left(\frac{\lambda_v^3 g \rho_v (\rho_l - \rho_v) h_{lv}}{\mu_v (T_{wall} - T_{sat})} \right) \left(\frac{g(\rho_l - \rho_v)}{\sigma} \right)^{1/2} \right]^{1/4} (T_{wall} - T_{sat}) \tag{1.7}$$

This boiling regime is most commonly used at high temperatures (more than 300°C). At such conditions, the heat transfer via radiation becomes very important heat transfer method and has to be taken into account. The heat transfer via radiation for two large parallel plates separated by transparent medium can be determined as follows [15, 31]:

$$q_{rad} = \epsilon \sigma (T_{wall}^4 - T_{sat}^4) \tag{1.8}$$

In the case when emmissivities of two objects are not equal the above equation have the following form:

$$q_{rad} = \epsilon \sigma F_{1->2} (T_{wall}^4 - T_{sat}^4) \tag{1.9}$$

where $F_{1->2}$ is the view factor from one surface to second surface.

Both heat transfer mechanisms, convective and radiative, affect each other, as the radiation from the surface to the liquid enhances the rate of evaporation increasing the thickness of the vapor film. This consequently limits the convection heat transfer. For the case when $q_{rad} < q_{film}$, the overall heat flux during film boiling can be calculated in a following way [15, 31]:

$$q_{total} = q_{film} + 0.75 q_{rad} \tag{1.10}$$

The transition boiling regime is usually avoided during operation of various systems, thus there was no real scientific interest in estimating correlations to describe heat transfer processes in this particular regime.

1.1.2.6 Methods of heat transfer enhancement

The heat transfer rate depends on the number of active nucleation sites on the heated wall as well as on the frequency of the bubble formation at each site. Consequently, a surface modification which would enhance nucleation on the surface could result in improving the heat transfer during nucleate pool boiling. Several studies indicated that any irregularities of the heated surface (e.g. increased roughness, dirt) contribute to additional nucleation sites during boiling process. Berensen [8] proved that roughening the surface contributes to the increase in the nucleate boiling heat transfer by 10 times. However, such simple approach of improving the heat transfer coefficient just by acting on the surface roughness is not very effective and its effect is degraded with time (the heat flux gradually comes back to its initial value obtained for a smooth surface). The surface roughness has also very little effect on the value of critical heat flux and the heat flux during film boiling.

To provide permanent enhancement of heat transfer during nucleate boiling, several techniques are available in the market. For that purpose, the heating surface might be coated with a thin layer (much less than 1 mm) of very porous material. The cavities might also be formed mechanically to provide continuous bubble nucleation. Those kind of treated surface were estimated to improve heat transfer in nucleate boiling regime even by 10 times and the critical heat flux up to 3 times.

Another way may be usage of structured surfaces [1, 16, 44, 45, 80, 108, 131], mechanical agitation [15] or surface vibration [15]. The latter two, however, are not commonly used because the process of creation of such surfaces is complicated. Structured surface is common form of passive method of heat transfer enhancement and the main advantage is that it do not require any additional energy and the effect of more intense nucleation process is more stable than acting only on the surface roughness.

1.1.3 Nucleation theory

The process of bubble growth inside the liquid pool (and not on the solid surface) is called homogeneous nucleation. The process in which the imperfection of the solid surface leads to bubble formation is called heterogeneous nucleation. The liquid superheat required for homogeneous nucleation is larger than for heterogeneous nucleation, and that is why the latter process is more common during pool boiling process. Every surface used in real life possess some irregularities (e.g. micro cracks, cavities, boundaries between solid crystals) in which the vapor may be trapped. Those places serve as a nucleation sites, because those small amount of the trapped vapor (known also as bubble embryos or nucleus) starts to increase its volume (thermal expansion) or its mass due to evaporation of the surrounding liquid.

For the bubble generation, the Laplace-Young equation must be fulfilled as the vapor/gas and liquid must be in an equilibrium [31]:

$$p_v - p_l = \frac{2\sigma}{r_b} \tag{1.11}$$

Eq. 1.11 correspond to fully degassed liquid pool. In the case when there is some non-condensable gas dissolved, its pressure also has to be included. From Eq. 1.11, one can see that the pressure of vapor has to be larger than the pressure of liquid.

At the beginning of the bubble growth, the liquid around the bubble needs to be superheated with respect to the saturated conditions (thus the heated wall also has to be superheated). The required wall superheat can be calculated according to the following formula [49]:

$$\Delta T_{wall} = \frac{2\sigma T_{sat}\nu_v}{r_b \cdot h_{lv}} + \frac{q \cdot r_b}{\lambda_l} \tag{1.12}$$

In Eq. 1.12, the first term of the right-hand side of the equation describes the thermodynamic equilibrium conditions inside the bubble, the second one - the heat conduction through the liquid with the thickness equal to the radius of the bubble. It is worth mentioning that the presence of noncondensable gases reduces the required wall superheat [114].

The ideal model of the surface cavity containing vapor embryo is presented in Fig. 1.2. The liquid-vapor interface at the early stage of a bubble growth is often considered spherical. Initially, as the bubble grows inside the cavity, the radius of the curvature (r_b) increases (see $r_2 > r_1$ in Fig. 1.2). However, after some time, the curvature radius starts do decrease (see $r_{cr} < r_3 < r_2$ in Fig. 1.2). The minimum bubble radius can be considered when a bubble becomes a hemisphere with radius the same as the radius of the cavity (r_c). Further evaporation, pushes the liquid-vapor interface beyond the surface of the cavity and the bubble radius increases again. In real-life, however, the variation of the bubble radius depends on the cavity angle ϕ and on the contact angle θ.

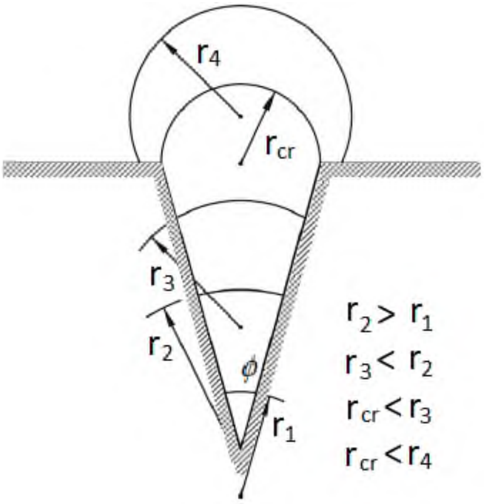

Figure 1.2: The rise of the bubble on the ideal cavity (adapted from [31]).

The highest temperature required to start nucleation is when the bubble radius is equal to the critical radius. The temperature which is required for a bubble to grow from a cavity has to be higher than saturation temperature by ΔT_{wall}. If a bubble has lower size it will collapse [31, 49, 114]. The critical radius is often expressed by the equation [31]:

$$r_{cr} = \frac{2\sigma T_{sat}}{h_{lv}\rho_v \Delta T_{wall}} \tag{1.13}$$

Another relation for effective cavity size is the one proposed by Hsu [50]. It relates the effective cavity size r_eff with the radius of equilibrium of a vapor nucleus r_{cr}:

$$r_{eff} = 0.8 r_{cr} \tag{1.14}$$

1.1.3.1 Nucleation site density

Considering the boiling process occurring on the whole heated wall, one important factor to describe boiling characteristics under certain working condition is the nucleation site density. The real surface possesses many cavities which could act as potential nucleation sites. In order to get activated, the cavity has to have a proper size [46, 50]. The minimal and maximal diameters of the cavities which can get activated depends on various parameters, such as the wall superheat, thickness of thermal boundary layer and thermo-physical properties of the working fluid.

The nucleation site density is defined as the total number of active nucleation sites per unit area. It is an imporant factor as it affect the number of bubbles present on the surface during boiling process and consequent movement of the liquid pool having impact on the heat transfer coefficient.

1.1.4 Bubble growth process

As explained earlier, to allow for a bubble growth, the temperature at the vicinity of the surface must be superheated. The whole process is transient, as the mass, momentum and energy are constantly changing over time. The bubble growth differs depending if the process is homogeneous (bubble growth inside the superheated liquid) or heterogeneous (bubble nucleates on the heated surface). For homogenous nucleation it is usually assumed that the bubble is surrounded by the uniformly superheated liquid. In the case of the bubble attached to the heating surface, the bubble growth process occurs in an nonuniform temperature field. The bubble can grow from a nucleation site only if the thermal layer above the site is thick enough.

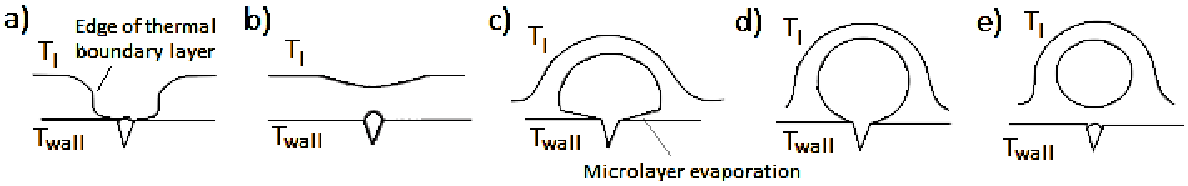

Figure 1.3: Schematic of the bubble growth process (adapted from [13])].

A bubble growth can be explained as follows. The schematic of this process is also shown in Fig. 1.3. Initially, the thermal boundary layer is broken after the detachment of a previous bubble causing re-wetting of the wall with cold liquid (see a in Fig. 1.3).

Some time is required for the thermal layer to grow again in the vicinity of the cavity (see b in Fig. 1.3). The time between the detachment of previous bubble and nucleation of the next one is called as "waiting period". After nucleation, the bubble starts to grow within the liquid thermal layer (see c in Fig. 1.3). Many researchers confirm the existence of microlayer placed below the expanding bubble [11, 21]. The liquid trapped between heated wall and bubble gradually evaporates.

The initial stage of the bubble growth is considered to be "inertia-controlled", because the liquid inertia tends to slow the expansion of the bubble. At the subsequent stage, the bubble growth starts to be "diffusion-controlled" (see d in Fig. 1.3). It is characterized by the reduction of the bubble growth rate due to lowered superheat of the surrounding liquid. The bubble at this stage has nearly spherical shape. After some time, the bubble detaches and breaks the thermal boundary layer. Liquid from the bulk rewets the wall and the whole process starts again.

The described bubble growth process assumes that the bubble is growing within the thermal boundary layer. The growing bubble can 'lift' the superheated layer above the wall boundary layer. The evaporation process occurs within the thermal layer and at the same time, the condensation takes place at the upper part of the bubble. To allow for the bubble to grow, the evaporation rate must be larger than the condensation rate.

Depending on the operating conditions, the bubble growth (and thus boiling phenomenon) is predominantly under the control of inertia or diffusion.

Carey [13] observed that the high wall superheat, low latent heat of evaporation and low pressure constitute to inertia-controlled bubble growth. That signifies that this kind of boiling process is characteristic for high values of Jacob number. The Jacob number is a dimensionless number which expresses the ratio of the sensible heat and latent heat:

$$Ja = \frac{\rho_l c_{p(l)} \Delta T_{wall}}{\rho_v \Delta h_{lv}} \tag{1.15}$$

Robinson and Judd [98] proposed another criterion to determine the relative importance of inertia and diffusion. It is based on a dimensionless number (I_R):

$$I_R = \left(\frac{4}{27}\right)\left(\frac{\sigma}{\rho_l \alpha_l^2}\right)\frac{r_{cr}}{Ja^2} \tag{1.16}$$

The authors stated that the bubble growth is controlled by inertia if $I_R \ll 1$. If $I_R > 1$, the diffusion controls the evaporation process.

1.1.5 Forces acting on a bubble

Forces acting on a bubble affect the shape of a bubble during its growth. Their balance also determines the time when a bubble detaches from the surface. Fig. 1.4 presents the schematic of major forces acting on a growing bubble.

These forces generally can be divided into two categories: static forces and dynamic forces. The first ones are connected to the stresses working on a static bubble and are present even in the absence of fluid motion around the bubble. Among static forces, one can distinguish: buoyancy forces F_B (result from the hydrostatic pressure acting on the bubble surface), pressure forces F_p (related to the difference between pressure inside and outside the bubble and resulted from the contact area between bubble and heated surface), surface tension forces F_σ (represent the effect of molecular interactions between various phases; they are driven by the surface tension along liquid-vapor interface) and thermocapillary forces (induced by a surface tension gradient due to temperature difference along the liquid-vapor interface).

The dynamic forces result from the bubble motion during the expansion process. Those are: inertia forces F_i (resulted from the reaction of the liquid due its acceleration caused by the movement of the liquid-vapor interface during bubble expansion), drag forces F_d (related to the viscous stress) and lift forces (present if the preceding bubble departs from the surface slightly before the next bubble nucleates; in such a case the liquid flow generated by initial bubble introduce additional rising force acting on a secondary one).

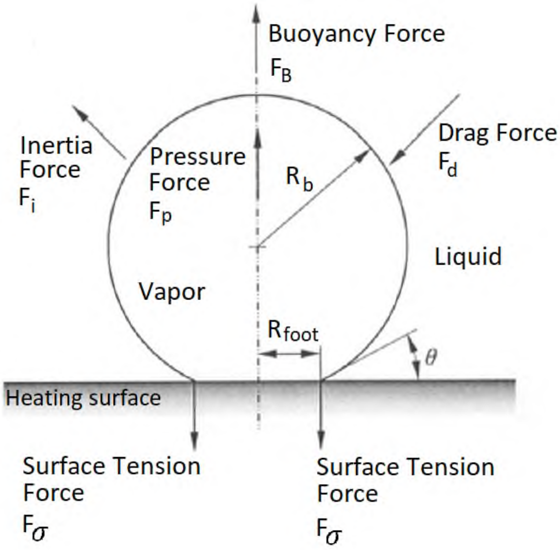

Figure 1.4: Forces acting on a bubble growing on a heated surface (extracted from [31]).

Depending on the boiling environment different forces can be dominant. It is assumed that under atmospheric conditions, the buoyancy, pressure forces and surface tension forces are considered to be dominant. However, under less conventional conditions (under high wall superheat, high liquid subcooling or at low pressure) the dynamic forces (especially inertia forces) become more important.

Generally, the surface tension forces tends to oppose to the bubble detachment. However, in some cases, e.g. when the bubble is strongly elongated in the vertical direction, this force can act in order to promote the departure of the bubble from the heated wall.

1.1.6 Bubble detachement

As shown in Section 1.1.5. different forces act on a bubble during its growth. The balance of forces can be created at the moment of detachment, as the forces which tend to attach the bubble on the surface have to be equal to the ones which try to lift the bubble [114]:

$$F_B + F_p = F_i + F_\sigma + F_d \tag{1.17}$$

Another important aspect, related to the bubble lifetime is the bubble size at the moment of departure. This parameter can be estimated based on the balance of forces acting on a bubble. In the case of small cavities ($r_{cr} < 10\ \mu m$ [31]), the size of bubble at detachment is mostly dependent on the buoyancy and liquid inertial forces. For larger cavities, the bubble growth process is slower and inertial forces tends to be less important. Instead, the buoyancy and surface tension forces start to dominate [31].

The correlation for bubble departure diameter was firstly proposed by Fritz [32]. He balanced the buoyancy and surface tension forces and obtained following equation:

$$d_b = 0.0208\theta\sqrt{\frac{2\sigma}{g(\rho_l - \rho_v)}} \tag{1.18}$$

where θ is the contact angle.

Various experiments confirmed that Eq. 1.18 gives a proper length scale for bubble diameter at the moment of detachment, however the boiling process is chaotic in nature, thus wide variation of the bubble diameters would be obtained during real-life boiling process.

Also Cole and Rohsenow [20] proposed correlations for the bubble diameter at the moment of departure. For water they obtained the following form:

$$d_b = 1.5 \cdot 10^{-4}\sqrt{\frac{2\sigma}{g(\rho_l - \rho_v)}}Ja^{5/4} \tag{1.19}$$

The bubble departure frequency, related to the waiting time between one bubble detachment and next bubble nucleation is another important aspect involved in the pool boiling process. Both bubble waiting time, similarly like bubble growth time, depends on the cavity size, fluid flow and heat transfer in the proximity to the active nucleation site. The bubble frequency can be expressed as follows:

$$f_b = \frac{1}{t_{growth} + t_{waiting}} \tag{1.20}$$

1.1.7 Subcooled boiling

The previous descriptions of the boiling process were mainly focused on the phenomenon occurring under saturation conditions. However, various systems operate with liquid which is subcooled. Subcooled boiling occurs when the liquid bulk temperature is lower than the saturation temperature corresponding to the pressure ($T_l < T_{sat}(p)$). Usually, the pool of liquid is at homogeneous pressure while the bulk liquid is cooled so as to kept at low temperature. The studies of Kutateladze [67] showed that subcooling increases the critical heat flux. Many researchers confirmed this dependency (e.g. Inoue et al. [55], Ivey and Morris [56], Rainey et al. [96]). They created multiple correlations predicting the occurrence of critical heat flux depending on the level of subcooling. It is crucial for the application where large quantities of heat needs to be removed (e.g. nuclear or fusion reactors [42]), as the CHF is the most important limiting factor of maintaining high heat transfer rate at feasible temperatures during the boiling process.

Besides, subcooling is described as having a little effect on the nucleate boiling regime [33, 135] and slightly enhance the natural convection heat transfer [135]. Nevertheless, Marek and Straub [77] and Petrovic et al. [92] noted the influence of the Marangoni effect on the convective heat transfer as a result of surface tension variation along liquid-gas interface when the subcooling is sufficient. Its effect gets more intense if more non-condensable gases are dissolved inside the working medium. Finally, as the subcooling has often negligible influence on heat transfer coefficient [96], most of the nucleate boiling correlations for saturation conditions can be used for subcooled boiling [13].

Concerning bubble dynamics, for a given operating pressure the subcooling reduces the size of bubbles, making this type of boiling beneficial for small thermal devices [64]. Inada et al. [53] and Wang and Chen [117] showed the existence of microbubble emission boiling. This phenomenon occurs for high subcooling (more than 30 K) and high heat fluxes. After their contact with cold surrounding liquid, the bubbles break into a cluster of microbubbles. Judd [58] described subcooled boiling as being submitted to two opposing phenomena. On the one hand, the larger wall to fluid temperature difference (with respect to saturated boiling) fosters convection, but on the other hand, the reduction of the bubble size limits the heat transfer. Because of these opposing phenomena, the bubbles frequency first decreases when increasing the subcooling, until it reaches a minimum and then starts increasing. Other researchers note different relations concerning this parameters. According to Shen at al. [107], the bubble frequency is lower in a subcooled environment than at saturation conditions. Goel et al. [42] stated that the subcooling generally results in the increase in the bubble frequency, but for subcooling smaller than 5 K, opposite trend can be observed.

1.2 Influence of low pressure on the boiling process

Over the last decades, knowledge on subatmospheric boiling has been gradually growing. The research efforts were driven by ecological concerns that make it necessary to study phase transitions of refrigerants evaporating at low pressures, e.g. water which is the most natural, safe and environmentally-friendly refrigerant. Such studies are especially important, as multiple factors are very sensitive to the decrease of pressure and boiling at sub-atmospheric conditions possesses its own characteristic features.

Probably the most important aspect concerning subcooling is caused by the hydrostatic pressure induced by the column of liquid. Liquid height is usually neglected at atmospheric conditions, however at the proximity to the triple point it has to be included as it causes variation of local pressure and saturation temperature. In Section 1.2.1, one discusses the pressure-induced subcooling occurring at low pressure. The nonhomogeneity of the boiling environment affects the basic parameters related to bubble dynamics: the size and shape of the bubbles, numbers of active nucleation sites, bubble frequency etc. The characteristics of the bubble dynamics are provided in Section 1.2.2. Section 1.2.3. describes the heat transfer during low pressure pool boiling.

1.2.1 Pressure-induced subcooled boiling

The liquid level plays an important role during low pressure boiling. At atmospheric conditions, the pressure in the whole liquid bulk usually can be considered homogeneous in typical operational conditions (few tenths of centimeters of liquid). This assumption is not valid if the pressure is significantly reduced. At low pressure the liquid column induces a hydrostatic pressure which is of similar order of magnitude as the vapor pressure. The value of local pressure inside the liquid pool increases from the vapor pressure (at free surface level) to the wall pressure (at heated surface level) which is written as:

$$p_{wall} = p_v + \rho_l(T_l) \cdot g \cdot H_l \tag{1.21}$$

During pool boiling experiments, when the liquid temperature is uniform in the whole volume of liquid and equal to the saturation temperature corresponding to the vapor pressure (this was experimentally verified for the experiments described in this manuscript - see Section 2.1.4.1) the saturation temperature rises due to the increase of local pressure. This increase of saturation temperature induces a pressure-induced subcooling which can be defined as the difference between local saturation temperature and liquid temperature. At the wall level, this subcooling can be expressed as:

$$\Delta T_{sub_{wall}} = T_{sat}(p_{wall}) - T_l \tag{1.22}$$

The importance of the pressure-induced subcooling at low pressure is schematically presented in Fig. 1.5. The first two cases (1.5a, 1.5b) show the boiling environment for the same vapor pressure $p_v = 5$ kPa and two liquid levels ($H_l = 10$ cm and 60 cm). The difference in the liquid height influences the value of the pressure at the wall, which is almost twice as high for $H_l = 60$ cm. This affects the local saturation temperature at the wall level, as well as the value of subcooling which increases from 4 K up to 13 K. To obtain the same pressure at the wall level and for the highest liquid height ($H_l = 60$ cm), the vapor pressure has to be reduced (see Fig. 1.5c). In this case, the liquid bulk temperature changes, also resulting in a variation of subcooling inside the pool.

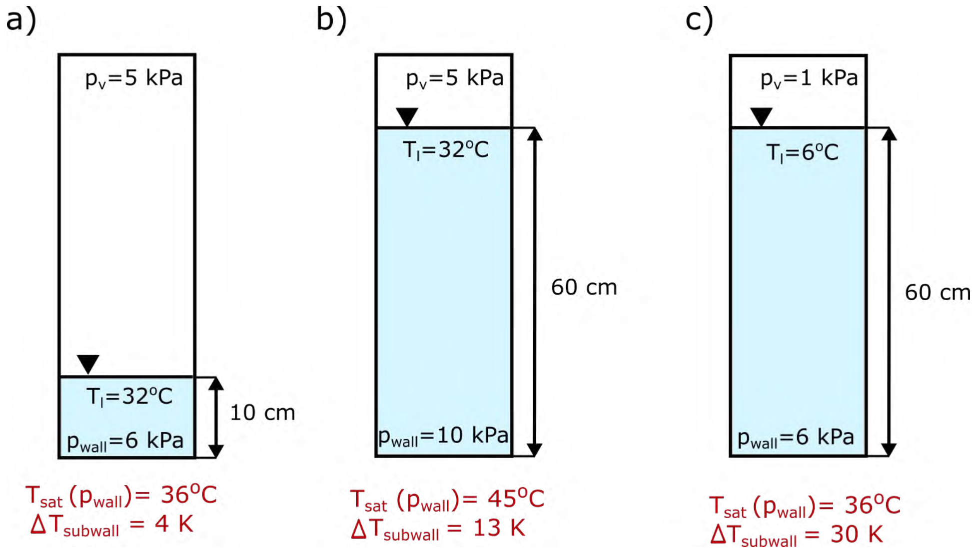

Figure 1.5: Configuration of three different situations of low pressure pool boiling highlighting the pressure-induced subcooling.

The influence of subcooling is stronger for higher liquid levels. Calculated values of pressure, saturation temperature, liquid temperatures and subcooling at the wall level for four various liquid heights (15 cm, 28 cm, 35 cm, 60 cm) are presented in Tab. 1.7. All the values of fluid thermophysical properties or liquid-vapor equilibrium data are taken from the open-source library of fluid properties CoolProp [7].

Table 1.1: Boiling parameters of water ($p_v = 3.1$ kPa, i.e. $T_{sat} = T_l = 24.6$°C)

H_l	15 cm	28 cm	35 cm	60 cm
p_{wall}	4.6 kPa	5.8 kPa	6.5 kPa	9.0 kPa
$T_{sat}(p_{wall})$	31.3°C	35.7°C	37.7°C	43.7 °C
T_l	24.6°C	24.6°C	24.6°C	24.6 °C
$\Delta T_{sub_{wall}}$	6.6 K	11.0 K	17.5 K	19.1 K

1.2.2 Thermophysical properties of water close to the triple point

As explained in Section 1.2.1, the liquid subcooling induced by the static pressure has a noticeable impact on the boiling process if the vapor pressure is low. Apart from that, many thermophysical parameters also vary a lot with the pressure when it approaches the triple point pressure.

First of all, the relation between the saturation temperature and the saturation pressure is exponential. Fig. 1.6 presents the value of saturation pressure as a function of saturation temperature for water close to its triple point. It is visible that the increase of saturation temperature from 5°C to 10°C increases the saturation pressure by 0.5 kPa. The increase of saturation temperature from 25°C to 30°C already results in a pressure increase of 1.1 kPa. This means that the subcooling induced by a given static pressure increases when the vapor pressure decreases and get closer to the triple point pressure.

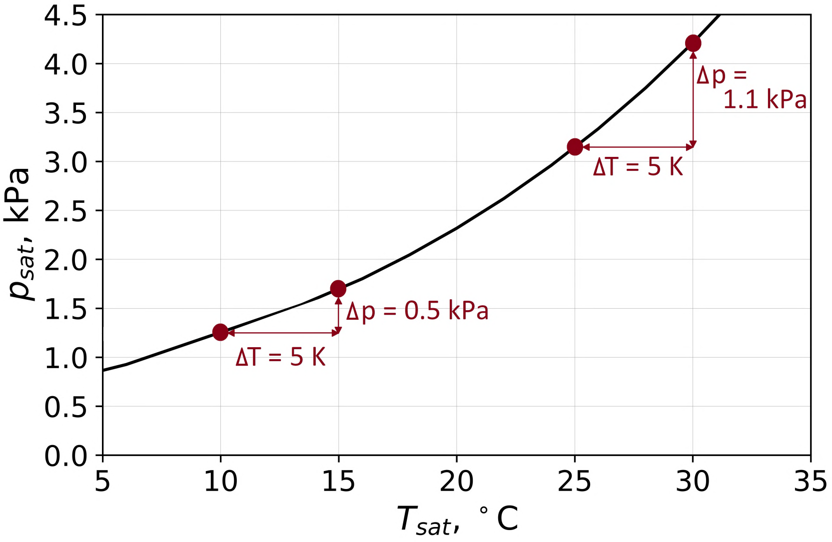

Figure 1.6: The relation between saturation temperature and pressure for water close to the triple point.

The comparison of several thermophysical parameters of water under atmospheric and low pressures ($p_{sat} = 100$ kPa and 2 kPa) is presented in Tab. 1.2. Not all listed parameters are responsible for the characteristic features related to the phase change at proximity to the triple point. Density, heat capacity or heat conductivity of liquid do not change more than 10% in comparison to atmospheric conditions. Among all properties listed in Tab. 1.2, the most intense change is observable for surface tension σ, liquid viscosity μ_l and vapor density ρ_v. The change of those parameters for a wide range of saturation pressure is presented in Fig. 1.7.

Table 1.2: Basic thermophysical parameters of water for atmospheric and low pressure (p_{sat} = 2 kPa). Obtained by open-source library of fluid properties CoolProp [7].

Parameter	p_{sat} **= 100 kPa**	p_{sat} **= 2 kPa**
Saturation temperature	100°C	17.6°C
Heat of evaporation	2257 kJ/kg	2484 kJ/kg
Surface tension	0.059 N/m	0.073 N/m
Liquid density	959 kg/m^3	998 kg/m^3
Vapor density	0.590 kg/m^3	0.015 kg/m^3
Liquid heat capacity	4.22 kJ/kgK	4.19 kJ/kgK
Liquid heat conductivity	0.68 W/mK	0.59 W/mK
Liquid viscosity	0.28 mPa·s	1.07 mPa·s

1.2.2.1 Surface tension

At p_v = 2 kPa, the value of surface tension rises by approximately 24% in comparison to atmospheric conditions (see Fig. 1.7 a). It is an important aspect as surface tension strongly influences heat and mass transfer of the two-phase systems [79, 111]. Surface tension is considered to be the most important force that opposes to bubble detachment. Its lower value tends to reduce the bubble diameter.

1.2.2.2 Liquid viscosity

Viscosity is responsible for the internal frictional force that arises between fluid layers that are in relative motion. It characterizes a fluid resistance to flow. The viscosity of water increases exponentially with the decrease of saturation pressure (see Fig. 1.7 b). The increase of liquid viscosity by almost 4 times for low saturation pressure indicates that at such conditions viscous effects might be considered affecting drag and inertia forces [81].

1.2.2.3 Vapor density

The vapor density decreases when the pressure decreases (see Fig. 1.7 c). As vapor density is inversely proportional to specific volume, its low value near the triple point is mostly responsible for large bubble diameters. It also increases the importance of the inertia and drag forces, despite the minor decrease of surface tension. Significant increase in the bubble size at low pressure is confirmed by various experimental studies [38, 45, 82, 95, 99, 115, 127].

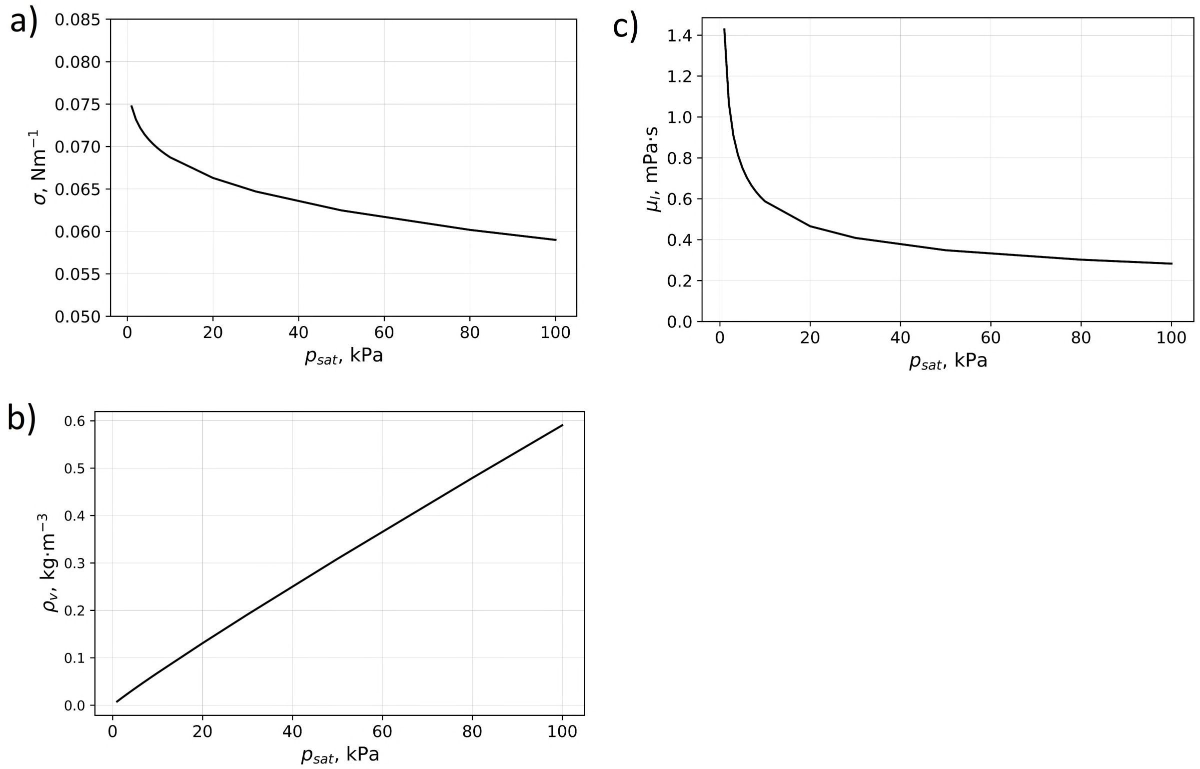

Figure 1.7: The relation between saturation temperature of water and a) surface tension, b) liquid viscosity, c) vapor density.

1.2.3 Bubble dynamics

Three main characteristic features are reported by researchers in respect to the bubble dynamics at low pressure: a reduced density of active nucleation sites, large bubble size at the moment of detachment and long waiting period between two successive bubbles (i.e. low bubble frequency) [38, 45, 82, 95, 99, 115, 127].

Pioro at al. [95] observed that bubble growth rate and bubble diameter at the moment of detachment increase with the reduction of pressure. For water at atmospheric pressure those values are determined as 10 mm/s and 1 mm, while for the lowest studied pressure (22 kPa): 500 mm/s and 100 mm. In the case of bubble frequency, the pressure reduction results in initial increase of bubble frequency. The maximum is reached for pressure of 220 kPa (f_b = 70 Hz). After that point, the bubble frequency starts to decrease. At minimum studied pressure (22 kPa), the bubble detachment frequency was equal to 20 Hz.

Michaïe et al. [82] studied bubble dynamics from a single artificial cavity for several vapor pressures and liquid level $H_l = 15$ cm. They examined bubble size and shape, as well as bubble detachment frequency. They noted four major boiling behaviors depending on the applied value of vapor pressure. The video sequences recorded for five different vapor pressures are presented in Fig. 1.8. At atmospheric pressure (see a in Fig. 1.8), the bubbles are small (size of millimeters) and have nearly spherical shape. The decrease of pressure to the level of 25.1 - 84.6 kPa results in a occurrence of transitional boiling regime (see b in Fig. 1.8). The columns of bubbles are formed, as bubble frequency is still considerable and one bubble is forming quickly after another. At pressure p_v = 20 kPa (see c in Fig. 1.8), so-called mushroom-shaped bubbles are observable. They consist of two consecutive bubbles rising one after another, merging with each other and forming characteristic bubble shape. At the lowest studied vapor pressures (see d and e in Fig. 1.8), the bubbles initially have hemispherical shape. The flattened spheroid shape is considered to be typical shape in an environment which is non-homogeneous in temperature [74]. Then the bubble is pulled towards the liquid free surface and thin bubble neck is formed. At low pressure the decrease of pressure results in a significant increase of the bubble diameter. Also, the waiting time is increasing with the decrease of pressure (for a vapor pressure of few kPa, the waiting time can reach even few seconds).

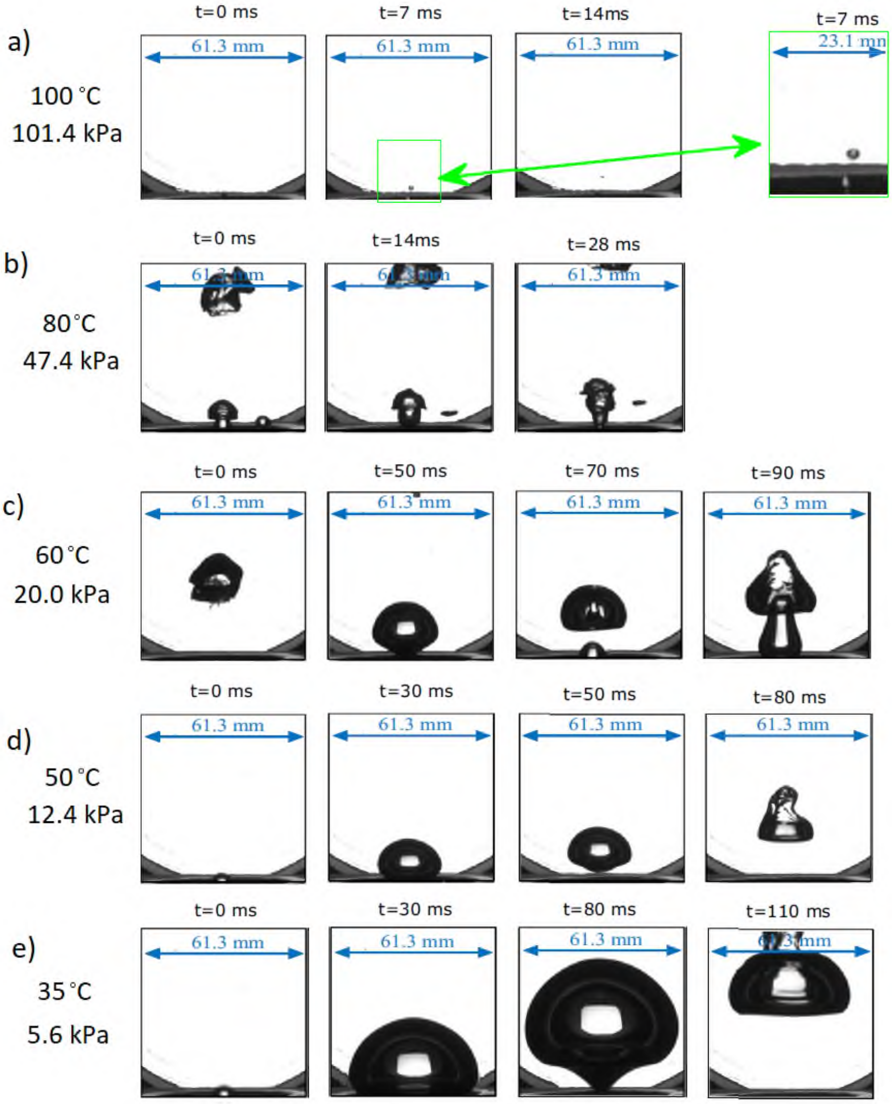

Figure 1.8: Typical bubble size and shape depending on the vapor pressure for $H_l = 15$ cm (extracted from [82]).

1.2.4 Heat transfer

Heat transfer during the boiling process is complex and depends on the variety of parameters such as: thermophysical properties of the working fluid, surface characteristics, presence of impurities and non-condensable gases dissolved in the liquid. It also strongly depends on the operating temperature and pressure [99, 116, 127, 131]. Depending on the working conditions, different heat transfer regimes during boiling process occur (see Section 1.1.1). During nucleate boiling regime, the generated bubbles often merge or interact with each other causing movement of the liquid pool. If the waiting period between two successive bubbles is small, the resulting lift force can help the next bubbles to detach in shorter period of time. Consequently, the type of the bubble dynamics influences the resulting heat transfer.

Giraud et al. [41] observed a new boiling regime occurring only at low pressure and for a sufficiently high level of liquid (above 50 mm) called ”cyclic boiling regime”. It is characterized by major variations of instantaneous heat flux and wall temperature through the process while a constant heat flux is applied by the back face of the heater block. Fig. 1.9 presents the instantaneous value of heat flux as a function of wall superheat for cyclic boiling regime, as well as for single-phase convection and fully developed boiling. The latter two display very stable values of heat flux and wall superheat (see green squares and red triangles in Fig. 1.9 - what appear as a single dot is in fact the superposition of 200 measurements during 600 seconds). For cyclic boiling regime the values of heat flux and wall superheat are constantly changing (see blue circles in Fig. 1.9). The authors observed that when the liquid level is reduced, the cyclic boiling regime is less prone to occur. This is probably related to the temperature gradient along the liquid height which strongly depends on the applied level of liquid.

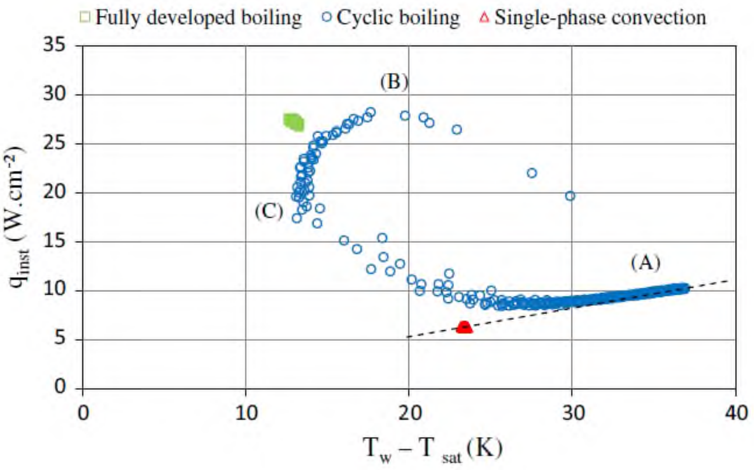

Figure 1.9: Instantaneous heat flux as a function of wall superheat for natural convection, fully-developed boiling regime and cyclic boiling regime (extracted from [41]).

The heat transfer at low pressure displays totally different characteristics in comparison to atmospheric or higher pressures. The main differences concern: higher wall superheat required to start nucleation process, intense wall temperature fluctuation (around 10-15 K), lowered heat transfer coefficient and lowered value of critical heat flux [44, 80, 81, 85, 99, 108, 115, 116, 131, 138].

Despite many studies concerning boiling, both experimental and theoretical, there is still no unified theory which would provide universal mathematical model describing this process. Many aspects of the process are still poorly understood, e.g. it is still not known what makes some cavities being activated or not during boiling process. Existing literature contains many correlations used to determine heat transfer coefficient during boiling process, mostly empirical or semi-empirical. They were usually created for systems operating under atmospheric or higher pressures. Zajaczkowski et al. [131] tested the most popular correlations of heat transfer coefficient for water (pressure from 1 to 10 kPa) and methanol (pressure from 0.3 to 20 kPa) with experiments. It occurred that the real heat transfer coefficient is much smaller than values obtained by the most popular correlations describing heat transfer during boiling process. Only for water, when applied heat flux was low the obtained results fell within the measurement error for most of the correlations [44, 131].

Many authors connect lowered heat transfer coefficient occurring at low pressure with the reduction of the number of active nucleation sites and long waiting time between two successive bubbles. In order to improve systems working close to the triple point, various studies tried to increase number of active nucleation sited by applying enhanced surfaces and by this way act on an improvement of heat transfer coefficient [1, 16, 44, 80, 108, 131].

Conclusions

This chapter provides a literature review concerning the phenomenon of pool boiling on a flat surface. This is necessary to properly interpret the experimental results discussed in the next Chapters.

The phenomenon of pool boiling of water at subatmospheric pressure presents many significant features with respect to atmospheric pressure. A pressure-induced subcooling induced by the static head of liquid introduces an inhomogeneity of the boiling environment and affects the bubble dynamics. At low pressure, the growing bubbles possess large size and the waiting time between two successive bubbles is long. There is also a reduced number of active nucleation site resulting in a lowered heat transfer. The commonly used correlations for heat transfer coefficient are no longer valid at low pressure. Wall temperature fluctuations (of 10 or even 15 K) can also be noticed under some circumstances.

Most of the studies presented in the literature were performed for a moderate level of liquid (H_l less than 15 cm). However, in order to better understand the boiling behavior at low pressure, it is crucial to investigate the effect of subcooling caused by the level of liquid and experimentally verify the boiling behavior for higher levels of liquid. The test bench utilized during work described in this manuscript is presented in Chapter 2. The analysis will be firstly performed for a single nucleation site (Chapter 3) to capture bubble dynamics of isolated bubbles. Then, the boiling process from a rough surface with multiple cavities will be described (Chapter 4) in order to investigate the configuration which is closer to a real applications.

Chapter 2

Experimental set-up and method

The objective of this chapter is to provide necessary information concerning the test facility employed for this thesis, experimental procedures and processing techniques used to describe the boiling or evaporation processes at low pressure. Section 2.1. focuses on the description of the vacuum-tight vessel, as well as on the heated surface equipped with a novel heat flux sensor. The specification of the acquisition system is also featured. Section 2.2. outlines the main experimental procedures which were applied for all performed tests. The data analysis and processing techniques which facilitated the determination of the sensor's zone limits or specific lengths during visualizations (e.g. bubble foot or bubble diameters, drop size) are included in Section 2.3.

2.1 Experimental facility

2.1.1 Overall view of the installation

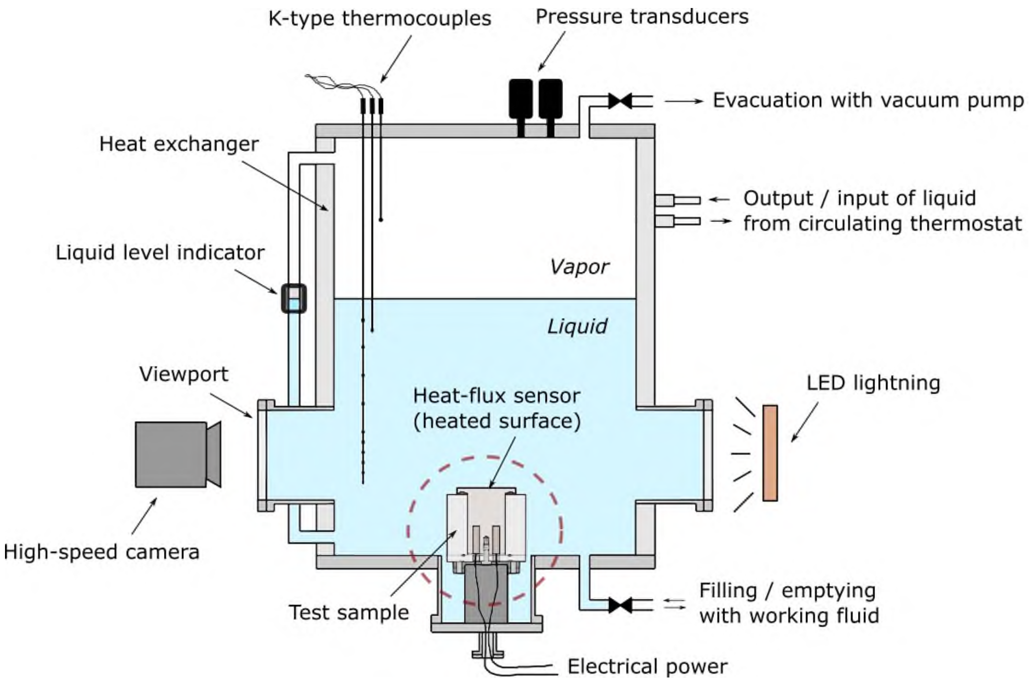

Figure 2.1: Experimental apparatus used for the experiments.

The main section of the experimental facility consists of a stainless steel cylindrical vessel with inner diameter of 200 mm and height of 420 mm (see Fig. 2.1). Four circular viewports with inner diameter of 100 mm allow for the visualization and observation of the boiling process. One viewport is used to illuminate the boiling area, while at the opposite one a high-speed camera is placed. A third viewport contains a home-made feedthrough for the sensor wires. All components were fabricated according to ISO-K vacuum technology to maintain required value of vapor pressure inside the tank.

2.1.2 Test heater

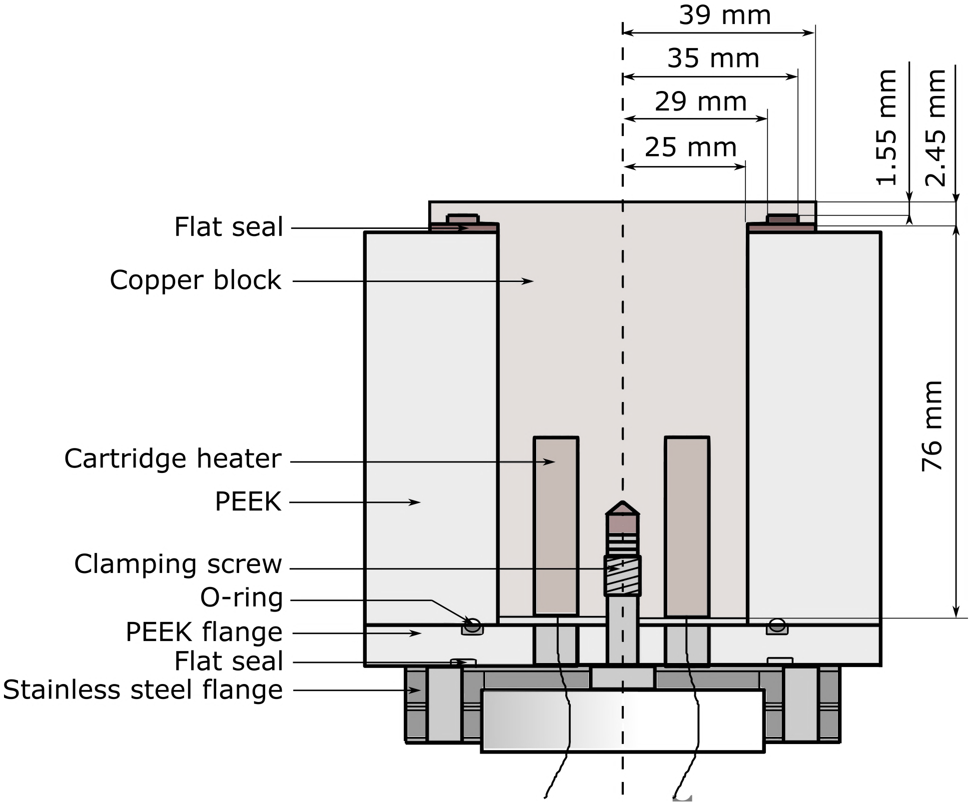

Figure 2.2: Detailed sketch of the test heater.

The test heater is a copper cylinder (diameter 50 mm, height 80 mm) and it is placed at the bottom of the vessel (see Fig. 2.1). Fig. 2.2 presents a more detailed schematic of the test sample. The copper block possesses an overhanging disc section with diameter of 78 mm and variable thickness (between 2.45 mm and 4 mm) in order to limit heat transfer in the radial direction, reduce peripheral boiling, and promote nucleation at the centeral part of the wall (what is important when a case of isolated bubble on a single nucleation site is studied). Two cartridge heaters (maximum power 450 W) are inserted from the bottom to provide sufficient heat flux to start nucleation process. The copper cylinder is insulated with a PEEK part and the resulting copper/PEEK block is then attached to a PEEK flange. Furthermore, the assembled set is attached to a stainless steel flange allowing for rigid connection with the vacuum vessel. O-ring and flat seals between different parts provide high vacuum tightness of the heater. The top of the heater is equipped with the heat flux sensor. This upper part creates the heated surface on which the boiling process takes place.

2.1.3 Operation principle of heat flux sensor

Heat flux sensors are commonly used to measure average values of heat flux transferred through a surface (in this manuscript - through the heated wall on which the evaporation or the boiling process occurs). Two main types of the heat fluxmeters can be distinguished: transient and stationary [90]. The first one associate the mass (m) and specific heat (c_p) to the absorbed amount of heat (Q) over a time interval. The second, more often used, is based on Fourier's law of conduction and relates heat flux q transferred through a body with known thermal conductivity with certain ΔT.

Another distinction is based on the way in which the sensor measures the temperature difference. If ΔT is measured in a direction transverse to the surface where the heat flux is evaluated, this is a transverse gradient fluxmeter. In the experiments described in this thesis, the applied sensor operates based on the tangential gradient method of measurement. In such device, there is a modification of the heat flux lines in a plane tangential to a plane of the measurements. The heat flux lines are deviated due to presence of the copper pins (visible in Fig. 2.3 b). This temperature difference is measured by the multiple junctions connecting metals with different thermoelectric power (e.g. copper and constantan) deposited on a thin layer of insulant (e.g. Kapton). This temperature difference is converted into Seebek electromotive force. The measurement of the electromotive force, along with the sensor sensibility, allows to obtain the value of heat flux crossing the sensor. The schematic of the tangential type heat flux transducer is presented in Fig. 2.3 This kind of sensor possesses many advantages in comparison to other types, such as high sensitivity and reduced thickness [90].

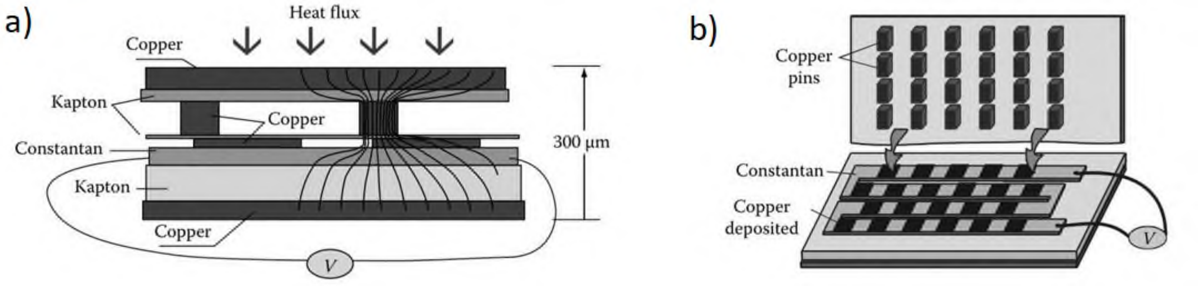

Figure 2.3: The schematic of operational principle of the tangential heat flux sensor a) cross-section, b) open view (extracted from [90]).

2.1.4 Discretized heat flux sensor used for the experiments

A customized discretized heat flux transducer is embedded to the upper part of the copper cylinder. The sensor has thickness of 0.5 mm and diameter equals to the diameter of the heated surface (78 mm). It is divided into seven annular zones allowing for independent measurements of heat flux at each section. The schematic of the sensor is shown in Fig. 2.4.

A part of the sensor's edge is covert by a ribbon cable with sixteen connections. Two pins per zone (thus fourteen connections) are associated with average heat fluxes in all seven zones. The two remaining connections are used to measure temperature difference between the connection ribbon cable and the center of the sensor ΔT. This facilitates the determination of the temperature at the center of the surface T_{center} which is calculated as the sum of temperature of the connecting cable T_{co} and ΔT. The temperature of the connecting cable T_{co} is measured with an independent T-type thermocouple. The uncertainty of the heat flux measurement is equal to ± 3%, while for thermocouples it is ± 0.5 °C.

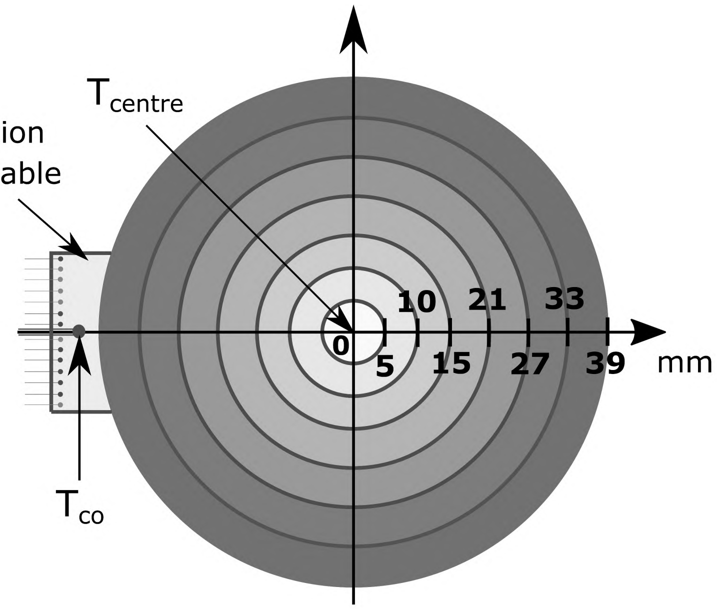

Figure 2.4: The schematic of heat flux sensor divided into seven concentric zones (first zone is in the center of the surface, seventh - at the periphery).

In most applications, heat flux sensors are used between two solid surfaces or sometimes between a surface and a surrounding gas. In the present experiments, the sensor is used to determine the heat flux between a surface and the surrounding liquid. To avoid liquid penetration, which could damage the sensor, an additional layer of acrylic clearcoat was deposited at the periphery of the fin surface after the sensor was glued to the copper block. The same varnish was used on the ribbon connection cable to electrically insulate the wires welds from the working fluid. A small layer of epoxy was also added on the sides of the surface to limit peripheral boiling. To avoid air penetration through the wires which have direct contact with low pressure side, the layer of cyanolite was applied at both ends of sensors' wires.

The top surface of the sensor is covered with a 0.3 mm thick copper foil. This allows for a proper surface treatment - polishing by a diamond paste and creation of an artificial cavity (such configuration was used for the test with a single nucleation site created at the center of the wall - see Chapter 3). To obtain multiple nucleation sites over the surface and promote more intense boiling process, the heated wall was roughened with emery paper resulting in an increased roughness of the surface (see Chapter 4). The rough surface was also used to study the evaporation process of small drop deposited on a hot surface (see Chapter 5). The basic surface characteristics, such as the nucleation site size (diameter 116 μm, depth 160 μm) and the surface roughness (0.4 μm for the studies with the single nucleation site and 3.5 μm for the test with multiple nucleation sites) were confirmed by means of a confocal microscope. The methodology of roughness measurements and graphs presenting measured values are available in Appendix A.

The sensitivities of the heat flux measurement for each zone are presented in Tab. 2.1.

These values were estimated during the calibration process conducted by the manufacturer of the sensor.

The heat flux for each zone can be calculated as the voltage output divided by the sensitivity of the given measurement zone:

$$q_n = \frac{U_n}{s_n} \tag{2.1}$$

The average heat flux for multiple zones (numbered from j to k) is determined as the average of individual heat fluxes weighted by their corresponding areas:

$$q_{j-k} = \frac{\sum_{n=j}^{k} q_n A_n}{\sum_{n=j}^{k} A_n} \tag{2.2}$$

The sensitivity of the temperature difference between the connection zone and the center of the heater ΔT is estimated as $s_{\Delta T} = 32\ \mu\ \mathrm{V} \cdot \mathrm{K}^{-1}$. The temperature difference is then calculated by dividing the signal output by this value of sensitivity:

$$\Delta T = \frac{u_{\Delta T}}{s_{\Delta T}} \tag{2.3}$$

Table 2.1: Sensitivities of measurement zones of the heat flux sensor (from zone 1 at the center to zone 7 at the periphery).

Zone number	**s, μ V(Wm^{-2})$^{-1}$**
Zone 1	0.667
Zone 2	2.50
Zone 3	4.14
Zone 4	8.02
Zone 5	11.7
Zone 6	14.1
Zone 7	13.8

2.1.4.1 Example of the signal output of the sensor for boiling on a single site

A typical example of the signal output of the sensor is presented in Fig. 2.5. To facilitate the understanding of the heat flux evolutions at each zone due to presence of the bubble, the analysis was performed for a polished surface with one artificial cavity at the center. Initially, as there is no bubble present on the surface, all heat fluxes are constant. Their values vary in respect to the distance from the center, as each section transfers different amount of heat. Nucleation (marked by point A in Fig. 2.5) and bubble growth cause a sudden increase of heat flux in the zones covered by the bubble. After detachment (point B in Fig. 2.5), the heat fluxes gradually return to their initial values. The sensor was observed to be highly sensitive to any event happening on the surface. Even bubbles of small diameter (few millimeters) actually cause a noticeable rise of heat flux. Peripheral boiling occurred frequently: such bubbles growing at the edges of the heater also caused detectable fluctuations of heat fluxes mainly at zones 6 and 7.

The value of the time constant of the sensor was estimated to be about 1 s (while bubble growth time would be of the order of magnitude of 0.1 s). Although all the heat flux curves have proper shape and measurements are well synchronized with camera recordings, the actual values of q are dampened. That is why only qualitative analysis of the bubble dynamics can be performed with the proposed sensor, which nevertheless can provide original insight into the phenomena.

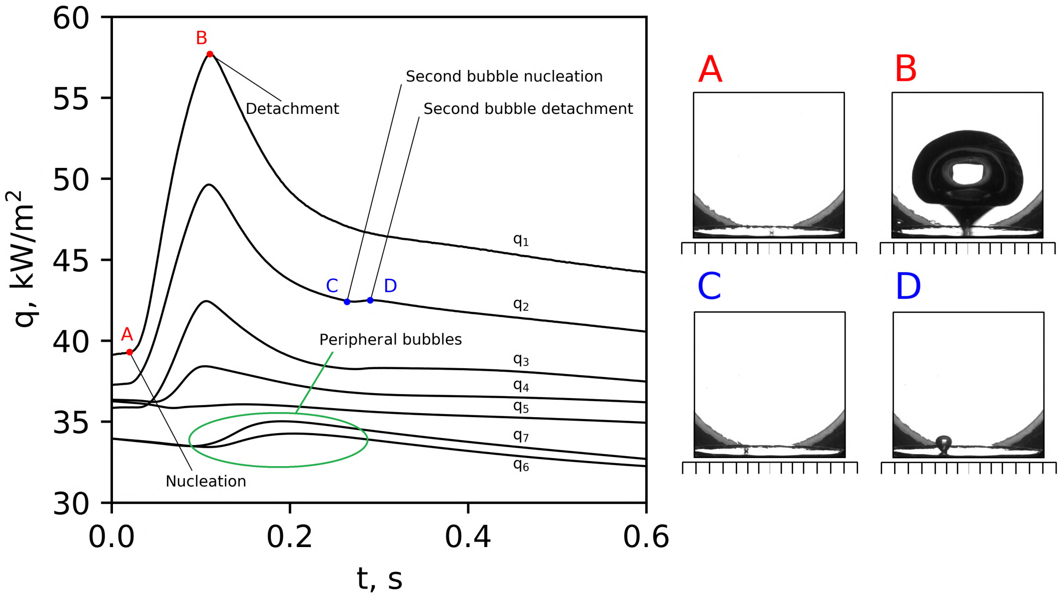

Figure 2.5: Example signal output of the sensor (p_v=4.1 kPa).

2.1.5 Acquisition system

2.1.5.1 Measurements of boiling environment

Temperature and pressure in the tank can be adjusted with a heat exchanger, jacketed around the vessel's wall and connected to a thermostated flow of water (with temperature in a range 0 - 40°C). The saturation pressure is monitored with two pressure transducers with operating pressures ranges 0 - 100 kPa and 0 - 16 kPa. Their accuracy is 0.25% of their full scale range (i.e. ±250 Pa and ±40 Pa respectively).

The temperature of the medium inside the vessel is monitored with twelve K-type thermocouples. The thermocouples named T_{low} and T_{high} on Fig. 2.6a measure temperature of liquid or vapor, depending on the applied liquid level. The remaining ten thermocouples 2.6a) form a multi-point probe (diameter 6 mm) and are spread across the distance of 15 cm. Their location was set in such a way that thermocouple T_1 is located at the same level as the heated wall. The other thermocouples are positioned more densely in the proximity of the surface level (T_1 to T_6) - see Fig. 2.6 a.

The temperature measurements inside the liquid pool for liquid level of 15 cm confirmed that the liquid temperature field in the vessel is fairly homogeneous (see Fig. 2.6 b). The difference between temperatures measured by thermocouples T_1 - T_9 and bulk liquid temperature T_{liq} never exceed 0.5 K. For this example, only the temperature measured by the thermocouple at the free surface level T_{10} was noticeably lower, because the sensor was placed on the liquid-vapor interface where vaporization occurs, which requires a heat extraction. The exact location of all thermocouples was determined with accuracy ± 0.2 mm.

Before running the tests, all thermocouples (thermal probe and also thermocouples T_{low}, T_{high}) were immersed in a thermostatic bath with a reference temperature probe (a calibrated Pt100) in order to perform their calibration. The electromotive force was measured for several temperatures in a range from 0°C to 100°C. This process produced calibration curves with estimated accuracy of ± 0.15 K. This value seems to be acceptable, especially taking into account high acquisition frequency. The T-type thermocouple T_{co} which is placed at the connection cable of the sensor was not recalibrated (the sensor itself was calibrated by manufacturer).

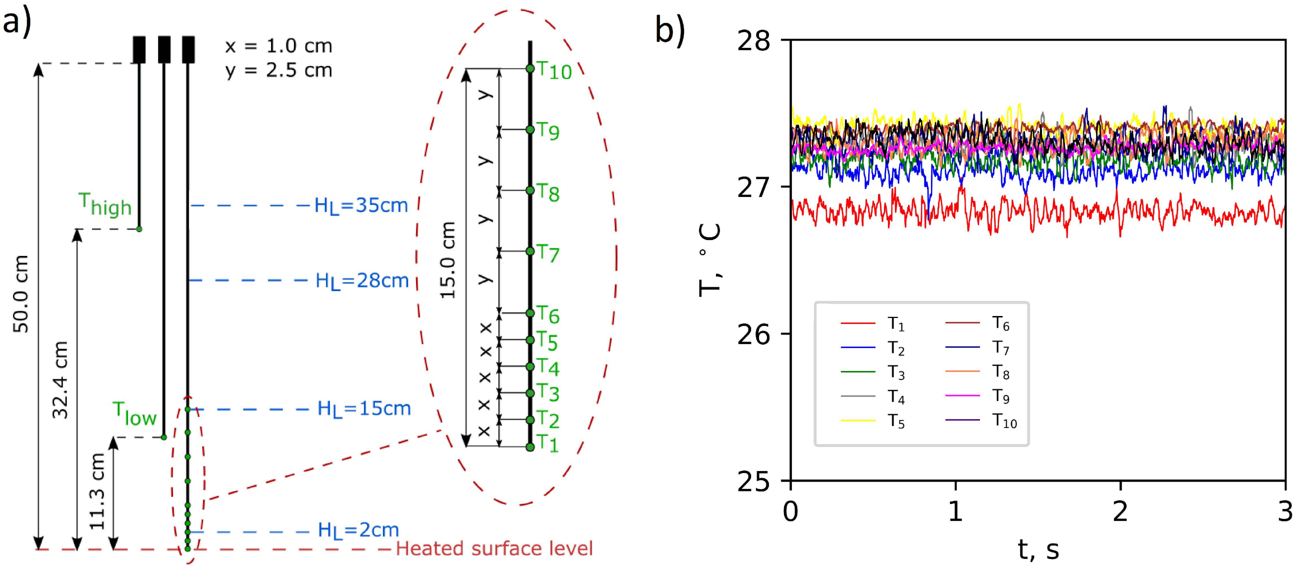

Figure 2.6: (a) Positioning of thermocouples, (b) Example measurement for H_l=15 cm.

2.1.5.2 High-speed camera recordings

The sample is located at the bottom region of the vessel (see Fig. 2.1) in such a way that the whole heated surface is visible through viewports. At one side, the high-speed camera is placed (Photron Fastcam 1024 PCI). At the opposite a white LED device

(Phlox SLLUB white led Backlight 100 mm x 100 mm) illuminates the boiling area with very intense homogenous light (luminance: 53 000 cd·m^{-2}, uniformity: 98.77%). This recording setup creates images of good contrast whilst maintaining sharpness of focus.

The Photron Fastcam Viewer (PFV) software control the operation of high-speed camera. It allows selection of the size of the image (maximum size: 1024 x 1024 px, minimum size: 128 x 16 px) and the acquisition frequency (1 Hz, 60 Hz, 125 Hz, 250 Hz, 500 Hz, 1000 Hz).

To obtain the best resolution with respect to an image size and duration of the video, the following parameters were applied:

- For the boiling process (Chapter 3 and 4): picture size: 1024 x 1024 px, acquisition frequency: 500 Hz, measurement step: 0.002 s, recording time: 3.072 s;
- For the evaporation process (Chapter 5): picture size: 1024 x 512 px, acquisition frequency: 125 Hz, measurement step: 0.008 s, recording time: 24.576 s.

The recordings could be performed in two triggering modes: 'start mode' (the recording starts simultaneously with the triggering of the camera) and 'end mode' (the moment when the experimenter trigger the camera corresponds to the last recorded image). To allow for the synchronization between visual observation and thermal measurements, the camera has to be used in the 'start mode'. After the end of the video recording, the thermal measurements still continued until the experimenter manually stopped the LabVIEW program.

2.1.5.3 Instrumentation system

As mentionned earlier, the high-speed camera possesses its own acquisition software PFV and the camera is connected to the first computer (PC1) via an acquisition card.

The other signals (from the thermocouples, heat flux sensor, pressure transducer, power supply) have to be conditioned before being acquired. The customized box with all electronics required for signals conditioning was designed and build in the laboratory and it is exactly the same as that used in [81]. It consists of four diffferent electrical circuits (for the thermocouples signals, for the singals of the heat flux sensor, for the pressure transducers and for the heating power). The delivered heating power is estimated as the multiplication of voltage U_{app} and current I_{app}:

$$HP = U_{app} \cdot I_{app} \tag{2.4}$$

After conditioning, the signals are acquired by a customized National Instrument (NI) module, which is connected to a second computer (PC2). This computer facilitates the recording, display and storage of the thermal measurements through a dedicated LabView program. The whole acquisition system with signals diagram is schematically shown in Fig. 2.7. The list of acquired signals with respect to the signal range and name of the NI module to which they are connected is described in Tab. 2.2.

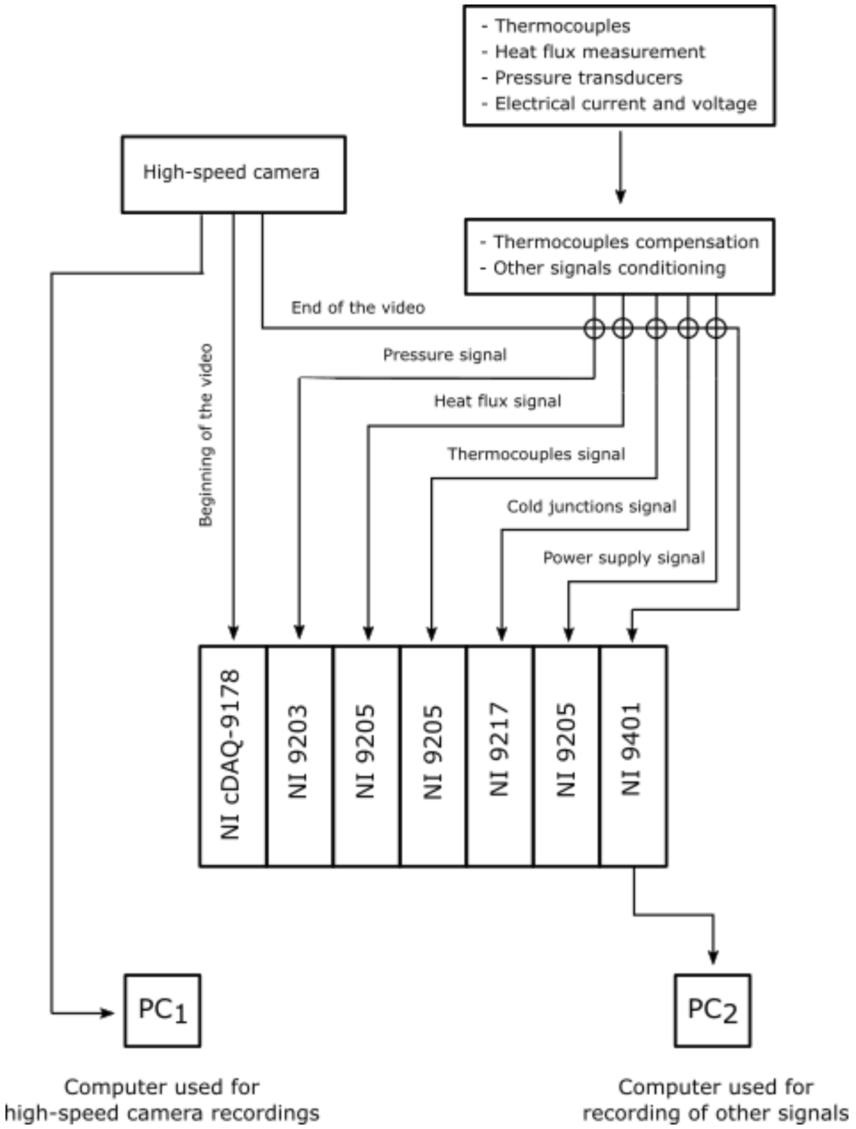

Figure 2.7: Schema of the acquisition system used for the experiments.

Table 2.2: Measurement ranges of the signals and their corresponding NI modules.

	Signal range	**NI module**
Thermocouple	± 200 mV	NI 9205
Pt100	0 - 400 Ω	NI 9217
Heat flux measurement	± 200 mV	NI9205
Pressure transducer	4 - 20 mA	NI 9203
Heating power supply	0 - 10 V	NI 9205
High-speed camera trigger	TTL	NI cDAQ-9178
End of the video recording	TTL	NI 9401

2.2 Experimental procedures

2.2.1 Filling the vessel with working fluid

For the purpose of pool boiling experiments (Chapter 3 and 4), the vessel is filled with distilled water (see Fig. 2.8). During tests of drop evaporation (Chapter 5), the tank also contains some amount of liquid (in order to maintain uniform operating conditions), however the liquid free surface is always kept below the level of the heated wall and the liquid height is not the parameter of importance in such case (more details in Section 5.2).

The test tank is equipped with two valves. The top one allows the connection to a vacuum pump for reducing pressure and removing any non-condensable gases from the vessel. The bottom valve is used to fill and drain the working fluid from the vessel. The level of the liquid is determined using a liquid level indicator, i.e. a transparent tube. The height of liquid column is calculated as the difference between positions of the free surface (x_{liq}) and the heater surface where boiling process occurs (x_{wall}):

$$H_l = x_l - x_{wall} \tag{2.5}$$

Necessary measurements are made with a cathetometer with an uncertainty of ±0.1 cm. The schematic description of liquid level measurements is presented in Fig. 2.8.

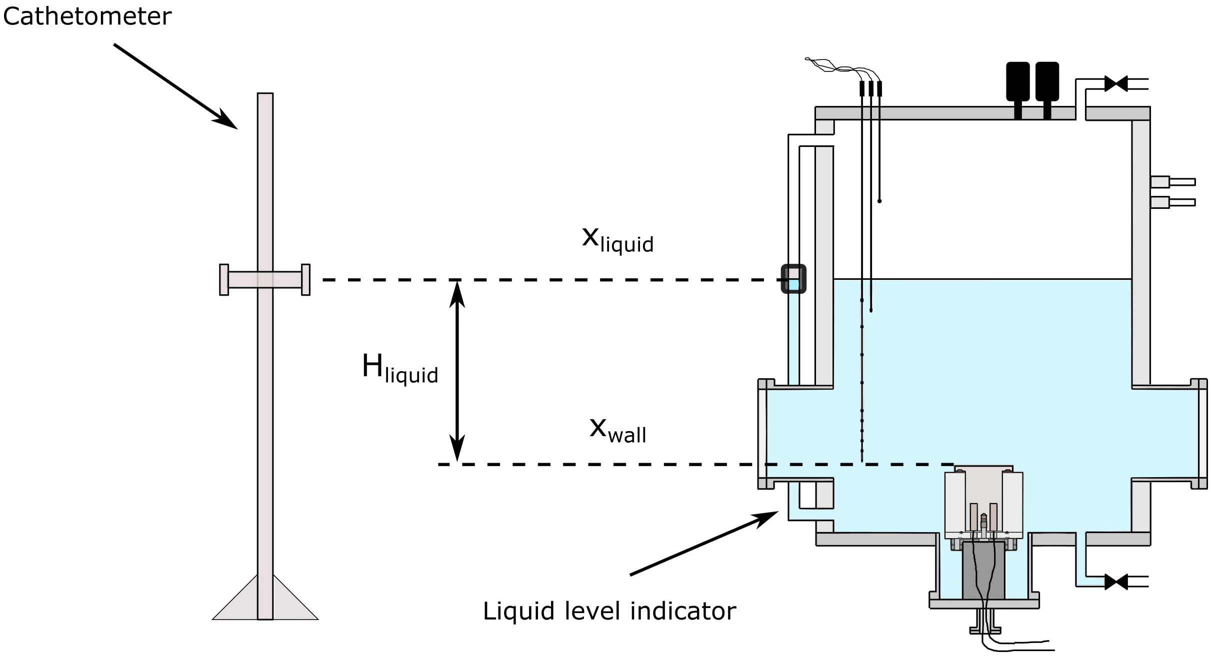

Figure 2.8: Liquid level estimation inside the vessel.

2.2.2 Setting the operating conditions

The required vapor pressure inside the tank is obtained by setting the desired value of liquid temperature at the circulating thermostat connected to the vessel's jacket (see Fig. 2.1). Depending on the amount of liquid inside the vessel, the system needed several hours to reach steady state.

The applied heating power is also set to the desired value (which can differ depending on the current demands). The heating power is gradually increased up to the maximum value. If several heating powers were studied successively, they were imposed by decreasing power (maximum heating power was examined first). At least 30 min waiting time between experiments with different heating powers was necessary to reach steady-state conditions.

2.3 Data analysis and processing techniques

Due to the parallax effect, two objects with the same size placed at different distances from the camera appear to have different dimensions. In the present experiments, the parallax effect significantly influences the perceived size of growing bubbles or falling droplets. In order to relate heat flux data to the images recorded with the high-speed camera, it is necessary to precisely determine the limits of each measurement zone.

Some recorded frames lack reference points that would allow for direct conversion of pixels into distances at the center of the heat flux sensor. It would be convenient to use the edges of the heating surface, but they are outside the scope of the camera. That is why for the pool boiling experiments, it is necessary to introduce a parallax correction factor. When liquid drop evaporation is studied, this approach is not necessary. The pipe used to generate the drop is always visible on the recordings, thus its diameter can be taken as a reference length.

2.3.1 Parallax correction factor

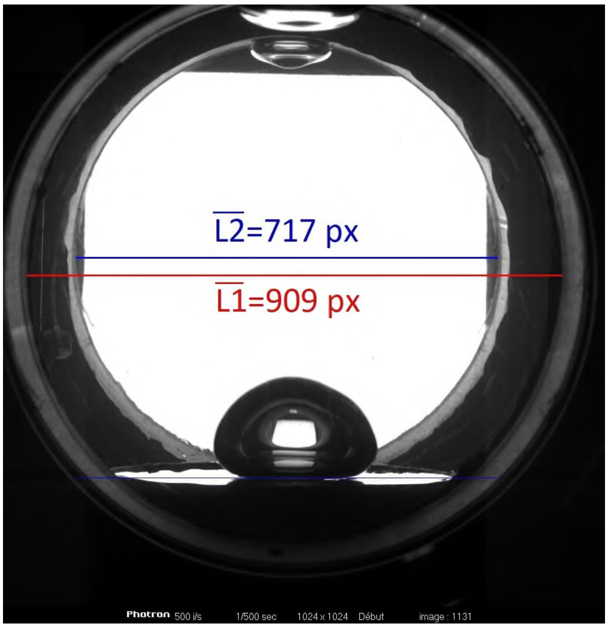

Figure 2.9: Difference in perceived diameters of viewports caused by the parallax effect.

The diameter of the viewports are 102 mm ± 1 mm and the edges of viewports are visible on all recorded frames (see Fig. 2.9). Image files allow the determination of their respective diameters in pixels (L_1 and L_2). The uncertainty of estimating L_1 and L_2 is caused by inaccuracy of determination of a viewport's edge on a given image, as welds, that are also visible on the picture, can obscure the actual diameter. There is also the possibility that the drawn line is not a diameter, but a chord. Based on multiple frames and drawn lines, it was estimated that the total error never exceed 5 pixels.

At the reference point 1: 102 mm translates to L_1 px and at the reference point 2: 102 mm translates to L_2 px (what corresponds to 909 px and 717 px respectively - see Fig. 2.9). Thus, at the center of the heating surface 102 mm equals to the calculated number of pixels $\overline{x}$.

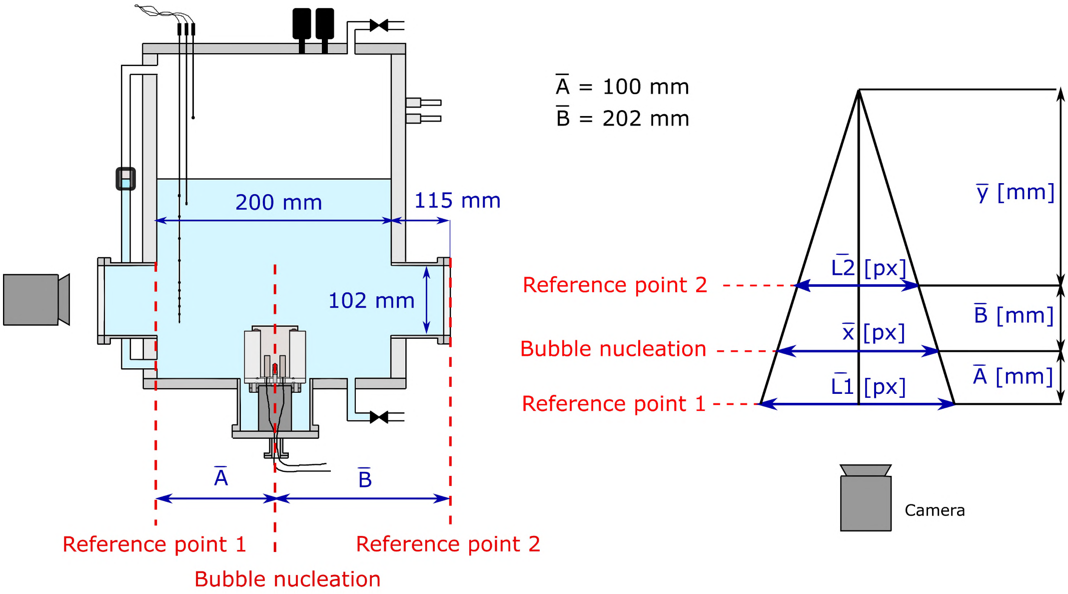

Figure 2.10: Reference points necessary to determine the parallax correction factor at the center of the boiling surface.

The exact position of two reference points used for the calculations and the distance conversion from pixels into millimeters is presented in Fig 2.10. Distances $\overline{L_1}$, $\overline{L_2}$, $\overline{A}$, $\overline{B}$ are known. Using similarity of triangles, both $\overline{y}$ and $\overline{x}$ (in Fig. 2.9 are calculated as follows:

$$\frac{0.5\overline{L_1}}{\overline{y}+(\overline{A}+\overline{B})} = \frac{0.5\overline{L_2}}{\overline{y}} \rightarrow \overline{y} = \frac{\overline{L_2}(\overline{A}+\overline{B})}{(\overline{L_1}-\overline{L_2})} \tag{2.6}$$

$$\frac{0.5\overline{L_2}}{\overline{y}} = \frac{0.5\overline{x}}{\overline{y}+\overline{B}} \rightarrow \overline{x} = \frac{\overline{L_2}(\overline{y}+\overline{B})}{\overline{y}} \tag{2.7}$$

The above equations allow the determination of the parallax correction factor at the center of the heating surface: 1 mm = $\overline{x}/102$ mm. If during experiments the camera position is adjusted in any way, the parallax correction factor needs to be re-calculated.

2.3.2 Image processing

Mirage effect can affect the perceived size of the recorded objects, e.g. bubble foot size. To reduce its impact on the accuracy of bubble size estimation (e.g. due to the mirage effect the estimated bubble foot diameter would be larger than the real one [108]), the camera was tilted by approximately 1°.

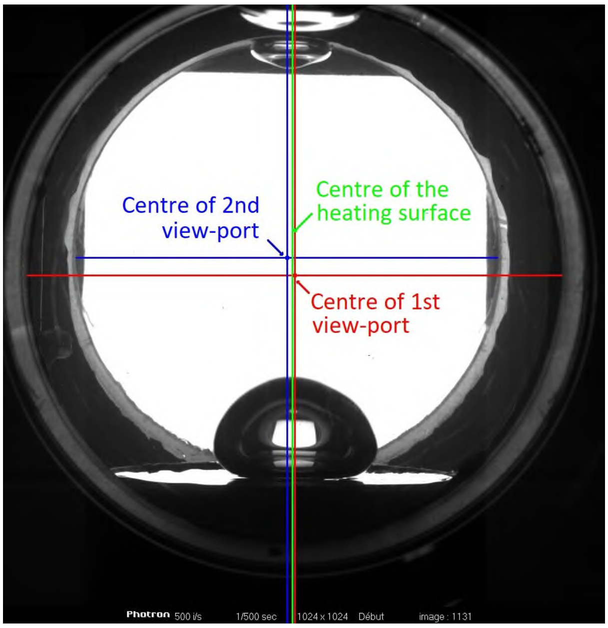

Figure 2.11: Construction for determination of the location of the center of the sensor.

2.3.2.1 Determination of the sensor's zones limit

Based on geometrical dimensions of the heat flux sensor used for the measurements (see Fig. 2.4) and taking into account the parallax conversion factor, the location of the measurement zones on recorded images was determined.

First, it is necessary to determine the location of the sensor center on a given frame using the viewports' diameters used during the calculation of the parallax correction factor (see Fig. 2.9). This allows location of the center of each viewport by drawing vertical line in the middle of each diameter (see Fig. 2.11).

As shown in Fig. 2.11 the centers of both viewports are not perfectly aligned, because small shifting of the camera in the horizontal direction cause minor displacements of the central lines of both sections. The center of the heating surface is determined in proportion to the distances from both viewports. The uncertainty never exceeds 3 px.

Knowing the location of the center of the surface, it becomes possible to determine the width of each measurement zone on the boiling surface. Measurement zones properly marked on a recorded frame are presented in Fig. 2.12.

The parallax correction factor and the location of each zone of the heat flux sensor are determined once for the entire experimental series (as long as the operational settings of the camera are not modified).

2.3.2.2 Calculation of the lengths from visualization

In order to relate the heat flux measurements to the corresponding recorded frames, it is necessary to develop a reliable method of estimation of the lengths for the entire series of images. This process needs to be automatic to obtain averaged characteristics over a large number of recorded frames. For this purpose, an in-house image processing script (written in Python) was developed. The steps of the processing algorithm are described below. The calculation of the bubble foot diameter was chosen as the example, although

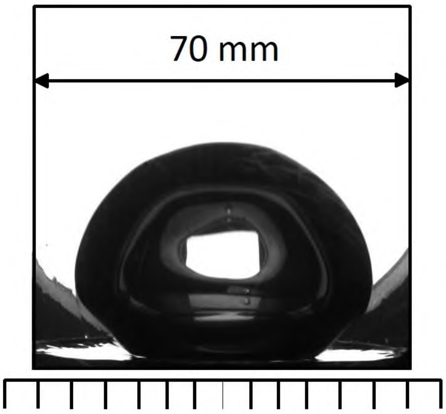

Figure 2.12: Heat flux sensor measurement zones, properly determined based on the parallax correction factor and the center of the heating surface.

this method of calculation could also be used to determine the bubble diameters (also for multiple nucleation sites) or drop size.

The process of image segmentation with a threshold value reduces noise and allows for accurate calculation of the distances on the treated images. The bubble foot diameter in this particular case was measured at the baseline, which is determined by the horizontal coordinate of the nucleation site on the frame. These two parameters, threshold value and horizontal position of the baseline, are the two most important factors determining the reliability of automated image processing, and as such need to be carefully evaluated.

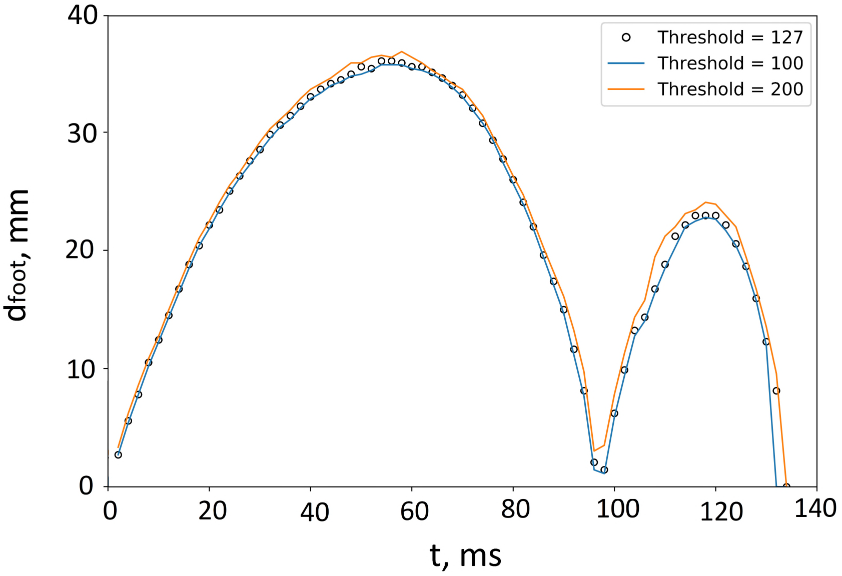

Figure 2.13: Difference between bubble foot diameters determined with three different threshold values.

Each experiment produces a series of grayscale photos depicting nucleation, growth, and departure of a bubble. The resolution of each frame is 1024x1024 pixels and each pixel assumes a value (grey level) between 0 (black) and 255 (white). Frames are then converted from grayscale image (0-255) to binary image (0-1) based on a predetermined threshold value. To calculate the bubble foot diameter, it is crucial to estimate a proper threshold value and baseline onto which calculations are made, as they affect obtained results.

Fig. 2.13 presents the time evolution of the bubble foot diameter for a mushroom-shaped bubble (which in fact consists of two consecutive bubbles) at three different greyscale threshold values (100, 127 and 200). The contrast of all analyzed photos obtained with high-speed camera is adequately high. As a consequence, the determined bubble foot diameter is insensitive to the selected threshold value, i.e. for threshold values between 100-200, the determined bubble foot diameter varies by max. 1-2 mm, i.e. changing the treshold value from 100 to 200 the obtained measurement error usually does not exceed 6% (it might only reach larger error values if the bubble foot is very small). For the analysis of the images, in the present series of experiments, the threshold value was set to 127.

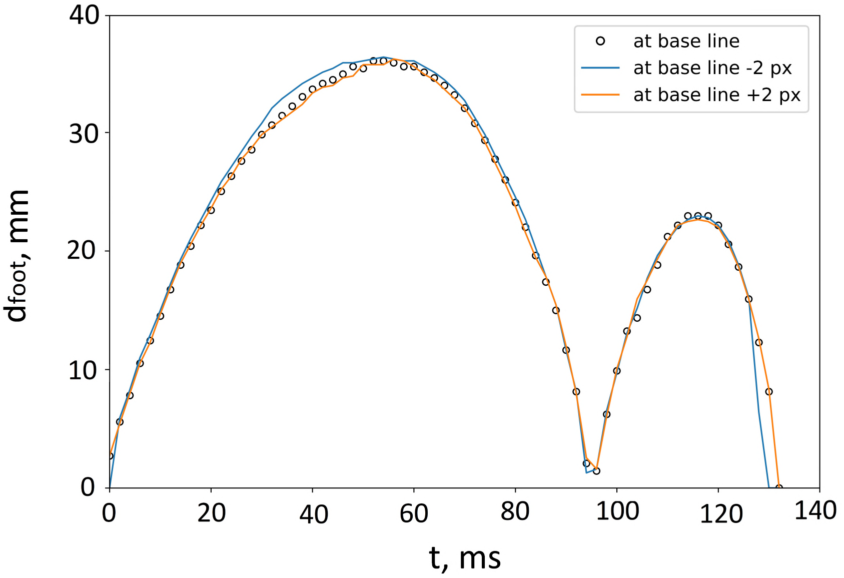

Figure 2.14: Difference between bubble foot diameters determined for three baselines.

The baseline, that is defined as the vertical coordinate of the position of the nucleation site, must be determined to perform the calculations of the bubble foot diameter. The sensitivity to an error in the baseline location can be assessed from Fig. 2.14, which represents the time evolution of the bubble foot diameter for a mushroom-shaped bubble for three neighboring baselines. It appears that within a 5 pixels range (baseline plus 2 pixels and baseline minus 2 pixels), the determined bubble foot diameter varies by no more than 1.5 mm and resulting measurement error is not larger than 5%.

Conclusions

The experimental facility facilitates the study of boiling or evaporation processes from a horizontal surface at low vapor pressure (up to the saturation temperature of 40°C, which for water corresponds to $p_{sat} = 7.4$ *kPa).*

The setup is flexible in its use: depending on the treatment of the heated wall, the boiling tests can be performed for the polished surface with a single nucleation site or for the rough surface where multiple cavities are activated simultaneously. Also, small sessile drops can be deposited on the surface in order to examine the evaporation process at low pressure.

The thermal measurements were supported by high-speed camera recordings to study the correspondence between heat transfer and bubble dynamics (or drop evaporation). Both parameters were synchronized to obtain an accurate overview of the boiling processes.

A method of the length calculations from visualizations was proposed, as there was no reference points on taken photographs. It was proven that this method is insensitive to the chosen threshold value or small offsets of the baseline on which the calculations are performed.

The novel heat flux sensor used in this work measures the heat flux evolution independently in seven annular zones of the sensor. This kind of transducer is especially beneficial while working at low pressure because of the large bubble sizes, which allows tracking of the motion of the bubble foot. To enable to broad analysis, the first tests were performed for a single bubble nucleated at the center of the heated surface. This approach was not been described in the literature previously, however it is crucial in the context of gaining deeper understanding of the boiling phenomenon. This is the scope of the upcoming chapter.

Chapter 3

Evaluation of the applicability of a novel heat flux sensor to study bubble dynamics

The heat flux sensor described in the previous chapter consists of seven concentric zones which independently measure value of instantaneous heat flux at each section. The analysis should be focused on the bubble foot as the part of a bubble in direct contact with the heating surface. This is an innovative approach and a good indication for studying growth of low-pressure bubbles.

This chapter describes the experimental investigation of water pool boiling which were conducted at low vapor pressure and upon a mirror-polished surface with an artificial cavity at the center. Section 3.1 contains a short introduction of measurement techniques used by different researchers to study boiling phenomenon. It also describes why the heat flux sensor is a good tool to study bubble dynamics at low-pressure conditions. Operating conditions and experimental procedures are presented in Section 3.2. Section 3.3 focuses on the experimental analysis of the bubble foot motion during its increase and decrease with respect to the local heat fluxes. The classification of low-pressure bubble types based on the thermal measurements and high-speed camera recordings is described in Section 3.4. The time evolution of bubble foot diameter is also calculated for each bubble type (Section 3.5). The analysis is extended by the experimental results obtained for different liquid levels (2 cm, 15 cm, 28 cm) in order to verify the impact of the degree of subcooling on the bubble dynamics.

3.1 Measurement techniques for the study of the boiling process

It is difficult to characterize the boiling process because of its chaotic nature: small variations in operating conditions can strongly affect the results, while some important parameters can hardly be controlled. For instance, the random nature of nucleation on surfaces of poorly controlled characteristics (roughness, structure, presence of impurities) is often invoked to explain discrepancies among experimental results. In addition, boiling is a stochastic phenomenon, so that any characteristic parameter usually presents a distribution rather than a single deterministic value. Strong couplings between thermohydraulic phenomena (e.g. including but not limited to micro-convection induced by bubble motion, thin liquid film evaporation at the bubble base, bubble interactions like coalescence or break-up, etc.) also come into play.

To circumvent these difficulties and isolate the most fundamental phenomena involved, a research track has developed over time to study boiling from isolated controlled nucleation sites. This allows observation of the life cycle of single bubbles, sometimes with interactions with the preceding or successive bubbles. An abundant amount of publications based on various optical techniques, taking the benefit of ever-improving high-speed video cameras with increased space- and/or time-resolution could be thus performed. The development originates in the early photographic studies of Gaertner [34] (not on single nucleation sites) and developed to the most recent high speed video recording analysis, that can be associated to automated image processing ensuring that the information extracted from thousands of bubble events can be treated [82].

3.1.1 Analysis based on temperature measurements

Beyond bubble dynamics that can be analyzed via visualization, to obtain more broad view of the boiling phenomenon, thermal processes should also be investigated. In the early era of research, the time evolution of the surface temperature below the heater was measured owing small thermocouples. For instance, Moore and Mesler [87] measured temperature variations up to 17 K below the bubble from its nucleation to departure. Similar measurement were performed by Cooper and Lloyd [21], which led to the formulation of the so-called "microlayer model" that is based on the assumption that a liquid film located under a growing bubble evaporates, which simultaneously feeds the bubble with vapor and ensure a strong heat extraction (temperature decrease) from the wall. The emergence of the microlayer model led to the development of major research efforts to measure the microlayer thickness. These were mostly done by taking the benefit from interference phenomena (e.g. with visible light [57] or with IR thermometry [63]). Interferometry was also used to evaluate the temperature field around the bubbles [6, 124].

Instead of thermocouples, liquid crystals have been quite successfully used to determine the temperature field and its time evolution on the backside of the heated element [61]. However, owing to its greater flexibility, IR thermography replaced the use of liquid crystals, initially for thin metallic heaters [43], and then for thin sapphire glass coated with ITO [36]. Indeed, ITO presents the advantage of being opaque to IR radiation but transparent to visible light, so that it is possible to observe the boiling process from below simultaneously with IR and visible light high-speed cameras.

3.1.2 Analysis based on heat flux measurements

A remarkable response to the need for more-resolved (both in space and time) thermal measurements started with the miniaturization of electronic components. Series of these so-called "microheater arrays" were developed during the late nineties and early noughties by Kim and his coworkers [4, 25]. These heating elements were composed of many (typically 96) individually-controlled platinum resistors integrated on a silicon wafer of square shape (edge lower than 1 mm). Interestingly, this architecture made it possible to operate in such a way to simulate conditions of imposed temperature while measuring the heat flux released locally below the bubbles. This kind of concept was successfully continued, owing to the improvements in MEMS technology, to the development of "MEMS sensors for boiling research" by Nakabeppu and his coworkers [125, 126]. Especially, by synchronizing video recordings and thermal measurements, Yabuki and Nakabeppu [125] managed to assess the contribution of microlayer evaporation to the overall heat transfer for an isolated bubble, whose size would however be often greater than the heater and sensor, during boiling of water at atmospheric pressure. An essential feature of the theories and models relying on the microlayer concept is the thickness of this layer of liquid. However, its dimension along the radial direction is also of importance as the volume of the microlayer (i.e. the energy that can be extracted under the form of latent heat) directly depends on those both dimensions. This is why Yabuki and Nakabeppu [125] also analyzed the dryout of the microlayer and the re-wetting phenomenon, i.e. the motion of a dry area which is the foot of the bubble (that in other publications is sometimes referred to as the bubble "neck" or the bubble "stem"). Indeed, many research works showed that the triple contact line (where solid, liquid and vapor meet) has a major contribution to the overall heat transfer as the local heat flux in the vicinity of that line is much higher than anywhere else (e.g. this was particularly well quantified by Stephan [66]). Depending on the shape of the bubble, the triple line description is sometimes approached by the macroscopic contact angle [93] (when bubbles can be viewed as a portion of a sphere), or by the bubble foot diameter when the bubbles tend to have the shape of "mushrooms" or "balloons". This kind of mushroom shape is commonly encountered during subcooled boiling or under low pressure conditions [40].

3.1.3 Novelty of the applied heat flux sensor

The experiments described in this Chapter focus on the local (i.e. measured independently in seven zones of the sensor - see Section 2.1.3) analysis of bubble dynamics and associated thermal effects involved in the pool boiling process. Like many studies described in the literature, tests were first conducted with isolated bubbles. At such configuration it is easier to capture bubble shape, size, and frequency. Contrary to previous contributions discussing local analysis of bubble dynamics, the heat is dissipated through a thick heated element (copper block with heat flux sensor embedded on its top - see Section 2.1.2), which seems to be closer to many practical configurations than thin foils or silicon wafers [4, 25]. The heat flux is generated far from the boiling surface, but a novel heat flux sensor is placed at this surface, so that local instantaneous variations of heat fluxes can be detected. The sensor diameter is larger than bubble diameter, which simplifies the studies of the bubble behavior (including microlayer evaporation and bubble foot motion). Low pressure pool boiling is of practical interest in evaporators of sorption chillers, but it was found to be a convenient way to investigate boiling with large and (relatively) long-lasting bubbles [38, 82]. In that sense, beyond application, studying boiling at low pressure improves our understanding of the boiling phenomena. The following Sections demonstrate the abilities of the novel heat flux sensor and exemplify how it can be used in the context of low pressure boiling, particularly to follow the motion of the bubble foot.

3.2 Operating conditions

The bubble dynamics were investigated at three liquid levels ($H_l = 2$ cm, 15 cm, and 28 cm) and three vapor pressures: $p_v = 2.6$ kPa, 3.6 kPa, and 4.1 kPa. For every measurement, the imposed heat flux was set at approximately 4.6 Wcm^{-2}.

Every experiment provided heat flux measurements synchronized with recordings of high-speed camera, which allowed corroboration of the measurements. To reduce the mirage effect which lowers accuracy of bubble size estimations (for example, due to the mirage effect the estimated bubble diameter would be larger than the real one) [108], the camera was leaned forward by approximately 1°. As already mentioned in Section 2.1.4.1, the time constant of the sensor was estimated to approximately 1 s (in comparison to bubble growth time of about 0.1 s). This affect the recorded time evolution of heat flux. The instantaneous values are dampened, although the heat flux curves have the proper shape. For that purpose, only qualitative analysis of the bubble dynamics can be provided.

The experiments were performed on a mirror-polished surface with mean roughness $S_q = 0.3$ µm. At the center of the surface, the artificial cavity was created. The details concerning the surface characteristics are included in Section A.1. It should be mentioned that not every bubble described in this Section nucleated from the artificially created nucleation site, however, all analyzed bubbles nucleated within the first measurement zone at the center (see Fig. 2.4). The test bench used to perform test is described in Section 2.1.

3.3 Bubble foot motion and associated thermal effects

The interesting aspect concerning the heat flux sensor is that it allows for a closer insight into the bubble foot motion and the associated thermal effects. A detailed study of the sensor response is presented during bubble growth under vapor pressure $p_v = 4.1$ kPa. The whole process can be divided into two steps: when the bubble foot diameter increases (Fig. 3.1) and when it decreases(Fig. 3.2). Camera recordings and heat flux measurements for both, increase and decrease of the bubble foot for an exemplary bubble will be analyzed in this Section. Below the images, the schematic of the heat flux sensor was drawned and the average value of heat flux in each zone was indicated by the proper color according to the scale.

3.3.1 Increase of the bubble foot

When a bubble nucleates in zone 1 at $t = 20$ ms (point A in Fig. 3.1) the heat flux q_1 immediately starts to increase. Based on camera recordings, the bubble foot reaches zone 2 (point B in Fig. 3.1) after 10 ms. However, thermal measurements show that heat flux in zone 2 (q_2) increases slightly earlier. This is due to the existence of a microlayer at the early stage of the bubble growth: the thin liquid film present below the bubble tends to evaporate, taking heat from the surface and thus increasing the instantaneous heat flux.

Zone 3 is reached at time $t = 40$ ms (point C in Fig. 3.1). On the video sequence, it appears that again, the heat flux rises slightly before the bubble foot is in direct contact with this zone due to the evaporation of the microlayer.

At time $t = 56$ ms, the bubble foot reaches zone 4 (point D in Fig. 3.1). Here, the microlayer is fully evaporated, so when the bubble foot reaches zone 4 the heat flux increases immediately.

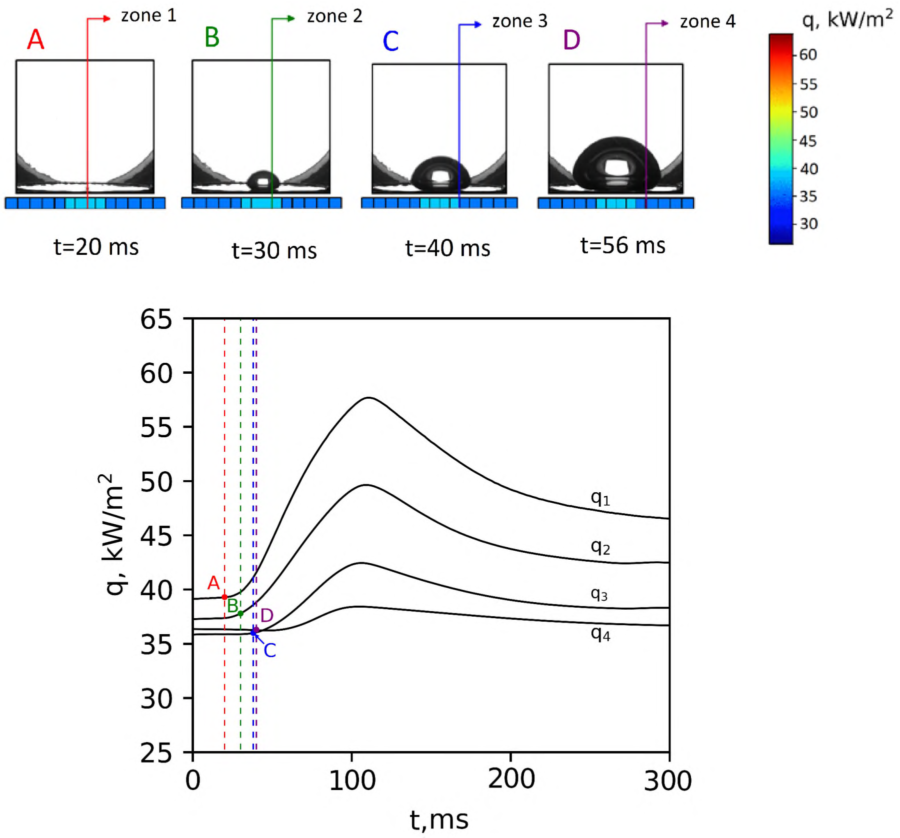

Figure 3.1: Evolution of the heat flux during increase of the bubble foot diameter ($p_v = 4.1$ kPa, $H_l = 15$ cm); A - bubble nucleation.

3.3.2 Decrease of the bubble foot

Similar analysis can be performed with respect to the bubble foot decrease which leads to the bubble detachment (see Fig. 3.2). Each point represents the last frame on which the bubble foot is present in a given zone. Point E corresponds to the last frame when the bubble foot is covering zone 4 (now it only covers 3 zones of the sensor). Even though the bubble foot is not directly interacting with this sensor's zone, an increase of the heat flux at this moment can be detected. This increase is not due to any microlayer effect, but to the expansion of the bubble that generates an intense mixing of the liquid inside the pool: cold liquid is pulled towards the surface where it can get superheated.

Point F corresponds to the last frame where the bubble foot is present in zone 3 (now it only covers 2 zones of the sensor). Like previously, a rise of the heat flux is noticeable even though the bubble foot has no further interactions with this part of the sensor. However, with respect to point E the time difference between considered frame and the maximum heat flux is smaller.

When the bubble foot is leaving zone 2 and is placed only within first zone (point G) a maximum in the heat flux at this part of the sensor exists. Most of the bubble volume is already far from the heated surface and the bubble foot diameter decreases to form a "long neck". This liquid motion induced by the large vapor volume intensifies at some distance from the heater, therefore not affecting the sensor's measurements.

Point H represents the moment of detachment. The bubble rises away from the surface after which there is no contact between the bubble and the surface. This results in a notable decrease of heat flux.

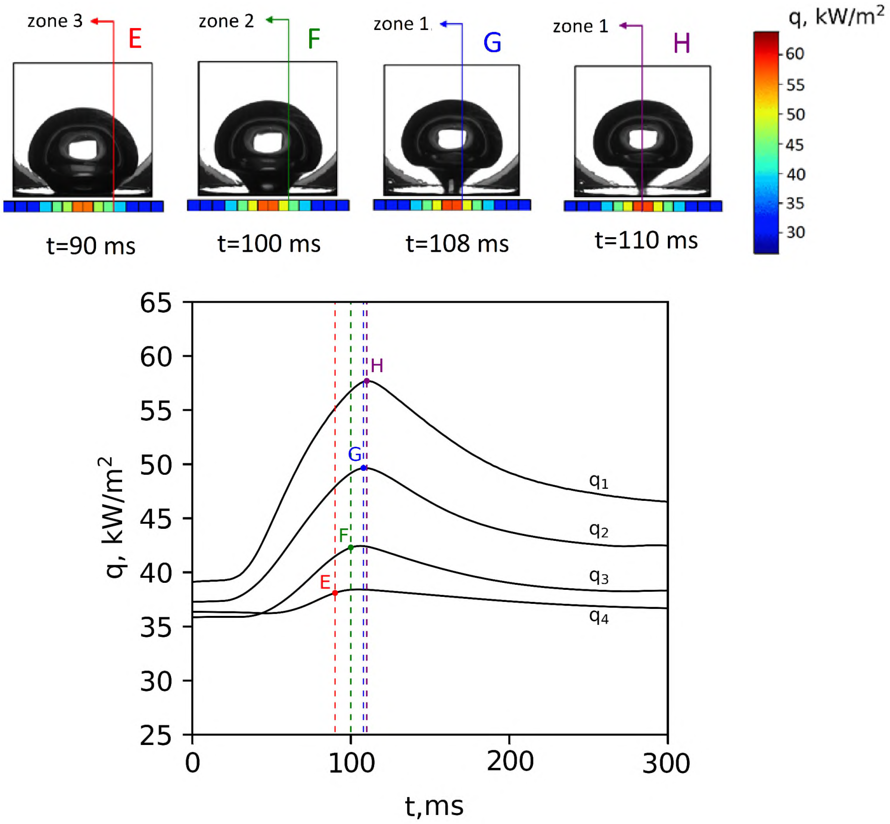

Figure 3.2: Heat flux evolution during decrease of the bubble foot diameter ($p_v = 4.1$ kPa, $H_l = 15$ cm); H - bubble detachment.

3.4 Classification of low pressure bubbles

During the experiments, bubbles nucleated in close proximity to the center of the heating surface where the nucleation site was created, i.e. they always grew from within the first zone of the heat flux sensor. Within the range of analyzed operating conditions (liquid heights and pressure levels) three different kinds of bubbles could be observed and categorized, namely: oblate spheroid-shaped bubbles [82, 83], mushroom-shaped bubbles [82, 83], and another type of bubbles that was not reported before in the literature related to boiling at low pressure. These bubbles were named "cavitation mushroom-shaped bubbles". They consist of two consecutive bubbles - the first being created by thermal effects and the other induced by a local depression. Video sequences for each type are shown in Fig. 3.3.

Each category of recorded bubbles differ by their thermal signatures that are revealed by the heat flux measurements conducted with the new sensor. The letters in Fig. 3.4-3.6 indicate points of interest (bubble nucleation, bubble departure, etc.). The numbers in Fig. 3.4-3.6 refer to recorded frames showing the shape and size of the bubble, and they correspond to the images in Fig. 3.3.

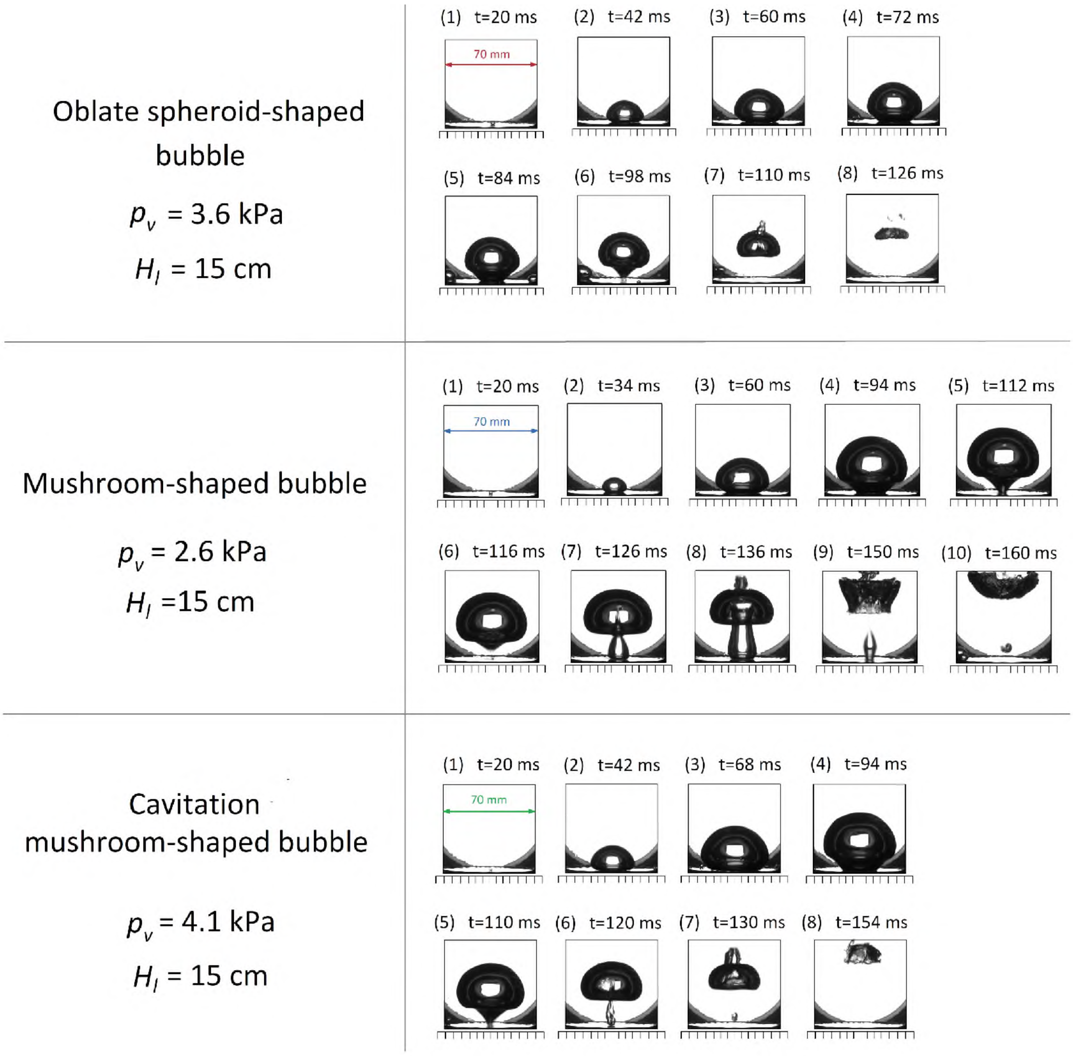

Figure 3.3: Three kinds of bubbles observed at different pressure levels (all within low pressure range).

3.4.1 Oblate spheroid-shaped bubbles

The first type of bubble (see Fig. 3.4) is oblate spheroid-shaped. Such bubbles were reported previously in low-pressure conditions [82, 83]. Such bubbles are successively created and they usually do not interact with each other. Once a bubble has nucleated (point A in Fig. 3.4), it grows keeping a hemispherical shape and then it morphs into an oblate spheroid. It has a large size (diameter of a few centimeters) and it is flattened on the top. After some time, the bubble still grows, but the diameter of its foot starts to decrease. Finally, the bubble detaches when buoyancy forces and bubble inertia overcome surface tension (point B in Fig. 3.4). The wake caused by its departure drags surrounding liquid and causes liquid jet penetration into the bubble. Hemispherical bubbles never reach the free surface of liquid: the pressure-induced subcooling forces rapid condensation of remaining vapor causing bubble collapse.

The thermal signal of this kind of bubble is a significant increase of instantaneous heat flux. The sensor in zone 1 always reacts first, as the bubble nucleates near the center. During bubble foot expansion, subsequent zones also react to the presence of the bubble.

Maximum heat flux is registered at the moment of detachment; then the recovery process takes place, i.e. temperature and heat flux gradually decrease to their initial values.

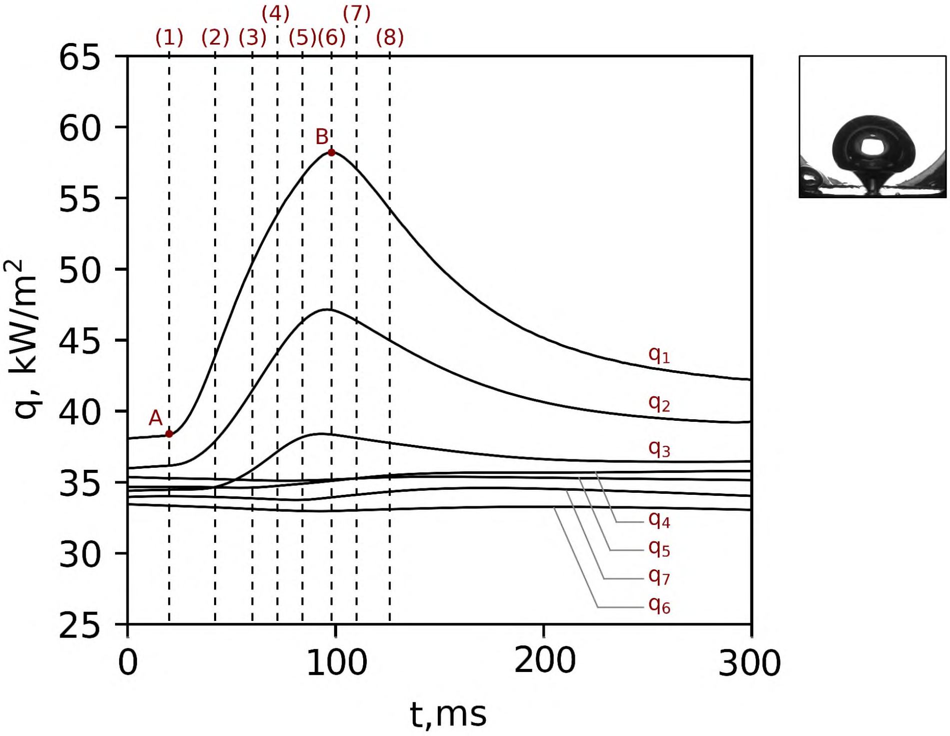

Figure 3.4: Typical time evolution of the heat flux for an oblate spheroid-shaped bubble ($p_v = 3.6$ kPa, $H_l = 15$ cm): A - nucleation of the bubble; B - detachment of the bubble. The numbers in parentheses refers to frames / states presented in Fig. 3.3.

3.4.2 Mushroom-shaped bubbles

The second type of bubble (see Fig. 3.5) is actually a pair of bubbles that interact with each other and form a characteristic mushroom shape. This was sometimes described as the formation of a secondary vapor column (Van Stralen et al. [115] for vapor pressure lower than 13 kPa), or as the existence of secondary bubbles (Giraud et al. [40] for pressures below 15 kPa). Later studies conducted by Michaïe at al. [82] associated this phenomenon with a pressure range between 20 kPa and 70 kPa. The discrepancies between these pressure ranges and the present work can be a result of different operating conditions (especially liquid levels and applied heat fluxes).

To form such mushrooms, the initial bubble is an oblate spheroid-shaped bubble. Immediately after its detachment (point B in Fig. 3.5) the initial bubble is followed by the nucleation of a secondary bubble (point C in Fig. 3.5). The wake created by the detachment of the first bubble promotes faster growth and causes vertically elongated shape of the second one. This secondary elongated bubble is a consequence of local depression created by the liquid jet or some remaining superheated vapor trapped in the nucleation site after detachment of primary bubble [115]. The time of growth - from nucleation to detachment is approximately 3 times shorter than for the primary bubble (e.g. 92 ms for the first bubble, only 34 ms for the second).

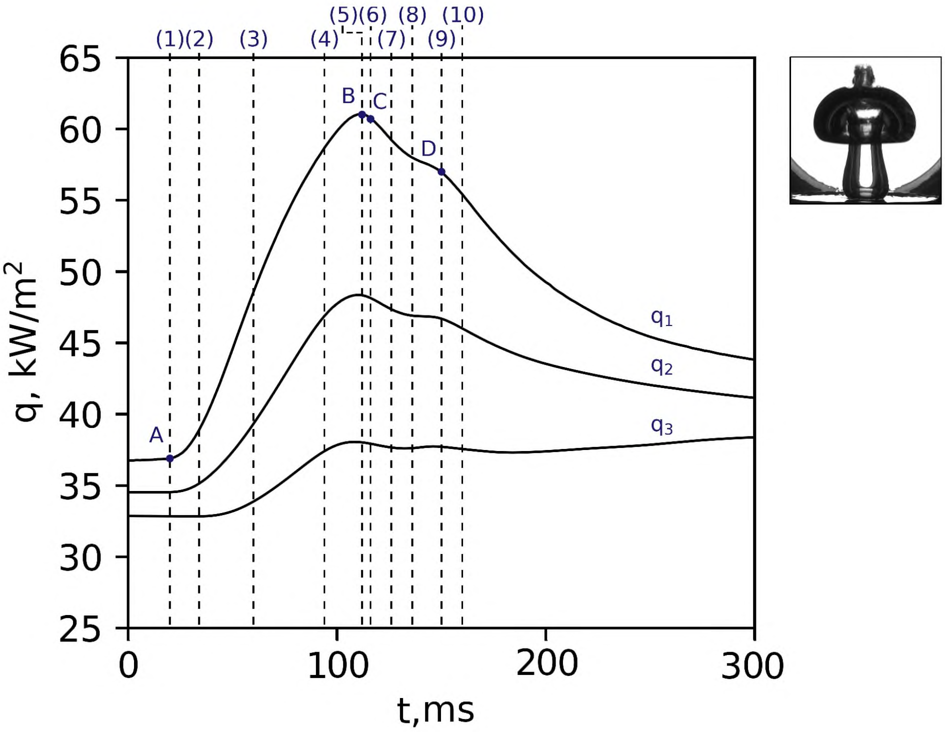

Figure 3.5: Typical time evolution of the heat flux for a mushroom-shaped bubble (p_v = 2.6 kPa, H_l = 15 cm): A - nucleation of the primary bubble; B - detachment of the primary bubble; C - nucleation of the secondary bubble; D - detachment of the secondary bubble. The numbers in parentheses refers to frames / states presented in Fig. 3.3.

The output signals of the heat flux sensor show noticeable differences between mushroom-shaped bubbles and oblate spheroid bubbles. In both cases, the heat flux starts to increase right after bubble nucleation and reaches maximum at the moment of detachment. However, due to the influence of the second bubble the decrease of heat flux is less steep and the curve has a second extremum at the moment of the second departure (see point D in Fig. 3.5).

3.4.3 Cavitation mushroom-shaped bubbles

This kind of bubble has not yet been reported in the studies of low pressure boiling. On frames recorded with a high-speed camera, this type of bubble is indistinguishable from the mushroom-shaped one because both consist of two consecutive bubbles forming a mushroom. The distinction was possible thanks to the synchronization of high-speed visualization and heat flux sensor measurements. Both types are represented by noticeably different types of heat flux signal (compare Fig. 3.5 and Fig. 3.6).

This difference cannot be detected with high-speed image recording only. The second bubble of a cavitation mushroom-shaped bubble does not nucleate on the heated surface, but slightly above it, right in the liquid pool. Its growth is induced by a rapid local reduction of pressure created in the liquid due to violent departure of the preceding spheroid bubble. For that reason, the secondary cavitation mushroom-shaped bubble has no direct contact with the heater. It does not give any thermal signal on the heat flux sensor and the output is similar to oblate spheroid bubbles. To summarize, cavitation mushroom-shaped bubbles look like mushroom-shaped bubbles on the video recording, but have the thermal signal of oblate spheroid bubbles.

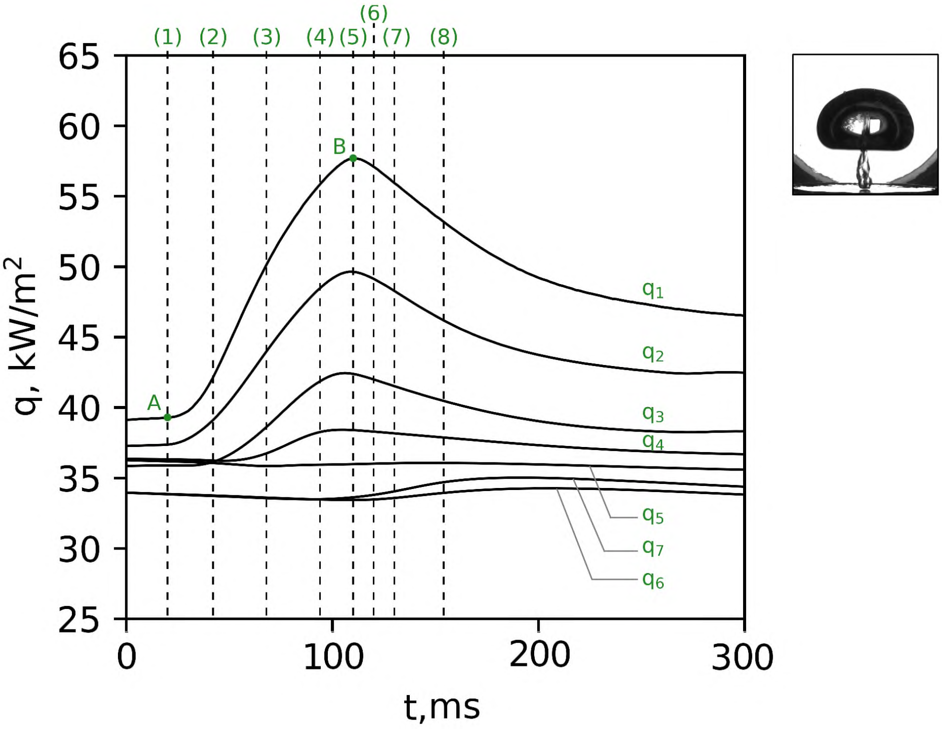

Figure 3.6: Typical time evolution of the heat flux for a cavitation mushroom-shaped bubble ($p_v = 4.1$ kPa, H_l=15 cm): A - nucleation of the primary bubble; B - detachment of the primary bubble. The numbers in parentheses refers to frames / states presented in Fig. 3.3.

3.5 Analysis of the bubble foot diameter

The analysis of the bubble foot growth presented in Section 3.3 highlighted the thermal effects associated with the growth of the bubble foot. A finer description of the bubble dynamics can be obtained by focusing on the dynamics of the bubble foot.

Fig. 3.7 presents the time evolution of the bubble foot diameter for all three types of bubbles described in Section 3.4 and shown in Fig. 3.3. The bubble foot diameter is calculated dynamically for all measurement points from the moment of nucleation up to the detachment with frequency 500 Hz (the images were recorded every 2 ms). All those bubbles were obtained for the liquid level $H_l = 15$ cm. The error of the bubble foot diameter is estimated as 5 px (approx. 0.6 mm).

The evolution of the bubble foot diameter displays an almost parabolic shape, revealing an increase of the bubble foot diameter, followed by its decrease. The increase of the bubble foot lasts slightly longer (usually about few ms) than decrease. Points A_1, B_1 and C_1 corresponds to the transition point between increase and decrease of the bubble foot. The whole bubble growth process for primary bubbles lasts less than 100 ms.

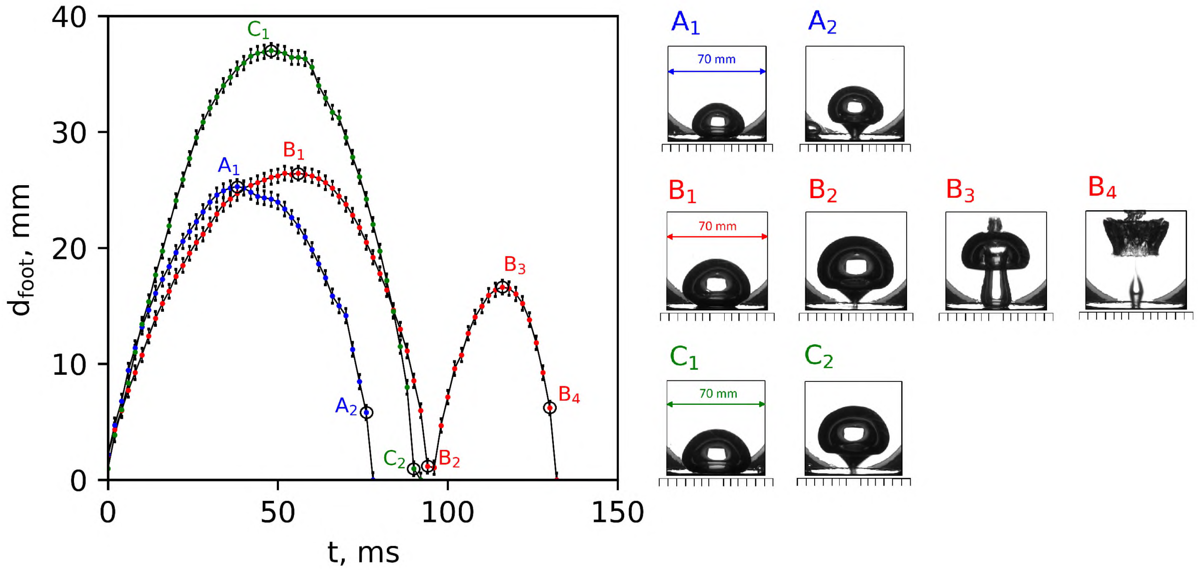

Figure 3.7: Bubble foot diameter for three bubble types registered by sensor ($H_l = 15$ cm): points A_1, A_2: $p_v = 3.6$ kPa, points B_1, B_2, B_3, B_4: $p_v = 2.6$ kPa, points C_1, C_2: $p_v = 4.1$ kPa.

3.5.1 Influence of the liquid level on the bubble foot size

The influence of the liquid level on the bubble foot diameter is clearly seen in Fig. 3.8. The bubble foot diameters for $H_l = 15$ cm and three vapor pressures are described in previous Section (see Fig. 3.7). The bubble foot evolution obtained for $p_v = 3.6$ kPa is also shown in Fig. 3.8 (photos B_1 and B_2) and it states a reference point for bubbles obtained for another liquid levels.

For a small liquid height ($H_l = 2$ cm, frames A_1 and A_2 in Fig. 3.8), a large bubble rises above the free surface causing splashing of the liquid due to movement of the liquid pool. Such behavior is visible on the high-speed camera recordings. This process was already noted in the literature [39, 40]. For $H_l = 2$ cm, the bubble foot has a similar shape as for moderate liquid level $H_l = 15$ cm (represented by photos B_2 and B_3 in Fig 3.8). Its diameter is, however, generally higher than for $H_l = 15$ cm - sometimes even bigger than the diameter of the heated surface. Additionally, when the liquid level is low, several bigger peripheral bubbles can appear around the surface, making more difficult to perform accurate calculations of the bubble foot diameter. It was often not easy to even clearly see the liquid-vapor interface by the naked eye. Because of these experimental limitations, Fig. 3.8 only shows one bubble with considerably small diameter (photos A_1 and A_2 in Fig. 3.8), where the bubble foot was clearly seen and its dimensions could be easily estimated. Additional quantitative analysis allows to conclude that for this liquid level, big hemispherical bubbles and cavitation mushroom-shaped bubbles are also likely to be observed.

Increasing the liquid level up to $H_l = 28$ cm completely changes the bubble dynamics with respect to the previous cases. This is associated with the rise of liquid subcooling intensifying the bubble condensation (more details about the pressure-induced subcooling is included in Section 1.2.1). Instead of big bubbles nucleating and departing with low frequency, many small bubbles (diameter less than 10 mm) pop up all over the surface. Occasionally, a bigger bubble nucleates near the center of the surface. For this level of liquid bubbles with different size could be noticed (e.g. photos C_1, D_1, E_1 present bubbles registered for the same operating conditions), but bubble diameters and bubble foot diameters are always smaller than for lower liquid heights. The bubble life is also different depending on the liquid level: the bubble growth time is reduced by 76% and 53% for the smallest and the biggest bubbles observed for the $H_l = 28$ cm in comparison to the bubbles growing for $H_l = 15$ cm.

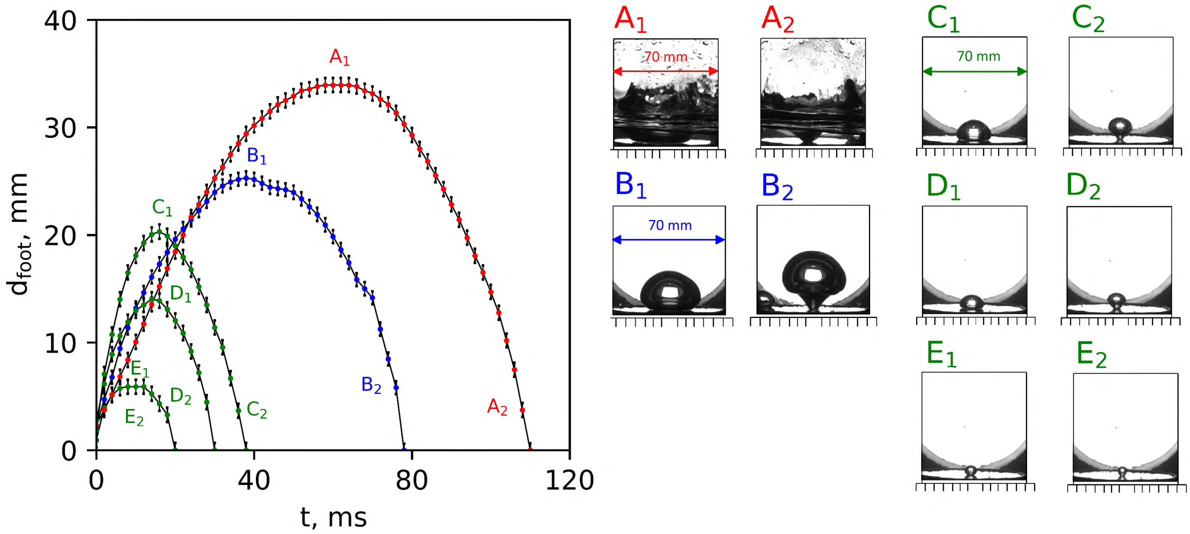

Figure 3.8: Bubble foot diameter for various liquid levels ($p_v = 3.6$ kPa): points A_1, A_2: $H_l = 2$ cm; points B_1, B_2: H_l=15 cm; points C_1, C_2, D_1, D_2, E_1, E_2: $H_l = 28$ cm.

Conclusions

In this chapter the applicability of the novel heat flux sensor for the analysis of bubble dynamics during boiling at low pressure is evaluated. The sensor response for various bubble shapes was discussed for vapor pressures ranging from 2.6 kPa to 4.1 kPa and three liquid heights (2 cm, 15 cm and 28 cm). Direct synchronization of high-speed visualizations and thermal measurements enabled to highlight the link between heat transfer and bubble dynamics. The use of this kind of sensor is especially beneficial at low pressure, for which larger diameters simplify the observation of the bubble foot. This is a way to provide an interesting and new approach into studies of bubble growth process and can extend fundamental knowledge concerning this process. In order to better capture general bubbles shape and size, the test were conducted for isolated bubbles growing in the center of the surface.

The heat flux sensor not only allows to follow the bubble foot increase and decrease, but also detects other accompanying phenomena, such as microlayer evaporation and the liquid movement due to vapor expansion inside the bubble. The comparison between the evolution of the local heat flux on subsequent zones and the bubble foot size agrees with microlayer theory. The thin liquid layer placed below the bubble evaporates at the early stage of the bubble growth. During bubble foot decrease, the huge volume of liquid that is displaced pushes cold liquid from the bulk towards the surface, resulting in further rise of heat flux.

Beyond the demonstration of the abilities of the novel heat flux sensor, some features of boiling at low pressure were discovered owing to the sensor. Three types of bubbles were *observed during experiments: oblate spheroid-shaped bubble, mushroom-shaped bubble and cavitation mushroom-shaped bubble. The difference between mushroom-shaped and cavitation mushroom-shaped bubble was confirmed thanks to the local thermal measurements allowed by the sensor. Now the distinction is clear between these two types of bubbles. Further research is required to discover which conditions promote their growth.*

The influence of the liquid level on the bubble dynamics was also studied. A small level of liquid (H_l = 2 cm) resulted in large bubble foot diameters. It was often larger than the size of the heater, making analysis impossible. For high level of liquid (H_l = 28 cm), many small popping bubbles were observed. The decrease of the bubble size with increase of the liquid column is caused by more intense subcooling.

The application of the heat flux sensor gives an interesting insight into single bubble dynamics. Further test should focus not only on the boiling dynamics from a single nucleation site, but rather from a rough surface with multiple cavities. Such approach is a step closer to a real-life heat exchanger and can be an interesting way to determine how different operating conditions affect the boiling dynamics. Performing multiple series of experiments would allow to create the boiling regime maps. Such graphical representation is helpful while designing low-pressure heat transfer equipment. The range of the experimental conditions should be extended with respect to operating range studied in this chapter. Especially higher liquid levels should be examined to better understand the effect of the pressure-induced subcooling. This kind of analysis, which covers various aspects of the boiling process from a rough surface, for different vapor pressures, liquid levels and applied heat fluxes will be described in Section 4.

Chapter 4

Boiling on a rough surface

Chapter 3 has already featured that the increase of liquid level (and consequently subcooling of liquid) significantly reduces the bubble size and bubble growth time. The analysis was conducted for isolated bubbles and only three levels of liquid (2 cm, 15 cm and 28 cm). In real-life heat exchangers, multiple bubbles are beneficial in order to intensify the phase change process. For that reason, this Chapter focuses on the experimental studies of boiling from multiple nucleation sites in order to get more general overview of this phenomenon. Also, the range of the experimental conditions was extended to more closely determine their influence on the boiling process.

Section 4.1 provides information about the operating conditions and the experimental procedures used in the experiments. Then, the phenomenon of boiling on a rough surface is investigated (Section 4.2). The analysis covers the interpretations of instantaneous heat flux for a single bubble growth and for multiple bubbles generated at different working conditions. Sometimes the heat flux at the wall level exhibits large variations with time, but its time evolution is hard to analyze. For that purpose, a statistical analysis is proposed. Based on that approach, extended by high-speed video recordings, four different low-pressure boiling regimes are identified. Section 4.3 focuses on the characterization of each regime. The influence of the liquid level and the applied heat flux on the boiling regimes is featured in Section 4.4. To provide a visual representation of the influence of working parameters on boiling behavior, a dimensionless boiling regime map was proposed (Section 4.5). This type of representation is a tool to predict the low pressure boiling regimes from a set of operating conditions. It is also useful to interpret the involved physical phenomena and to understand how they differ from those occurring at higher pressure. Additionally, as two different surface roughnesses were investigated, their influence on the heat transfer coefficient and boiling regimes map is discussed in Section 4.6.

4.1 Operating conditions and experimental procedures

Experiments were performed for three different vapor pressures ($p_v = 2.4$ kPa, 3.1 kPa, 4.1 kPa) and four distinct liquid levels (H_l = 15 cm, 28 cm, 35 cm, 60 cm). Various applied heat fluxes q_{app} were applied: 3.6 Wcm^{-2}, 4.4 Wcm^{-2}, 5.2 Wcm^{-2}, 6.1 Wcm^{-2} and 7.1 Wcm^{-2} (which corresponds to values of applied heating powers: 174 W, 220 W, 248 W, 293 W, 331 W). The surface was roughned with emery paper in order to obtain a surface with multiple nucleation sites. For initial tests (described in Sections 4.3, 4.4, 4.5), the average roughness of the surface was equal to $S_q = 3.5$ µm. The experiments were repeated for another surface roughness ($S_q = 2.8$ µm.) what was described in Section 4.6.

When the surface temperature exceeded 80°C, the measurements were stopped because excessive wall temperature could damage the sensor. Each measurement was recorded over 60 s. The acquisition frequency was equal to 500 Hz (every 2 ms). The thermal measurements were complemented with high-speed video recordings with framerate 500 Hz (recorded over 3.072 s due to camera memory limitations).

4.2 Boiling behavior on a rough surface

This Section focuses on heat flux analysis during boiling process for only one vapor pressure ($p_v = 3.1$ kPa). The analysis was performed based on boiling curves and statistical analysis.

4.2.1 Instantaneous heat flux for a single bubble growth

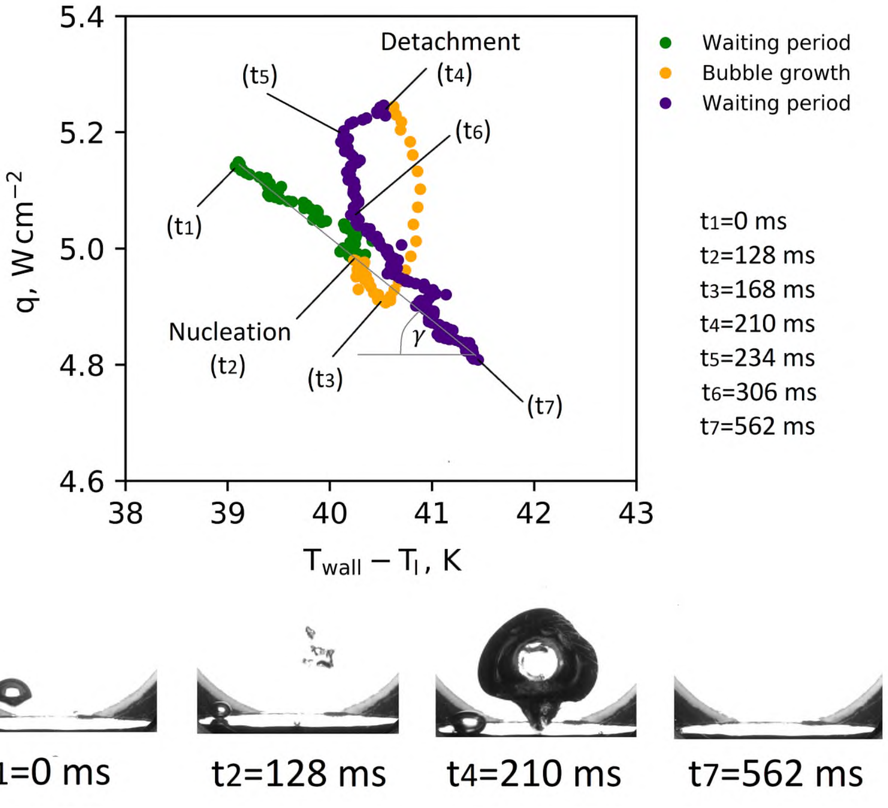

Figure 4.1: Instantaneous heat flux vs. instantaneous wall superheat for a single bubble growth.

Fig. 4.1 shows the value of instantaneous average heat flux for a single bubble growth. The waiting period between successive bubbles is indicated by the straight line at certain angle γ. Physically, this line represents the heat flux decrease and the wall temperature rise after the detachment of the previous bubble. The nucleus of vapor does not always appear at the same surface temperature and heat flux conditions. Certain scattering of points belonging to the waiting periods exist. That is why the end of the waiting period (t_7) is not at the same coordinates as the end of the preceding waiting period (t_2). However, the line of evolution during the waiting period has the same slope: the angle of the line between t_1 and t_2 is the same as between t_6 and t_7.

The bubble growth is always associated with sudden increase of heat flux. The maximum value corresponds to the moment of detachment (point t_4 in Fig. 4.1). After departure, even though the heat flux slightly decreases, the wall temperature drops by about 1 K for the next 24 ms (from point t_4 to t_5 in Fig. 4.1). This temperature decrease is caused by the liquid wake created after bubble departure. This wake leads to the liquid mixing and pulling of the cold mass towards the surface. The transfer of heat into this subcooled layer of liquid is responsible for further wall temperature decrease. Initially (between t_5 and t_6), the heat flux drops very quickly, while the wall superheating stabilizes at the value of around 40°C (this part of the graph forms almost the straight line). After that, parameters start vary with linear dependency under the tilting angle that was pointed out previously (γ).

The visible delay between the nucleation t_2 and the following heat flux increase t_3 is caused by the misalignment of the nucleation site. As the wall temperature is evaluated at the center of the boiling surface, it takes time for the sensor to notice the bubble presence if nucleation occurred at certain radius from the center.

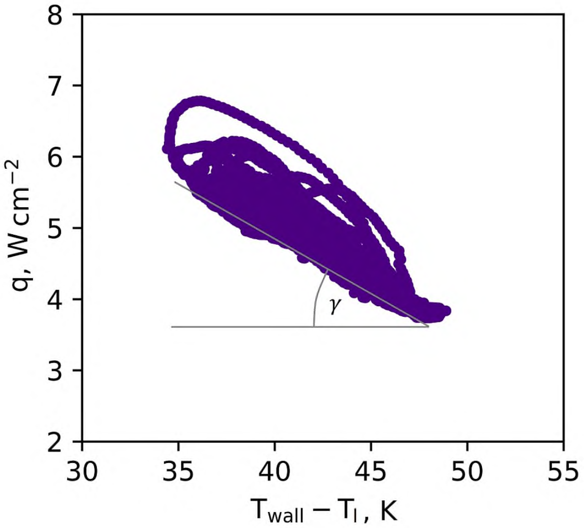

Figure 4.2: Instantaneous heat flux vs. instantaneous wall superheat recorded for 60 s (30 000 data points and over dozen successive bubbles).

Fig. 4.2 shows the instantaneous heat flux and wall superheat (T_{wall}-T_l) recorded for 60 s, which gives 30 000 data points of over a dozen of successive bubbles. Because of the scatter of thermal conditions at nucleation, variation in the bubble size, bubble growth time, and because this graph shows the superimposed signature of multiple growing bubbles, the overall curve occupies a certain area of the graph. Nevertheless, one can still detect the angle γ that characterizes the waiting time for all these bubbles. However, analyzing the graph visible in Fig. 4.2 without considering camera recordings, it is not possible to distinguish if those curves corresponds to a bunch of single bubble events or there are multiple active nucleation sites which sometimes get simultaneously active.

4.2.2 Instantaneous heat flux for multiple bubbles and various working conditions

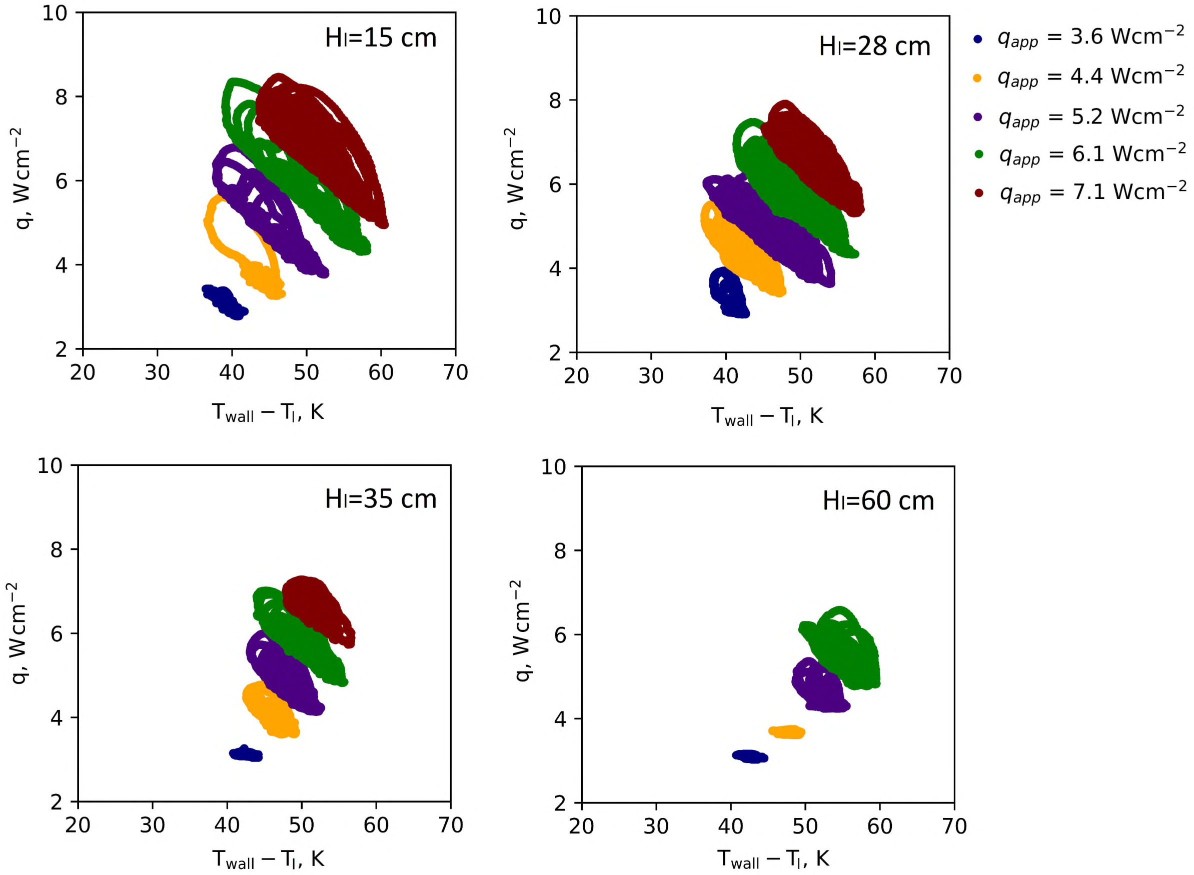

Figure 4.3: Instantaneous heat flux vs. instantaneous wall superheat ($p_v = 3.1$ kPa).

The boiling curves obtained for different subcooling degrees and heating powers are shown in Fig. 4.3. The points which are gathered around the same value of heat flux with small scatter of wall superheat represent single-phase convection. It happens when applied heat flux is too small to initiate boiling for specific conditions (e.g. measurement for $H_l = 35$ cm, $q_{app} = 3.6$ Wcm^{-2}, $HP = 174$ W). If the heating power is high enough, the boiling process starts causing intense rise of heat flux and drop of wall temperature (explained in Fig. 4.1). Higher values of applied heat fluxes lead to more intense boiling process. Data points fill almost all the space below the curve drawn by the biggest bubble.

Regarding the cases with higher subcooling of liquid, larger values of heat flux are necessary to initiate boiling. For applied heat flux $q_{app} = 6.1$ Wcm^{-2} ($HP = 293$ W), the bubbles appear for all analyzed liquid level, except for $H_l = 60$ cm. Also, the curves obtained for higher liquid level are shifted to the right - towards higher wall superheat. Because of that, the measurements for applied heat flux of 7.1 Wcm^{-2} (HP = 339 W) and for liquid level $H_l = 60$ cm were not recorded. The wall temperature was too high which could lead to damage of the sensor.

In order to provide better comparison of results obtained for various liquid levels (and thus different subcoolings), the heat flux curves with the same value of applied heat flux $q_{app} = 6.1$ Wcm^{-2} ($HP = 293$ W) were plotted on a single graph (see Fig. 4.4). One can notice that higher subcooling is associated with smaller peaks of heat flux and wall temperature fluctuations.

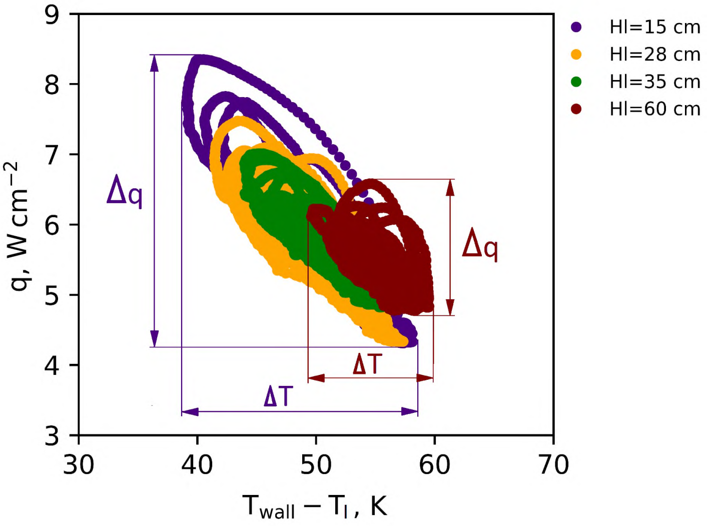

Figure 4.4: Instantaneous heat flux vs. instantaneous wall superheat (p_v = 3.1 kPa, q_{app} = 6.1 Wcm^{-2}, HP = 293 W, S_q = 3.5 µm).

Fig. 4.5 shows selected frames from high-speed camera recorded for various liquid levels. Those pictures corresponds to the thermal measurements shown in Fig. 4.4.

At low liquid level and low level of subcooling, bubbles grow large and nucleate with small frequency (see Fig. 4.5 A). This causes high fluctuations of wall temperature (up to 20 K) (see purple points in Fig. 4.4). Usually there is only one bubble on the surface at a time. For higher subcooling of liquid, the bubbles are smaller. They nucleate more often and there are several bubbles at the same time in different locations on the surface (see Fig. 4.5 D). This results in more uniform wall temperature evolution (red points in Fig. 4.4 are less scattered in the horizontal direction than purple, yellow or green). Despite the increase of the numbers of bubbles on the surface, the heat flux peak Δq is smaller for higher level of liquid. Several small bubbles extract less heat from the surface than one, large bubble. Additionally, highly subcooled conditions require higher heat fluxes to initiate boiling.

4.2.3 Calculation of heat transfer coefficients

Heat transfer coefficient is one of the most important parameters while designing heat transfer devices. It is defined as:

$$h = \frac{q}{T_{wall} - T_l} \tag{4.1}$$

Fig. 4.6 shows heat transfer coefficient plotted for all data points and four different liquid levels. The graph presented in Fig. 4.6 corresponds to conditions where applied heating power was set to q_{app} = 6.1 Wcm^{-2} (equivalent of heating power 293 W). The maximum instantaneous heat transfer coefficient can be obtained for the lowest level of liquid. However, this peak of heat transfer coefficient is temporary and can be noticed only during the bubble growth process. At such working conditions, the waiting period between two successive bubbles is longer (several seconds). Thus, the averaged heat

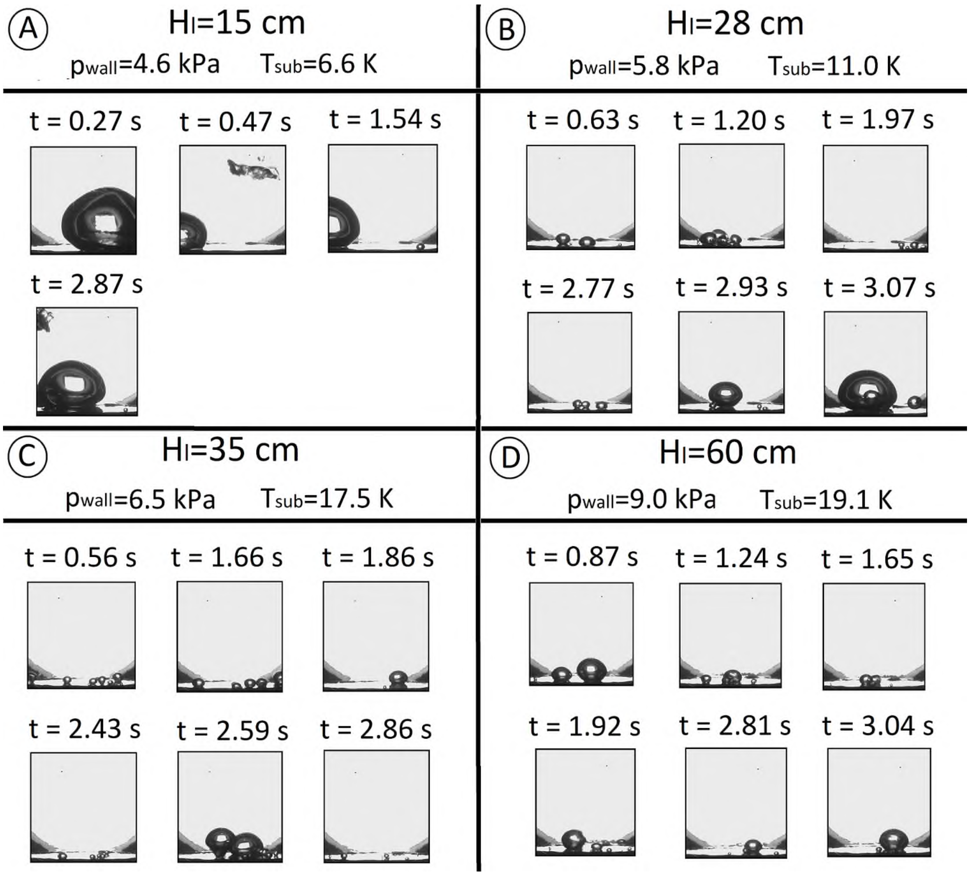

Figure 4.5: The difference in the bubble size and shape depending on the value of applied heat flux.

transfer coefficient is the lowest for $H_l = 15$ cm (see Tab. 4.1). For $H_l = 28$ cm, the average heat transfer coefficient is 10% higher in comparison to the lowest level of liquid.

Tab. 4.1 presents the averaged values of heat transfer coefficient for all operating conditions under vapor pressure $p_v = 3.1$ kPa. The maximum averaged value of heat transfer coefficient for each value of applied heat flux is put in bold. At the lower heating power $q_{app} = 3.6$ Wcm^{-2}, the averaged values of heat transfer coefficient are similar for all liquid levels. This is associated with the fact that the boiling process is still not fully developed and there are long periods of single-phase convections with no bubbles appearing on the surface. The peaks of heat flux and consequently the heat transfer coefficient which could increase the averaged value of h are associated with the bubble growth process.

For larger values applied heat flux, the maximum averaged heat transfer coefficient is observable for $H_l = 28$ cm. The boiling process at such conditions is intense than for $H_l = 15$ cm - there is more bubbles on the surface (see Fig. 4.5 A and B). The shape, size, and frequency of bubbles strongly depend on the liquid level. Apparently, the best trade-off between the bubble size and frequency is reached at $H_l = 28$ cm. More subcooled conditions increase the frequency of the bubble growth, but they decrease bubble size and thus the contact area between the bubble and the heater. It is also worth mentioning that the obtained values of heat transfer coefficient for all operating conditions are low (especially while comparing with boiling heat transfer of water at atmospheric conditions) and do not differ significantly from heat transfer coefficient reached by the single-phase convection. This is a real problem for heat transfer devices which operate at proximity to the triple point.

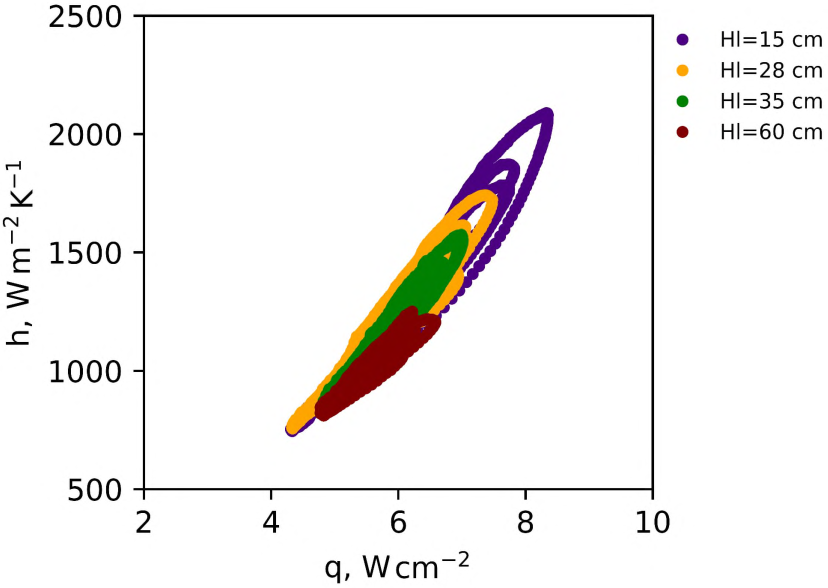

Figure 4.6: Instantaneous heat transfer coefficient vs. instantaneous heat flux (p_v = 3.1 kPa, q_{app} = 6.1 Wcm^{-2}, HP = 293 W, S_q = 3.5 µm).

Table 4.1: Averaged heat transfer coefficient (p_v = 3.1 kPa, S_q = 3.5 µm).

		H_l			
h, Wm$^{-2}K^{-1}$		15 cm	28 cm	35 cm	60 cm
q_{app}, Wcm^{-2}	3.6	**662**	637	634	623
	4.4	726	**727**	681	656
	5.2	788	**826**	760	695
	6.1	835	**918**	893	754
	7.1	960	**1029**	1002	-

4.2.4 Time evolution of heat flux

Previous sections described boiling process based on the graphs of instantaneous heat flux as a function of instantaneous wall superheat. The boiling process is dynamic phenomenon, thus it would be beneficial to study the time evolution of instantaneous heat flux. The value of heat flux transferred through the heating surface is irregular (see Fig. 4.7 a). The nucleation occurs at different values of heat flux and bubbles possess different sizes resulting in the observed temporal variation of the heat flux. When the applied heat flux increases, the peaks of heat flux become more densely packed making the analysis even more difficult. All this prohibits from drawing any general conclusion about the frequency, the size or the number of bubbles.

Highly fluctuating physical phenomena can be analyzed statistically, using tools like the Probability Density Function. The graph showing time evolution of instantaneous heat flux over all seven zones of the sensor (calculated according to Eq. 1.10) can be divided into intervals. Example interval is marked red in Fig. 4.7a. The set of intervals for the whole range of heat flux allows the creation of the density histogram. Fig. 4.7b shows the histogram created for the heat flux intervals with the exact thickness as shown in Fig. 4.7a. This kind of graph represents the occurrence frequency of each heat flux interval. If the interval's thickness approaches zero, the histogram will turn into a continuous probability density function - PDF (see Fig. 4.7c).

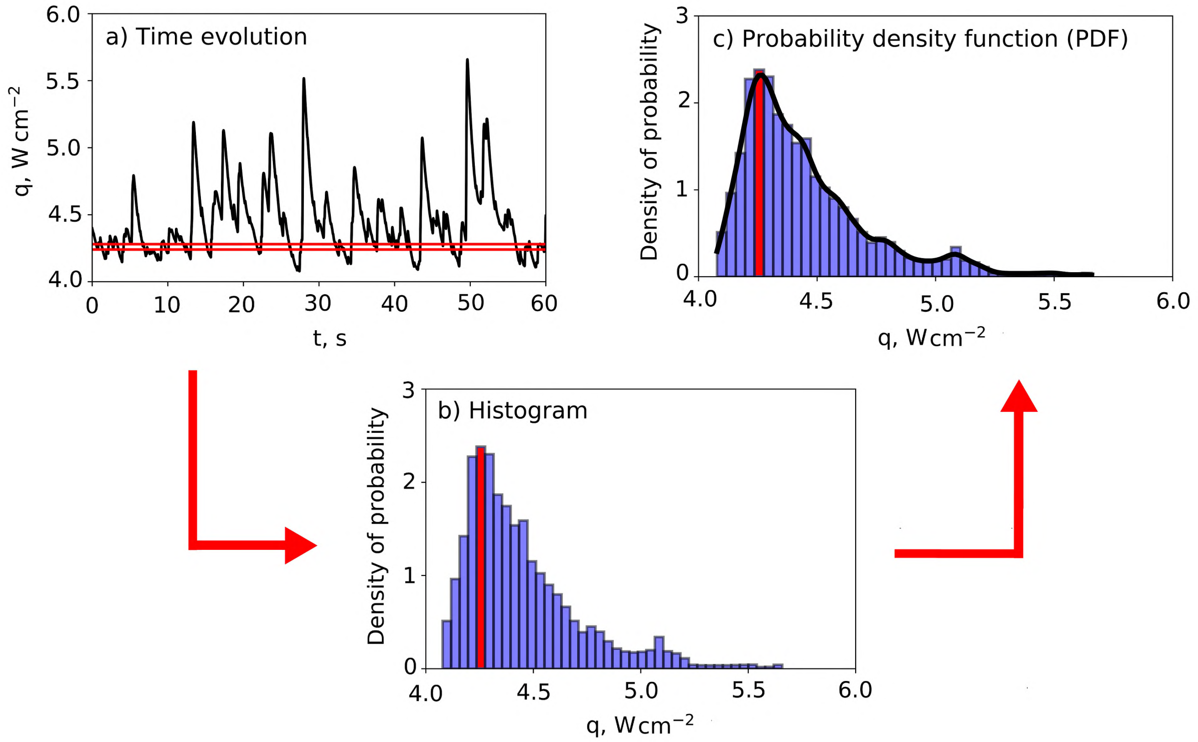

Figure 4.7: Formation of the PDF from the function of time evolution (for all seven zones of the sensor).

4.2.5 Statistical analysis of heat flux evolution

To apply the PDF for statistical analysis, one has to consider continuous variables (e.g. heat flux distribution for high acquisition frequency). The PDF represents a distribution of probability, not the probability itself. The exact value of probability of a certain interval can be calculated by integration, as shown in Fig. 4.8a. The area under the PDF graph over the interval $[0; x_p]$ represents the probability of occurrence of any value from this interval. The values on the ordinate axis are expressed in an arbitrary unit: they do not represent probability of occurrence of certain value 'x'. The values on the ordinate axis depend on the range of 'x' for which the calculations were performed and a change of the measurement time would change the values on the ordinate axis. For that purpose, the analysis described in the next Sections was performed for the same measurement time of 60 s.

Fig. 4.8b shows the cumulative distribution function (CDF) which is based on the PDF shown in Fig. 4.8a). The ordinate of the CDF diagram for a certain point x_p gives the actual value of probability that any value from the interval $[0;x_p]$ can occur. This value is equal to the area under the PDF graph. Since the vertical axis of the CDF is probability, it must fall between zero and unity.

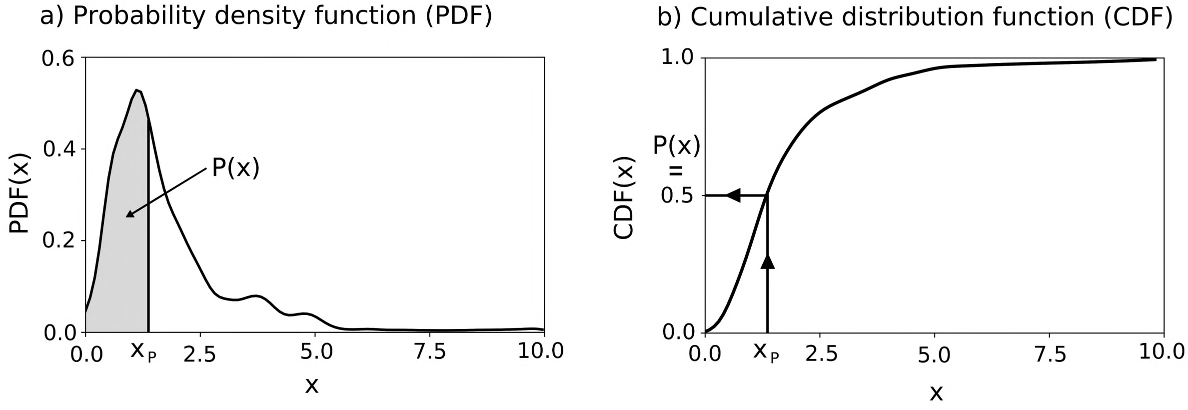

Figure 4.8: The difference between probability density function (PDF) and cumulative distribution function (CDF).

4.3 Identification of low pressure boiling regimes

Individual PDF graphs were created for various operating conditions (different vapor pressures p_v, liquid levels H_l, applied heat fluxes q_{app}). Four distinct boiling regimes were identified based on: visual observations (performed with high-speed camera - examples in Fig. 4.9), thermal signals recorded by the heat flux sensor (see Fig. 4.10 - 4.13 upper part) and the PDF graphs (see Fig. 4.10 - 4.13 bottom part). Those regimes were accordingly: the convection or small popping bubbles regime, the isolated bubbles regime, the intermittent boiling regime and the fully developed boiling regime. The frames from video sequences of each type of low-pressure boiling in different regimes are presented in Fig. 4.9.

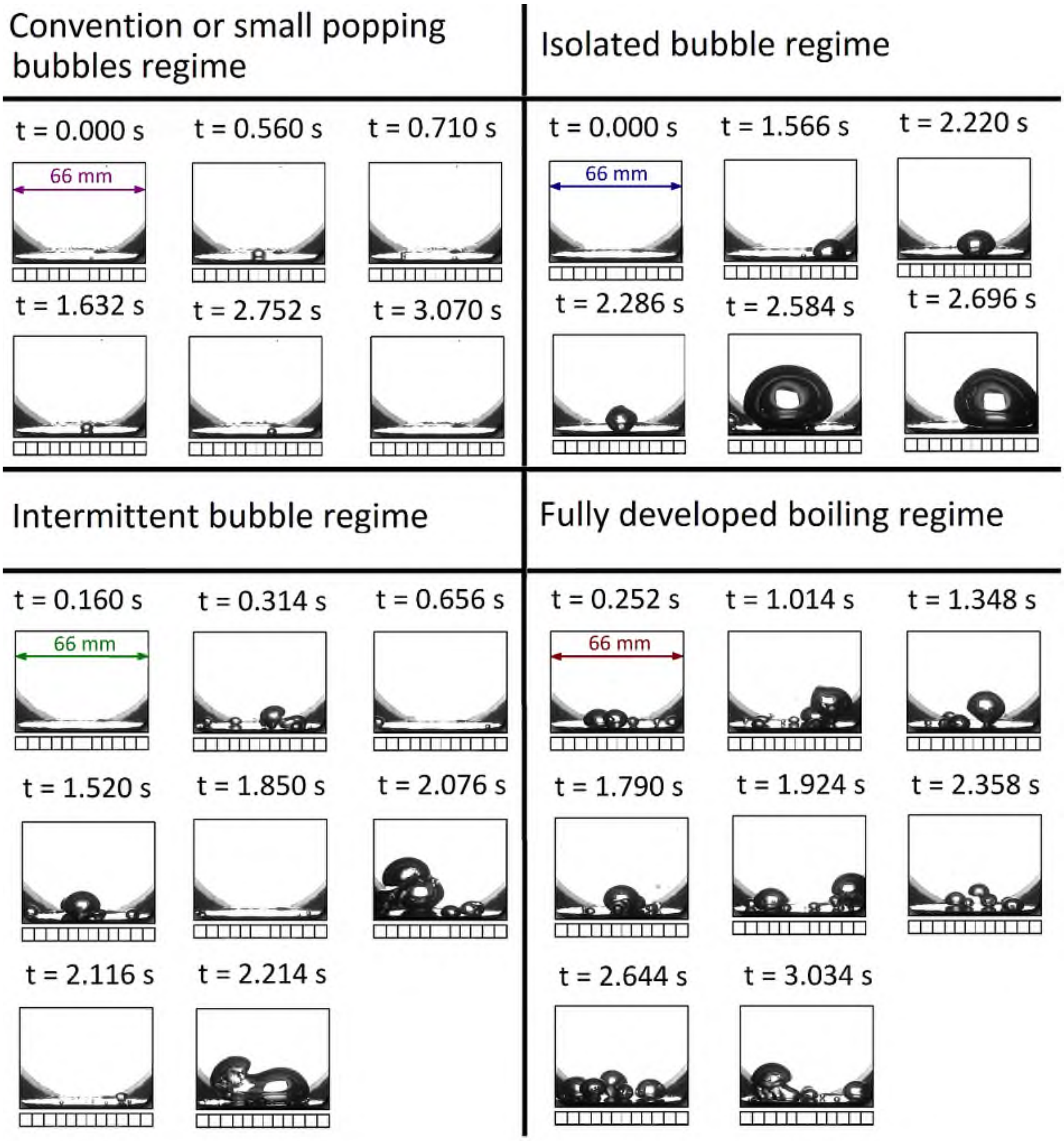

Figure 4.9: Frames from video sequences of various boiling regimes occurring at low pressure.

4.3.1 Regime of convection or small popping bubbles

This regime primarily occurs when the heat flux is too small to initiate any substantial nucleation. For highly subcooled liquid (when the liquid level is high enough), small popping bubbles (few millimeters in size) can nevertheless grow on the heated wall, but because of their size, they are almost undetectable by the heat flux sensor. The bubbles actually pop because of the subcooling that induces intense condensation of vapor and rapid bubble collapse. The lack of frequently detaching bubbles significantly decreases the effectiveness of heat extraction from the surface, which results in almost constant heat flux. In such conditions, no major fluctuation of heat flux was detected (Fig. 4.10, top). The PDF, due to low heat flux fluctuation ($\Delta q < 0.5$ Wcm^{-2}), is characterized by a single very narrow peak - several times narrower in comparison to other regimes (see Fig. 4.10, bottom).

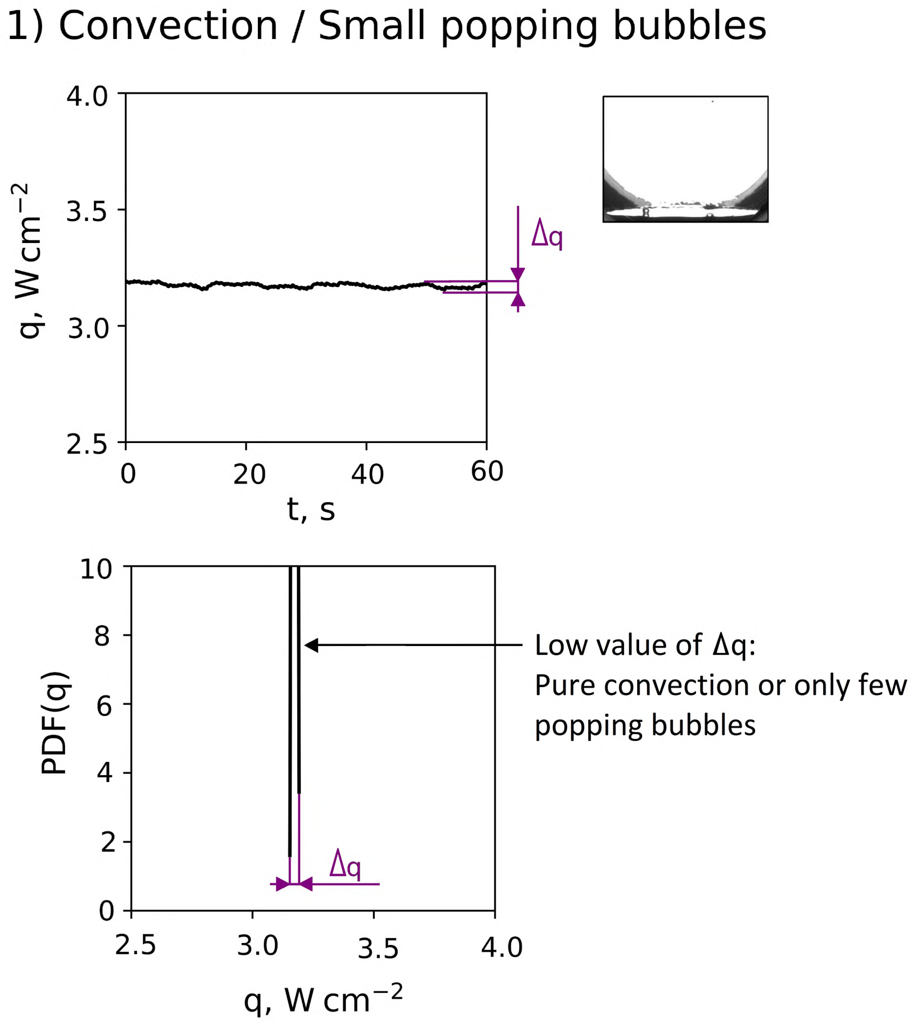
1) Convection / Small popping bubbles

Low value of Δq:
Pure convection or only few
popping bubbles

Figure 4.10: Example of a thermal signature (heat flux vs. time) and a PDF for convection or small popping bubbles regime ($p_v = 2.4$ kPa, $H_l = 60$ cm, $q_{app} = 4.4$ Wcm^{-2}).

4.3.2 Regime of isolated bubbles

This regime consists of the succession of large bubbles separated by long waiting time. The formed bubbles are large and they do not interact with each other (in most of cases there is just one bubble at a time due to large bubble diameters (few centimeters), comparable to size of the heated surface). This type of boiling is the most commonly described in the literature [41, 81, 121], as this regime exists for the most often applied working conditions (level of liquid between 10 cm and 20 cm, moderate value of heat flux). Analyzing the heat flux evolution (Fig. 4.11, top), one can notice visible peaks occurring at low frequency. Single phase convection is present for most of the time, except when a bubble is emitted. These characteristics locate a peak of the PDF on the left side of the graph (towards the low values of q), which represents a high probability of the waiting period occurrence during this regime (Fig. 4.11, bottom). The bubbles rarely appear on the surface, so the values of PDF(q) at high heat fluxes are close (but not equal) to zero.

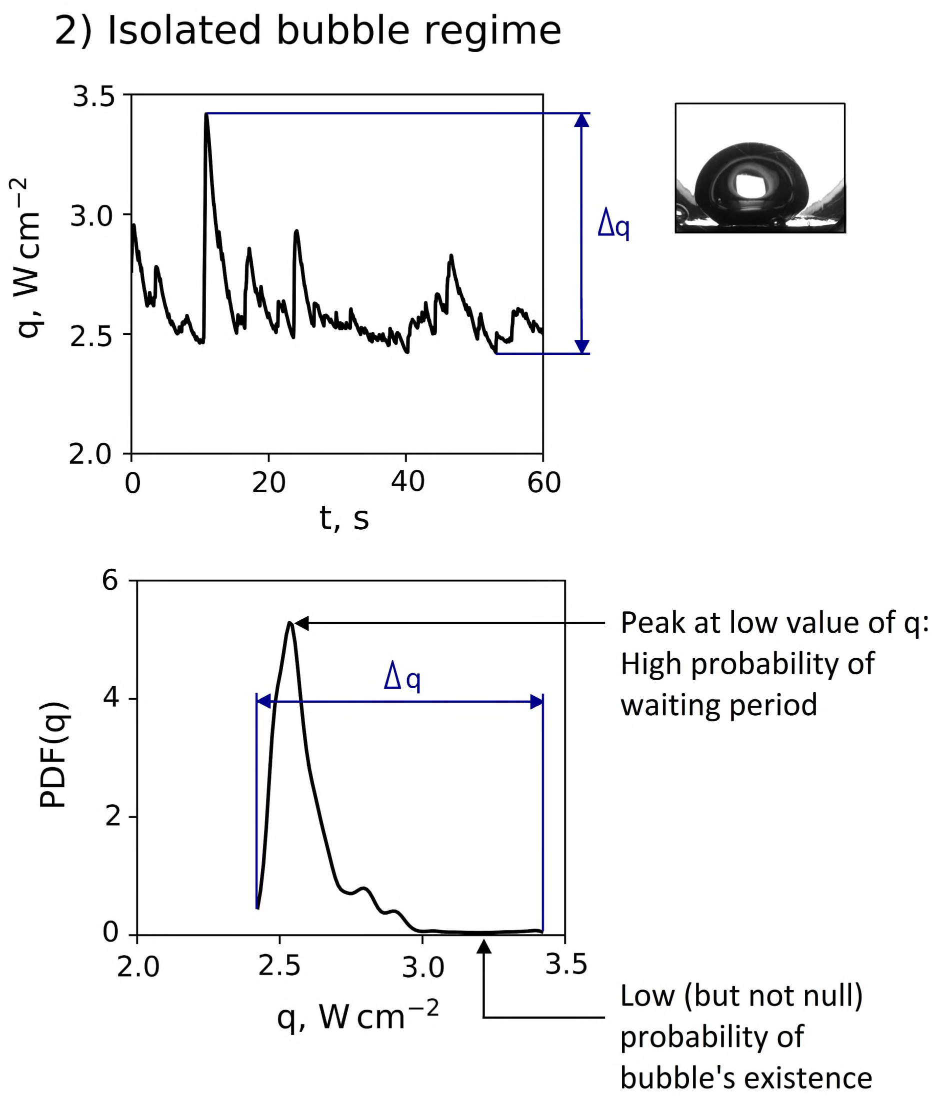

Peak at low value of q: High probability of waiting period

Low (but not null) probability of bubble's existence

Figure 4.11: Example of a thermal signature (heat flux vs. time) and a PDF for isolated bubbles regime ($p_v = 2.4$ kPa, $H_l = 15$ cm, $q_{app} = 3.6$ Wcm^{-2}).

4.3.3 Regime of intermittent boiling

This regime is characterized by many bubbles appearing on the surface. The bubbles have a reduced size with respect to those of the isolated bubble regime. They interact with each other and form bigger bubble columns. Single phase convection intervals are observed (resembling the long waiting period at the isolated bubble regime). During these periods, the heat flux has almost a constant value over time (Fig. 4.12, top). The PDF in such case is represented by a flat peak and symmetrical shape, meaning that high and low values of heat flux have similar probabilities (Fig. 4.12, bottom).

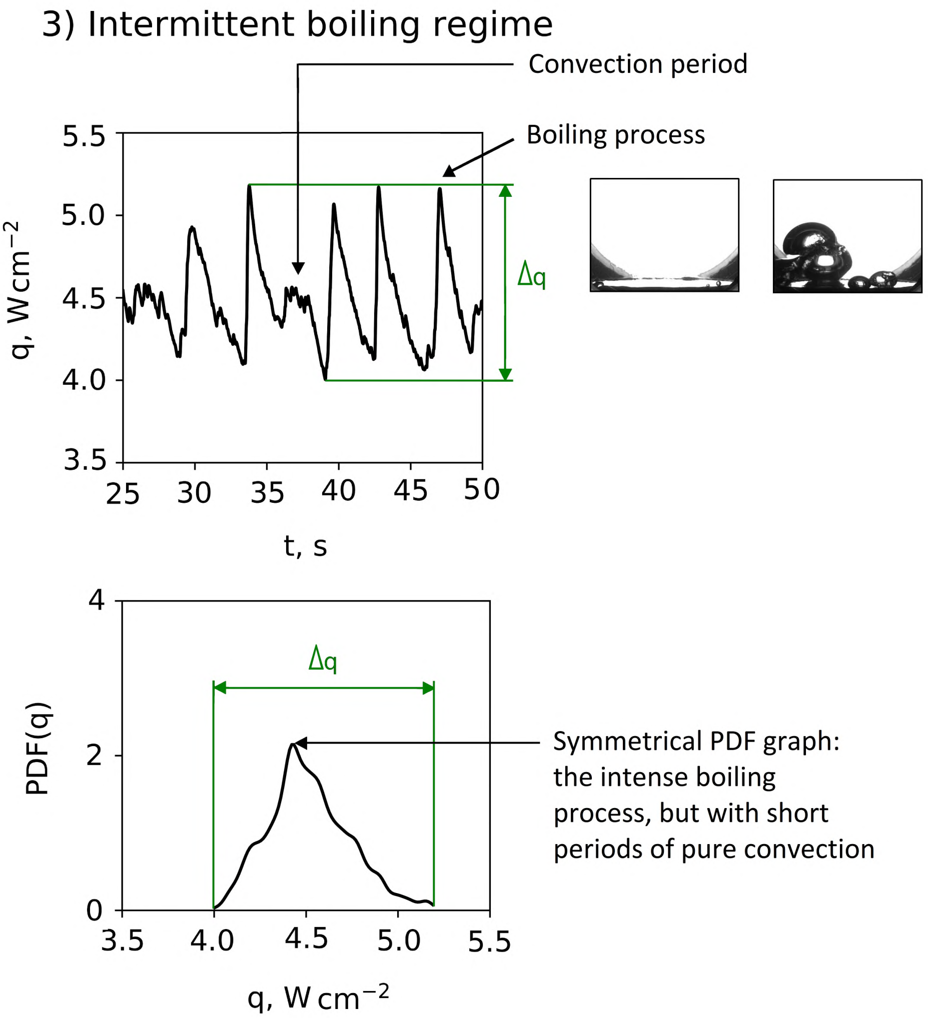

Symmetrical PDF graph: the intense boiling process, but with short periods of pure convection

Figure 4.12: Example of a thermal signature (heat flux vs. time) and a PDF for intermittent boiling regime (p_v = 4.1 kPa, H_l = 28 cm, q_{app} = 6.1 Wcm^{-2}).

4.3.4 Regime of fully developed boiling

Fully developed boiling is characterized by an intense boiling process. A large number of bubbles nucleate at the same time and they can interact with each other and form larger bubble clusters. The heat flux evolution is densely packed (see Fig. 4.13, top) as the applied heat flux is sufficient enough to avoid periods of single phase convection without bubbles on the surface. For this type of boiling, the PDF graph (Fig. 4.13, bottom) can be symmetrical or skewed right towards high values of heat flux (which indicates a high probability of bubble occurrence).

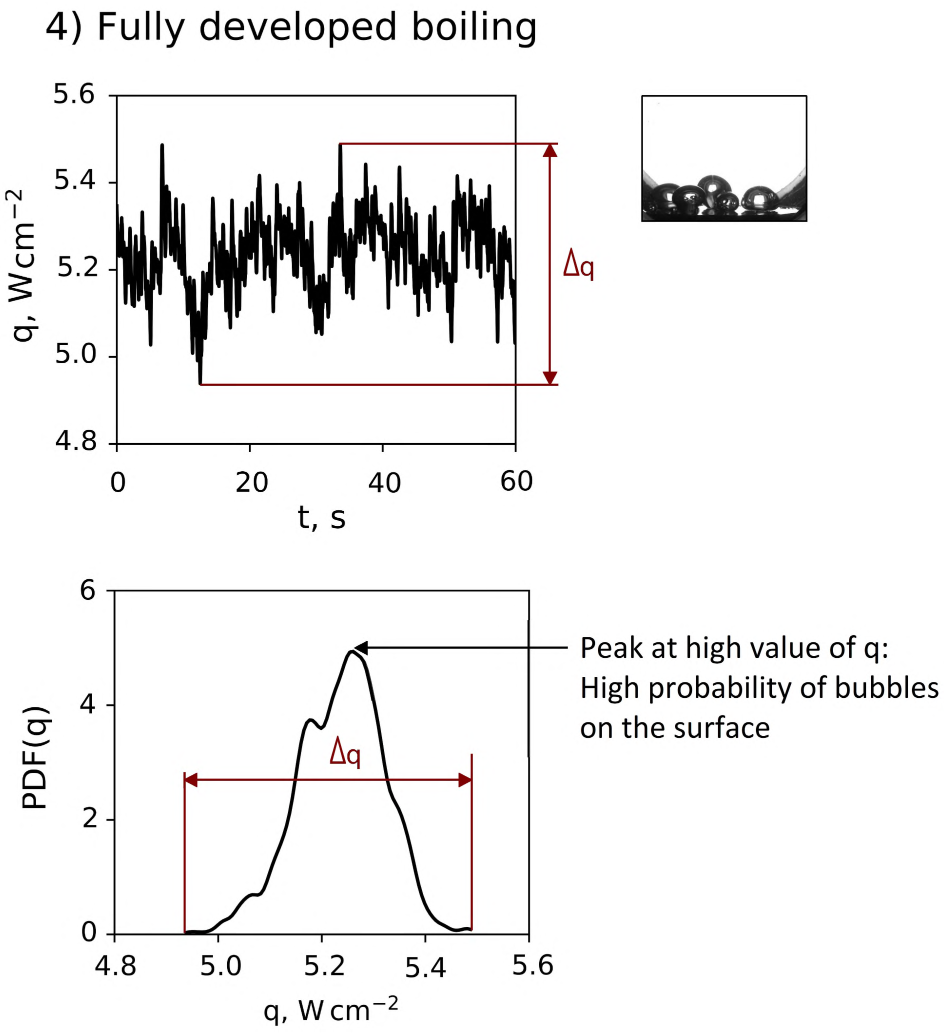

4) Fully developed boiling

Peak at high value of q: High probability of bubbles on the surface

Figure 4.13: Example of a thermal signature (heat flux vs. time) and a PDF for fully developed boiling regime ($p_v = 2.4$ kPa, $H_l = 15$ cm, $q_{app} = 7.1$ Wcm^{-2}).

4.4 Influence of the liquid level and heating power on the boiling regimes

The set of PDF graphs created for a vapor pressure of $p_v = 2.4$ kPa and four distinct liquid levels ($H_l = 15$ cm, 28 cm, 35 cm, 60 cm) is presented in Fig. 4.14. Each graph represents the PDF for a specific liquid level and five different applied heat fluxes ($q_{app} = 3.6$ Wcm^{-2}, 4.4 Wcm^{-2}, 5.2 Wcm^{-2}, 6.1 Wcm^{-2} and 7.1 Wcm^{-2}, what corresponds to heating power of 174 W, 210 W, 248 W, 293 W and 331 W, respectively). The PDF graphs generated for other vapor pressures ($p_v = 3.1$ kPa and $p_v = 4.1$ kPa) are displayed in Appendix B. Increasing the applied heat flux shifts the values of instantaneous heat flux q detected by sensor towards higher values. Boiling regimes in Fig. 4.14 are marked by different colors: convection or popping bubbles regime in purple, isolated bubbles regime in blue, intermittent boiling regime in green and fully developed boiling regime in red. When the PDF graphs were not sufficient to definitely distinguish the intermitted boiling regime from the fully developed boiling regime (e.g. cases for $H_l = 15$ cm and $q_{app} = 5.2$ Wcm^{-2} and $q_{app} = 6.1$ Wcm^{-2}), the video recordings were used to make the final decision. If periods of pure convection were observed, the experiment was assigned to the intermitted boiling regime. In the opposite case - the measurement was assigned to the fully developed boiling regime.

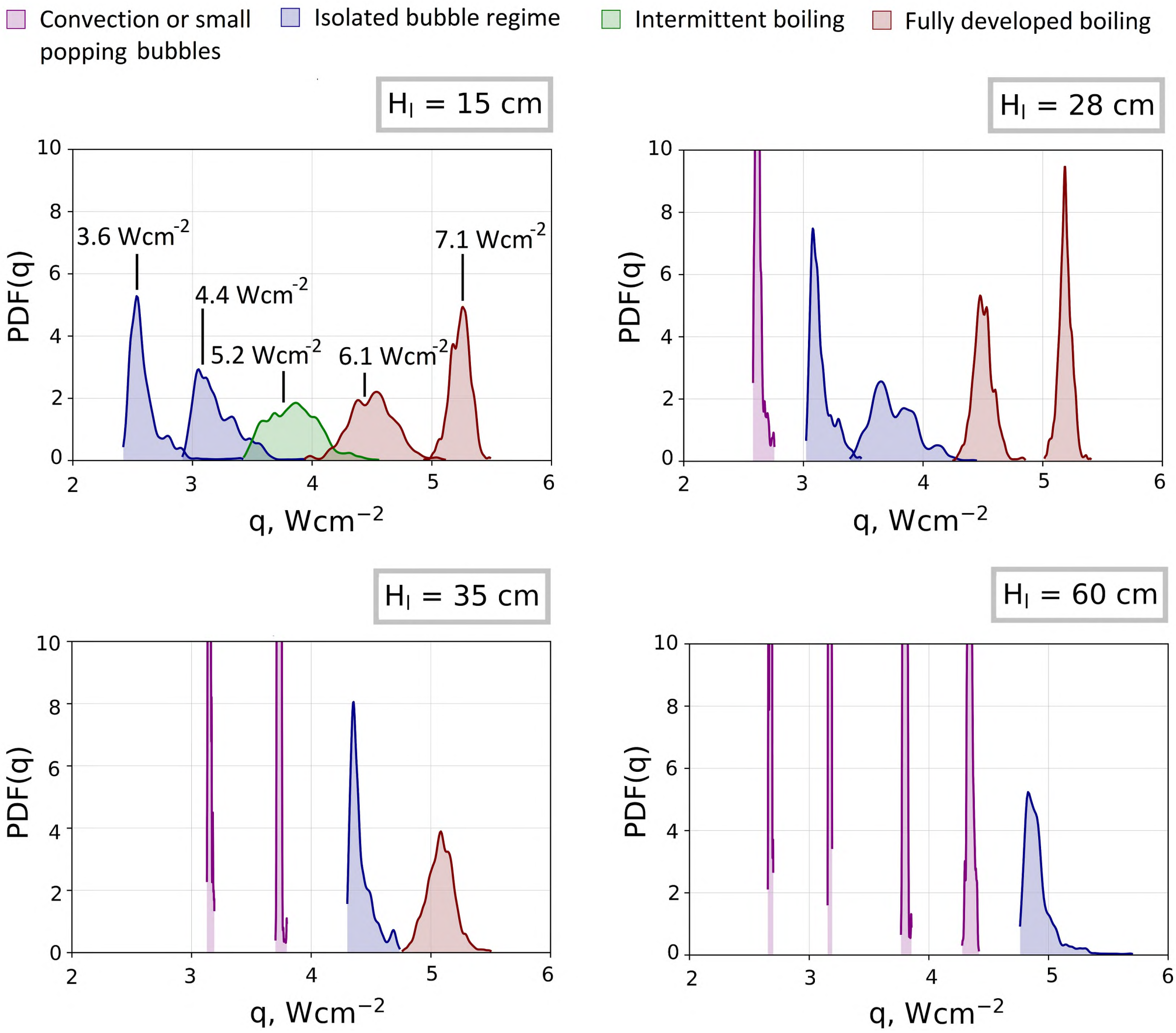

Figure 4.14: PDF graphs for vapor pressure $p_v = 2.4\,\mathrm{kPa}$, $S_q = 3.5\,\mathrm{\mu m}$ (applied heat fluxes for the graphs from left to right: 3.6 W·cm^{-2}, 4.4 W·cm^{-2}, 5.2 W·cm^{-2}, 6.1 W·cm^{-2} and 7.1 W·cm^{-2}).

It is more difficult to initiate the boiling process for a high level of liquid due to increased degree of liquid subcooling (see Section 1.2.1). More energy is required to heat up the liquid, i.e. higher wall superheat is necessary to initiate boiling. Larger subcooling of the liquid reduces the size of bubbles because of the condensation mechanism caused by high subcooling of liquid. That is why, for the highest level of liquid $H_l = 60$ cm and almost entire range of applied heat fluxes, convection or small popping bubbles regime were observed.

The span of heat flux Δq on the PDF graphs is the highest for liquid level $H_l = 15$ cm and low or moderate heat flux. At such conditions bubbles have large diameters, provoking strong fluctuations of heat flux. The waiting time is long, thus the probability of high heat flux occurrence is close to zero. For the fully developed boiling regime, increasing applied heat flux leads to higher values of instantaneous heat flux (corresponding to more intense boiling process). Bubbles are nucleating, growing and detaching continuously. The waiting time remains low and there are always some bubbles on the surface. Although multiple bubbles are present on the surface at the same time, the heat flux span Δq tends to be reduced due to their small diameters. One can also notice that the intermittent boiling regime at this vapor pressure is observed only for $H_l = 15$ cm and $q_{app} = 5.2$ Wcm^{-2}. This indicates that this boiling mode exists only for a narrow set of operating parameters.

4.5 Boiling regime map

The analysis of the PDFs was performed for all operating conditions (three vapor pressures, four levels of liquid, five applied heat fluxes). To illustrate how changes of the operating parameters affect the type of the boiling regime, the boiling regime maps are proposed. These maps identify the regime as a function of applied heat flux (abscissa) and liquid level (ordinate) for a given vapor pressure (Fig. 4.15).

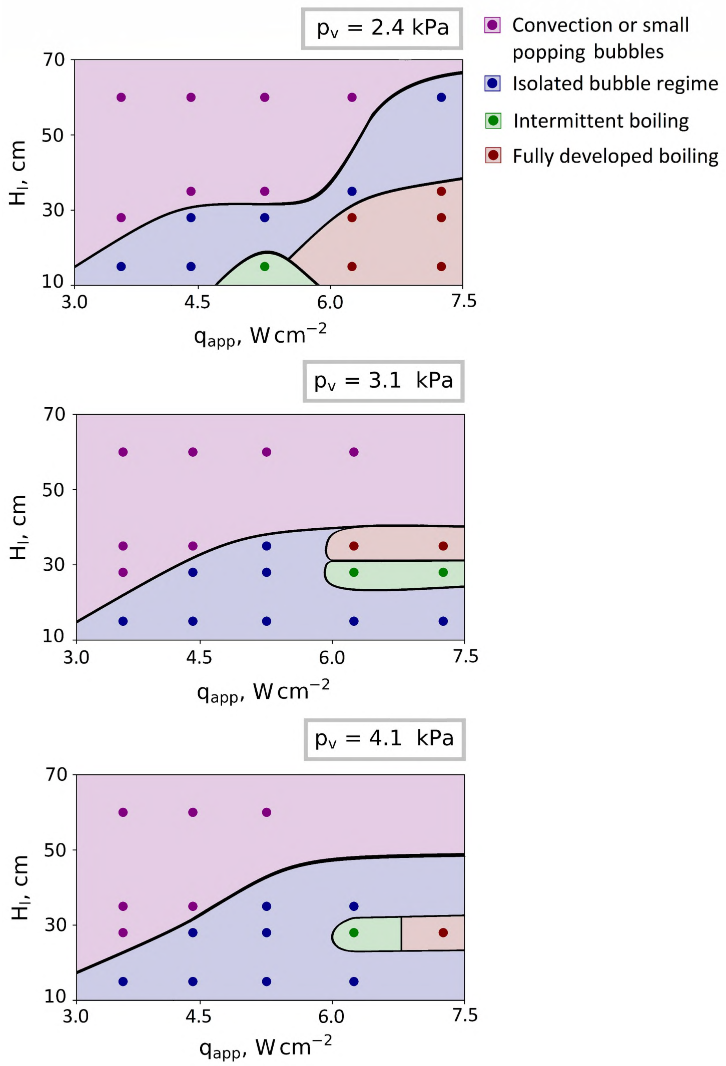

Figure 4.15: Boiling regime maps created for various pressures, liquid levels and applied heat fluxes ($S_q = 3.5$ µm).

For the studied values of vapor pressures, all boiling maps look different, although they possess some common features - at least, for all cases, the same boiling regimes can be observed. When increasing the applied heat flux, first there is a region of convection or eventually small popping bubbles (purple region). Then, isolated bubbles not interacting with each other start to be formed (blue region). At low pressure, due to low vapor density, the bubbles usually exhibit a large size, comparable to the size of the heated surface, so only one bubble is present on the surface at a time. When the applied heat flux is increased further, the fully developed boiling regime occurs, which is characterized by existence of multiple bubbles, often interacting with each other (red region). For certain conditions also the intermittent boiling regime is detected (green region).

For given level of liquid and value of applied heat flux, the regime depends on the vapor pressure. For instance, for $p_v = 2.4$ kPa and $H_l = 15$ cm, with increasing applied heat flux, one can observe successively isolated bubble regime, intermittent boiling regime and fully developed boiling regime. For the other vapor pressures ($p_v = 3.1$ kPa and $p_v = 4.1$ kPa), only the isolated bubble regime is observed. These differences are caused by the increase of saturation temperature for higher vapor pressures, as it requires higher applied heat flux to initiate boiling or reach specific type of regime.

4.5.1 Generalized, non-dimensional boiling map

To develop a dimensionless boiling map for low pressure boiling, the abscissa was chosen to be the ratio of the vapor pressure to the static pressure (p_v/p_{stat}). This ratio is believed to be good representative of both – low pressure conditions (p_v) and intensity of the subcooling degree (p_{stat}). For the ordinate, physical considerations led to the definition of a modified Jakob number.

The Jakob number is dimensionless number, often used in the analysis of phase change heat transfer as it represents the ratio of the sensible and the latent heat. One of its common forms was given in Chapter 1 by Eq. 1.13. In such form, Eq. 1.13 results high values of Jakob number at sub-atmospheric conditions, due to the very small vapor density [127]. Such strong dependence on the vapor density is not beneficial for the current analysis as it could double the information about low pressure conditions (if the graph is plotted with respect to vapor or wall level pressure). A better option is usage of second form of Jacob number which does not depend on fluid densities [15, 54]:

$$Ja = \frac{c_{p(l)} \Delta T_{wall}}{h_{lv}} \tag{4.2}$$

This form of the Jakob number is nevertheless suitable to constant temperature conditions. It cannot be used directly to include the heat flux in the analysis, while it was demonstrated that the heat flux strongly affects the boiling regimes. To include the effect of the heat flux, it was decided to replace the temperature difference of the Jakob number by one scaling of it. This is a common practice for instance in the case of single phase convection, when the classical Grashof number is changed to the so-called "modified Grashof number" [59].

The proposed scaling for the wall superheat is based on the process of heat diffusion in the thermal boundary layer, in the fluid above the heated wall. This was the physical basis of the nucleation model of Mikic and Rohsenow [84]: in this model, the thickness of the boundary layer was supposed to be of the order of magnitude of the bubble size, that can be scaled by the capillary length. Therefore, assuming that:

$$\Delta T \sim \frac{q_{app} L_c}{\lambda_l} \tag{4.3}$$

the modified Jakob number can be defined as:

$$Ja^* = \frac{c_{p(l)} L_c q_{app}}{h_{lv} \lambda_l} \tag{4.4}$$

The boiling map created based on the modified Jakob number defined by Eq. 4.4 is presented in Fig. 4.16 and various boiling regions are marked in the same manner as on previous boiling maps (purple color - convection or small popping bubbles region, blue color - isolated bubble region, green color - intermittent boiling region, red color - fully developed boiling region).

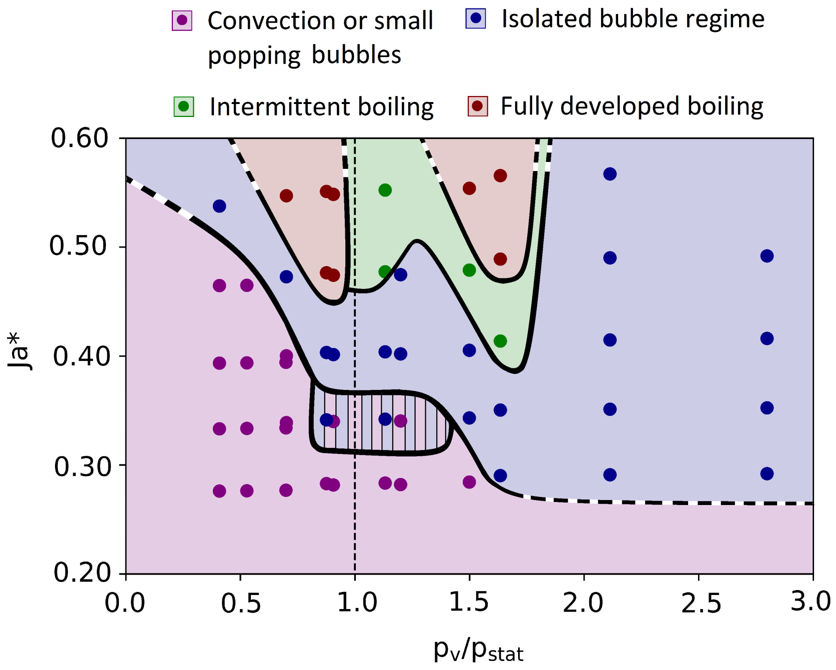

Figure 4.16: Dimensionless boiling map for subatmospheric pressure (S_q = 3.5 µm).

The map is divided into two parts. For $p_v/p_{stat} < 1.0$, the boiling process is mainly driven by high value of subcooling. This explain the existence of large regions of convection or small popping bubbles. In the case of $p_v/p_{stat} > 1.0$, the boiling process is under the influence of the sharp change of thermophysical properties of the liquid at low pressure (see Section 1.2.2). The hydrostatic pressure influences the boiling behavior to a smaller extent because it has lower value than the vapor pressure. At such conditions, low values of heating power (low Jakob number) cause immediately the existence of isolated bubble regime

High values of heat flux lead to fully developed boiling regime. This type of boiling was obtained for lower Jakob number in the close proximity of $p_v/p_{stat} = 1$. For the highest applied heat flux reached in the present experiments ($q_{app} = 7.1$ Wcm^{-2}), if p_{stat} or p_v are too large, the isolated bubble regime is observed. For high heat fluxes and p_v/p_{stat} value in the range [1; 1.6], the intermittent boiling regime was also observed.

The region close to $p_v/p_{stat} = 1$ and $Ja^* = 0.35$ occurred to be the transition between the convection or small popping bubbles region (purple area) and isolated bubble regime (blue area).

The experiments were performed for low vapor pressure ($p_v/p_{stat} < 5$). However, most of the experiments for water reported in the literature were conducted close to the atmospheric pressure. For $p_v = 100$ kPa and $H_l = 15$ cm, the pressure ratio p_v/p_{stat} is equal to 70. At such conditions, three different regimes are usually distinguished. For instance, Gaertner [34] observed the convection regime up to $q_{app} = 3.3 \cdot 10^4$ Wm^{-2} (Ja$^* = 0.25$), the isolated bubbles regime ($3.3 \cdot 10^4$ Wm^{-2} $< q_{app} < 1.5 \cdot 10^5$ Wm^{-2} which corresponds to $0.25 <$ Ja$^* < 1.08$) and the fully developed boiling regime ($q_{app} > 1.5 \cdot 10^5$ Wm^{-2} which corresponds to Ja$^* > 1.08$). The region which was the scope of the present experiments, is thus quite narrow in respect to all possible operating conditions: Fig. 4.17 shows how the present boiling map could be extended to the range of high p_v/p_{stat} corresponding to Gaertner's observations and where the boiling regimes this author distinguished would be located on such a map.

This graph reveals that major differences exist between the conditions studied in the present work and the published data on pool boiling close to the fluid normal point. It also highlights that the regime of intermittent boiling is specific to low pressure boiling. The complexity of the distribution of the regimes on the map justifies the importance of further investigation of the pool boiling close to the triple point. The high pressure is much less sensitive to the changes of the liquid level, thus the borders between specific regimes are very clear and form straight, almost horizontal lines.

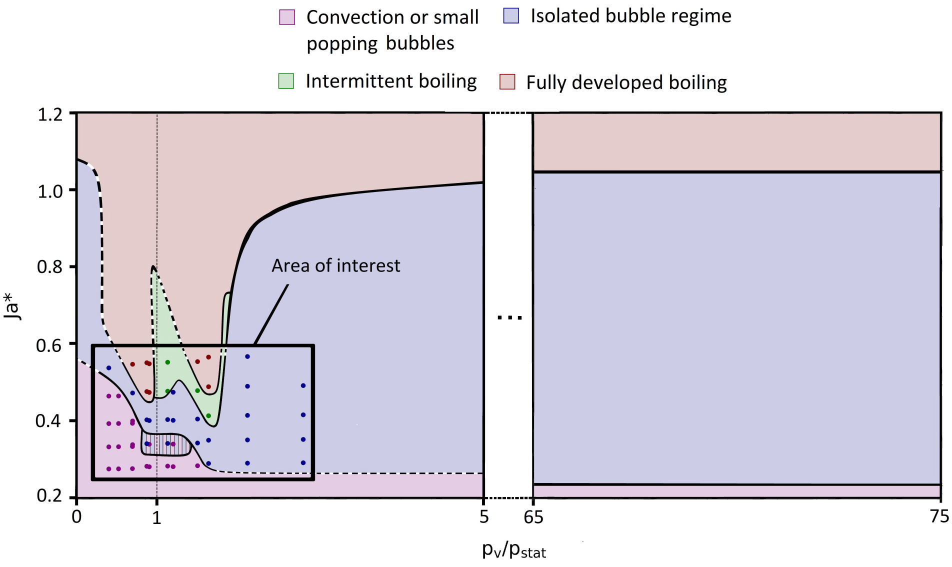

Figure 4.17: Dimensionless boiling map for a broad range of input parameters (up to atmospheric pressure).

4.6 Influence of the surface roughness

When all the tests described in Sections 4.4 - 4.5 were already performed, the surface was treated again with emery paper in order to obtain a surface with different roughness. The measurements conducted with the confocal microscopy (see Appendix A) have estimated that the surface roughness decreased to the level of $S_q = 2.8$ µm. Such approach allows to compare the boiling behavior for the same operating conditions (vapor pressure, applied heat flux, liquid level) with different surface characteristics (meaning that different numbers of nucleation sites are present on the surface). In this Section the impact of the surface roughness on the boiling regimes and heat transfer coefficient will be described.

4.6.1 Impact of the surface roughness on the boiling regimes

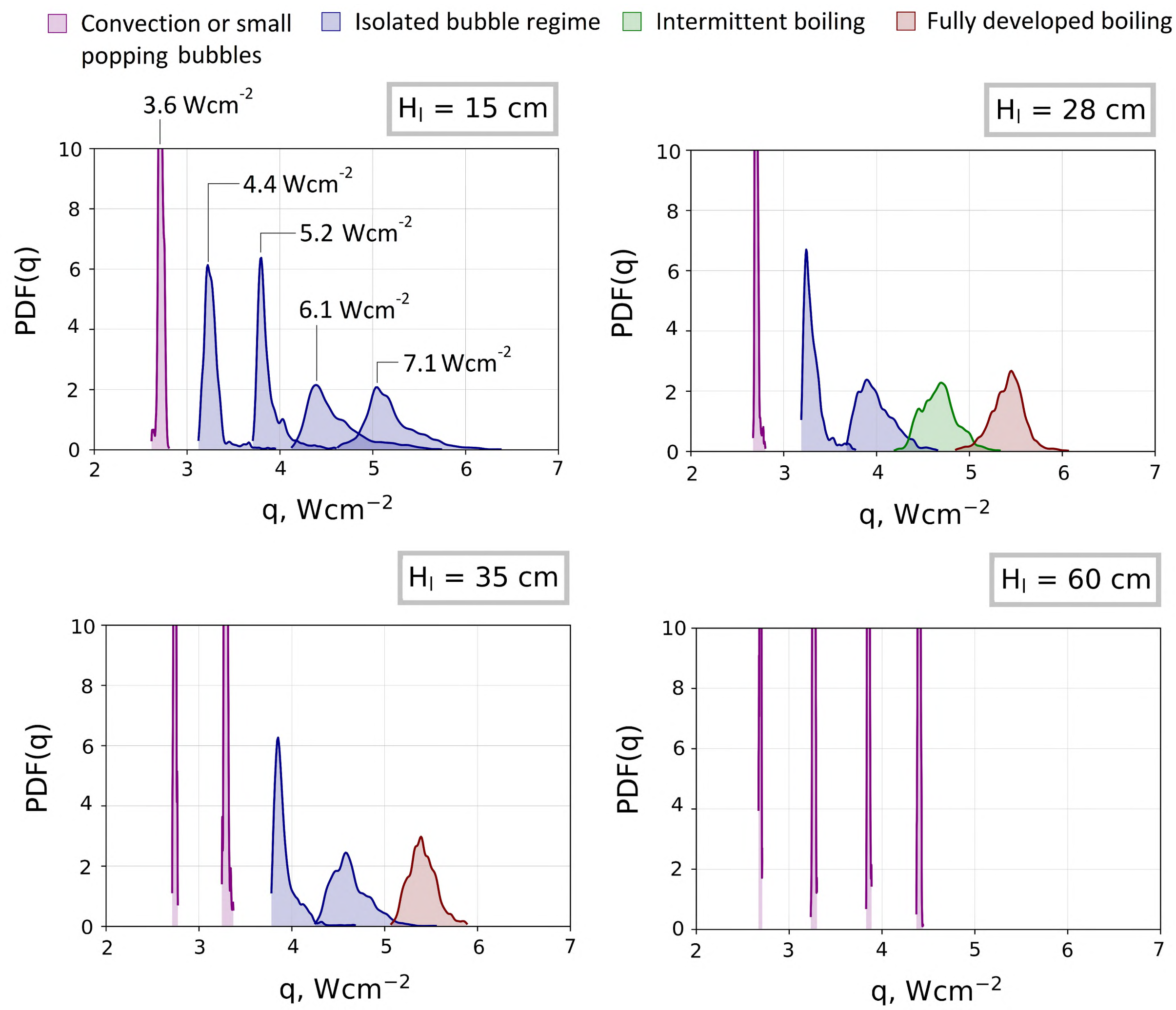

Figure 4.18: PDF graphs for vapor pressure $p_v = 2.4$ kPa, $S_q = 2.8$ µm (applied heat fluxes for the graphs from left to right: 3.6 Wcm^{-2}, 4.4 Wcm^{-2}, 5.2 Wcm^{-2}, 6.1 Wcm^{-2} and 7.1 Wcm^{-2}).

The PDFs obtained for the same working conditions as in Section 4.4 ($p_v = 2.4$ kPa, four liquid levels, five applied heat fluxes) are plotted in Fig. 4.18. One can observe that distinct regimes generally occur in a similar manner as for the surface with initial roughness (see Fig. 4.14 and Fig. 4.18). Results obtained for $H_l = 28$ cm, 35 cm and 60 cm in most of the cases are classified into the same boiling regime for both roughness. Only the PDFs for $H_l = 15$ cm differs more significantly. For roughness $S_q = 3.5$ µm (see

Fig. 4.14) with increasing applied heat flux, isolated bubble regime, intermittent boiling regime and fully developed boiling regime are observed consequently. For $S_q = 2.8$ µm (see Fig. 4.18), the lowest applied heat flux results in a convection or small popping bubbles regime. Further increase of heat flux in the studied range led to the observation of the isolated bubble regime.

This difference might be associated with lower value of roughness. Smaller number of active nucleation sites require higher wall superheat and higher heat fluxes to reach fully developed boiling regime. However, at low value of vapor pressure and moderate level of liquid (e.g. 15 cm), the number of active nucleation sites is generally low. Additionally, the boiling process is a stochastic phenomenon, thus even the same surface and operational conditions would give slightly different results. For that purpose it is not fully known if the difference in the boiling regimes is mostly due to change of the surface roughness or rather due to statistical character of the boiling process itself.

It was not possible to easily obtain higher difference in the surface roughness. The scratching of the surface was done manually. More intense treatment of the surface could not be performed because of several reasons. Firstly, a layer of acrylic clearcoat was deposited at the periphery of the surface in order to prevent the liquid penetration into the system and this layer should not be removed. The cables connected at the ribbon connection could also be damaged during the intense surface polishing. Furthermore, the layer of copper above the heat flux sensor is very thin (0.3 mm) and too intense interference into the surface could be dangerous for the system. Detailed description of the heating surface and is preparation is given in Section 2.1.3.

4.6.2 The influence on the boiling regime maps

Fig. 4.19 presents the boiling regime maps created for all operating conditions with three vapor pressures $p_v = 2.4$ kPa, 3.1 kPa, 4.1 kPa. It is shown that the boiling regime map closely resembles the one obtained for previous surface roughness (see Fig. 4.15). The main difference is the fact for lower studied roughness ($S_q = 2.8$ µm), high values of applied heat flux often results in a regime with smaller number of bubbles present on the surface. E.g. for $p_v = 2.4$ kPa and $H_l = 15$ cm, the intermitted and fully developed boiling regimes are obtained at high heat fluxes when roughness is equal to $S_q = 3.5$ µm (see Fig. 4.15). For $S_q = 2.8$ µm only the isolated bubble regime is reached for applied heat fluxes larger than 3.6 Wcm^{-2} (see Fig. 4.19). Analogical situation is observable for $p_v = 4.1$ kPa and $H_l = 28$ cm. However, most of the points corresponds to the same regime for specified working conditions.

The dimensionless boiling map (p_v/p_{stat} vs. Ja*) created based on Eq. 4.4 and according to the description included in Section 4.5.1 was developed also for roughness $S_q = 2.8$ µm (see Fig. 4.20). It resembles the map obtained for roughness $S_q = 3.5$ µm (see Fig. 4.16). For low values of p_v/p_{stat}, the boiling process is mostly driven by high subcooling of liquid (thus mostly the convection and small popping bubbles regime is observed). At high values of p_v/p_{stat}, the low value of vapor pressure itself, through the strong variation of some thermophysical properties, influences the boiling behavior. In this case, the isolated bubble regime (usually associated with low pressure pool boiling) is dominant.

In the proximity of the line $p_v/p_{stat} = 1$ another regime also occurs: the fully developed boiling and intermittent boiling. For Ja* from 0.3 to 0.4, the transition between the convection or small popping bubbles regime (purple area) and isolated bubble regime

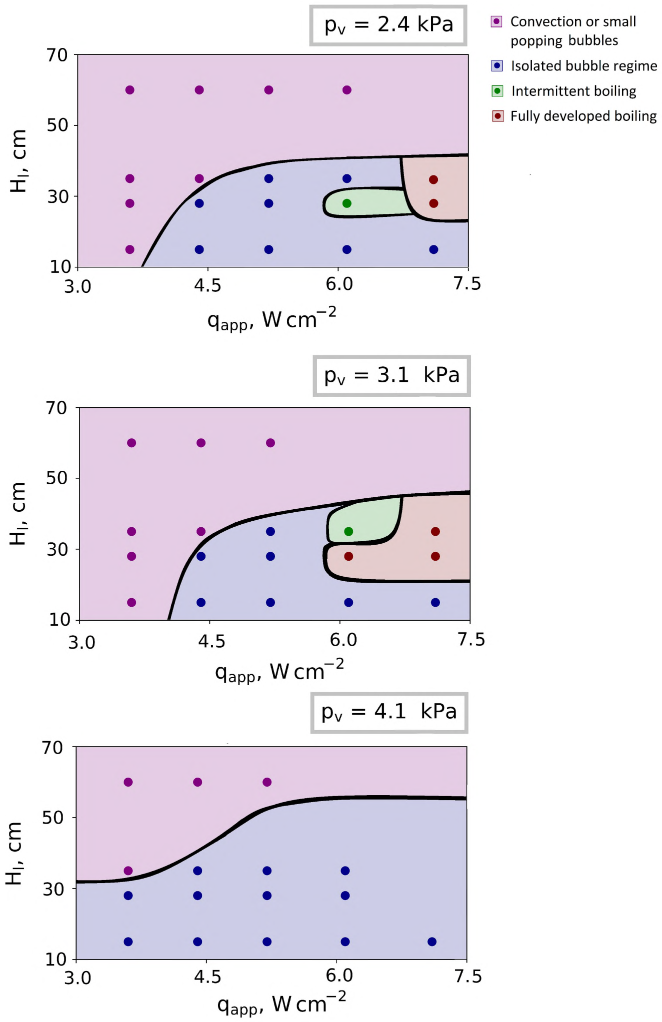

Figure 4.19: Boiling regime maps created for various pressures, liquid levels and applied heat fluxes.

(blue area) is also present. Such arrangement of the regimes corresponds to the ones obtained for previous roughness (see Fig. 4.16). The main difference, however, lies in the fact that for $S_q = 3.5$ µm (see Fig. 4.16) the fully developed and intermittent boiling regimes are observed for wider range of operating parameters and are more spread along the p_v/p_{stat} axis (for $S_q = 3.5$ µm the fully developed boiling regime is observed up to $p_v/p_{stat} = 1.75$, while for $S_q = 2.8$ 3.5 µm only up to $p_v/p_{stat} = 1.25$).

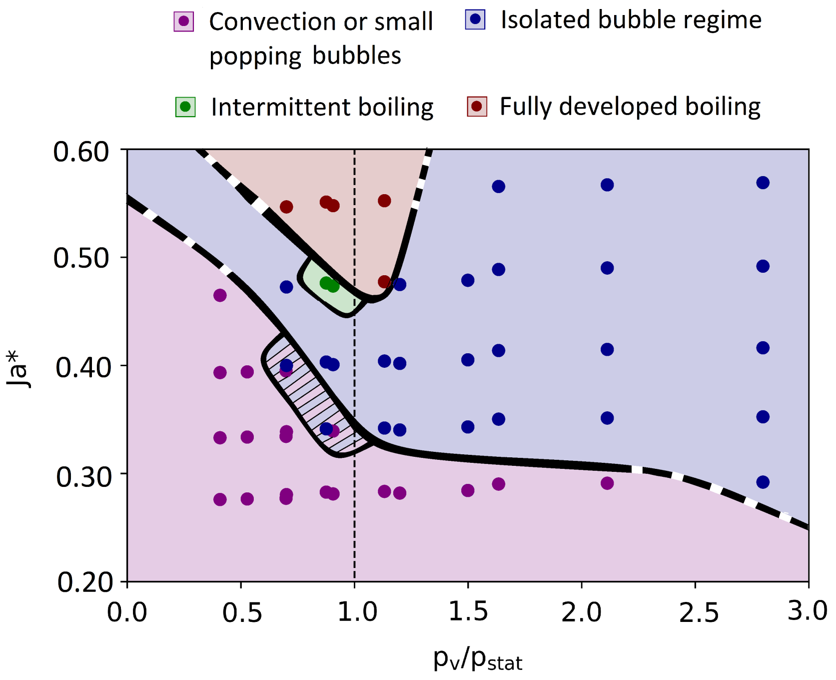

Figure 4.20: Dimensionless boiling map for subatmospheric pressure (S_q = 2.8 µm).

4.6.3 Influence on the heat transfer coefficient

To compare the thermal performance of the boiling process for both roughness, the average heat transfer coefficient was calculated for the same value of vapor pressure as in Section 4.2.3 (p_v = 3.1 kPa). Tab. 4.2 presents the outcome of such measurements for S_q = 2.8 µm and various working conditions (five applied heat fluxes and four liquid levels). It occurs that similarly like for S_q = 3.5 µm (see Tab. 4.1), the maximum values of heat transfer coefficient are obtained for liquid level 28 cm (those values were marked in bold in Tab. 4.2). They have the same order of magnitude as the ones reached for S_q = 3.5 µm (see Tab. 4.1), however for most of the cases they are several percent lower.

Table 4.2: Averaged heat transfer coefficient (p_v = 3.1 kPa, S_q = 2.8 µm).

h, $\mathrm{Wm}^{-2}K^{-1}$		H_l			
		15 cm	28 cm	35 cm	60 cm
q_{app}, $\mathrm{W{\cdot}cm^{-2}}$	3.6	640	**659**	640	624
	4.4	708	**731**	692	650
	5.2	746	**829**	777	670
	6.1	827	**929**	868	-
	7.1	893	**1007**	956	-

Conclusions

Subatmospheric pool boiling experiments were conducted for various working parameters: vapor pressures ranging from 2.4 kPa up to 4.1 kPa, liquid levels of 15 cm, 28 cm, *35 cm, 60 cm and several applied heat fluxes. The liquid level is of specific importance for subatmospheric boiling: it controls, through the static pressure it imposes, the subcooling of the liquid that affects the heat transfer.*

Boiling with higher liquid levels is associated with larger values of wall temperature and heat fluxes required to initiate nucleation process. It appears that there is an optimal liquid level for which the bubbles size and detachment frequency give the highest value of heat transfer coefficient (in the present experiment the maximum averaged heat transfer coefficient was reached for $H_l = 28$ *cm).*

To discover how different operating parameters influence the boiling behavior, the analysis of the time evolution of heat flux was performed statistically based on probability density functions (PDFs). It was then exemplified how this type of analysis constitutes a good tool for studies of the boiling behavior. Owing to this type of statistical analysis, supported by visual observations, four distinct boiling regimes were distinguished and characterized: the convection or small popping bubbles regime, the isolated bubble regime, the intermittent boiling regime, the fully developed boiling regime.

For the liquid levels $H_l = 15$ *cm and* $H_l = 28$ *cm, the most common regime is the one of isolated bubbles. It is characterized by bubbles with large diameters detaching with low frequency. For the high level of liquid mostly the convection or small popping bubbles were observed.*

The variety of the regimes observed at low pressures at different liquid levels proves the importance of the subcooling caused by the static head. In the future, it would be of interest to study the difference between the temperature-induced subcooling and pressure-induced subcooling. For this purpose, the boiling process should be studied firstly for high level of liquid (e.g. $H_l = 60$ *cm,* $T_l = T_{sat}$*) and then lower the liquid level with liquid bulk temperature lower than saturation temperature (e.g.* $H_l = 15$ *cm* $T_l < T_{sat}$*) in such a way that at wall level both subcoolings are equivalent.*

To provide a more general description of boiling regimes over the range of operating conditions tested, a dimensionless boiling regime map was proposed. The abscissa was chosen to be the ratio of vapor pressure to the static pressure. It is a good representative of both low pressure conditions (p_v*) and subcooling of the liquid (strongly dependent on* p_{stat}*). As a ordinate, a modified Jakob number was adapted to conditions of constant heat flux encountered in the present experiments. When* $p_v/p_{stat} < 1.0$*, the boiling mode is mostly driven by intense liquid subcooling (thus, mostly convection or small popping bubbles regime are observed as the subcooling induced by the high static pressure results in a strong condensation of any generated vapor). When* $p_v/p_{stat} > 1.0$*, even for low values of applied heat fluxes, other regimes are often already noted. This boiling regime map is useful to determine the thermo-hydrodynamic features of subatmospheric boiling. Its consistency with the knowledge developed for higher pressures (typically close to atmospheric pressure) remains to be investigated in detail, both for saturated and subcooled conditions. Finally, to truly validate the correctness of the dimensionless boiling map, more experiments with various working fluids should be conducted.*

The analysis of the boiling regimes and averaged heat transfer coefficient was performed for two different roughnesses. However, no significant difference between regimes for both surface characteristics were noted. Probably, the changes in the surface characteristics was not enough to really influence the boiling process.

Important conclusion, however, can be drawn from the fact that for all operating conditions, the average heat transfer coefficient is low and does not differ much from that typically reached during single phase convection. Because of that, the pool boiling process *at low pressure seems not to be very effective cooling method. It is possible that at the proximity to the triple point, alternative cooling solutions should be identified. One idea is to apply spray cooling instead of the boiling process. This phenomenon relies on evaporation of small droplets or thin film from a hot surface. The preliminary studies concerning this topic will be described in Section 5.*

Chapter 5

Preliminary studies of the process of evaporation at low pressure

The work reported in the previous chapters focused on the boiling process at low pressure. In Chapter 3, experimental results of a study of boiling on a polished surface with a single nucleation site were presented to interpret the dynamics of a single bubble and to reveal an applicability of the novel heat flux sensor. Chapter 4 dealt with the experiments conducted on a rough surface with multiple cavities in order to capture more general boiling behavior as this configuration is closer to real-life heat exchangers. It was confirmed that when boiling at low pressure, water possesses many characteristic features, such as increased size of the bubbles, long waiting time between two successive bubbles, much lower heat transfer coefficient in comparison to atmospheric pressure etc. All those aspects influence the effectiveness of low-pressure heat exchangers and hinder the wider application of such technologies.

An alternative idea for some types of the heat exchangers (e.g. shell and tube) could be the evaporation of small droplets sprayed onto the heated wall. At low pressure this method can be more proficient than boiling process, as large bubbles can form dry patches on the heated wall inhibiting effective heat transfer. However, there is a lack of knowledge concerning these kind of devices operating at proximity to the triple point. As the thermophysical properties of water at reduced pressures are significantly different, it would be beneficial to first study the heat transfer processes involved in the evaporation of a single drop from a hot horizontal surface. The information about the thermal behavior of such phenomenon would be helpful to interpret the evaporation process for more complex surfaces and multiple droplets simultaneously which could be conducted in the future.

A literature review concerning liquid drop evaporation is presented in Section 5.1. The operating conditions and experimental procedures are featured in Section 5.2. Section 5.3. deals with thermal effects involved in the droplet evaporation. Finally, as multiple drops can form a thin liquid film on the surface, the evaporation process of such thin layer of liquid is described in Section 5.4.

5.1 Literature review on liquid evaporation on horizontal surface

To allow for conducting the detailed analysis concerning the droplet evaporation from horizontal surface at low pressure, a review of the available literature is necessary. However, this topic at low pressure has not gained interest in the literature until now, thus the conducted analysis will refer to evaporation of water only at atmospheric conditions. Evaporation process is already widely applied in various systems. The most common applications of drops evaporation are: coating [62], inkjet printing [129] and spray cooling [103]. The last one is considered as very effective cooling method and it is often considered for systems where large amount of heat need to be removed from small heat transfer areas (e.g. cooling of electronic microchips).

5.1.1 Basic parameters describing drops and droplets

The shape of a drop is obtained by the effect of the surface tension and gravity. To form a drop, its dimensions has to be small enough to provide conditions where surface tension has similar order of magnitude as gravity. This size is often quantified by a characteristic length which in this case is named capillary length [109]:

$$l_c = \sqrt{\frac{\sigma_{lv}}{\rho_l \cdot g}} \tag{5.1}$$

Based on the size, distinction between drops and droplets can be performed. Drops consist of droplets, so they have much larger volume. It is usually assumed that a droplet has diameter between 1 and 50 µm. The drop, however could reach a diameter of 0.5 mm or larger [136]. The experiments described in this manuscript concern the drop evaporation, because the diameter of analyzed drops reaches 1 mm or more.

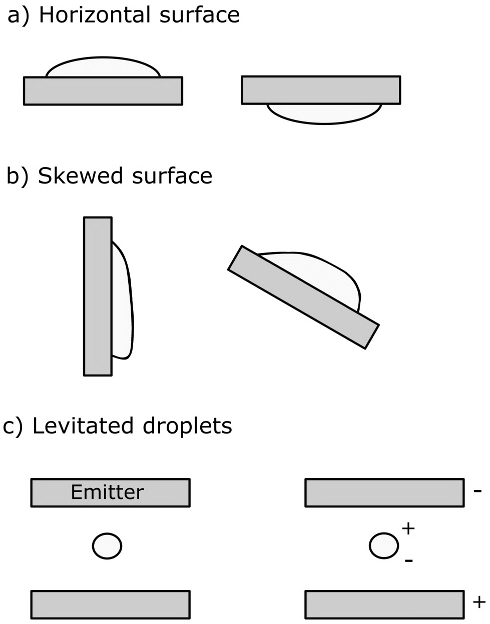

Figure 5.1: Different types of drops: a) sessile (left) and pendant (right) drop; b) drop on a vertical (left) and skewed (right) wall; c) levitated droplets via acoustic (left) and via electrostatic (right) field (redrawn based on [136]).

Such small drop size improves the heat and mass transfer between a drop and a surrounding. The most common phenomenon connected to drops is its evaporation. In the literature, different types of drops have been studied. The possible drops or droplet configurations are schematically presented in Fig. 5.1. On a horizontal surface (Fig. 5.1 a) the drop can be sessile or pendant. Such drop is axisymmetrical. Its shape is determined by the wettability of the substrate and as mentioned earlier, the competition between surface tension and gravity. The shape of sessile drops can be described by the Gauss-Laplace equation of capillarity. When the surface is skewed, the triple-phase contact line is still preserved, but a drop is no longer axisymmetric (Fig. 5.1 b). The total separation between a drop and a solid surface can be achieved by means of ultrasound levitation [132, 134] or electrostatic levitation [89] (Fig. 5.1 c). Despite the broad range of drop types, in this manuscript the attention is put only towards the sessile drops (Fig. 5.1 a). This is the most basic configuration which should be studied first while totally new working conditions are considered.

The wettability between a droplet and an ideal surface (flat, homogeneous, smooth, rigid, and isotropic) can be expressed by apparent contact angle θ described by Young-Dupré equation [133]:

$$cos\theta = \frac{\sigma_{sv} - \sigma_{sl}}{\sigma_{lv}} \tag{5.2}$$

where σ_{ij} is the interfacial tensions between various phases. For a sessile drop of water deposited on a solid wall, the surface is considered hydrophilic if contact angle is less than 90°. For a contact angle more than 90°, the surface is hydrophobic. Super hydrophobicity is observed for contact angles larger than 150° [26].

The rate of evaporation of a drop depends on its shape. In most studies, a drop is considered to form a spherical cap with radius r and contact angle with the solid surface θ [29, 100]. Evaporation rate in such a case can be calculated based on the diffusion equation [94, 100]:

$$\frac{dV}{dt} = -2\pi D\Delta p \frac{M}{\rho RT} f(\theta) \left(\frac{3V}{\pi\zeta}\right)^{1/3} \tag{5.3}$$

Drop volume is calculated in a following way:

$$V = \frac{\pi}{3} r^3 \zeta \tag{5.4}$$

For such analysis, θ is considered to be less than 90°. The factor $f(\theta)$ and ζ are coefficient dependent on the contact angle.

Schönfeld et al. [100] modified the Eq. 5.4 and discovered that generally in the function of the contact angle, the volume decreases in non-linear way. However, for the contact angle less than 90°, the volume was found to decrease linearly with time within 3% error. This can be expressed by the formula:

$$V(t) = V_0 \left(1 - \frac{t}{t_0}\right)^{(3/2)} \tag{5.5}$$

where t_0 is the total time of evaporation and V_0 is initial volume of the drop.

5.1.2 Types of the drop evaporation dynamics and associated thermal effects

Only a very small amount of liquid deposited on the surface (less than 1 mg) forms a spherical cap on a smooth homogenous surface [94]. Larger mass of drops results in its spreading and flattening. In such a case, initially the triple phase contact line (TPCL) is circular and then expands until the equilibrium contact angle is reached. The radius of TPCL usually can be estimated by empirical relation, so-called Tanner's law [10]:

$$r_{drop} \backsim t^{0.1} \tag{5.6}$$

Many reviews on droplet evaporation have been published. They unveiled some important and interesting aspects concerning droplet evaporation, such as coffee ring effect [47, 76] and pattern formation [91, 101] (it will be more detailly described in Section 5.1.4). Also, two main modes of evaporation can be distinguished based on the behavior of the TPCL during the process, what will be described in the next Section.

5.1.2.1 Modes of evaporation

The evolution of the TPCL and the contact angle are two most important factors involved in the droplet evaporation process. Based on those parameters, Picknett and Bexon distinguished two modes of droplets evaporation [94]:

- **Constant Contact Radius (CCR)**: the contact area remains constant during the drying process (Fig. 5.2 a);
- **Constant Contact Angle (CCA)**: the contact angle does not change with time during the drying process, although the contact radius of the drop with the surface decreases with time (Fig. 5.2 b).

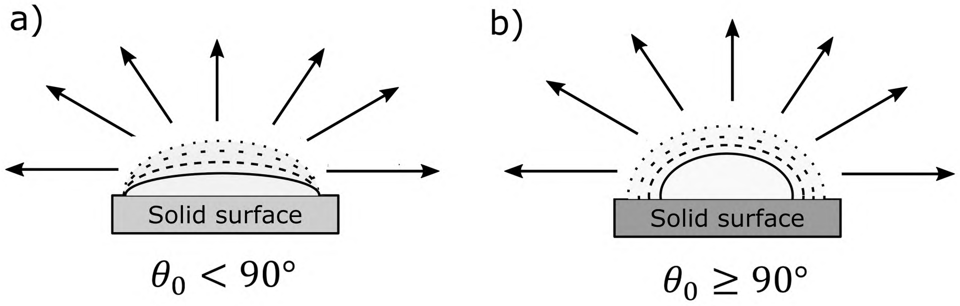

Figure 5.2: Sketch of two modes of evaporation: a) Constant Contact Radius (CCR); b) Constant Contact Angle (CCA).

Both modes of evaporation are schematically presented in Fig. 5.2. The different colors of the solid surface are to show that the evaporation mode can be different for different surfaces even with the same liquid. In practice, both modes of evaporation often occur during the process of evaporation of a given drop and can change from one to another, depending on the drop volume and current operating conditions. Also mixed state can exist for certain drops. In such state there is simultaneous increase of the contact angle and reduction of the contact diameter or a simultaneous decrease of both parameters.

Bardi and Vu [5] determined that when the contact angle is smaller than 90°, the evaporation rate is linear with time and the contact radius is not changing (CCR mode) - see Fig. 5.2. In another case, when $\theta > 90°$ the evaporation rate is non-linear, the contact radius is decreasing while contact angle remains constant (CCA mode). The speed of the drying process also affects the CCR-CCA mode changing process.

Other researchers confirmed those observations. They noted that CCR mode is usually valid for liquids with weak Marangoni number (see Eq. 5.10) placed on high energy surfaces, as such wall property allow for a better spreading of a drop and obtaining smaller contact angle [30, 105, 109]. The CCA mode can be observed for superhydrophobic surfaces until the drop reaches a certain critical height. To minimize the Gibbs energy, there is switching between CCA-CCR modes at the critical thickness [2]. This all finally signifies that for water, the CCR mode is considered to be dominant during the evaporation process if the initial contact angle is smaller than 90°.

The process of the contact area reduction (CCA evaporation mode) is called depinning. Similarly, the stage of evaporation where the contact area (or radius) is constant is named as pinning process. During evaporation when the drop is pinned to the surface (CCR mode), the apex height and the contact angle decrease (the drop gets flattened at its top).

The process of evaporation at the periphery of the drop is significantly more intense than in the center [24] because at the edges, the liquid layer is thinner than at the other parts of the drop. This could be thought to result in the decrease of the contact radius. However, at certain conditions CCR evaporation mode exists in which the contact line is fixed. It implies the mass transfer at the edges of the drop have to be replaced by the liquid flowing from the center to the periphery in order to maintain the constant radius of a drop.

5.1.2.2 Flow driven by evaporation process

When a droplet is placed onto a surface, firstly it has to spread to reach equilibrium conditions. The important aspects influencing the spreading are the surface chemistry and microstructure and the method of drop positioning onto a substrate (usually some kind of mechanical dispenser is used). It was estimated that parallel arrangement of microgrooves (formed by grinding of the substrate) promote spreading, but transverse grooves inhibits this process [112]. Because of the shape of a drop, the process of evaporation may not be uniform because it can induce local temperature gradients inside its volume resulting in convection process. If additionally, the droplet contains some solutes (salts, colloids, polymers, surfactants etc.), their concentration will also change. Both, the temperature and concentration gradients lead to the distribution of surface tension along the triple phase contact line (TPCL) causing Marangoni flow. This process in respect to droplet evaporation will be more detailly described in the following sections.

5.1.2.3 Convection inside a drop

Convection inside a drop may have different sources and two types of convection inside drop can be distinguished: **buoyancy-driven convection** and **capillary convection**. The first one is associated with the temperature gradient inside the drop in the vertical direction. This convection is more significant for thick liquid films. In the case of drops, it usually occur in pendant [48] and levitating drops [52] (see Fig. 5.1 a) right and c)) or drops deposited on super-hydrophobic surfaces [17]. The buoyancy convection is often characterized by Rayleigh number:

$$Ra = \frac{g\beta}{\nu\alpha}(T_s - T_\infty){l_c}^3 \tag{5.7}$$

where l_c is the characteristic length which for levitating drops is the drop diameter and for sessile drops is the drop height.

At high Rayleigh numbers, heat transfer through convection starts to exceed the heat transfer via conduction. This transition point depends on the fluid nature. In the literature, some researchers claim that the buoyancy convection is responsible for the coffee-ring effect [65] (Section 5.1.3).

The capillary convection may have two different origins: the gradient of Laplace pressure and the surface tension gradient. The distortion from equilibrium shape of a drop free surface results in a gradient of the Laplace pressure [14]. This additional pressure on the concave side of the surface is connected with the fact that the interface of a drop is curved. It is described by the following equation:

$$\Delta p_{La} = \sigma_{lv}(\frac{1}{r_1} + \frac{1}{r_2}) = \sigma_{lv}\kappa \tag{5.8}$$

where r_1, r_2 are the principal radii of curvature and κ is the mean curvature. The arising pressure may induce outward or inward flows depending on the shape of the free surface [23].

The dimensionless number used in the characterization of free surface dynamics is the Laplace number. It is expressed as the ratio of the surface tension and the momentum-transport (e.g. dissipation) inside a fluid and is expressed as:

$$La = \frac{\rho l_c \sigma_{lv}}{\eta^2} \tag{5.9}$$

Deegan [24] showed that the evaporation rate has its maximum near the TPCL (what was schematically shown in Fig. 5.2). In the case of the CCR mode of evaporation (see Fig. 5.2 a), when the triple line is pinned to the surface, the mass loss of the evaporated liquid near the contact line must be balanced by the fresh liquid coming from the bulk of droplet. Consequently, a capillary flow can exist during evaporation of a sessile drop. Such flow is directed radially towards the edges of the droplet. The velocity of the flow near the edges can achieve tens of micrometers per second [133]. The schematic of the capillary flow induced inside a drop of liquid is presented in Fig. 5.3 a.

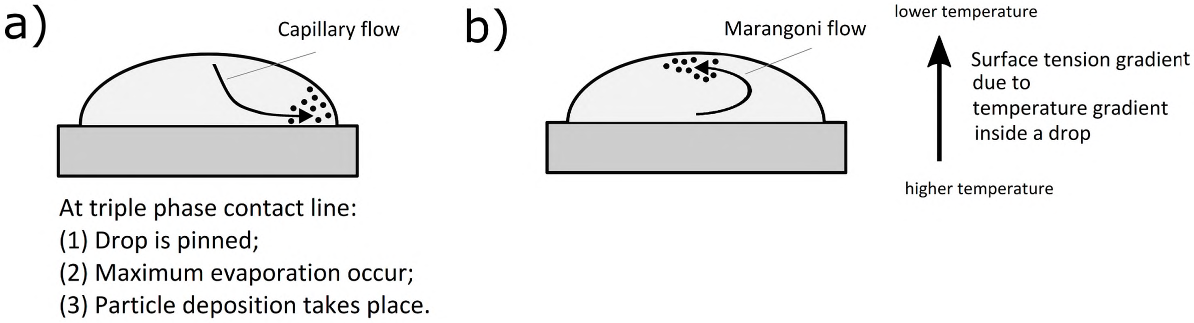

Figure 5.3: Schematic of a) Capillary flow due to non-uniform evaporation flux; b) Marangoni flow as a result of temperature gradient inside a drop (redrawn based on [136]).

The second source of capillary convection is the surface tension gradient. This type of capillary convection is termed as Bérnard-Marangoni convection or Marangoni flow (see Fig. 5.3 b). In sessile drops of pure liquids, Marangoni flow arises because of non-uniform evaporation flux resulting in temperature gradient along the droplet interface [128, 37]. The edges or peak of the drop might have higher temperature depending on the thermal properties of liquid and substrate [97]. Surface tension decreases with the rise of the temperature, thus its gradient along the free surface appears [51, 110, 123]. To describe the convection which may occur in such a situation, the thermal Marangoni number is used. It is defined as the ratio of the surface tension due to temperature gradient along the liquid free surface to the adhesive forces [136]:

$$Ma_T = -\frac{d\sigma_{lv}}{dT}\frac{l_c\Delta T}{\eta\alpha} \tag{5.10}$$

It is worth mentioning that the surface tension also depends on the concentration of the dissolved substances. When the evaporation takes place in a drop of binary mixture or saline solution, solutal Marangoni effect is present [60]. The concentration of salts generally increases the surface tension, while the concentration of colloids or polymers results in the surface tension decrease. Solutal Marangoni number is analogical to the thermal Marangoni number (Eq. 5.10) [136]:

$$Ma_C = -\frac{d\sigma_{lv}}{dC}\frac{l_c\Delta C}{\eta\alpha} \tag{5.11}$$

5.1.3 Dried patterns during evaporation process

If an evaporating droplet contains non-volatile material, various dried pattern can be observed. Such patterns confirms the convective flows inside a drop, but also additional important information might be revealed. E.g. as drops of a blood contain biological matter, their dry patterns might reveal important biological information [9, 18].

To study small particles dissolved inside a liquid drop, image velocimetry is commonly used. Marin et al. [78] managed to track the micro-particles inside a drop of water. They noticed that the particle velocity increased significantly at the end of the evaporation process when the droplet height and contact angle were reaching zero. The reduction of the droplet height squeezed the particles suspended in the liquid in the vertical direction. Additionally the particles were unable to move towards the peripheral part of the droplet as the contact angle was also strongly reduced. This caused sudden acceleration of the particles.

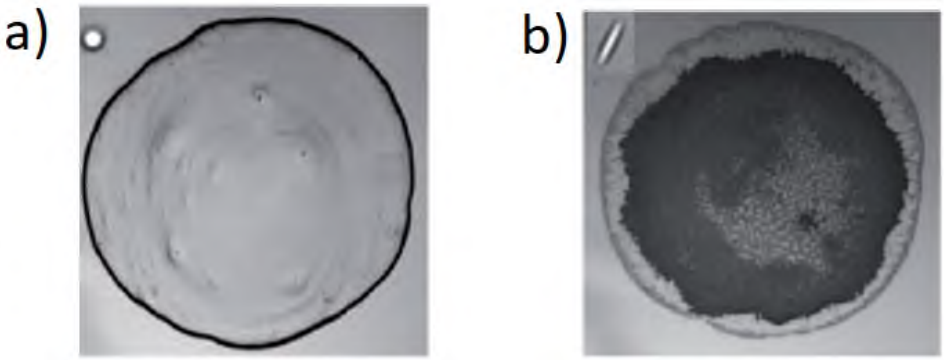

Figure 5.4: Particle deposition: a) spherical microparticles - creation of coffee-ring effect; b) elliptical particles - centrally-located distribution (extracted from [130]).

The evaporation process is affected by various parameters, such as substrate properties, the moisture of surrounding air and the heating conditions. However, it was estimated that distinct flow patterns during the process are induced by the relative importance of the rate of evaporation, the thermo-capillarity and the buoyancy [133]. As described earlier, the capillary convection tends to move liquid towards the TPCL. If some inclusions are suspended inside the drop, they are moved together with the fluid and in the CCR mode they can be deposited along the TPCL forming ring pattern visible when the liquid evaporates from the surface. Such deposition is often called coffee-ring effect as it forms circular ring around initial contact area of a drop (see Fig. 5.4 a). However, not every drop even in the CCR is associated with such pattern formation. Hu and Larson [51] determined that the high evaporation rate at the TPCL region contributed to temperature reduction and larger concentration of the solute at this part of the drop. This leads to the concentration-driven Marangoni flow (due to created surface tension gradient - see Fig. 5.3 b) which moves the solute in the opposite direction than the capillary flow. For this reason, the coffee-ring effect can be observed only when solutal Marangoni flow is weak.

5.1.3.1 Parameters influencing the dried patterns

It was estimated, that both size and shape of the particles can influence the resulting flow pattern. Weon et al. [120] utilized polystyrene particles dispersed inside water drop. For particles with diameter of 20 µm they obtained centrally-located deposition on the surface. On the same substrate, the smaller particles formed the coffee-ring pattern (the deposition located on the initial TPCL).

Yunker et al. [130] applied elliptical particles which were suspended in the drop of water. Such particles are not influenced by the depinning or rewetting processes. Their anisotropic shape influences interactions during the flow and prevent from forming large clusters at the TPCL. Instead, the particles are uniformly spread on the central part of the surface (see Fig. 5.4 b). The comparison between the dried patterns generated by the contaminants with different (spherical or elliptical) shapes are visible in Fig. 5.4. In both cases the same type of drop was applied.

The deposition pattern is also influenced by the substrate temperature, as the wall temperature drives the intensity of the thermal gradient along the drop in the vertical direction [3, 75]. For a hydrophilic surface, the usual deposit formation is the coffe-ring effect. The rise of the substrate temperature, however, results in the thinner rings of the deposition because of the stronger impact of Marangoni effect (what moves the particles towards the central part of the drop - see Fig. 5.3 b). In the case of a hydrophobic surface usually the deposits uniformly spread at the central part of the surface. If the wall temperature is high enough and the temperature at the center of a drop is higher than at the periphery, the change in the surface tension gradient may lead to a coffe-ring deposition.

The type of the substrate itself is also of a great importance as the flow pattern is influenced by the adhesion between a drop and a substrate [133]. Other factors which can influence the generated drying patterns are: application of external forces (e.g. electrostatic forces [27]) and type of the suspended contaminants (polymers or surfactants disturb the flows inside a drop) [29, 104].

5.1.4 Forces involved in the droplet evaporation

A droplet placed onto the surface can be described as being composed of three different regions, starting from droplet periphery to its center: molecular region, transitional region and capillary region [137]. Fig. 5.5 presents the regions of a drop deposited on the surface along with the forces involved in the evaporation process. Each region is associated with different dominant forces, thus it is not possible to describe the droplet dynamic uniformly for its whole volume.

At the periphery of a droplet, outside what is normally considered as the TPCL, a precursor film is often formed due to the disjoining pressure [70, 122]. This layer is extremely thin (∽ nm). The precursor film thickness is determined by the competition between van der Waals forces and surface tension forces (see Fig. 5.5 - Molecular region) and it is important in wetting/rewetting aspects.

Capillary forces as well as Marangoni forces are associated with certain flow patterns inside a drop what was discussed in Section 5.1.3.

Type of the region	**Molecular region**	**Transitional region**	**Capillary region**
Length scale of the region	$<10^{-9}$ m	$10^{-9} \sim 10^{-7}$ m	$10^{-7} \sim 10^{-2}$ m
Forces involved in the process	Viscous forces, Intermolecular forces	Viscous forces, Capillary forces	Capillary forces

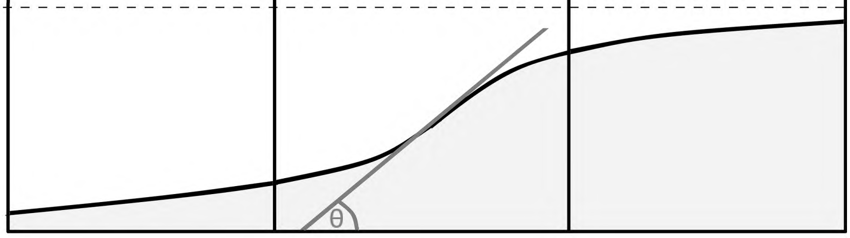

Figure 5.5: Sketch of the wetting of a sessile drop with respect to different regimes along the drop radius (redrawn from [137]).

5.1.5 Influence of the surface properties on the drop evaporation

The surface temperature [35] and surface roughness [72] were discovered to have a major impact on the modes of drying (Section 5.1.3). Larger wall temperature impede the evaporation process, while larger roughness leads to the domination of the CCR mode. The imperfectness of the surface results in a Contact Angle Hysteresis (CAH) [28] and may have an influence on the drying pattern formation [73]. It can also impact the adhesion between the drop and the surface. The strong CAH contribute to the creation of the coffee-ring effect. Other parameters as subtrate rigidity and applied surface treatment will be described in the following Sections.

5.1.5.1 Effect of the substrate rigidity

On the soft substrates with low rigidity (e.g. immiscible liquids, gels), the deposited drop cause deformation of a substrate [12]. The schematic of drops deposited on various

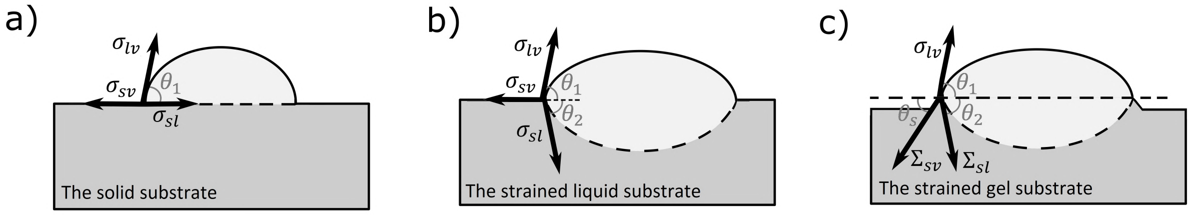

Figure 5.6: Water drop deposited on different types of substrates: a) solid substrate; b) liquid substrate; c) polymer soft substrate. (redrawn based on [133]).

substrates (solid, liquid and polymer gel) is presented in Fig. 5.6. The surface deformation is the effect of the vertical component of the surface tension at the TPCL.

5.1.5.2 Effect of the substrate treatement

Surface roughness was discovered to be another parameter which strongly affects the properties of the wall, because it acts on its wettability [102]. E.g., the hydrophobic surface was observed to possess self-cleaning properties [106]. The particles on this kind of surfaces leave spots and do not form ring patterns during evaporation process [69]. Such substrates are beneficial in order to reduce adhesion forces between the dirt or oil and the surface.

The proper selection of the surface treatment method is important in order to obtain the required properties. The wall characteristics, however, might change with time, as there is period of properties stabilization. E.g. application of the laser technologies for metal surface treatment allow to obtain highly hydrophilic properties of the wall. However, after 7-10 days, those hydrophilic properties are replaced by hydrophobic and highly hydrophobic [113]. Modification of the surface properties due to various treatments of the substrate influences the way in which liquid is deposited on the surface. Due to changed wettability, different surfaces produce different shapes of a drop.

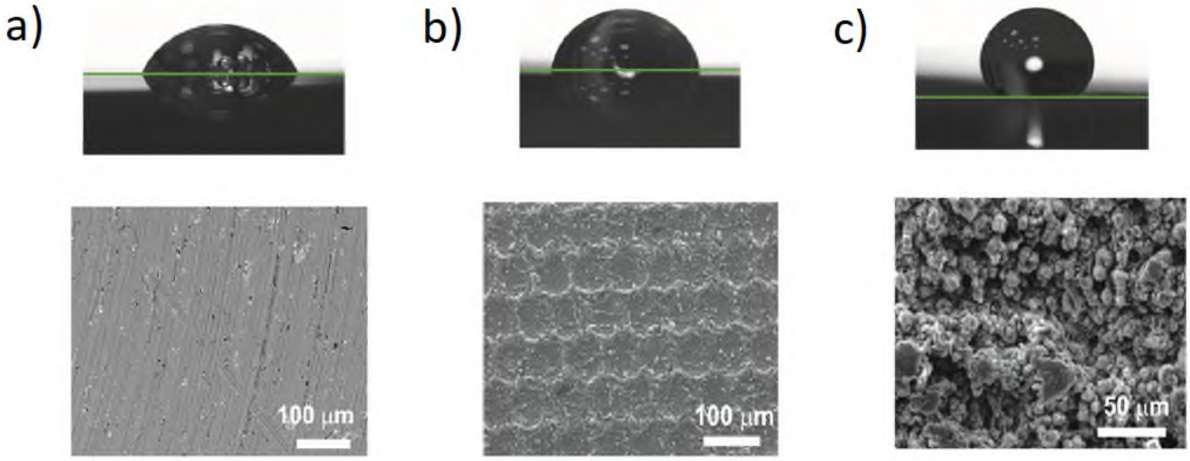

Figure 5.7: Static constant angles of a drop and SEM images of the surface for a) unstructured rough; b) structured hydrophilic; c) structured hydrophobic surfaces (extracted from [86]).

Misyura et al. [86] conducted experiments of water drop evaporation for aluminum-magnesium alloy substrate. The surfaces were structured with a changing of laser pulse and laser parameters enabled to change the surface wettability. They obtained structured hydrophilic ($\theta_0 = 83.7° \pm 2.9°$ - see Fig. 5.7 b) and hydrophobic surfaces ($\theta_0 = 131.0° \pm 4.6°$ - see Fig. 5.7 c) and compared drops deposited on these surfaces to drops on rough unstructured surface ($\theta_0 = 72.3° \pm 2.5°$ - see Fig. 5.7 a). Fig. 5.7 presents the pictures of a deposited drop and SEM images for surfaces with different properties. The volume of the drops was the same for all cases and equal to 0.4 mL. They also observed that the hydrophilic structured surface resulted in a intensification of convection and evaporation processes by 10-12%.

It was also estimated that the surface roughness influences the spreading of a drop even if no special structuring of the surface is performed. Shanahan and Bourges [105] conducted experiments by placing water drop on Teflon, epoxy resine and polyethylene. Wayner et al. [118] performed similar tests but they deposited water on a copper surface. They all confirmed that a drop spreads less on a smooth substrate. Zhang et al. [136] experimentally investigated the evaporation process on rough hot-spots. They etched the surface for 2, 4 or 6 h in order to obtain various roughnesses of the surface. Longer etching was correlated with larger roughness of the surface (they obtain values of S_q of 0.719, 1.114 and 2.761 µm respectively with error ±0.038 µm). They noted that an increase of the surface roughness resulted in the rise of the contact angle. The top view of the surface, the picture of a drop and cross-sectional profile of a wall obtained by Zhang [136] are presented in Fig. 5.8.

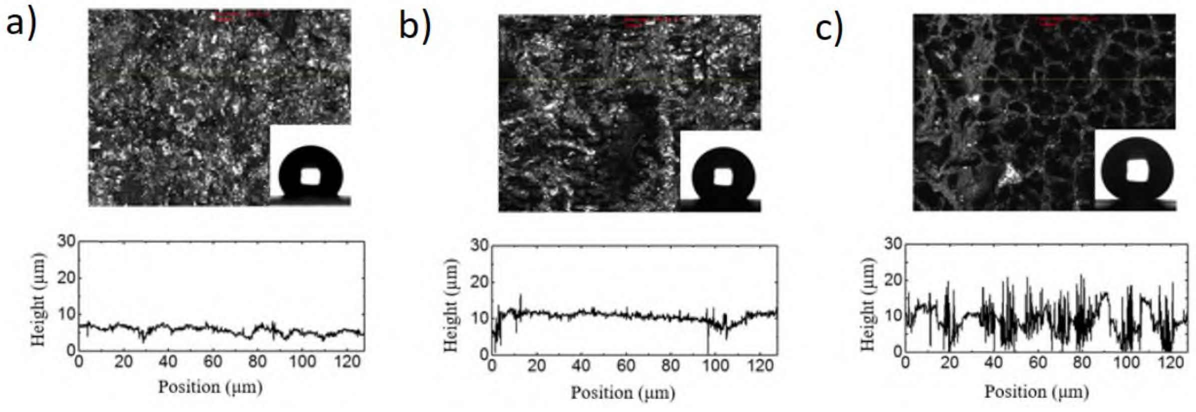

Figure 5.8: Top view of the surface along with the water drop image (top) and cross-sectional profiles of the surface (bottom) for surfaces etched for a) 2 h; b) 4 h; c) 6 h (extracted from [136]).

5.1.6 Drop boiling

Drop boiling on hot surfaces is considered to be much different than pool boiling process. Liang et al. [71] deposited drops of water on a hot surface. The wall temperature in their experiments was set as 220°C, 156°C and 97°C. At the highest studied temperature they observed a violent nucleate boiling process with multiple bubbles rising above the liquid free surface (see Fig. 5.9 a). The first bubbles were observed to nucleate at the periphery, because the thickness of liquid is smallest in this part resulting in maximum temperature. Reduction of wall temperature resulted in more gentle boiling process (smaller amount of bubbles on the surface with less interaction with each other). However, lots of bubbles were still observable (see Fig. 5.9 b). When the wall temperature was below the water boiling point, film evaporation occurred (see Fig. 5.9 c). Still several bubbles at the liquid-solid interface were present, but they never exceeded the liquid free surface. Probably those were small air bubbles trapped while impacting the surface. The pictures of boiling process inside a drop during experiment of Liang et al. [71] is presented in Fig. 5.9.

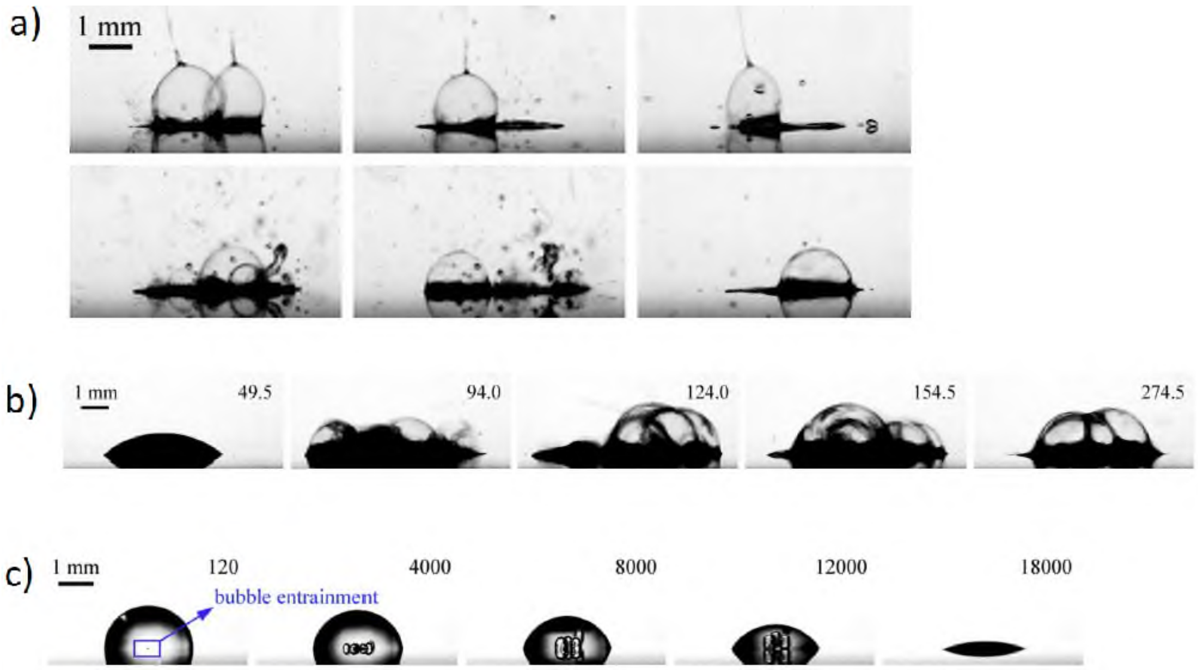

Figure 5.9: Bubbles generated by drop impacting on a hot surface: a) $T_{wall} = 220$°C; b) $T_{wall} = 156$°C; $T_{wall} = 97$°C (extracted from [71]).

Cui et al. [22] placed a drop of pure water and water containing dissolved CO_2 on the surface with various temperatures (100°C, 130°C, 220°C, 300°C). At the temperature 100°C no boiling occurred. Addition of CO_2 reduced the time of evaporation. For a wall temperature of 130°C, the nucleate boiling process was already observed. When water got deposited on a surface with temperature higher than 210°C, the regime of transition boiling was present. Drops started to evaporate so rapidly that vapor created at liquid-solid interface generated pressure which was sufficient to lift a drop off the surface. The time of droplet evaporation was rising with the increase of temperature for 210°C $<$ T_{wall} $<$ 240° C. Maximum lifetime of a drop was obtained for a temperature which is commonly known as Leidenfrost temperature [68]. Above this temperature, droplets start to levitate on a thin vapor film. Drops containing CO_2 were characterized by smaller amount of bubbles than droplet of pure water. In the moment of a drop reaching the surface, dissolved CO_2 quickly escapes from the liquid, because its solubility intensely decreases with the rise of water temperature. Gas which escapes from bottom part of the drop forms a film which prevent from further contact of liquid with a hot surface what suppress nucleation. This explain the fact that the dissolved gases make the vapor film which is form around the drop more stable.

5.2 Experimental procedures

The first tests reported in this Chapter are focused on the evaporation process of a liquid drop. The experiments were conducted for a horizontal surface at subatmospheric conditions (vapor pressure 1.8 kPa). The schematic of the test bench used for the experiments is presented in Fig. 5.10. The test vessel was the same as for the pool boiling tests (Chapter 3 and 4), with only few components necessary to generate drops being added. To maintain a state of saturation (i.e. liquid-vapor equilibrum) during experiments, the test vessel was filled with liquid, but its free surface was always kept below the level of the heated wall. Of course, the drop evaporation lead to a small distortion from saturation condition (the excess of vapor from evaporated drop affects the equilibrium), but its influence is not so significant, because the volume of vapor generated by the evaporation of the drop is much lower than volume of the vessel ($V_{excess} \ll V_{vessel}$). Taking the volume of a drops obtained during experiments (0.9 mm^3 and 28.7 mm^3), the volume of the evaporated drop constitue to 0.5% or 16.1% of the volume of the vessel.

A drop was generated by opening a manual valve placed above the main vessel and connected to a small, closed tank filled with distilled water. Opening the valve caused the flow through a pipe because of the difference between pressure inside the test main vessel and pressure inside small tank. When the valve was opened, the tip of the pipe was carefully observed until a small amount of liquid would show. At this moment, the valve was closed and the measurements started.

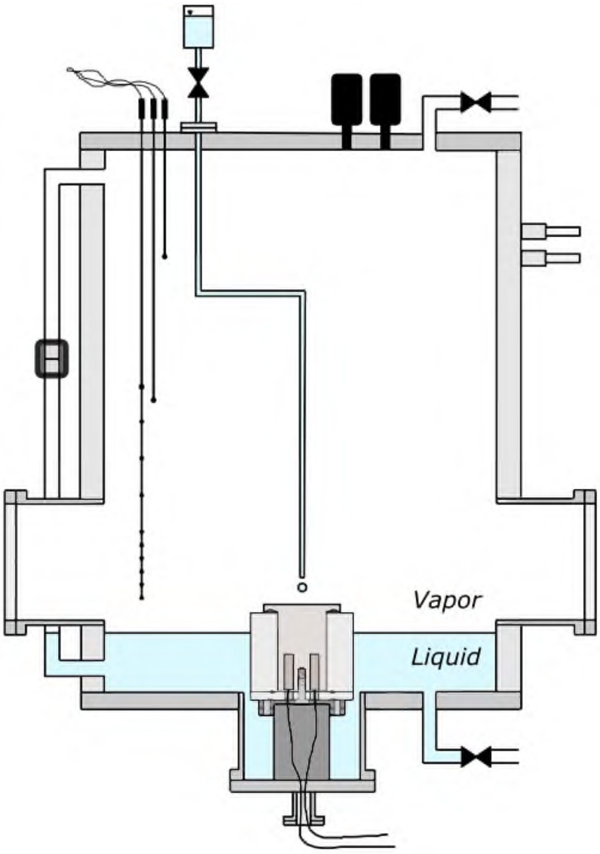

Figure 5.10: Experimental apparatus used for the experiments of droplet evaporation.

Two different pipe sizes were tested during experiments - a wide pipe (inner diameter of 4.0 mm, outer diameter 6.0 mm) and small pipe (inner diameter of 1.8 mm, outer diameter 3.0 mm). The analysis proposed in this Chapter covers the description of thermal proccesses involved in the evaporation of two drops with different volume (28.7 mm^3 and 0.9 mm^3, respectively) generated by both pipes. The tubes were also located at different distances from the heated surface. The pictures showing typical drops along with basic geometrical parameters are shown in Fig. 5.11. All the distances were calculated based on the known outer pipe diameter. The accuracy of distance calculation was estimated as ±3 px (thus ±0.5 mm for wide and ±0.2 mm for small pipe, respectively). Some amount of air was always getting into the system with the working medium. After a series of tests, when the vapor pressure increased significantly, the vessel was evacuated to get rid of the dissolved gasses and reduce value of vapor pressure.

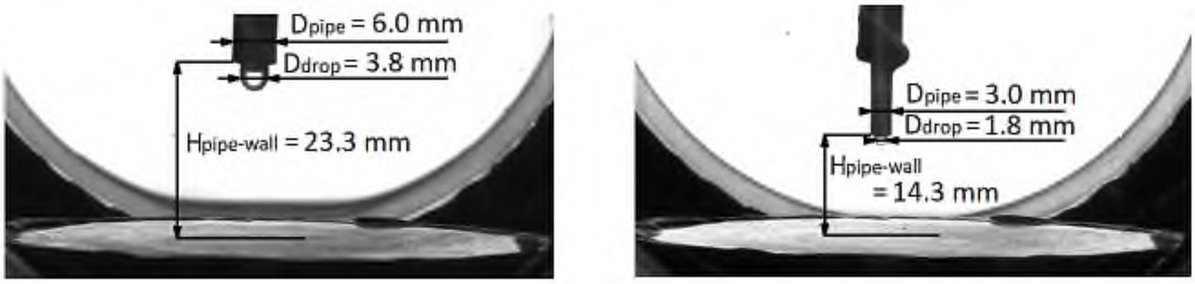

Figure 5.11: Basic parameters concerning the size of the pipes used to generate drops and the diameter of the drops before their detachement from the tip of the pipe.

5.3 Thermal effects involved in the droplet evaporation

5.3.1 Operating conditions

Tests involving a single drop were conducted for the vapor pressure $p_v = 1.8$ kPa ($T_{sat} = 16°\mathrm{C}$). The heating power applied to the surface was equal to 20 W which corresponds to applied heat flux of $q_{app} = 0.4$ Wcm^{-2}. The measurement frequency was set to 500 Hz. Like for the previous experiments, the heat flux measurements were synchronized with the high-speed camera recordings (thus both frequencies were kept constant). The image size was equal to 1024 x 1024 px, which allows to record videos for 3.072 s. The same sensor as in previous Chapters was utilized (see Fig. 2.4) which enabled instantaneous measurements of heat flux individually in seven annular zones.

5.3.2 Problems involved with droplet generation

There were several challenges involved in the generation of a single drop, especially when the wide pipe was used. Sometimes instead of a single drop, considerable volume of liquid was poured onto the surface instantenously. In such a case, it was necessary to wait for the whole volume to evaporate and for the surface conditions to reach the initial state. After that, the next attempt was performed.

Additionally, other specific behaviors associated with non-condensable gases inside the working medium were observed. Water used for the experiments always contained some amount of dissolved air and it happened that instead of a liquid drop detaching from the tip of the pipe, a large air bubble was formed. The pictures recorded during such process are presented in Fig. 5.12. The air bubble forms at the tip of the pipe (picture A in Fig. 5.12). Firstly, it grows uniformly forming almost spherical shape (picture B in Fig. 5.12). Then, the bubble starts to elongate in the vertical direction and reaches the heated surface (picture C in Fig. 5.12). After that, it starts to spread horizontally. When the contact with the pipe is lost, the bubble is large and covers significant area of the heated wall (picture D in Fig. 5.12). After some time, it eventually breaks and vanishes.

Another often observed event is presented in Fig. 5.13. It sometimes happened that the air bubble firstly grew uniformly (picture B in Fig. 5.13), but eventually stopped. Instead, it broke (picture C in Fig. 5.13) causing splashing of several small droplets of liquid on the heated wall (pictures D-F in Fig. 5.13). All such events were considered as failures for the repeatibility of successful drop generation.

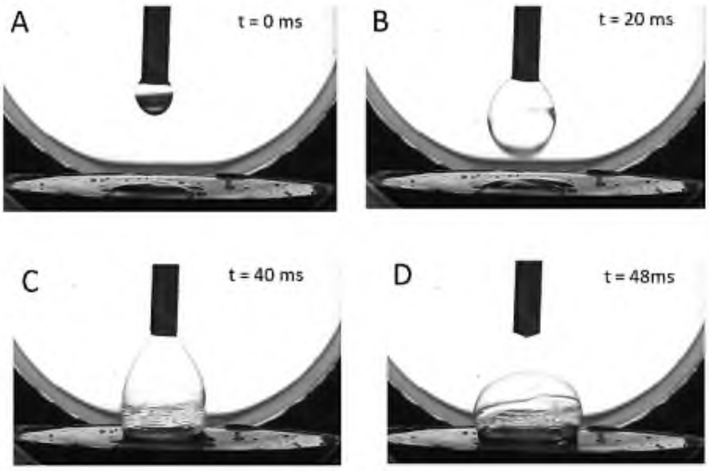

Figure 5.12: Generation of a large air bubble.

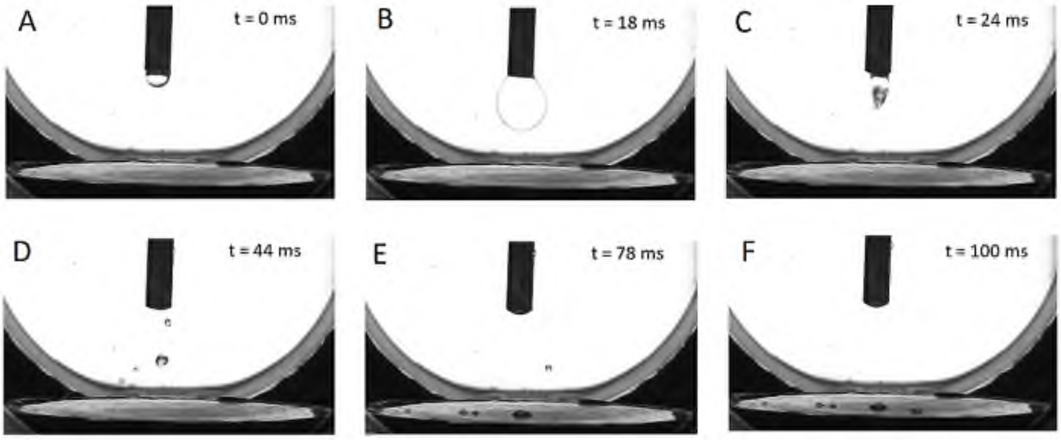

Figure 5.13: Splashing of liquid on the heated surface.

5.3.3 Difference in the sensor's response for evaporation and boiling processes

All the previous analyses in the manuscript were conducted for the pool boiling process, thus the heated wall was located below the liquid free surface. This Section, however, focuses on the evaporation of small volume of liquid. The differences between these two processes are schematically presented in Fig. 5.14. The dynamics of the process itself is also significantly different. A first distinction lies in the duration of the process. The bubble lifetime is short - for low pressure bubble with moderate liquid level, the total process lasts a few hundreds milliseconds. The evaporation process requires more time - it takes over a dozen of seconds for the whole liquid to disappear from the surface.

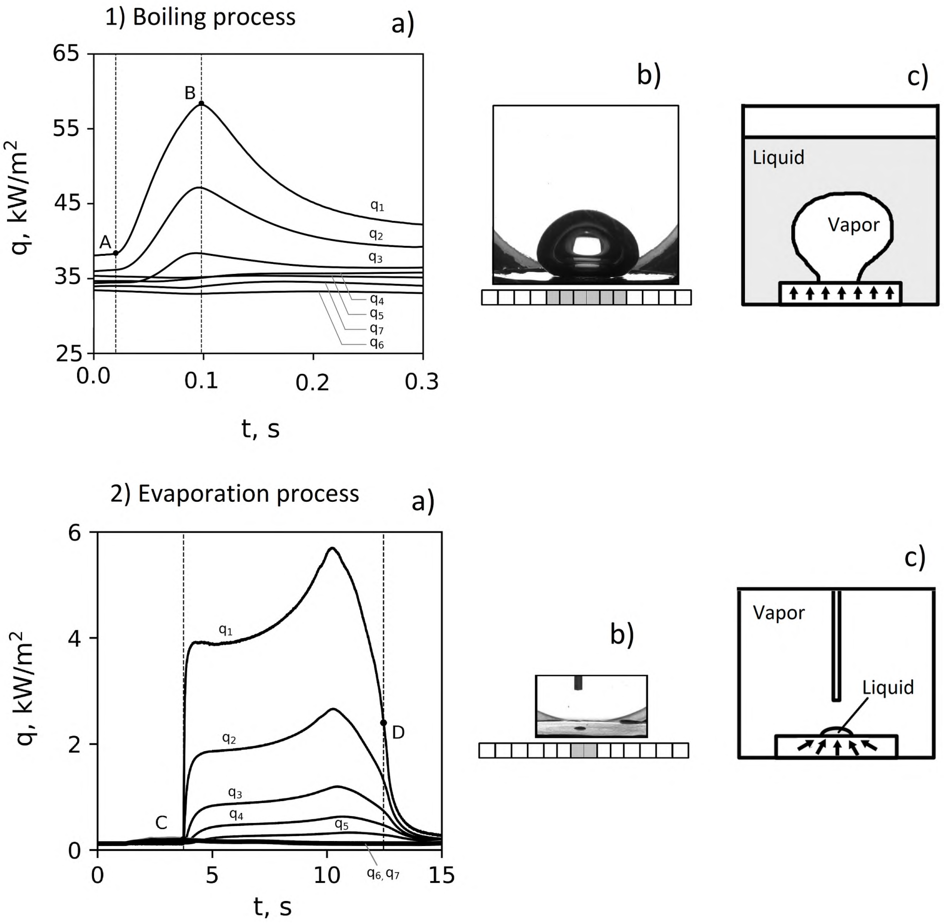

Figure 5.14: Comparison of the heat flux evolution detected by sensor for the boiling and evaporation cases.

The environment of the sensor also affects its response. The boiling process leads to an increase of heat flux starting from the moment of nucleation (point A in Fig. 5.14 1a). However, mostly only zones covered by the bubble foot are reacting during the bubble evolution. In this particular case, the bubble foot covers a maximum three zones of the sensor (see 5.14 1b), so only those ones react to the bubble presence by a sudden rise of instantaneous heat flux.

On the contrary, when a drop falls on the surface, the contact line between wall and liquid is much smaller. The example of a drop showed in Fig. 5.14 2b) covers only part of the first measurement zone. Despite its small size, all the zones of the sensor reacts during the evaporation process (see Fig. 5.14 2a). This reaction is caused by the fact that the heat transfer between heated wall and vapor is much lower than heat transfer between wall and liquid. For a drop, the heat is prone to be transferred towards the cold liquid by lateral conduction in the wall thickness, as the surrounding vapor acts as an insulation.

The transfer of heat in these two cases might is shown by drawing schematic heat flow lines (5.14 c). During bubble formation the heat flow lines are quasi vertical probably with minor deformation close to the triple line (5.14 1c). The heat is transferred uniformly, as some heat has to be used for the phase change, but a large amount is utilized to heat up the cold liquid in the proximity to the heated surface. The growth of the large low-pressure bubble causes mixing of liquid and constantly cold, fresh liquid is pushed close to the heated wall enhancing the heat transfer process. During evaporation of liquid, very low heat transfer inside the vapor direct the heat lines towards the liquid phase (see 5.14 2c). It happens even though the drop area is much smaller than surrounding vapor phase (in this case, the contact area of the liquid with the heated wall constitutes to less than 2% of the total surface of the heater).

5.3.4 Drop falling on an unheated surface

Before conducting the tests of drop evaporation from a heated wall, the first attempt was to generate a small drop on an unheated surface. The water temperature inside small storage tank filled with water was equal to the room temperature (approx. 20°C), while the wall temperature was equal to the vapor saturation temperature inside the test vessel ($T_v = 16°\text{C}$). The time evolution of heat flux recorded for five zones of the sensor is presented in Fig. 5.15 a. The location and size of the analyzed drop is visible in Fig. 5.15 b. Unfortunately, the moment when the drop reached the surface was not captured. That is why the initial rise of heat flux, which correspond to the first contact with the surface, is not observable.

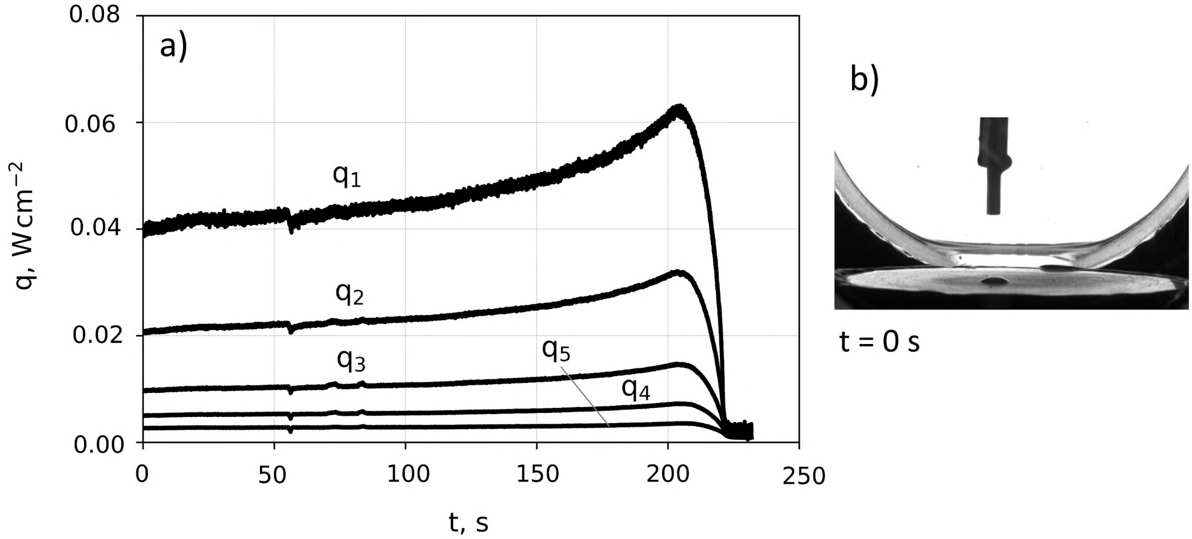

Figure 5.15: Drop falling on an unheated surface.

Although the wall was not heated and the water in the storage water tank had higher temperature than surface temperature, droplet evaporation occurred. Indeed, the liquid inside the pipe was subjected to a strong pressure decrease (i.e. expansion) resulting in a temperature decrease so strong that the drop temperature was below 16°C when the liquid reached the surface. Unfortunately, the liquid temperature could not be measured to quantify this effect. The whole process was however long and lasted more than 200 s (thus more than 3 min).

5.3.5 Drop falling on a heated surface

To intensify the evaporation process the experiments were conducted for a heated surface. The applied heating power was set to 20 W what corresponds to an applied heat flux of 0.4 W/cm^2. Two different kinds of drops were considered - smaller ones with volume of 0.9 mm^3 generated by the thin pipe and second - larger generated by the wide pipe (volume of 28.7 mm^3). The measurements of heat flux evolution for both drops were evaluated by high speed camera recordings. This allowed to distinguish the various thermal processes observable during lifetime of a drop.

5.3.5.1 Drop generated by the thin pipe

Fig. 5.16 presents several frames captured during the evaporation of a drop generated with the thin pipe. The drop is small (radius less than 5 mm) and it is fully located within the first measurement zone. As described in Section 5.3.3, all the zones respond to the presence of a drop. Thus, the heat is more prone to be transferred towards the cold liquid. Analyzing video sequences in Fig. 5.16, one can see that the drop firstly evaporates in the vertical direction (the thickness of the drop is reduced, while its diameter remains constant). When the thickness starts to be small enough, the drop shrinks in the horizontal direction as well. Most of the process occurs according to CCR evaporation mode (the contact area is constant during most of the process - the tripple contact line is pinned). It is in agreement with literature data, as CCR evaporation type was considered to be the dominant mode for water.

The time evolution of heat flux for the drop generated by the thin pipe is shown in Fig. 5.17. For a better clarity, only the heat fluxes for the five central measurement zones (q_1 - q_5) are presented. The change of heat flux in two peripheral zones was very small. Points (1 - 5) in Fig. 5.17 represent different stages of drop lifetime, starting from the first contact with the heated surface (1) to the moment when the whole volume has evaporated (5). The frames from the high speed camera (Fig. 5.16) are marked in the same manner and they indicate exactly the same moment, as both measurements were synchronized.

The moment when the drop reaches the heated wall corresponds to a sudden increase of instantaneous heat flux. In about 400 ms the value of heat flux at the center of the surface q_1 reaches the local maximum. Analysis of the pictures in Fig. 5.16 indicates that the drop size did not change notably during this period, what means that very little phase change has taken place. The falling droplet has low temperature (what was proven by the test for an unheated surface - Section 5.3.4) and firstly it has to be heated for evaporation process to start. When reaching point (2), the dynamics of the heat flux evolution is different. Up to the point (3), the heat flux is almost constant, or it slightly decreases. The drop at this stage is visibly thinner in comparison to the drop in point

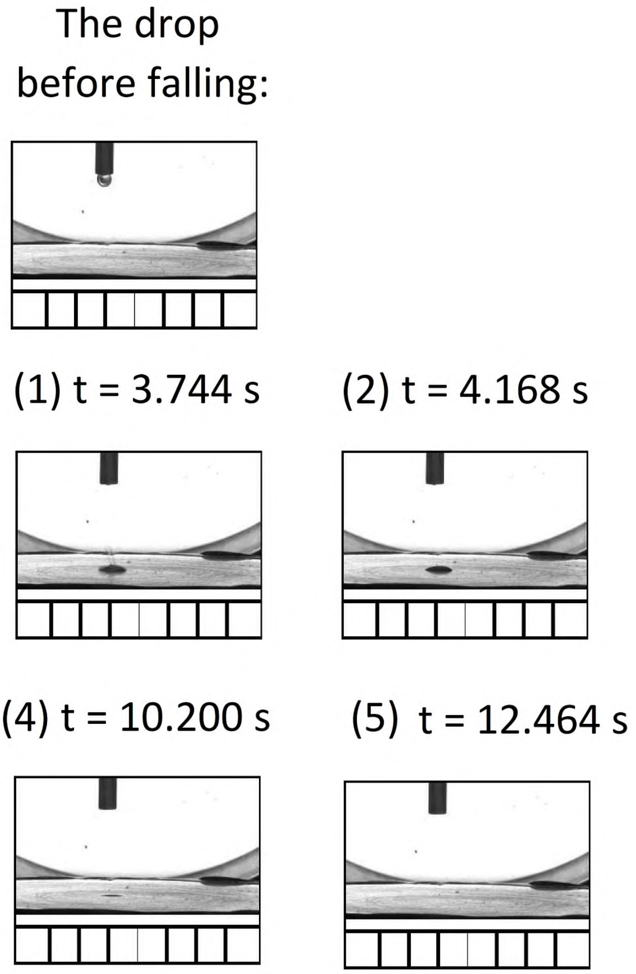

Figure 5.16: Lifetime of a droplet generated by the thin pipe.

(2) (see points 2 and 3 in Fig. 5.16) and demonstrates that the evaporation process commenced. Later the heat flux starts to increase more rapidly and reaches a second local maximum at point (4). At this point the thickness of the drop is very low, however its horizontal diameter is still the same as at the very beginning of the process (see point 4 Fig. 5.16). After that, the drop starts to shrink in the horizontal direction and it totally disappears at point (5). It is visible that the heat flux is still dropping for more than 1 s after the droplet is not visible on the video recordings.

5.3.5.2 Drop generated by the wide pipe

The same test was conducted with the wide pipe to generate the drop. The video sequence of drop lifetime is presented in Fig. 5.18. The volume of the drop is 30 times larger than in the previous test which results in a larger spreading of the drop on the heated wall. This particular drop covers two zones of the sensor. The behavior of the evaporating drop is the same as previously described. Firstly, the drop gets thinner only in the vertical direction. When its thickness gets small enough (i.e. the contact angle of the drop reaches the receding contact angle), the shrinking starts to be progressing also in the horizontal orientation. However, point 5 does not correspond to the moment when the whole volume of liquid has evaporated. Instead, it represents the last recorded frame

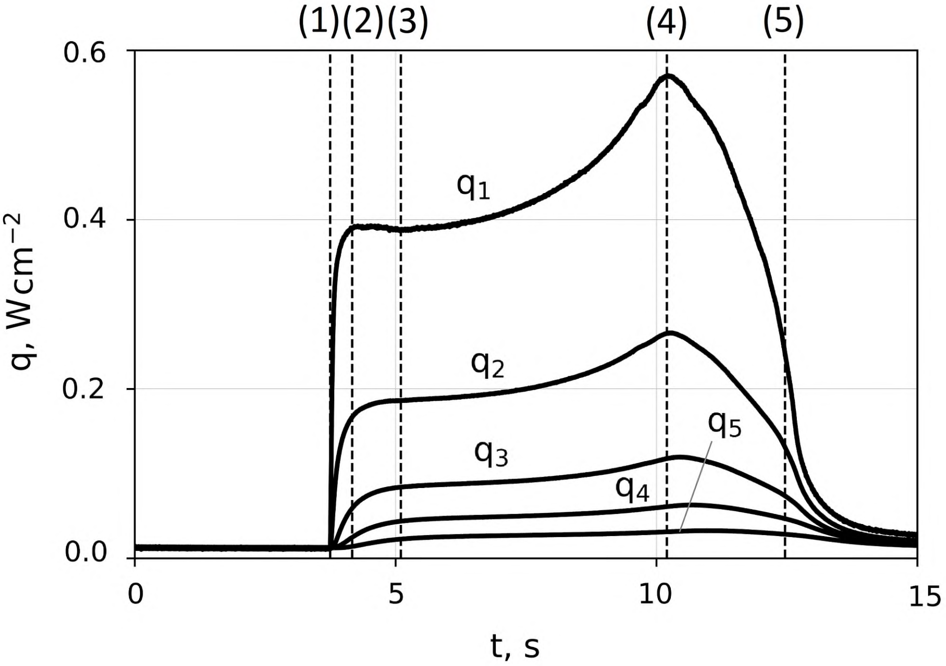

Figure 5.17: Heat flux evolution for a drop generated by the thin pipe.

(the camera measurements started slightly too late to capture the whole process).

Fig. 5.19 shows the heat flux evolution for the wide pipe. Again, all the points marked on the graph correspond to the pictures presented in Fig. 5.18. The shape of the curves is the same as for the thin pipe (Fig. 5.17). However the whole process lasts longer because larger amount of liquid has to evaporate. Another visible difference is the significant decrease of heat flux at the center of the heated wall from the point 2 to the point 3 (see 5.19). For the amll drop (Fig. 5.17), this part of the curve is almost constant. This distinction is also related to the drop volume. The evaporation at this stage of the drop lifetime is strongly limited by the heat diffusion inside the droplet (more information concerning the heat transfer processes involved in the process will be given in the following Section). When a drop has larger size, it gets more difficult to distribute heat inside the whole volume. Larger mass requires more energy to evenly distribute the heat inside a drop. If the heat cannot be transferred efficiently enough from the surface, the evaporation process gets limited and the heat flux slightly decreases.

5.3.5.3 Heat and mass transfer processes involved in the lifetime of a drop

To understand the heat and mass transfer processes involved in the droplet evaporation, the video recordings (Fig. 5.16 and Fig. 5.18) and heat flux evolutions (Fig. 5.17 and Fig. 5.19) were thoroughly analyzed. The size of the analyzed drops is small, thus it is difficult to immediately notice all characteristics only based on the video recordings. To provide better clarity, the lifetime of a drop is schematically presented in Fig. 5.20. The associated heat and mass transfer processes involved in its evaporation are described in the following paragraph. Due to the quality of the pictures and camera positioning it is not possible to estimate the apparent contact angle of a drop θ. From the literature studies conducted before, it can be estimated that the contact angle for water is less than 90° [30, 105, 109]. It is confirmed by the fact that most of the evaporation takes place

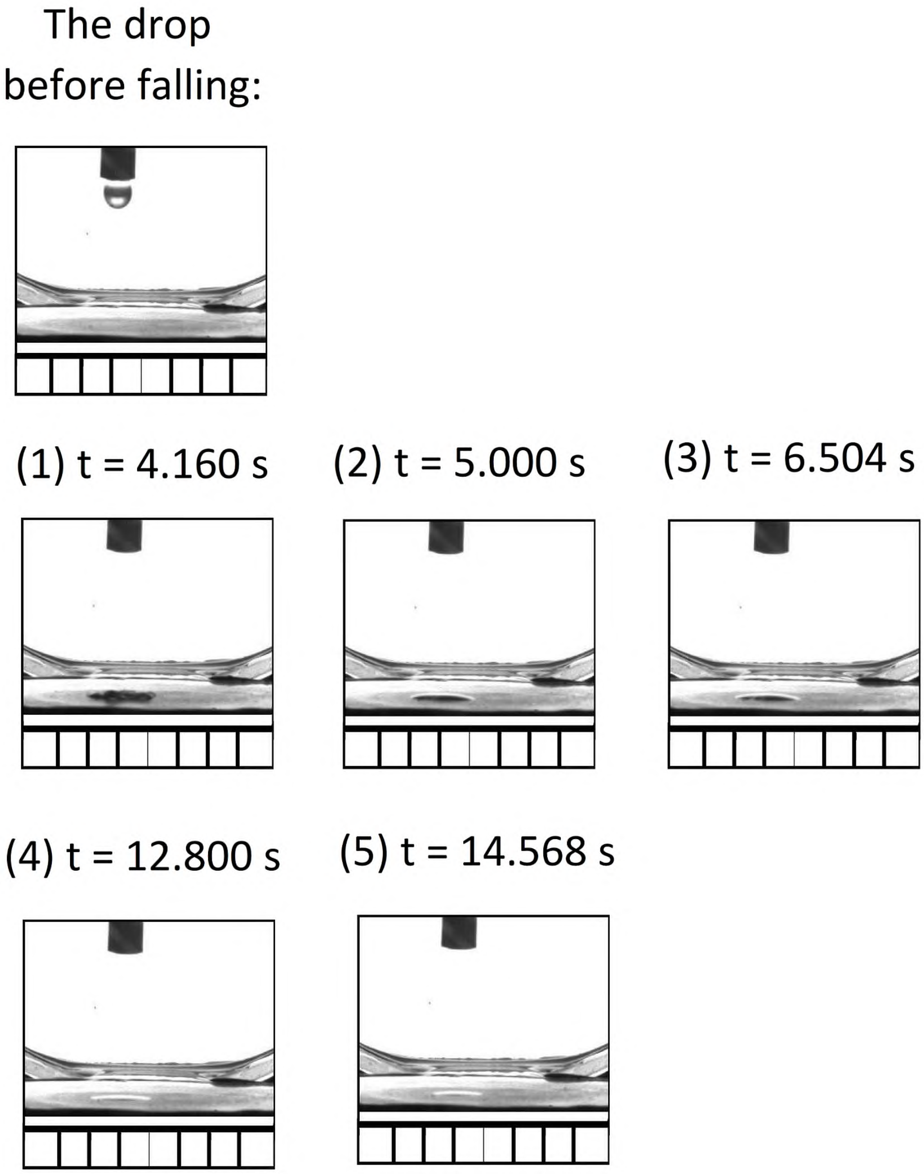

The drop before falling:

(1) t = 4.160 s

(2) t = 5.000 s

(3) t = 6.504 s

(4) t = 12.800 s

(5) t = 14.568 s

Figure 5.18: Lifetime of a droplet generated by the wide pipe.

in CCR mode. Only at the end of the process (from (4) to (5) in Fig. 5.20) the contact radius starts to be reduced. While the drop is not visible on the surface, the heat flux is still decreasing for several seconds. This might be associated with the existance of the thin precursor film with very small thickness (order of few µm), so it is not visible by the naked eye (more details about this are available in Section 1.1.4). This extremely thin layer of liquid still evaporates, extracting heat from the surface (process E in Fig. 5.20).

Fig. 5.21 presents the heat flux evolution obtained for the small drop (which was detailed in Section 5.3.5.1), distinct thermal processes involved in droplet evaporation are however marked on the graph.

The phenomenon begins when a drop hits the wall (point (1) in Fig. 5.21). This moment is followed by the intense increase of heat fluxes within few hundred milliseconds (transition A from (1) to (2)). It corresponds to the thermal diffusion, as the drop located on the surface has low temperature and firstly it has to be heated for the evaporation

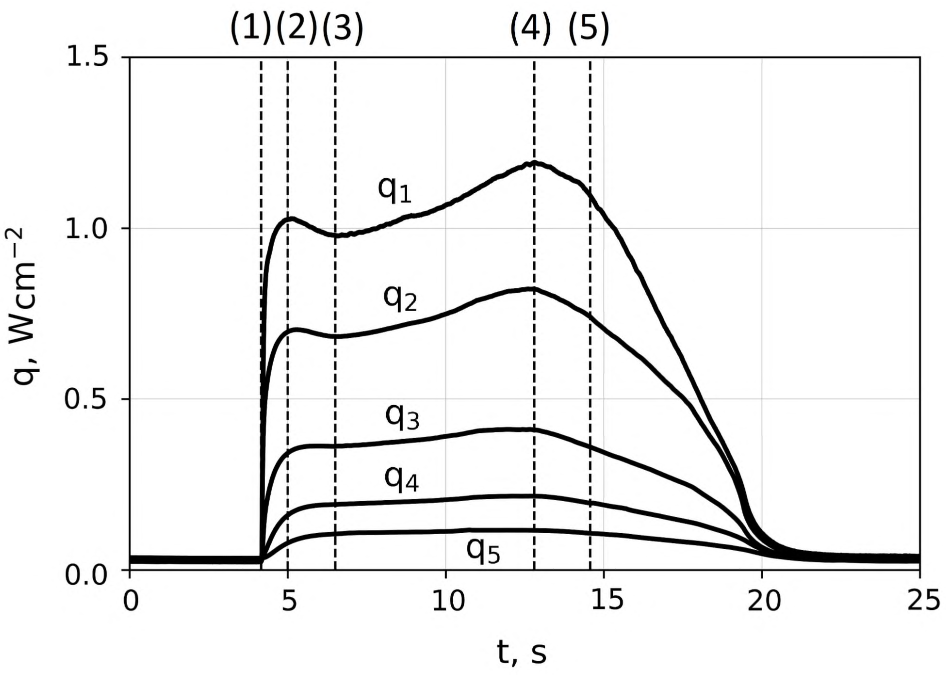

Figure 5.19: Heat flux evolution for a drop generated by the wide pipe.

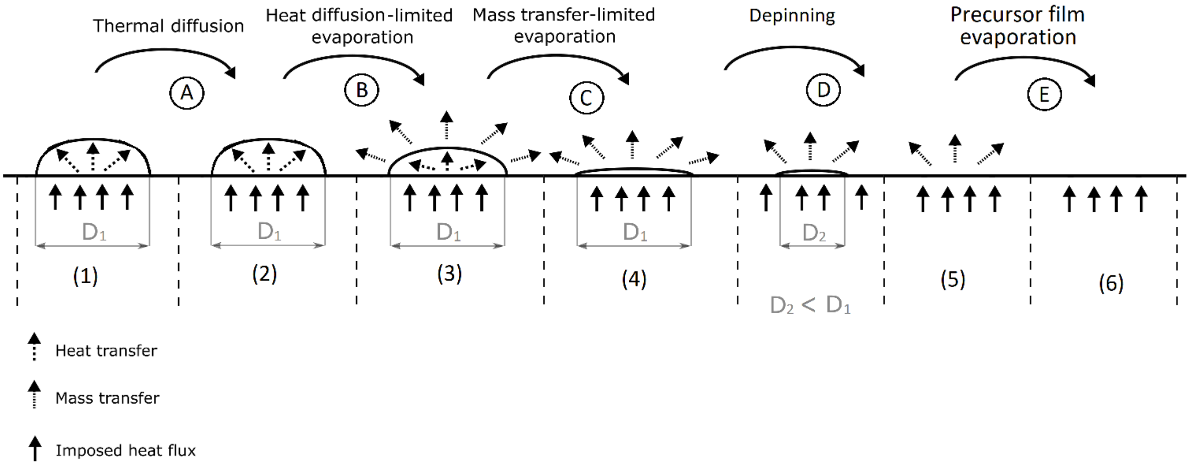

Figure 5.20: Schematic of the heat transfer processes involved in single drop evaporation at low pressure.

process to start.

During this process the volume of liquid remains constant. When the drop temperature is high enough, evaporation starts. At the beginning, the drop shrinks only in the vertical direction and its diameter remains constant (see Fig. 5.20). The initial evaporation can be divided into two steps. First step is a stage during which evaporation is limited by the heat diffusion through the drop (transition B from (2) to (3): the volume of liquid is still significant, so that the diffusion inside the drop remains the limiting factor of the process. While the heat needs to diffuse through a large volume of liquid, the mass transfer at the interface is favored by the large area of the drop surface. The second stage of evaporation is limited by the mass transfer at the interface (transition C from (3) to (4)). When liquid film thickness becomes smaller, its thermal resistance decreases so that heat diffusion is not limiting. However, the small interfacial area limits the mass transfer. When the contact angle becomes small enough, the depinning starts (transition D from (4) to (5)). At this stage, the drop begins to shrink also in the horizontal direction until it completely vanishes. In this step, the wetted surface area starts to decrease. The thermal resistance starts to increase due to lowering area of heat transfer. The last process - precursor film evaporation (transition E from (5) to (6)) corresponds to evaporation of very thin layer of liquid not visible on the camera recordings due to too low resolution. At point (6) the total volume of liquid has evaporated.

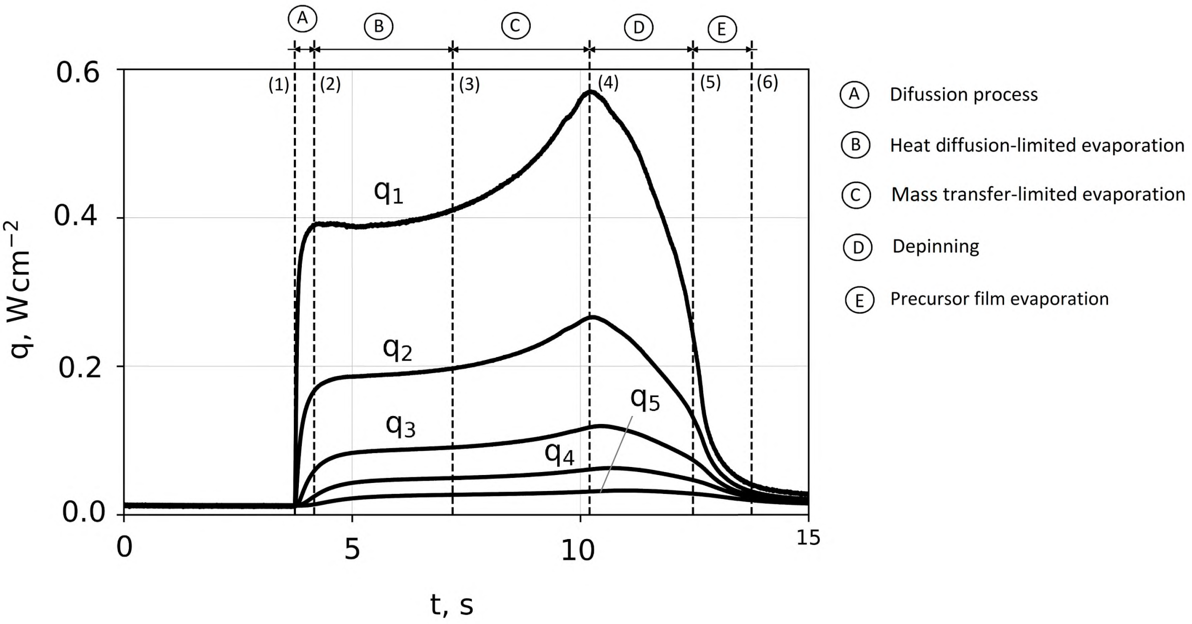

Figure 5.21: Thermal processes involved in the evaporation of liquid droplet generated by smaller drop.

5.3.5.4 Time of thermal diffusion

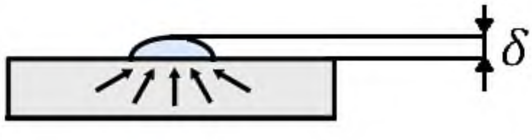

Figure 5.22: Sketch of a droplet on the heated surface.

The location of point 2 in Fig 5.17 and Fig. 5.19 (the end of thermal diffusion) was determined based on the video analysis. Up to this point, the volume of the drop seems not to be changed. To confirm the interpretation, it would be beneficial to compare the experimentally obtained value to at least, an order of magnitude of a theoretical time. The thermal diffusivity is defined as:

$$\alpha_l = \frac{\lambda_l}{\rho_l \cdot c_p(l)} \tag{5.12}$$

Neglecting the curvature of the drop and assuming that the heat inside a drop is conducted uniformly in the whole thickness, the time of thermal diffusion scales as:

$$t \sim \frac{\delta_{drop}^2}{\alpha_l} \tag{5.13}$$

For saturated liquid water at the considered vapor pressure ($p_v = 1.8$ kPa), the thermal diffusivity is equal to $1.41{\cdot}10^{-7}$ m$^2{\cdot}$s^{-1}.

The thickness of a drop was estimated as 0.5 mm and 0.3 mm for the drop generated by the thin and the wide pipe, respectively. The scalings of the time of ideal diffusion for both drops along with their experimental values (assessed from Fig. 5.17 and Fig. 5.19) are presented in Tab. 5.1. The order of magnitude of experimental values respect the theoretical scaling. The reason for shorter diffusion time in the experiments is firstly due to the choice of neglecting the curvature of the drop. It might also be caused by the movement of liquid. As the drop is released from the pipe placed above the heated surface it has some impact velocity. The frames of the video recording right after the drop reaches the wall are presented in Fig. 5.23. The picture (1) represents the moment of first contact with the surface. The time between two following frames is equal to 8 ms. It takes several dozens of seconds for the drop to reach a shape with no distortion. The shape of the liquid free surface changes shortly after the drop is deposited on the surface (see frames (2) - (6) in Fig. 5.23). There is no distinction between drops presented in frame (7) and (8), which indicates that the drop has reached its final shape.

Table 5.1: Theoretical and experimental values of time of thermal diffusion inside a droplet.

V_{drop}, mm^3	δ_{drop}, mm	t_{theory}, s	t_{exp}, s
28.7	0.5	1.8	0.840
0.9	0.3	0.6	0.424

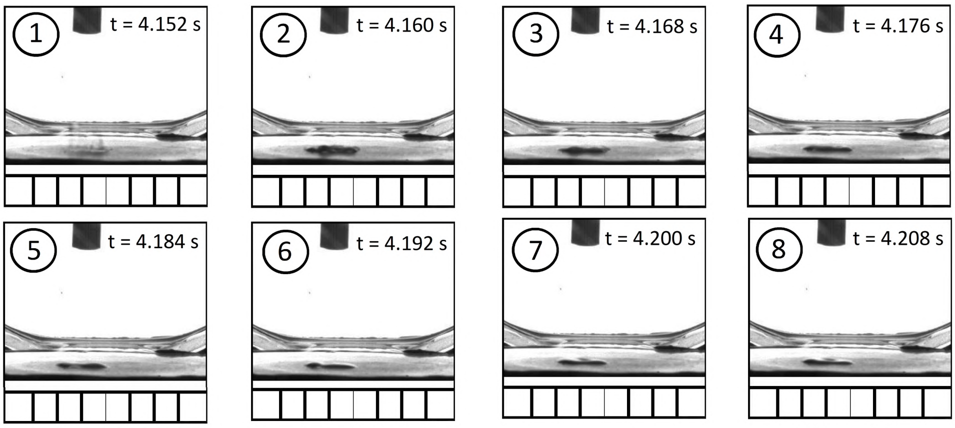

Figure 5.23: Movement of the drop after hitting the heated surface.

5.3.6 Heated wall temperature evolution during drop evaporation

The example of a wall temperature evolution recorded for the large drop is presented in Fig. 5.24. This parameter was plotted on the same graph as time evolution of heat flux for the first zone of the sensor q_1, because the temperature measurement was performed at the center of the heated wall (the sensor was described in Section 2.1.4). It is noticeable that both parameters are well correlated with each other. When the drop reaches the surface, the heat is extracted from the surface leading to a sudden decrease of wall temperature (of more than 5 K). The shape of the curve mirrors that of the heat flux evolution. When the heat flux returns to its initial value, the same happens with surface temperature.

This occurrence is different than what was observed for the boiling process. For moderate liquid level and low pressure, a bubble nucleation led to a sudden decrease of wall temperature. The bubble has a high diameter and causes a decrease of wall temperature of 10 or even 15 K. However, this lowered wall temperature persisted even after the bubble had detached from the surface. It took several dozens of seconds for the heated surface to reach the initial conditions.

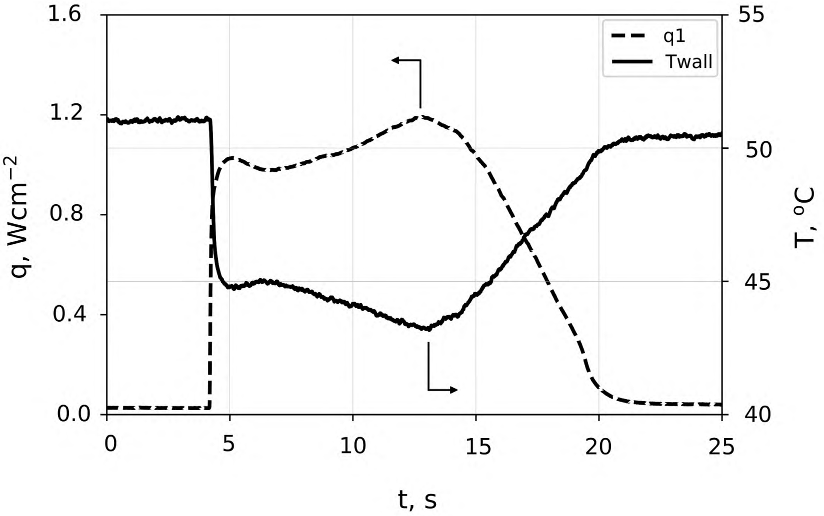

Figure 5.24: Simultaneous time evolution of the wall temperature and heat flux (vapor pressure: 1.8 kPa, saturation temperature: 15.8°C).

5.3.7 Several drops falling one after another

In view of heat transfer analysis for heat exchangers, another interesting aspect could be to comprehend the behavior of drops falling on previously wetted surface, e.g. if several drops fall shortly one after another in a way that the previous one did not have enough time to evaporate. Fig. 5.25 presents the heat flux evolution for such configuration. At time $t = 0$ s there was already small amount of liquid on the surface. During the 3 s measurement time, there are three clear peaks. Two of them are associated with the subsequent drops falling on the layer of liquid (peaks (2) and (4) in Fig. 5.25). Even though the heating surface is covered with liquid, the sensor still reacts by the rise of heat flux, because more heat is required to heat up the cold upcoming liquid. Apart from those new drops falling on the surface, the sensor reacts also when some bubbles occur inside the liquid. Those bubbles (marked as (1) and (3) in Fig. 5.25) are probably boiling bubbles (in contrast to air bubbles which sometimes occur due to air entrapment inside the water which was used to generate drop, e.g. see Fig. 5.12). Boiling bubbles exhibit a small amount of liquid at their top. As the liquid level is very small, the bubble rise above the drop free surface. It happened that during this event several bubbles were generated one after another in a short period of time.

Selected frames which corresponds to each heat flux peak detected by the heat flux sensor (see Fig. 5.25) are shown in Fig. 5.26. Numeration of the pictures corresponds to the the nomenclature on the graph of heat flux evolution in Fig. 5.25. Pictures (1) and (3) corresponds to the boiling bubbles which were observed during experiment. Several frames corresponding to the new drops falling on the surface are given in Fig. 5.26 (2) and (4). When a new drop is falling onto the surface, the dynamics of heat flux evolution is similar (slope 2 $\approx$ slope 3 in Fig. 5.25). The initial slope (starting from $t = 0$ s and disturbed by the presence of bubble) is however different (slope 1 $\neq$ slope 2 in Fig. 5.25). This is associated with the overall dynamics of the drop evaporation. When a drop reaches the surface, the immediate rise of heat flux is followed by its slight decrease at the beginning of diffusion-limited evaporation (see heat flux evolution during drop evaporation in Fig. 5.19). In the examples in Fig. 5.25, the decrease of heat flux is even more noticeable because of larger amount of liquid deposited on the surface. After some time, however, the heat flux evolution gets flattened (the slope of heat flux is reduced), what is captured at the beginning of the recording in Fig. 5.25. Probably, analogically to the single drop evaporation, this flattened curve would be followed by successive local maximum at the moment of depinning (if no more drops of liquid were to wet the surface).

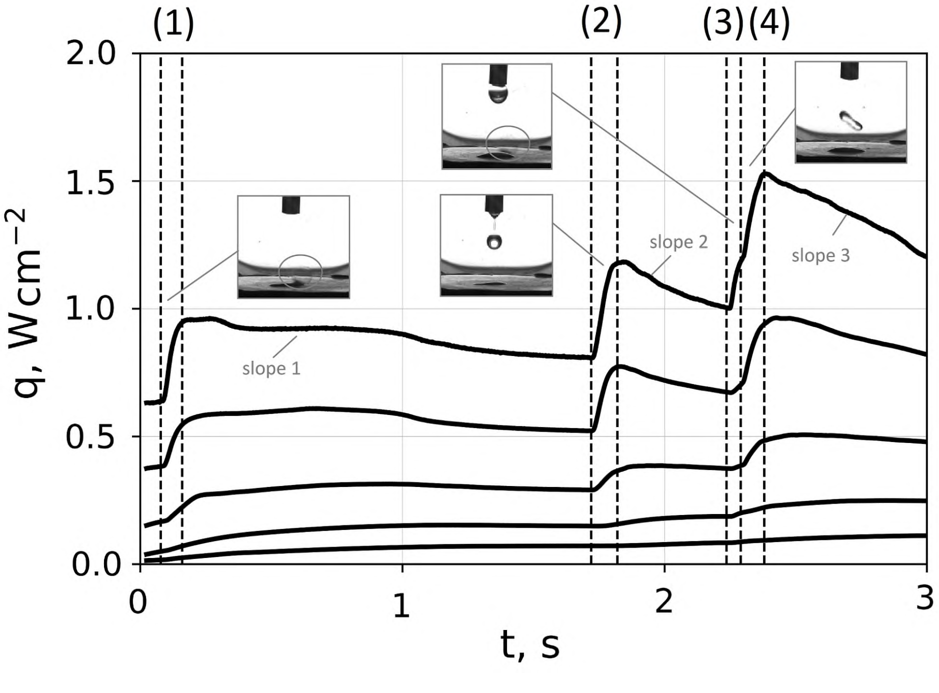

Figure 5.25: Heat flux evolution for a case when several drops falls down one after another.

The obtained results concerning droplet evaporation are really promising. The time of evaporation lasts over a dozen of seconds and depends on the drop size, which to a certain extent can be controlled. It might occur that droplets evaporation is more proficient at low pressure than the boiling process, where the long waiting time and small amount of active nucleation sites worsen the heat transfer condition. Moreover, even during evaporation process, several bubbles were observed from time to time and this events should intensify heat transfer. Additional advantage of this process in comparison to boiling is the fact that much lower applied heat flux is required to obtain necessary wall temperature. On the other hand, in the case of issues with the spraying system, the heated wall temperature could become too high and damage the system.

In the case of the heat exchangers, such studies should be extended by evaporation of multiple drops on the larger heated area. Of course, to definitely quantify the applicability of such cooling method, more complex configurations should be examined experimentally. For instance, spraying of the droplets on the whole heated surface (initially - flat and horizontal) would enable to calculate the heat transfer coefficient which then could be compared to the boiling experiments under similar working condition. In its current state, the experimental set-up cannot allow for such analysis. For this purpose, to get a general overview of the evaporation process from a larger heat transfer area, the thin film evaporation was studied and some results are presented in the following Section.

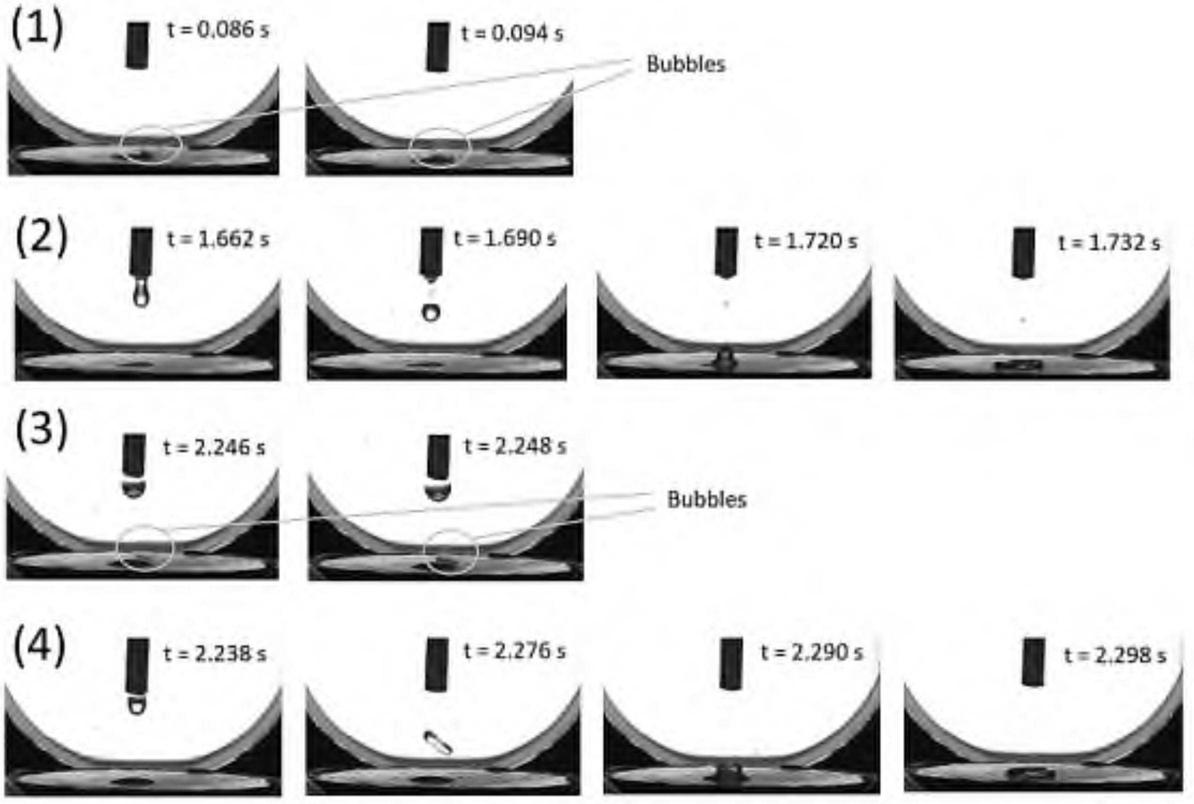

Figure 5.26: Frames from video recordings presenting drops and bubbles corresponding to heat flux evolution in Fig. 5.25.

5.4 Evaporation of thin liquid layer

It was hard to obtain a satisfying repeatability during measurement of a drop evaporation. The present system does not allow to keep exactly the same conditions for all the tests, especially with respect to the volume of a drop. The generated drops had various volumes and shapes even for the same pipe. For that purpose it is not possible to make a comparative studies of evaporation process for various working conditions, such as heating power or pressure. To obtain the same volume of evaporating liquid it was decided to perform tests also for a thin layer of liquid pouring known amount of liquid on the heated wall. Such approach would allow for the comparative studies of evaporation process at different operating conditions.

To do so, before each test, the small liquid tank placed above the vessel (see Fig. 5.10) was filled with required volume of liquid (V_l was set to 1 mL, 2 mL or 3 mL). Four different heating poweres were applied (7 W, 11 W, 16 W, 21 W) what corresponds to applied heat fluxes of (0.15 Wcm^{-2}, 0.23 Wcm^{-2}, 0.33 Wcm^{-2}, 0.44 Wcm^{-2}). The syringe was used to accurately dose the amount of liquid which was store inside the tank. The connection to this tank was then closed by vacuum-tight clamp. When the required conditions were reached (proper value of pressure, temperature inside the test vessel and wall temperature) the measurements started and the valve got fully open. The total volume of liquid formed a thin layer of liquid which covered more or less of the heating surface depending on the applied volume of liquid. The pictures taken from high speed camera for all studied volumes are shown in Fig. 5.27. For the smallest amount of liquid ($V = 1$ mL), the resulted pool of liquid tends to have higher thickness. When volume of 3 mL was applied, the liquid was more uniformly spread on the whole surface and resulting thickness was reduced.

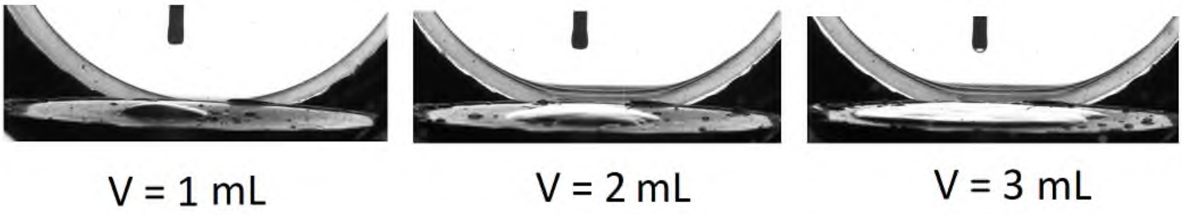

Figure 5.27: The thin layer of liquid formed on the heated surface depending on the applied volume of liquid.

5.4.1 Problems involved with conducting the experiments

Several problems arose when conducting these experiments. A first issue was that the liquid was poured with high impact velocity leading to splashing. Some splashed liquid could rebounce away from the surface and fall outside the surface. And even if all the liquid remained on the heated wall, its distribution on the surface was quite random: it could form an uniform pool with a regular shape or a smaller pool with lots of multiple droplets around. The example of such situation is shown in Fig. 5.28.

The other issue was the fact that even though the valve which controls the process was fully opened and the pressure difference existed, several droplets could still remain inside or on the pipe. All those aspects result in an inaccurate estimation of liquid volume and can lead to different dynamics of evaporation process. For that purpose it was decided that the test conducted for certain working parameters (volume of liquid, applied heating power) would be repeated at least 10 times to be able to obtain some averaged parameters to characterize the process of evaporation at such conditions.

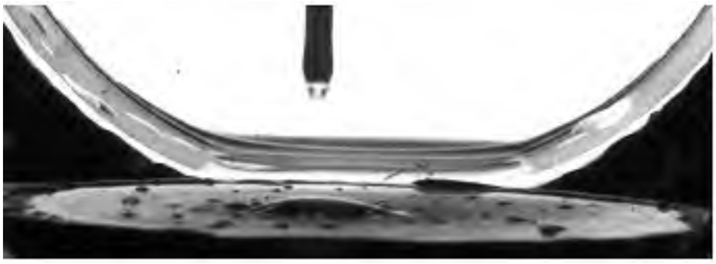

Figure 5.28: The example of the situation when lots of small bubbles is formed on the heated wall instead of forming regular liquid pool.

5.4.2 Time evolution of heat flux for a thin layer of liquid

Fig. 5.29 presents example of the time evolution of heat flux obtained for the liquid layer of volume $V_l = 1$ mL. The heat flux applied to the heating surface was equal to 0.44 $\mathrm{Wcm^{-2}}$ (heating power 20 W). The shape of the graph presents some similarities that of the graph for a single drop with a volume even few hundred times smaller than the considered liquid pool (the sharp increase of heat flux at the beggining of the process and second extremum the at the end of the evaporation, where the depinning process start). This signifies that the dynamics of evaporation process and liquid pool have some common features. The main difference is the time of the process. Due to enlarged volume of the working medium it takes longer time to evaporate the whole liquid. The moment when a first drop reaches the wall is marked as (A) and the end of the evaporation process, when all the liquid vanishes from the surface as (B). It is also worth mentioning that some air was entering the system with the working fluid. The amount was bigger for smaller volume of liquid (the tank where the liquid was stored was only slightly larger than 3 mL). This along with the velocity of the pouring liquid caused considerable movement of the liquid free surface at the beginning of the process.

5.4.2.1 Thermal effect associated with thin liquid film evaporation

At beginning of the evaporation process (starting from point (A) in Fig. 5.29) the curves are very noisy. There is lots of smaller peaks especially visible in the proximity to the center of the surface. Those peaks might be associated with the drops of liquid which are still falling on the surface (or rather on the liquid pool which covers the heated wall). It is exactly the same behavior as was shown in Section 5.3.8. Based on the video observations, in some cases also the boiling bubbles were observed (see Fig. 5.30). They are similar to boiling bubbles seen in Fig. 5.25 and Fig. 5.25, but their dimensions are larger. Again, as the liquid level is very low the bubbles are growing above the liquid free surface. Their characteristic feature is small cap of liquid gathered at the upper part of the bubble. After some time the bubble burst and vanishes. It is however impossible to definitely see the difference between peaks caused by the boiling process and the ones associated with the falling droplets.

5.4.3 Time of evaporation for various working conditions

The influence of the amount of liquid on the evaporation time for different applied heat fluxes is presented in Fig. 5.31. Different volumes of liquid were marked in a different manner (circle - 1 mL, square - 2 mL, triangle 3 mL). Due to the problems described in

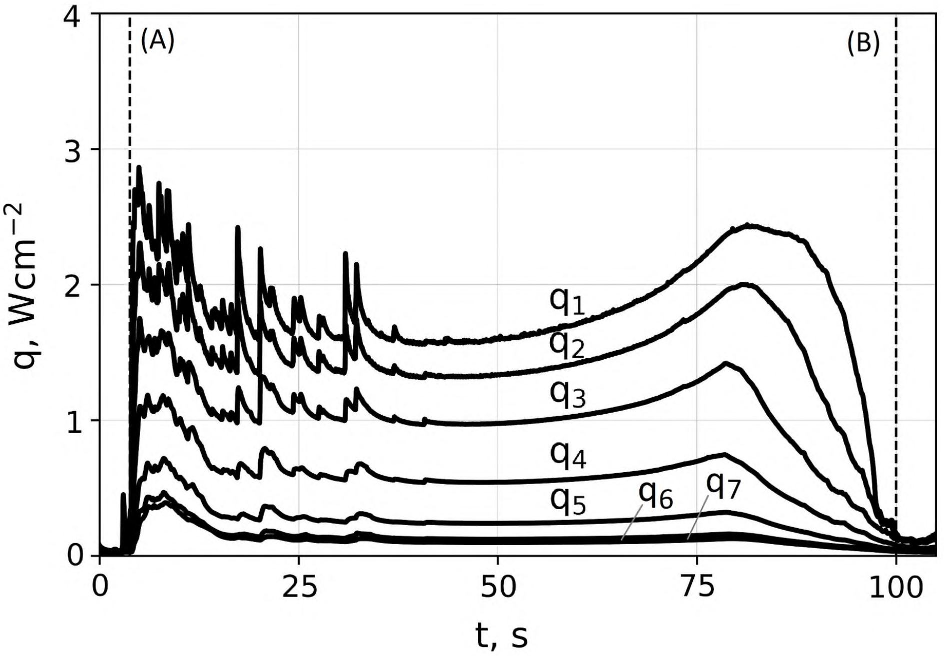

Figure 5.29: The time evolution of heat flux for evaporation of thin layer of liquid (V_l = 1 ml, HP = 21 W, q_{app} = 0.4 Wcm^2).

Figure 5.30: The boiling bubbles created at the thin layer of liquid.

Section 5.4.1, there is noticeable discrepancy between measurement points obtained for a specific condition. This discrepancy is more significant when lower heat flux is applied. Nevertheless, the general trend is clearly observable. If the applied heat flux is small it gets more time for the liquid layer to evaporate. Larger volume also requires more time to totally disappear from the surface. The influence of the applied heat flux on the time of evaporation is clearly exponential. For low values of applied heat fluxes, its increase results in an intense drop of evaporation time. However, when the applied heat flux gets larger, its further rise results in more slight decrease of evaporation time. Also, the increase of the liquid volume from 1 mL to 2 mL resulted in larger increase of evaporation time than the rise of volume from 2 mL to 3 mL. This was associated with the reduced thickness of the liquid film when larger volume was poured on the surface (see Fig. 5.27).

The performed tests did not allow to obtain a perfect repeatability of the evaporation processes for certain operating condition. However, the general trend of how the volume of liquid affects the evaporation time was captured. The proper liquid distribution on the whole liquid surface is crucial, because it limits the effect of conduction inside the liquid layer, reducing time of evaporation (i.e. the same volume of liquid evaporates more quickly if the liquid is uniformly spread on the whole surface instead of forming more

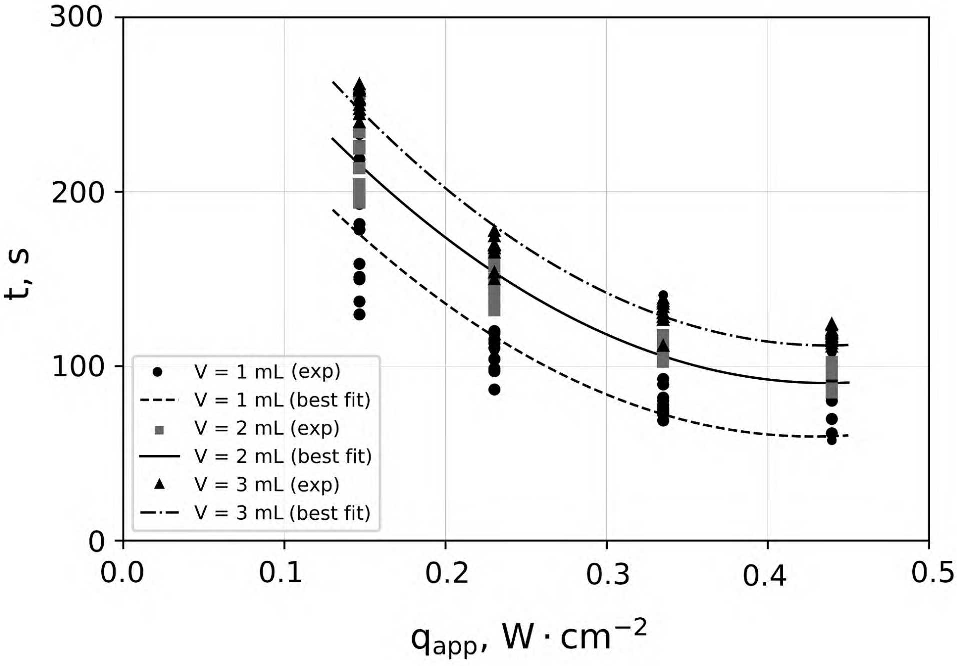

Figure 5.31: Evaporation time for various working conditions.

thick pool with smaller diameter). For future tests, it would be convenient to compare the effectiveness of heat transfer during evaporation of thin layer of liquid covering the whole heating surface with small drops or droplet with different sizes spayed on the same surface area. It would help distinguish the most important parameters associated with evaporation process at low pressure in order to obtain the best thermal performance of the system.

Conclusions

The brief literature review first presented in this chapter indicated that there is lack of knowledge concerning the phenomenon of evaporation on horizontal surface at low pressure. At atmospheric conditions, however, many researchers investigated the thermal aspects of this process. They distinguished two main evaporation modes of a drop: constant contact radius or constant contact angle. The authors noted different types of flows which can occur inside a drop due to temperature or surface tension gradient along the liquid free surface and resulting dried patterns. The important parameters influencing the spreading of a drop and evaporation process were also discussed. This is e.g. wettability, roughness and rigidity of the substrate and surface temperature. If the temperature of the heated wall is high enough, boiling occurs inside the drop, with multiple bubbles rising above the liquid free surface.

All those information cannot be easily transposed to conditions in the proximity to the triple point. Boiling processes under atmospheric and under low pressure are quite different and it also might be the case for the evaporation phenomenon. For that purpose, an experimental study of drop or liquid layer evaporation at low pressure was conducted.

For the drop evaporation, the most basic configuration was chosen - a sessile drop deposited on a hot solid wall. The analysis covered evaporation process of two sessile drops with different volume 28.7 mm^3 and 0.9 mm^3)) deposited on a hot horizontal surface *(heating power 20 W). The same heat flux sensor was used as in Chapters 3 and 4, thus firstly the difference between sensor response for boiling and evaporation processes were discussed. Based on the heat flux measurements and high-speed camera recordings distinct thermal processes were distinguished. Those are consequently: thermal diffusion (where no mass transfer occurs, just the heating up of the liquid), heat diffusion-limited evaporation, mass transfer-limited evaporation and finally depinning. For most of the processes, the TPCL is pinned to the surface (CCR mode of evaporation). Only the last stage is associated with the reduction of the triple contact line. Several boiling bubbles were also observed during the experiments. For the future experiments it would be beneficial to compare the case of several droplets sprayed on the heated surface with the boiling process under similar operating conditions. It might occur that droplets evaporation is a more efficient heat transfer mode at low pressure than the boiling process that suffers from several limitations.*

It was not possible to obtain several droplets with fixed volume in order to evaluate the influence of different operating parameters (e.g. heating power, pressure) on the evaporation process. That is why it was decided to perform tests also for a thin layer of liquid. The experiments were conducted for three volumes of liquid (1 mL, 2 mL, 3 mL) and four heating powers (7 W, 11 W, 16 W, 20 W). They were repeated at least 10 times to statistically capture the overall dynamics of the process. It occurred that the thermal dynamics somehow resembles the process obtained for a single drop. The main difference is the time of the process (which is longer as more liquid needs to evaporate). Due to difficulties in pouring out the liquid in a very accurate way, there are always some discrepancies between results obtained for specific working conditions. The general trend of the process can be nevertheless observed. Multiple smaller peaks on the heat flux evolution at the beginning of the process were also distinguished. This noise is associated with subsequent droplets falling down towards the surface to form a liquid pool. Some of those peaks are also associated with the boiling bubbles. The proper liquid distribution on the whole liquid surface is important. The thinner layer of liquid limits the conduction inside the liquid reducing evaporation time. In the future, it would be interesting to compare the effectiveness of heat transfer during evaporation of thin layer of liquid covering the whole heating surface with small drops or droplet with different sizes spayed on the same surface area.

Conlcusion and perspectives

Synthesis

The study of water pool boiling under low pressure conditions has recently become of high scientific interest. This is mostly driven by importance of implementing more environmentally-friendly solutions in the cooling and air-conditioning systems. A promising ecological alternative is indeed the utilization of water as a refrigerant, mostly in sorption chillers. Such systems have to operate at low operating temperatures (around 10°C what corresponds to vapor pressure of 1.2 kPa). Currently, low-pressure heat transfer devices are design mostly in an empirical way, as there is lack of knowledge concerning boiling process at sub-atmospheric conditions. Based on that need, this thesis focuses on the fundamental aspects involved in thermal processes during boiling and evaporation at low-pressure. The studies concerned the bubble dynamics (size, shape and frequency of the bubbles), as well as, thermal analysis of the process.

The first part of the manuscript was devoted on the literature review concerning pool boiling process, with special respect to the studies focused on boiling at the proximity to the triple point. The low-pressure bubble dynamics possesses many characteristic features, i.e. large bubble size, sometimes with characteristic mushroom shape, long waiting time between two successive bubbles, reduced number of active nucleation sites and consequently smaller number of bubbles present on the surface. The influence of pressure on the heat transfer was also reported. Large bubbles introduce characteristic wall temperature fluctuations (of 10 or even 20 K). The thermal performance of low pressure systems is reduced in comparison to atmospheric pressure. The empirical or semi-empirical correlations for heat transfer coefficients are not valid at such conditions. First, some thermophysical properties of the fluid, especially vapor density, are very different than at higher pressure. Then, the most important driving force which affects low pressure boiling is a static pressure-induced subcooling. It is generated by the static head of liquid having similar order of magnitude as the vapor pressure, so it cannot be neglected. This creates a non-homogeneous saturation temperature field along the liquid height that strongly affects the bubble growth (i.e. stronger liquid subcooling results in smaller and more quickly condensing bubbles).

The same experimental test-bench as in [40] and [81] was used to perform experiments. Nevertheless, for a given analysis, the heated wall was treated differently. For a mirror-polished surface with single nucleation site, the isolated bubbles were formed. On a rough surface with multiple cavities, several bubbles occur on the surface simultaneously. Apart from the boiling process which occur on a fully wetted surface (with fixed value of liquid level), the small amount of liquid was deposited on the surface in order to investigate the evaporation process. For all the tests, the thermal measurements were performed with a novel flux sensor. Such transducer measures the value of instantaneous heat flux independently in seven annular zones of the sensor. Such way of measurements is especially beneficial for bubbles with large size (which is usually the case while working at low pressure), as tracking of the bubble foot is possible. Also, the analysis of heat fluxes at different parts of the surface during liquid evaporation gave an interesting insight into this phenomenon. To allow for a broad analysis of the boiling and evaporation phenomena, the thermal measurements were always synchronized with the high-speed camera recordings. Such approach enabled to study the correspondence between heat transfer and bubble dynamics (or drop evaporation).

The first tests described in the manuscript were conducted for a polished surface with a single cavity located at the center. Owing to the heat flux sensor, the bubble foot evolution could be observed and analyzed in a totally innovative way. Such analysis enabled to detect a number of phenomena present during boiling process, such as the existence of microlayer evaporation at the early stage of the bubble growth or the liquid movement due to vapor expansion inside the bubble. Comparing thermal signatures with video recordings allowed to distinguish three types of low-pressure bubbles. Those are named as: oblate spheroid-shaped bubble, mushroom-shaped bubble and cavitation mushroom-shaped bubble. The latter one was never described in the literature before. The distinction between mushroom-shaped and cavitation mushroom-shaped bubble was possible owing to the heat flux sensor. The evolution of the bubble foot diameter was also analyzed for three liquid levels (2 cm, 15 cm, 28 cm). The moderate liquid level ($H_l = 15$ cm) is the most often studied in the literature and it is associated with bubbles with large size and low frequency (what is usually considered as low-pressure conditions). A small level of liquid ($H_l = 2$ cm) resulted in enlarging of the bubble foot diameter. The bubble foot often became even larger than the size of the heated surface. For high level of liquid, many small and quickly condensing bubbles were observed. This due to increase of local subcooling generated by the column of liquid.

The second experimental campaign was conducted for a rough surface with multiple nucleation sites in order to obtain more intense boiling process with several bubbles on the surface. This enabled to capture the interactions between bubbles and get one step closer into real-life heat exchangers. The pool boiling experiments were conducted for a variety of working parameters (i.e. vapor pressures, liquid levels, applied heat fluxes) and two surface roughness. It occurred that the highest heat transfer coefficient was obtained for liquid level $H_l = 28$ cm. The heat flux evolution, especially for high heat fluxes, was very noisy and had many peaks, thus the analysis was performed based on probability density functions (PDFs). Owing to this kind of statistical analysis extended by camera recordings, four boiling regimes were distinguished: the convection or small popping bubbles regime, the isolated bubble regime, the intermittent boiling regime and the fully developed boiling regime. Lower liquid level was usually associated with isolated bubble regime. For the highest analyzed liquid level ($H_l = 60$ cm), mostly the convection or small popping bubble regime was observed. In order to provide more general description of the boiling regimes for wide range of working parameters, a dimensionless boiling regime map was proposed. The 'x' axis was chosen to be the ratio of vapor pressure to the static pressure (p_v/p_{stat}). The Jakob number, modified to fit into constant heat flux conditions, was chosen as a ordinate. The dimensionless boiling map composes of two main regions. For $p_v/p_{stat} < 1.0$, the resulting boiling regime is mostly due to intense liquid subcooling (thus, convection or small popping bubble regime is the most often reached). For $p_v/p_{stat} > 1.0$, even when applied value of heat flux is relatively low, different boiling regimes are often observed. The same analysis was performed for the surface with two different roughness. No significant difference between regimes for both surface characteristics were noted. Probably, the changes in the surface characteristics were not enough to really influence the boiling process.

The important conclusion arising from these boiling experiments is that for all operating conditions, the average heat transfer coefficient is low and do not vary too much from a single-phase convection. It is possible that for the systems operating at the proximity to the triple point, one should look for an alternative cooling solution. One idea is to apply spray cooling instead of the boiling process. This phenomenon relies on evaporation of small droplets or thin film from a hot surface. To examine this option, the last part of this manuscript focused on the preliminary study of the evaporation process at low pressure. A brief literature review concerning this phenomenon was introduced. No published work on evaporation at low pressure was found in the open literature. Boiling phenomena under atmospheric and low pressure are totally different, thus this also might be the case for evaporation process. The experimental studies described in this thesis were performed for a sessile drop deposited on a hot surface. The detailed analysis was conducted for two drops with different volumes. Several thermal processes were revealed by the experimental results, named as follows: thermal diffusion (no mass transfer occurs, initially the liquid is only heated), heat diffusion-limited evaporation, mass-transfer limited evaporation and depinning. Most of the processes occur with the triple phase contact line being pinned to the surface (constant contact radius mode of evaporation). Only the last stage of the process (i.e. depinning) is associated with the reduction of the drop radius. Several boiling bubbles were also noticed during experiments. It was not possible to generate several bubble with a fixed volume in order to compare system thermal performance for various working parameters. For that purpose, the test for various operating conditions were performed for a thin liquid layer (volume of 1 mL, 2 mL or 3 mL). The observed thermal dynamics somehow resembles the process obtained for a single drop, but the time of the process is much longer.

Perspectives

The analysis described in this manuscript gave several ideas concerning the direction of the future works. As a consequence of this thesis, they are focusing on improving the knowledge concerning boiling and evaporation processes at low pressure. Those ideas will be described in the following points.

- The experiments performed with the heat flux sensor were very innovative and allowed to obtain the interesting insight into low-pressure boiling and evaporation processes. New bubble type was discovered, the boiling processes for various working conditions were grouped into four boiling regimes and thermal processes involved in the drop evaporation were distinguished. All those analysis were however purely qualitative. Unfortunately, the time constant of the heat flux sensor was quite high. To allow for a quantitative analysis in the future, a new heat flux sensor with lower time constant could be developed. This should be particularly helpful in order to perform a heat balance of a growing bubble.

- The performed analysis highlighted the importance of liquid level on the bubble dynamics and resulting boiling regimes. The experiments, however were conducted only for a pressure-induced subcooling. It was done by adjusting the liquid level to a required value what influenced the local saturation temperature. The liquid bulk temperature remained constant. In the future tests, it would be of a great interest to study difference between the temperature-induced subcooling (when T_l is lower than T_{sat}) and pressure-induced subcooling. It could be done by obtaining the same value of subcooling for both cases and observing how boiling regimes and thermal behaviors differ in any way.

- The dimensionless boiling regime map of water was generated for three vapor pressures, several liquid levels and heat fluxes. In order to truly validate the correctness of such representation, it would be beneficial to perform similar analysis for different working fluids. The influence of the surface roughness on the boiling regimes was also investigated, but the difference in regimes for both surface characteristics was not really observable. Probably the variation in the averaged roughness was not sufficient to really influence the bubble dynamics. The more intense surface treatment was not possible because of the design of the sensor. To really examine how the surface characteristics affect the boiling process, the way of increasing the surface roughness in more significant way should be developed.

- The thermal performance of low pressure systems is low and resulting heat transfer coefficient do not vary much from a single-phase convection. For that purpose, interesting idea is to more closely investigate the evaporation process which occur at the proximity to the triple point. The studies described in this manuscript concerned basic configuration - i.e. small drop or thin liquid layer deposited on a hot, horizontal surface. The future tests should be extended by other configurations (e.g. pendant drop or multiple drops sprayed on the whole heating surface simultaneously). In order to do that, the drop generation system should be improved. Currently, the drops are generated in a random way. It is not possible to predict when exactly the drop will fall from the pipe and what will be the size of a drop. This prohibits from performing fully repeatable and comparable tests. The valve responsible for drop generation is controlled manually and camera memory is limited. Replacing the manual valve with electronically-controlled would allow to improve the quality of the experiments. In order to study spray cooling, the pipe which was used to generate drops should be equipped with a nozzle. Another interesting aspect is to perform experiments on the surfaces with different configurations, such as outer side of the tubes. This would simulate more accurately conditions occurring inside the shell-and-tube heat exchangers.

Appendix A

Characterization of the heated surface

A.1 Measurements of surface characterization with confocal microscope

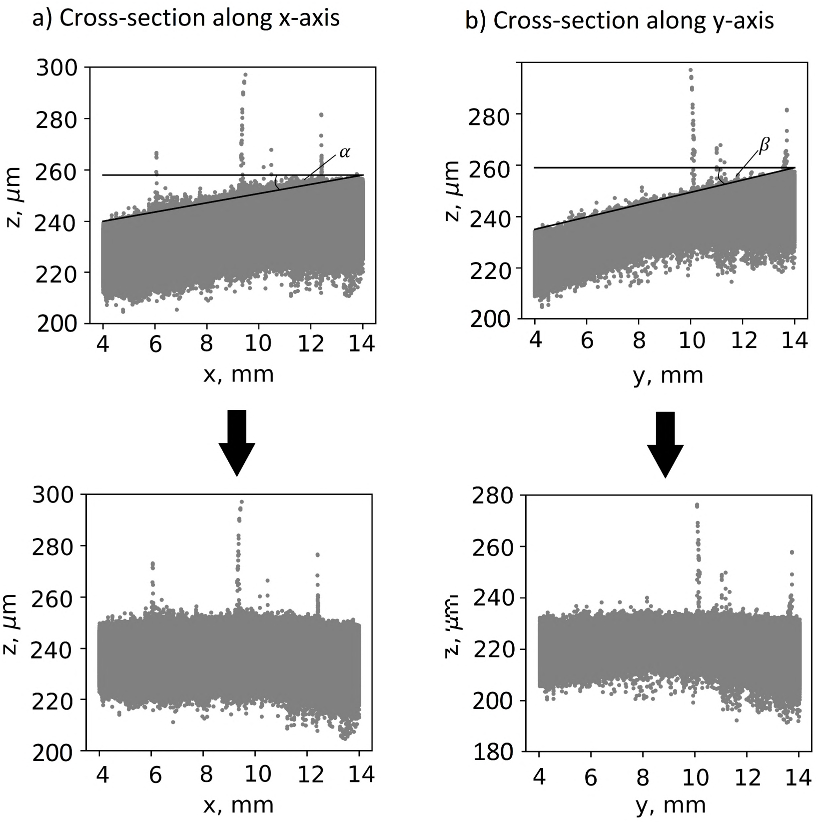

Figure A.1: Inclination of the surface visible on the cross-sections of surface altitude measurements.

The heated surface described in Chapter 2 was observed with confocal microscope in order to determine the averaged roughness at different parts of the sensor and estimate the size of artificial nucleation site created at the center of the heated wall. The tests were performed for polished surface (to study isolated bubble dynamics), as well as on a rough surface with multiple nucleation sites (to investigate more general boiling behavior).

During measurements, the surface was slightly inclined (see Fig. A.1). For this purpose, a correction factor was applied, in order to turn the surface into fairly horizontal position. This operation enables to avoid the changes of altitude z caused by the inclination of the surface rather than irregularities in the structure. This kind of correction was made independently for every measurement.

A.2 Polished surface with a single nucleation site

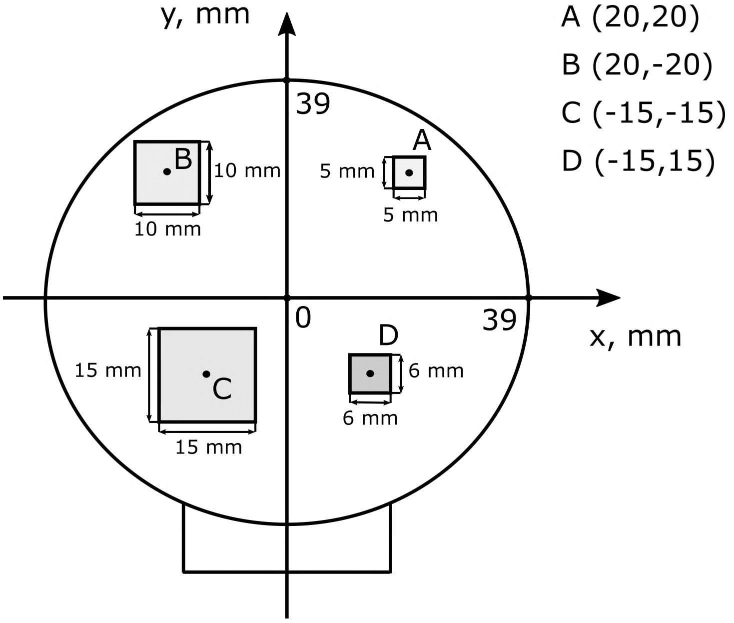

Figure A.2: Location of the zones measured with confocal microscope (polished surface).

At such conditions, four distinct parts of the sensor (named A, B, C, D - see Fig. A.2) were analyzed with high accuracy. The list of all the zones for which measurements were performed along with their parameters is presented in Tab. A.1.

The spatial step (step between two points for which altitude z is measured) was equal to $sp = 8$ µm. The measurements were conducted along both, x and y axes.

Additionally, the whole surface was observed with larger spatial step ($sp = 35$ µm) in order to reduce time of the measurement. The measurements were conducted for an area of a square 80 mm x 80 mm. Due to low resolution, roughness measurements were not provided, only the general surface condition was analyzed.

The measurements of the artificial nucleation site was also conducted for the square area 1.5 mm x 1.5 mm in the center of the surface with spatial step $sp = 3$ µm.

A.2.1 Characterization of the nucleation site

The created cavity has circular base and almost conical shape, what can be seen in Fig. A.3. Its size was estimated as: 116 μm diameter and 160 μm height. The nucleation site is located at the center of the heated surface.

Table A.1: The main parameters of the confocal microscope measurements for different parts of the heated surface (polished surface)

	S, mm x mm	sp, µm
Nucleation site	1.5 x 1.5	3
Total surface	85 x 85	35
Area A	5 x 5	8
Area B	10 x 10	8
Zone C	15 x 15	8
Zone D	6 x 6	8

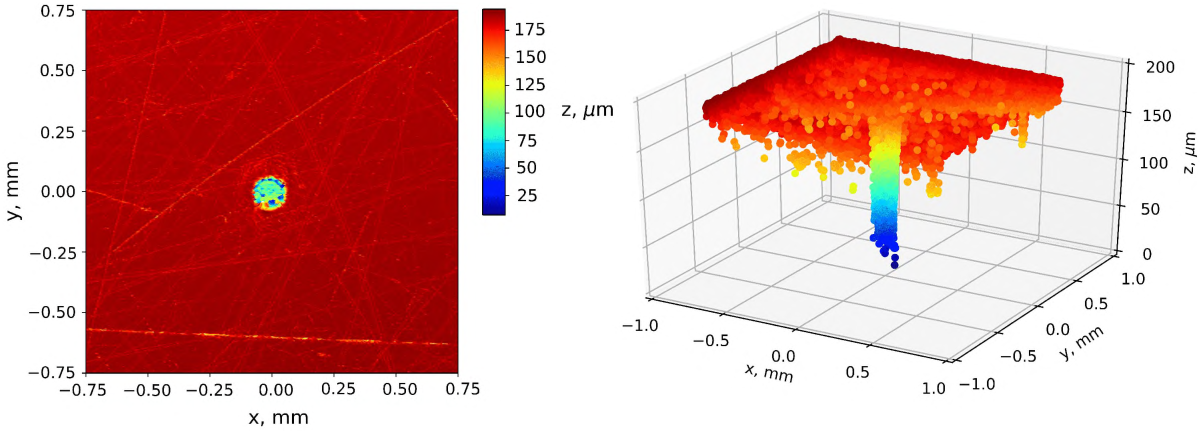

Figure A.3: Visualization of the artificial nucleation site created at the center of the heated surface ($sp = 3$ µm).

A.2.2 Rougness measurements of several zones on the heated surface

The zones were chosen randomly to cover significant surface area at different parts of the sensor (their location and actual size are presented in Fig. A.2). Visualizations of the surface characteristics are presented in Fig. A.4. The surface is relatively smooth for all the measured zones, apart from the right bottom corner of zone B (see Fig. A.4b). In this place, the measured altitude is lower than for the rest of the surface. Despite polishing of the surface, all the zones possess some scratches visible on the pictures (zones A - D in Fig. A.4).

Roughness of the surface was estimated for each measurement zone. For this purpose, the root mean square roughness S_q was calculated based on the following equation:

$$S_q = \sqrt{\frac{1}{M_x M_y} \sum_{k=0}^{M_x-1} \sum_{i=0}^{M_y-1} [z(x_k, y_i) - z_{mean}]^2} \tag{A.1}$$

where M_x and M_y are the number of points for which the altitude is measured, along x and y axes.

Tab. A.2 shows the value of the root mean square roughness calculated for each considered part. All the values have the same order of magnitude. Taking into account the area of each zone, the averaged roughness can be estimated as 0.42 µm.

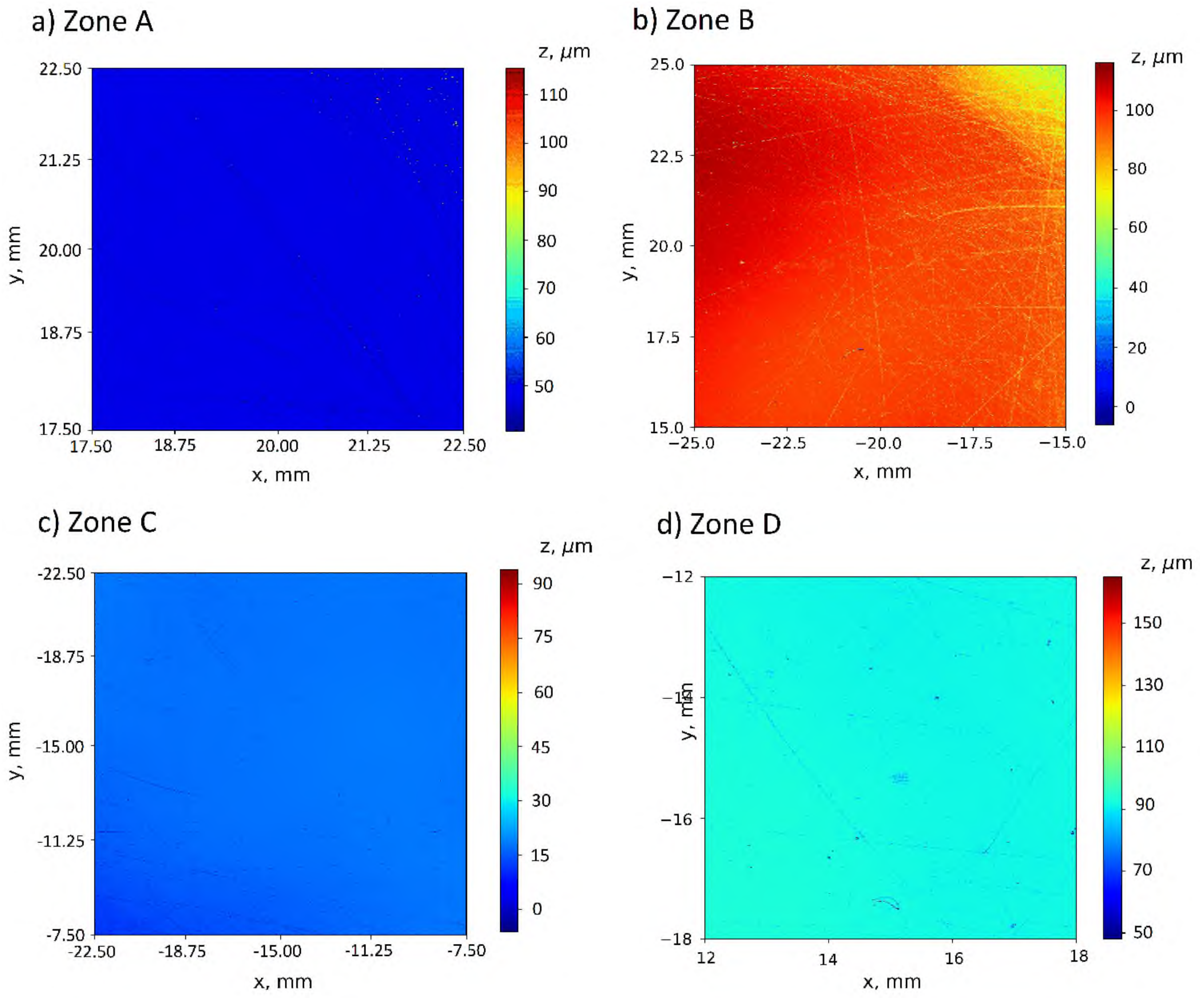

Figure A.4: Visualization of the surface characteristics for different parts of the heated surface with $sp = 3$ µm (polished surface).

Table A.2: Root mean square roughness for all measurement zones (polished surface).

Name of the zone	S_q, μm
Zone A	0.41
Zone B	0.66
Area C	0.35
Area D	0.21

A.2.3 Roughness measurements of the whole surface

The total surface was also measured to obtain rough estimation of its altitude. For this purpose, and to limit the measurement time and the file size, lower spatial resolution was applied ($sp = 35$ µm). Analyzing Fig. A.5, one can see that the surface is uniform, apart from the upper right corner, where points are located lower than the rest of the surface.

Additionally, vertical lines are visible on the wall. They correspond to grooves made at the bottom of the sensor's coper foil in order to provide its proper work (by creating asymmetry between copper and constantan - more details about the sensor's construction and operation might be found in Chapter 2.1.3) and to obtain sufficient gluing between foil and the rest of the sensor. Despite all of that, the difference in the altitude for the whole surface can be still estimated as around 50 µm.

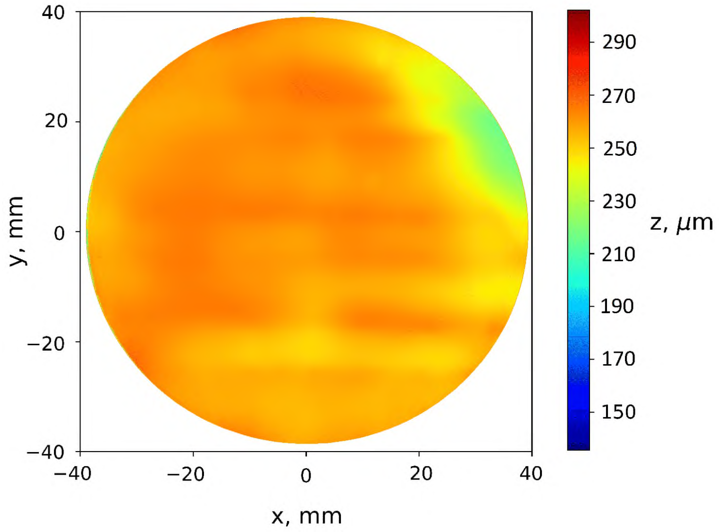

Figure A.5: Total surface measurements (polished surface).

A.2.4 Conclusions

Based on the measurements conducted with confocal microscope it is concluded that the heated surface is relatively smooth. The roughness was estimated as $S_q = 0.42$ μm. The heated wall quality is good enough to study dynamics of isolated bubbles.

The created cavity possesses symmetrical shape, with diameter of 116 μm and height of 160 μm. It is located at the center of the heated surface. Those parameters should be sufficient to provide bubble nucleation at this point, as it is similar to the nucleation sites used by different authors [40, 81].

A.3 Rough surface with multiple nucleation sites (first measurement series)

In this part, five different zones were measured (named A, B, C, D, E - see Fig. A.6). They are located at various parts of the surface, but they have the same size (10 mm x 10 mm). The calculations were made with spatial resolution of $sp = 3$ μm.

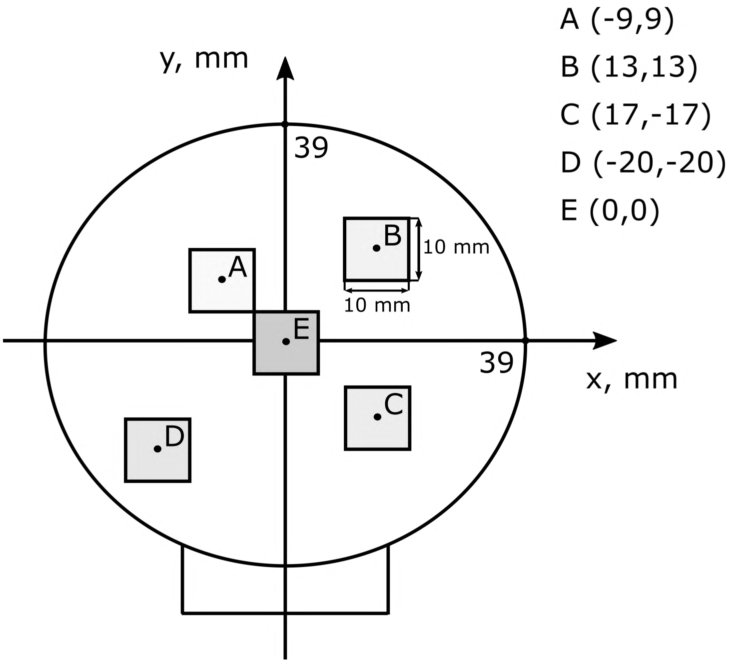

Figure A.6: Location of the zones measured with confocal microscope (first measurements with a rough surface).

A.3.1 Roughness measurements of several zones of the sensor

The surface condition for each zone is presented in Fig. A.7. As the heated wall was treated with emery paper, more scratches are visible on the surface in comparison to the previous case, when the surface was polished (Section A.2).

To estimate the root mean square roughness, the calculations were made according to Eq. A.1. Values of the mean roughness for different part of the sensor are shown in Tab. A.3. The averaged value, can be thus estimated as approx. 3.5 μm.

Table A.3: Root mean square roughness for all measurement zones (first measurements on a rough surface)

Name of the zone	S_q, μm
Zone A	3.76
Zone B	3.56
Area C	3.15
Area D	3.72
Center	3.10

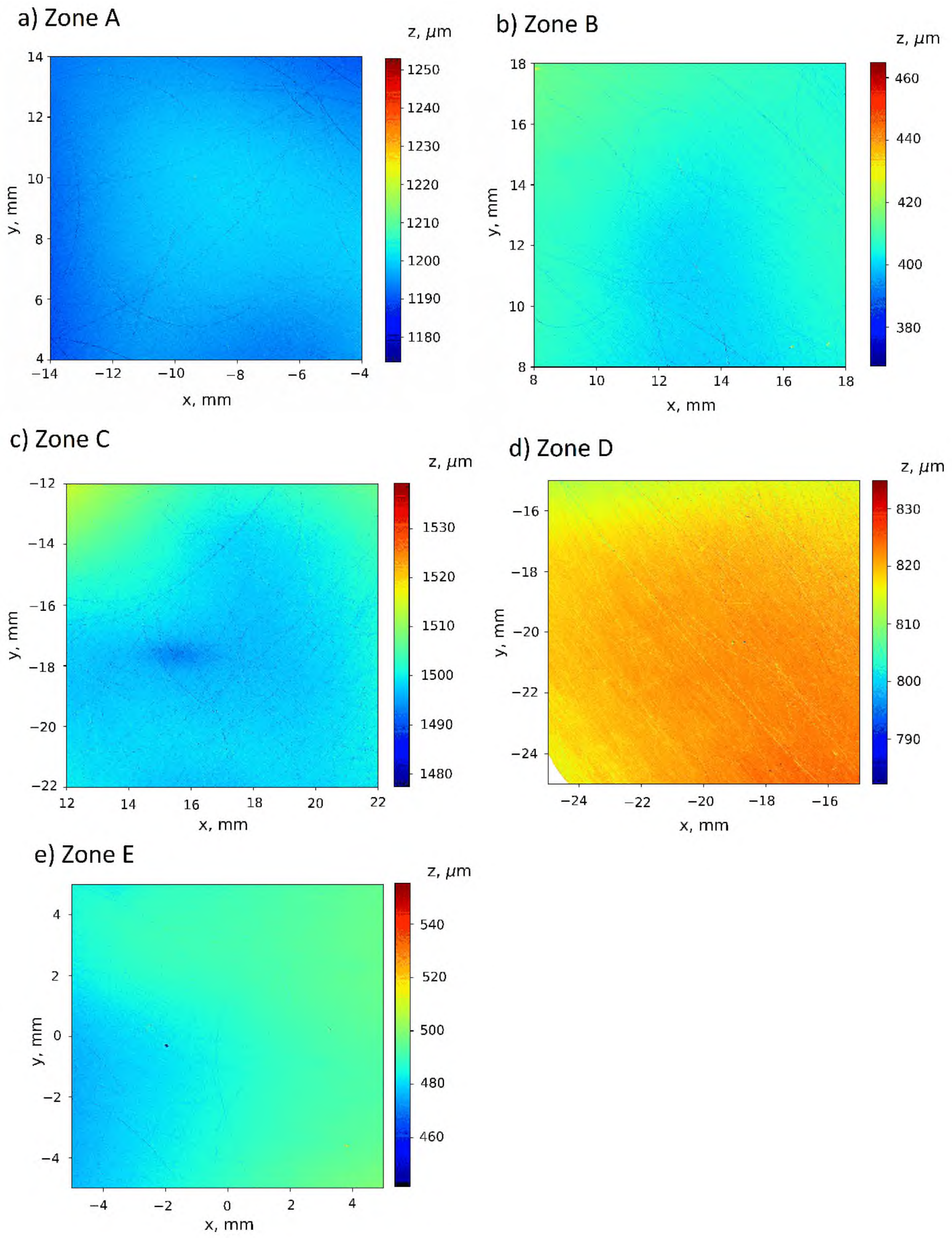

Figure A.7: Visualization of the surface characteristics for different parts of the heated surface with sp = 3 µm (first measurements with a rough surface).

A.3.2 Roughness measurements of the whole surface

The measurements of the whole heating surface was also conducted. The roughness measurements were not performed for this case, because of too low spatial resolution (sp = 35 μm). The results of this analysis are presented in Fig. A.8. It is noticeable that the surface possesses more irregular changes of the altitude in comparison to the polished surface (Section A.1). The horizontal grooves are not visible anymore, which was the case for the smooth wall (see Fig. A.5). The edges of the sensor are currently more irregular, because these measurements were conducted after adding layer of epoxy resin at the peripheral part of the sensor (in order to reduce the intensity of peripheral boiling).

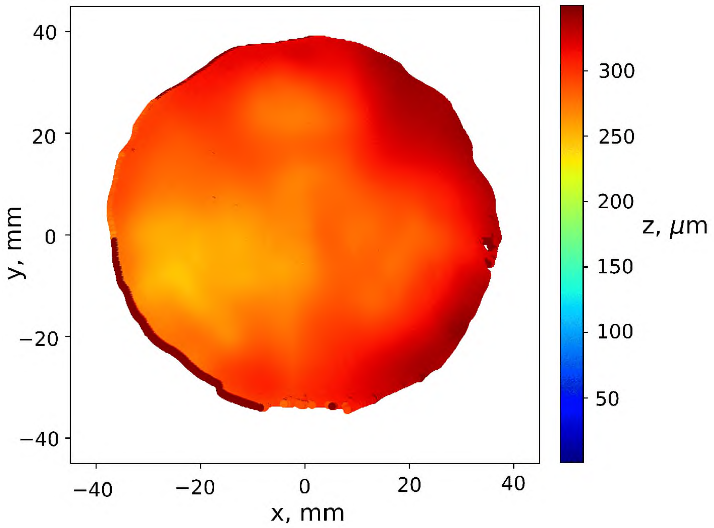

Figure A.8: Total surface measurements (first measurements with a rough surface).

A.3.3 Conclusions

The roughness calculations for a surface treated with emery paper gave results approx. 10 times larger than for a polished surface - the root mean square roughness was estimated as $S_q = 3.5\ \mu$m.

A.4 Rough surface with multiple nucleation sites (second measurement series)

Similarly like for first series of measurement (see Section A.3), the characterization of the surface was conducted in five measurement zones named A, B, C, D, E (see Fig. A.9). They cover different parts of the heated wall, but they have the same size (8 mm x 10 mm). Unfortunately, the measurements were stopped earlier than they should, so square 10 mm x 10 mm like in first measurement series was not reached. The spatial resolution was equal to $sp = 3$ μm. The measurements of the whole heated surface for this conditions were not performed.

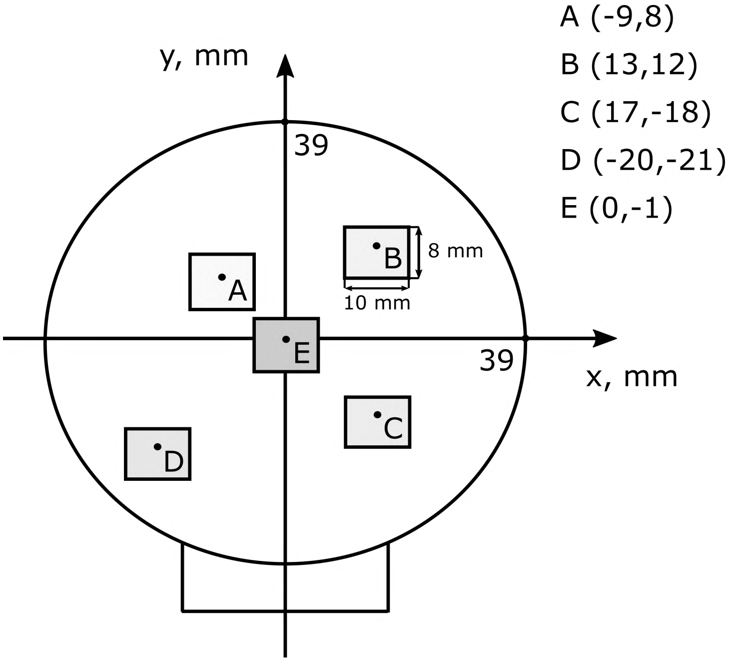

Figure A.9: Location of the zones measured with confocal microscope (second measurements with a rough surface).

A.4.1 Roughness measurements of several zones of the sensor

Fig. A.10 presents the surface condition for each zone during second measurement section with a rough surface. The root mean square roughness was calculated according to Eq. A.1. Tab. A.4 shows the values of the mean roughness for each section. The averaged roughness for the whole surface was estimated as approx. 2.8 μm.

Table A.4: Root mean square roughness for all measurement zones (second measurements with a rough surface).

Name of the zone	S_q, μm
Zone A	3.04
Zone B	2.92
Area C	2.23
Area D	2.89
Center	2.73

A.4.2 Conclusions

The roughness calculations during second series of experiments conducted on a rough surface does not vary too much from the first measurement series. The root mean square roughness was estimated as $S_q = 2.8$ μm (during first series of experiments, the averaged roughness was equal to $S_q = 3.5$ μm).

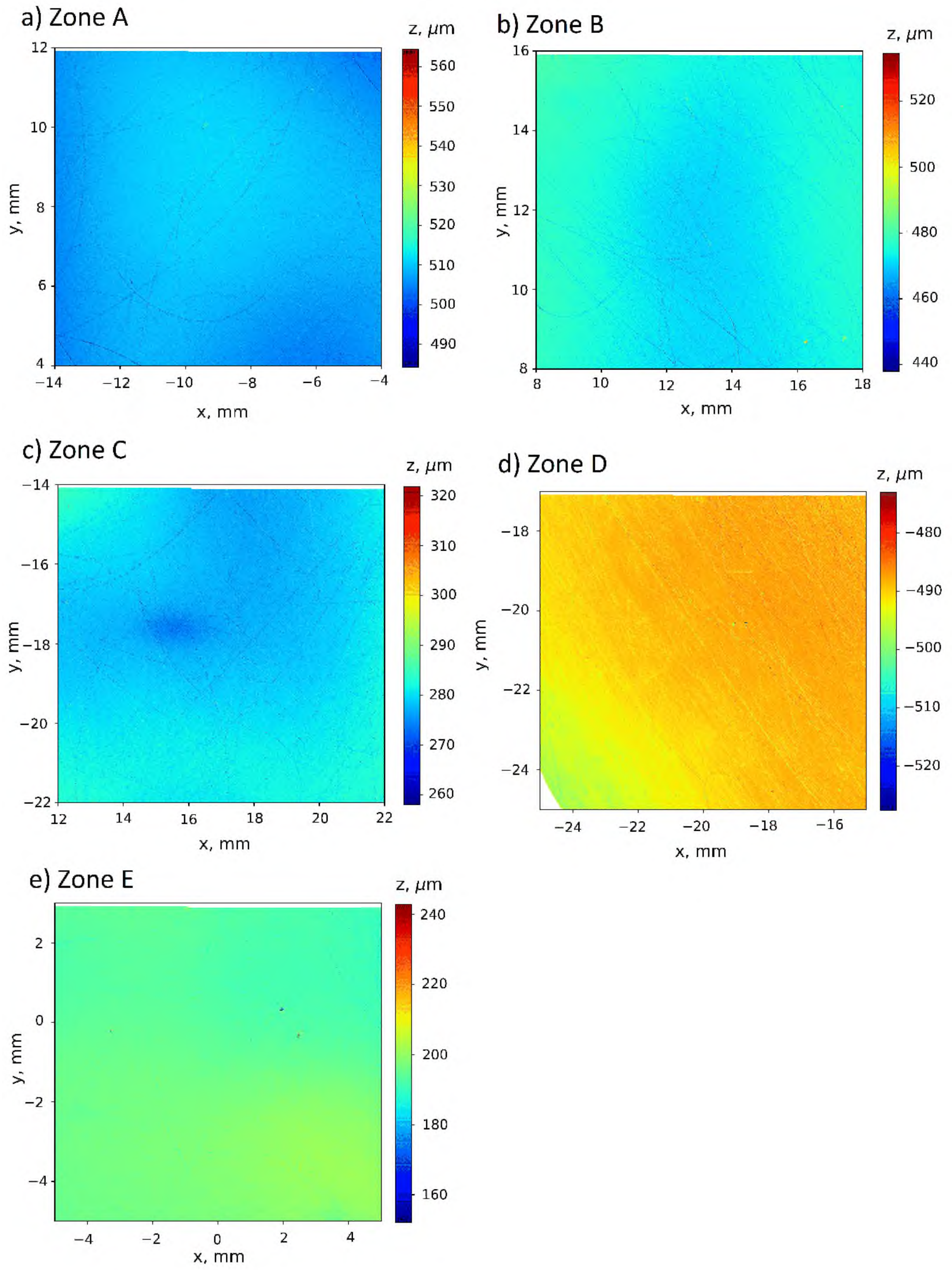

Figure A.10: Visualization of the surface characteristics for different parts of the heated surface with $sp = 3$ µm (second measurements with a rough surface).

Appendix B

PDF graphs for various operating parameters

Section 4 presented PDF graphs only for vapor pressure $p_v = 2.4$ kPa. They are created based on the heat flux evolution over all seven zones of the sensor. The shape of PDF graph, along with the instantaneous heat flux time evolution and video recordings, enable to group each measurement into specific boiling regime. Based on those distinction, the boiling regime maps were created (see Section 4.5 and 4.6.2). The analysis of boiling regimes were provided for surface with two different roughness. Fig. B.1 and B.2 correspond to surface with roughness $S_q = 3.5$ µm. The detailed analysis concerning the regimes observed for this surface properties is described in Section 4.5. Fig. B.3 and B.4 represent PDF for roughness $S_q = 2.8$ µm. They correspond to the analysis described in Section 4.6.

All the PDF graphs are plotted for four liquid levels ($H_l = 15$ cm, 28 cm, 35 cm and 60 cm) and five applied heat fluxes ($q_{app} = 3.6$ Wcm^{-2}, 4.4 Wcm^{-2}, 5.2 cm^{-2}, 6.1 Wcm^{-2}, 7.1 Wcm^{-2}, what corresponds to heating power of 174 W, 210 W, 248 W, 293 W, 331 W). The specific regimes were plotted in the same manner as in Section 4.4 (convection or small popping bubble regime in purple, isolated bubble regime in blue, intermittent boiling regime in green and fully developed boiling regime in red).

Analyzing Fig. B.1 and B.2, one can see that for specific working condition (fixed applied heat flux and liquid level), the resulting boiling regime may different for different vapor pressure. E.g. for $H_l = 35$ cm and $q_{app} = 6.1$ Wcm^{-2}, there is fully developed boiling regime for $p_v = 3.1$ kPa and isolated bubble regime for $p_v = 4.1$ kPa. However, the general order of heat flux with increasing value of applied heat flux is hold and corresponds to one observed for $p_v = 2.4$ kPa and described in Section 4.4. That means that if heating power is small, the convection or small popping bubble regime is reached. Further increase of the heating power leads to switching into isolated bubble regime and fully developed boiling regime. Sometimes in between those latter two, intermittent boiling regime can be observed.

The increase of the liquid level increases the level of liquid subcooling. This implies that higher wall superheat would be required to initiate boiling process. Because of that, for higher level of liquid the convection or small popping bubbles regime is more often visible. For $H_l = 60$ cm and all studied pressures only this regime is noticed under heat flux conditions studied in this manuscript.

B.1 Influence of the liquid level and applied heat flux on the boiling regimes (S_q = 3.5 µm)

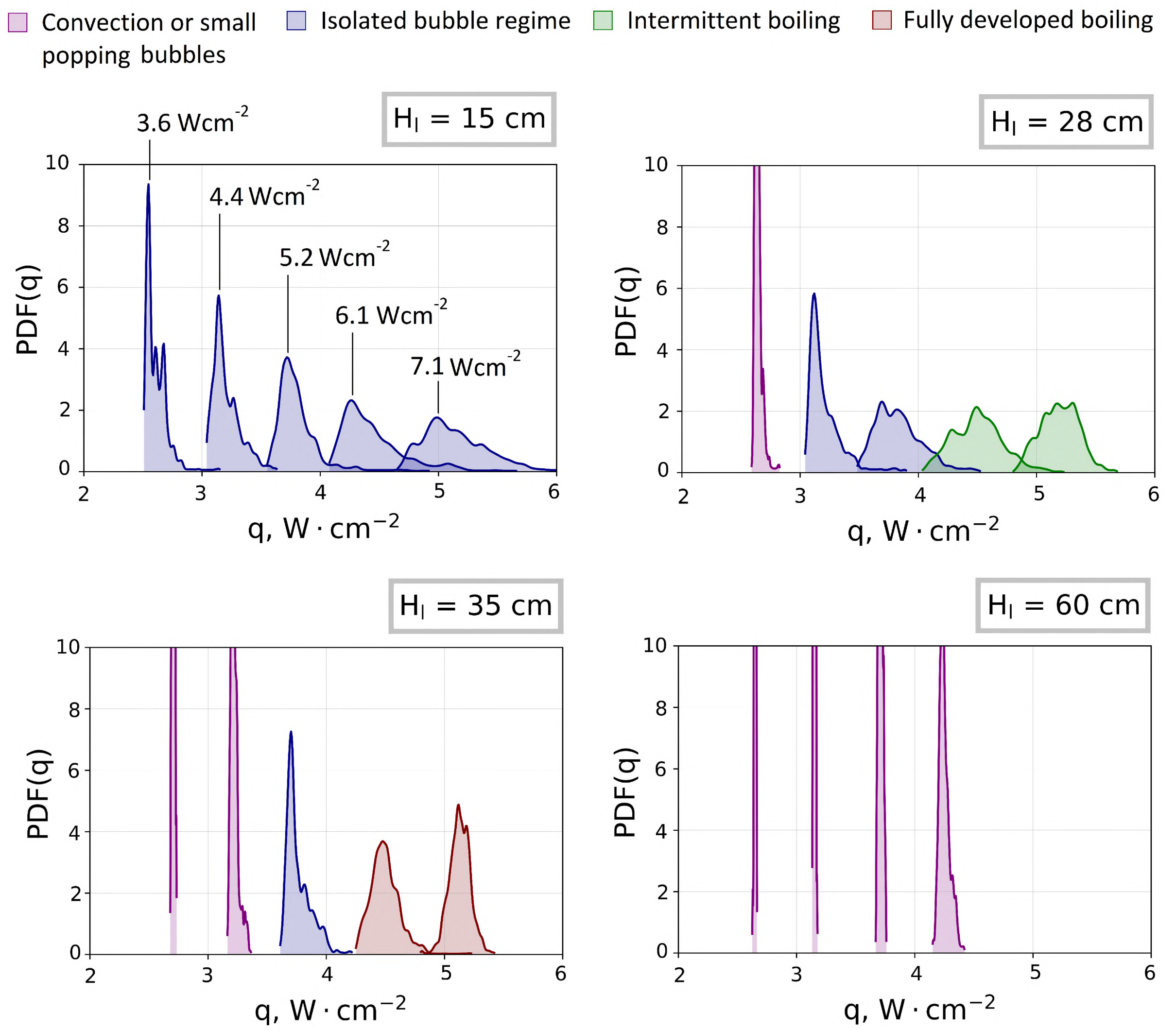

Figure B.1: PDF graphs for vapor pressure p_v = 3.1 kPa, S_q = 3.5 µm (applied heat fluxes for the graphs from left to right: 3.6 Wcm^{-2}, 4.4 Wcm^{-2}, 5.2 Wcm^{-2}, 6.1 Wcm^{-2} and 7.1 Wcm^{-2}).

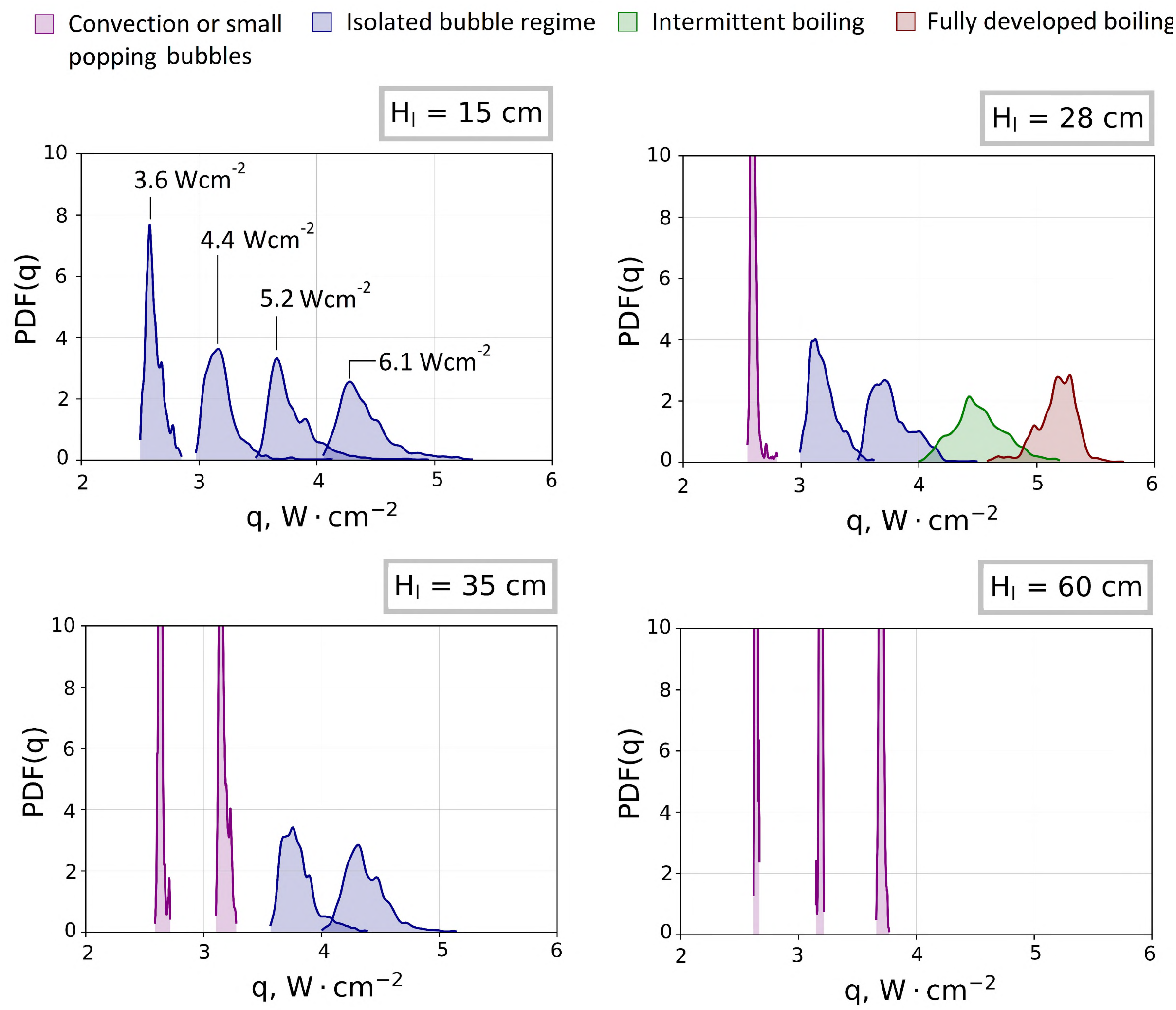

Figure B.2: PDF graphs for vapor pressure $p_v = 4.1$ kPa, $S_q = 3.5$ µm (applied heat fluxes for the graphs from left to right: 3.6 Wcm^{-2}, 4.4 Wcm^{-2}, 5.2 Wcm^{-2}, 6.1 Wcm^{-2} and 7.1 cm^{-2}).

B.2 Influence of the liquid level and applied heat flux on the boiling regimes ($S_q = 2.8$ µm)

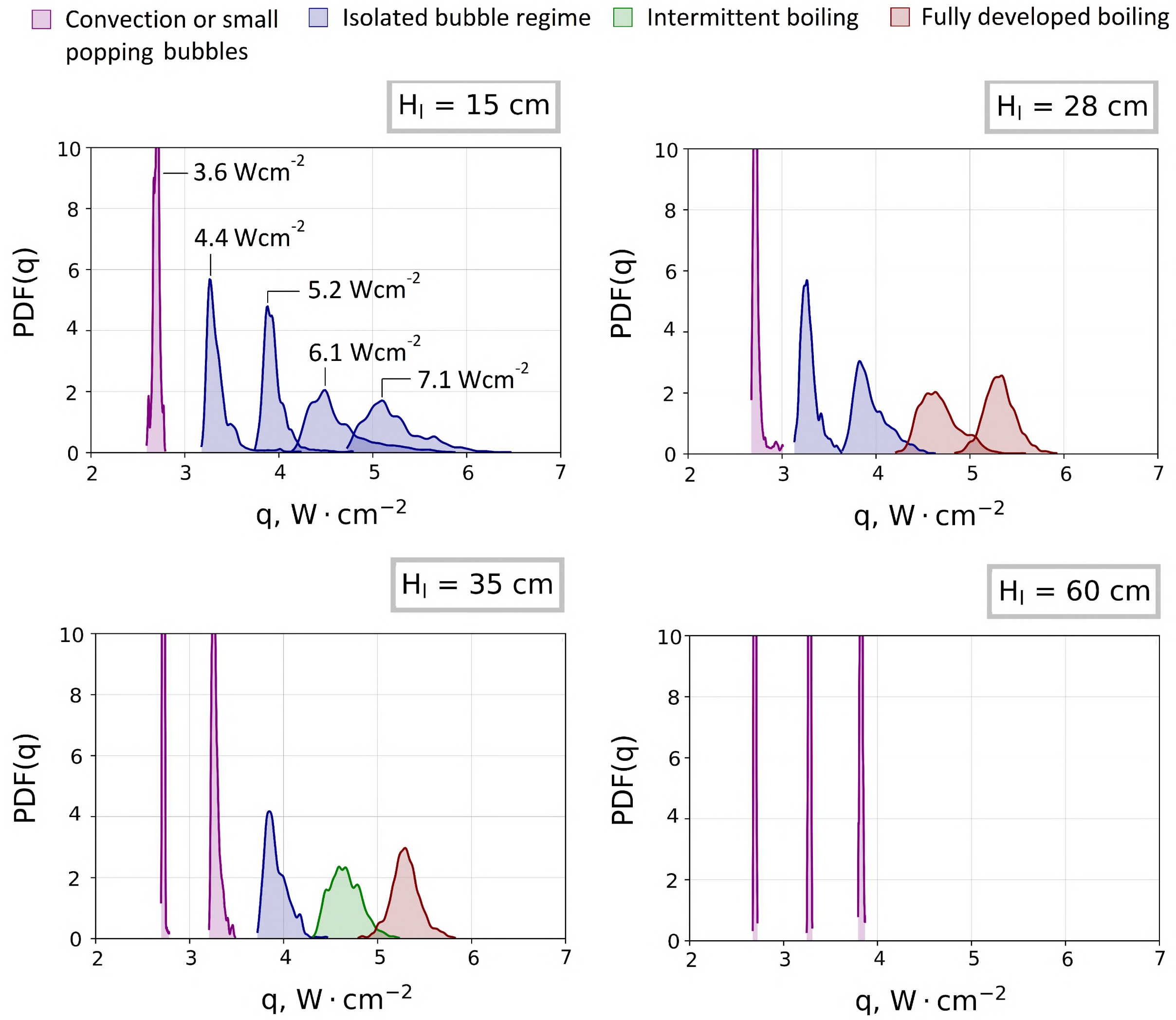

Figure B.3: PDF graphs for vapor pressure $p_v = 3.1$ kPa, $S_q = 2.8$ µm (applied heat fluxes for the graphs from left to right: 3.6 Wcm^{-2}, 4.4 Wcm^{-2}, 5.2 Wcm^{-2}, 6.1 Wcm^{-2} and 7.1 Wcm^{-2}).

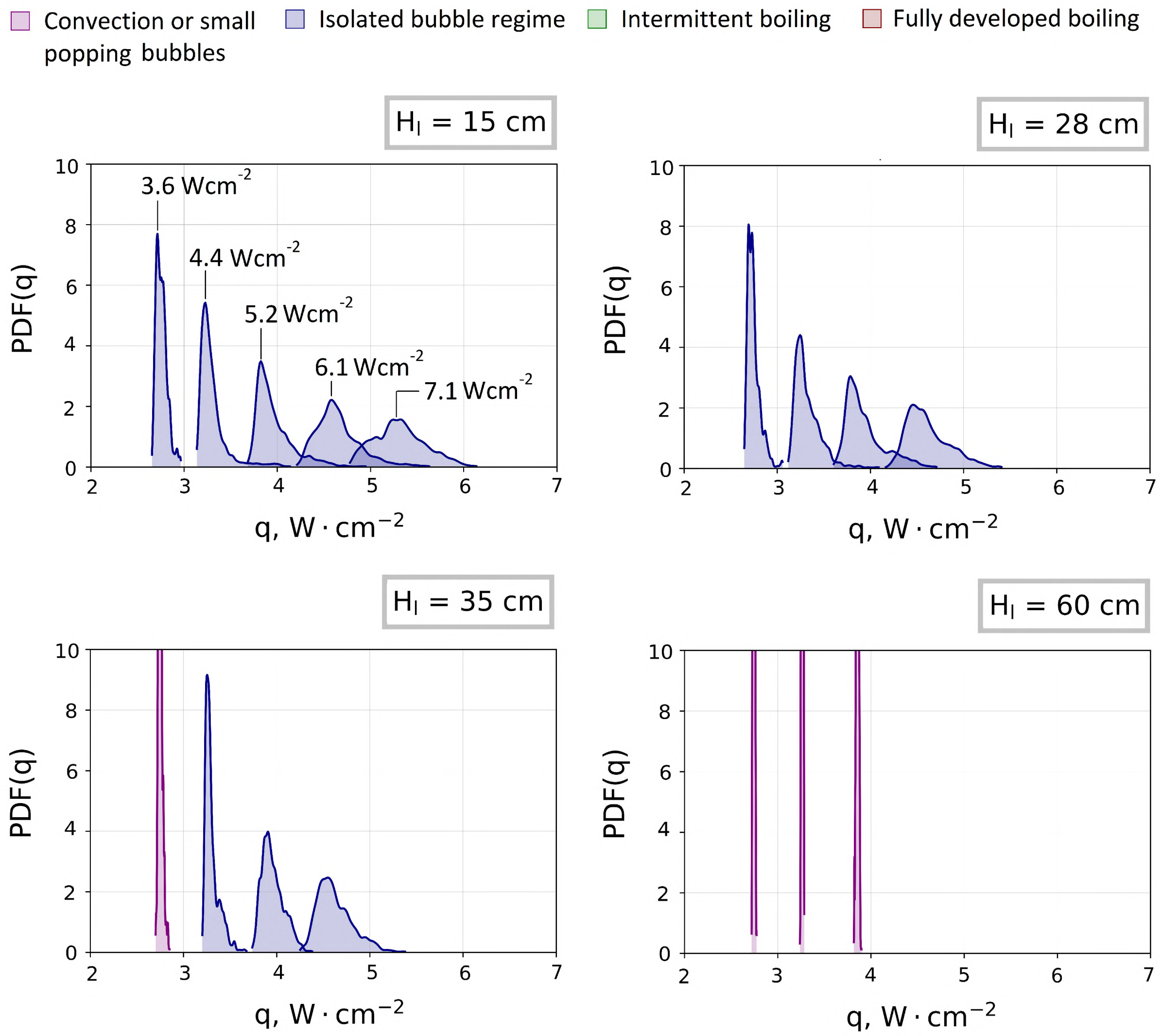

Figure B.4: PDF graphs for vapor pressure p_v = 4.1 kPa, S_q = 2.8 µm (applied heat fluxes for the graphs from left to right: 3.6 Wcm^{-2}, 4.4 Wcm^{-2}, 5.2 Wcm^{-2}, 6.1 Wcm^{-2} and 7.1 Wcm^{-2}).

Bibliography

[1] Alam M. S., Prasad L., Gupta S. C., Agarwal V. K. Enhanced boiling of saturated water on copper coated heating tubes. Chemical Engineering and Processing: Process Intensification, 47, pp. 159–167 (2008).

[2] Amini A., Homsy G.M. Evaporation of liquid droplets on solid substrates. I. Flat substrate with pinned or moving contact line. Phys. Rev. Fluids 2 (2017).

[3] Baek J.M., Yi C., Rhee J.Y. Central spot formed in dried coffee-water-mixture droplets: Inverse coffee-ring effect. Curr. Appl. Phys. 18 (4), pp. 477-483 (2018).

[4] Bae S., Kim M., Kim J. Improved technique to measure time- and space-resolved heat transfer under single bubbles during saturated pool boiling of FC-72. Exp. Heat Tranfer. 12 (3), pp. 265–278 (1999).

[5] Birdi K.S, Vu D.T. Wettability and the evaporation rates of fluids from solid surfaces. J. Adhes. Sci. Technol. 7 (6), pp. 485-493 (1993).

[6] Beer H. Das dynamische Blasenwachstum beim Sieden Flüssigkeiten an Heizflächen, Forschung auf dem Gebiete des Ingenieurwesens. 37, pp. 85–90 (1971).

[7] Bell Q., Ian H. S., Wronski L., Jorrit V. Pure and pseudo-pure fluid thermophysical property evaluation and the open-source thermopysical library CoolProp. Ind. Eng. Chem. Res. 54 (6), pp. 2498-2508 (2014).

[8] Berensen P. J. Experiments in pool boiling heat transfer. Int. J. Heat Mass Transfer. 5 pp. 985–999 (1962).

[9] Brutin D., Sobac B., Loquet B., Sampol J. Pattern formation in drying drops of blood. J. Fluid Mech. 667, pp. 85-95 (2011).

[10] Brutin D. Droplet Wetting and Evaporation. Academic Press, Oxford (2015).

[11] Buyevich Y. A., Webbon B. W. Dynamics of vapour bubbles in nucleate boiling. Int. J. Heat Mass Transf. 39, pp. 2409-2426 (1996).

[12] Cao Z., Dobrynin A.V. Polymeric droplets on soft surfaces: From Neumann's triangle to Young's law. Macromolecules 48 (2) pp. 443-451 (2015).

[13] Carey V.P. Liquid–Vapor Phase-Change Phenomena. CRC Press. Taylor & Francis Group (2008).

[14] Cazabat A.M., Guéna G. Evaporation of macroscopic sessile droplets. Soft Matter 6, pp. 2591-2612 (2010).

[15] Çengel Y.A., Ghajar A.J. Heat and Mass Transfer Fundamentals & Applications. 5th Edition. Chapter 10: Boiling and condensation. Grawhil Education, Stillwater (2015).

[16] Chan M. A., Yap C. R., Ng K. C. Pool boiling heat transfer of water on finned surfaces at near vacuum pressures. J. Heat Transfer. 132 (3) (2010).

[17] Chen L., Evans J.R.G. Drying of colloidal droplets on superhydrophobic surfaces. J. Colloid Interface Sci. 351 (1), pp. 283-287 (2010).

[18] Chen R., Zhang L., Zang D., Shen W. Blood drop patterns: Formation and applications. Adv. Colloid Interface Sci. 231, pp. 1-14 (2016).

[19] Cichelli M.T., Bonilla C. F. Heat transfer to liquids boiling under pressure. Transaction of AIChE. 41, pp. 755-787 (1945).

[20] Cole R., Rohsenow W.M. Correlations for bubble departure diameters for boiling of saturated liquid. Chemical Engineering Progress. 65, pp. 211-213 (1969).

[21] Cooper M., Lloyd A. The microlayer in nucleate pool boiling. Int. J. Heat Mass Transfer. 12 (8), pp. 895-913 (1969).

[22] Cui Q., Chandra S., McCahan S. The Effect of Dissolving Gases or Solids in Water Droplets Boiling on a Hot Surface. Journal Heat Transf. 123, pp. 719-729 (2001).

[23] Deegan R.D., Bakajin O., Dupont T.F., Huber G., Nagel S.R., Witten T.A. Contact line deposits in an evaporating drop. Phys. Rev. 62 (1), pp. 756-765 (2000).

[24] Deegan R.D. Pattern formation in drying drops. Phys. Rev. 61 (1), pp. 475–485 (2000).

[25] Demiray F., Kim J. Microscale heat transfer measurements during pool boiling of FC-72: effect of subcooling. Int. J. Heat Mass Transfer. 47 (14-16), pp. 3257-3268 (2004).

[26] Dorrer C., Rühe J. Some Thoughts on Superhydrophobic Wetting. Soft Matter. 5, pp. 51-61 (2009).

[27] Eral H.B., Augustine D.M., Duits M.H.G., Mugele F. Suppressing the coffee stain effect: how to control colloidal self-assembly in evaporating drops using electrowetting. Soft Matter. 7, pp. 4954-4958 (2011).

[28] Eral H.B., Mannetje D.J.C.M., Oh J.M. Contact angle hysteresis: a review of fundamentals and applications. Colloid Polymer Sci. 291 (2), pp. 247-260 (2013).

[29] Erbil H.Y. Control of stain geometry by drop evaporation of surfactant containing dispersions. Adv. Colloid Interface Sci. 222 (Suppl. C), pp. 275-290 (2015).

[30] Erbil H.Y, McHale G., Newton M.I. Drop evaporation on solid surfaces: Constant contact angle mode. Langmuir. 18 (7), pp. 2636-2641 (2002).

[31] Faghri A., Zhang Y. Transport phenomena in multiphase systems. Chapter 10: boiling. Academic Press, pp. 765-852 (2006).

[32] Fritz W. Maximum volume of vapor bubbles. Phys. 36, pp. 379-384 (1935).

[33] Forster K., Greif R. Heat transfer to a boiling liquid - mechanism and correlations. Progress Report. United States. 7, pp. 58-40 (1958).

[34] Gaertner R.F., Photographic study of nucleate pool boiling on a horizontal surface. J. Heat Transfer. 87 (1), pp. 17-27 (1965).

[35] Gatapova E.Y., Semenov A., Zaitsev D.V., Kabov O.A. Evaporation of a sessile water drop on a heated surface with controlled wettability. Colloids Surf. 441, pp. 776-785 (2014).

[36] Gerardi C., Buogiorno J., Hu L.W., McKrell T. Study of bubble growth in water pool boiling through synchronized, infrared thermometry and high-speed video. Int. J. Heat Mass Transfer. 53 (19-20), pp. 4185-4192 (2010).

[37] Girard F., Antoni M., Sefiane K. Infrared thermography investigation of an evaporating sessile water droplet on heated substrates, Langmuir. 26 (7), pp. 4576-4580 (2010).

[38] Giraud F., Toublanc C., Rullière R., Bonjour J., Clausse M. Experimental study of water vaporization occurring inside a channel of a smooth plate-type heat exchanger at subatmospheric pressure. Appl. Therm. Eng. 106 (5), pp. 180-191 (2016).

[39] F. Giraud, C. Toublanc, R. Rullière, J. Bonjour, M. Clausse. Preliminary experimental investigation on water boiling phenomena in a liquid layer at subatmospheric pressure. In Proceedings of 24th Int. Congress Refrigeration (2015).

[40] Giraud F. Vaporization of water at subatmospheric pressure: fundamentals of boiling phenomena and path towards the design of compact evaporators for sorption chillers. PhD thesis, Institut National des Sciences Appliquees de Lyon (2015).

[41] Giraud F. Rullière R., Toublanc C., Clausse M., Bonjour J. Experimental evidence of a new regime for boiling of water at subatmospheric pressure. Exp. Therm. Fluid Sci. 60, pp. 45-53 (2015)

[42] Goel P., Nayak A. K., Kulkarni P.P., Joshi J.B., Experimental study on bubble departure characteristics in subcooled nucleate pool boiling. Int. J. Multiphase Flow. 89, pp. 163-176 (2017).

[43] Golobic I., Petkovsek J., Baselj M., Papez A., Kenning D.B.R. Experimental determination of transient wall temperature distributions close to growing vapor bubbles. Heat Mass Transfer. 45 (7), pp. 857-866 (2009).

[44] Halon T. Optymalizacja parametrow procesu wrzenia ziebnika w niskocisnieniowym adsorpcyjnym systemie trigeneracyjnym. PhD thesis, Wroclaw University of Science and Technology (2017).

[45] Halon T., Zajaczkowski B., Michaïe S., Rullière R., Bonjour J. Enhanced tunneled surfaces for water pool boiling heat transfer under low pressure. Int. J. Heat Mass Transf. 116 pp. 93-103 (2018).

[46] Han C. Y., Griffith P. The mechanism of heat transfer in nucleate pool boiling. Part I: Bubble initiation, growth and departure. Int. J. Heat Mass Transf. 8 pp. 887-904 (1965).

[47] Han W., Lin Z. Learning from coffee rings: Ordered structures enabled by controlled evaporative self-assembly. Angew. Chem. Int. Ed. 51 (7), pp. 1534–1546 (2012).

[48] Hegseth J.J., Rashidnia N., Chai A. Natural convection in droplet evaporation. Phys. Rev. 54, pp. 1640–1644 (1996).

[49] Hewitt G.F. Handbook of heat transfer. Chapter 15: Boiling. Editors: W. Rohsenow, J. Hartnett, Y. Cho. McGraw-Hill (1998).

[50] Hsu Y. Y. On the size range of active nucleation cavities on a heating surface. J. Heat Trans. 84, pp. 207-213 (1962).

[51] Hu H., Larson R.G. Marangoni effect reverses coffee-ring depositions. J. Phys. Chem. 110 (14), pp. 7090-7094 (2006).

[52] Hyers R.W. Fluid flow effects in levitated droplets. Meas. Sci. Technol. 16 (2) (2005).

[53] Inada S., Miyasaka Y., Sakamoto S., Chandratilleke G.R. Liquid-solid contact state in subcooled pool transition boiling system. J. Heat Mass Transf. 108, pp. 219-221 (1986).

[54] Incropera F. P., Dewitt D.P, Bergman T.L., Lavine A.S. Fundamentals of heat and mass transfer. Sixth edition. John Wiley & Sons (2007).

[55] Inoue T., Kawae N., Monde M. Effect of subcooling on critical heat flux during pool boiling on a horizontal heated wire. Heat Mass Transf. 33, pp. 481-488 (1998).

[56] Ivey H., Morris D. On the relevance of the vapour-liquid exchange mechanism for sub-cooled boiling heat transfer at high pressure. Reactor Development Division, Atomic Energy Establishment (1962).

[57] Jawurek H. Simultaneous determination of microlayer geometry and bubble growth in nucleate boiling, Int. J. Heat Mass Transfer. 12 (8), pp. 843-848 (1969).

[58] Judd R.L. The influence of subcooling on the frequency of bubble emission in nucleate boiling. J. Heat Transf. 111, pp. 747-751 (1989).

[59] Kakac, S., Shah, R.K., Aung, W. Handbook of single-phase convective heat transfer. Ed. Wiley (1987).

[60] Karpitschka S., Liebig F., Riegler H. Marangoni contraction of evaporating sessile droplets of binary mixtures, Langmuir. 33 (19), pp. 4682–4687 (2017).

[61] Kenning D.B.R., Yan Y. Pool boiling heat transfer on a thin plate: features revealed by liquid crystal thermography. Int. J. Heat Mass Transfer. 39 (15), pp. 3117-3137 (1996).

[62] Kim H., Boulogne F., Um E., Jacobi I., Button E., Stone H.A. Controlled uniform coating from the interplay of Marangoni flows and surface-adsorbed macromolecules. Phys. Rev. Lett. 116 (2016).

[63] Kim H., Buongiorno J. Development of an Infrared-based visualization technique to study phase dynamics on boiling surfaces, in: Proceedings of the 4th International Conference on Heat Transfer and Fluid Flow in Microscale, Fukuoka, Japan (2011).

[64] Kim J., Benton J.F., Wisniewski D. Pool boiling heat transfer on small heaters: effect of gravity and subcooling. Int. J. Heat Mass Transfer. 45, pp. 3919-3931 (2002).

[65] Kistovich A.V., Chashechkin Y.D., Shabalin V.V Formation mechanism of a circumferential roller in a drying biofluid drop, Tech. Phys. 55, pp. 473–478 (2010).

[66] Kunkelmann C., Stephan P. Numerical simulation of the transient heat transfer during nucleate boiling of refrigerant HFE-7100. Int. J. Refrig. 33, pp. 1221-1228 (2010).

[67] Kutateladze S. Heat transfer during condensation and boiling. Translated from a publication of the State Scientific and Technical Publishers of Literature and Machinery, Moscow-Leningrad, as AEC-TR-3770 (1962).

[68] Qiao Y. M., Chandra S. Boiling of Droplets on a Hot Surface in Low Gravity. Int. J. Heat Mass Transf. 39 (7), pp. 1379–1393 (1996).

[69] Lee J., Duy P.K., Park S.C., Chung H. Development of hydrophobic surface substrates enabling reproducible drop-and-dry spectroscopic measurements. Talanta 153, pp. 31-37 (2016).

[70] Leger L., Erman M., Guinet-Picard A.M., Ausserre D., Strazielle C. Precursor film profiles of spreading liquid drops. Phys. Rev. Lett. 60 (23), pp. 2390-2393 (1988).

[71] Liang G., Mu X., Guo Y., Shen S., Quan S., Zhang J. Contact vaporization of an impacting drop on heated surfaces. Exp. Therm. Fluid Sci. 74, pp. 73-80 (2016).

[72] Lin T.S., Zeng Y.H., Tsay R.Y., Lin S.Y. Roughness-induced strong pinning for drops evaporating from polymeric surfaces. J. Taiwan. Inst. Chem. 62, pp. 54-59 (2016).

[73] Li Y.F., Sheng Y.J., Tsao H.K. Evaporation stains: Suppressing the coffee-ring effect by contact angle hysteresis, Langmuir. 29 (25), pp. 7802-7811 (2013).

[74] Madjeski J. Activation of nucleation cavities on a heating surface with temperature gradient in superheated liquid. Int. J. Heat Mass Transf. 9, pp. 295-300 (1966).

[75] Malinowski R., Volpe G., Parkin I.P., Volpe G. Dynamic control of particle deposition in evaporating droplets by an external point source of vapor. J. Phys. Chem. Lett. 9 (3), pp. 659-664 (2018).

[76] Mampallil D., Eral H.B. A review on suppression and utilization of the coffee-ring effect. Adv. Colloid Interface Sci. 252, pp. 38–54 (2018).

[77] Marek R., Straub J. The origin of thermocapillary convection in subcooled nucleate pool boiling, Int. J. Heat Mass Transf. 44, pp. 619–632 (2001).

[78] Marín A.G., Gelderblom H., Lohse D., Snoeijer J.H. Order-to-disorder transition in ring-shaped colloidal stains. Phys. Rev. Lett. 107 (2011).

[79] McGillis W.R., Carey V.P., Fitch J.S., Hamburgen W., Fitch J.S., Hamburgen W.R. Pool boiling enhancement techniques for water at low pressure. 7th IEEE Semi thermsymposium, Phoenix, USA, Western Research Laboratory, pp. 64–72 (1991).

[80] McNeil D. A., Burnside B. M., Rylatt D. I., Elsaye E. A., Baker S. Shell-side boiling of water at sub-atmospheric pressures. Int. J. Heat Mass Transf. 85, pp. 488-504 (2015).

[81] Michaïe S. Experimental study of the fundamental phenomena involved in pool boiling at low pressure. PhD thesis, Institut National des Sciences Appliquees de Lyon (2018).

[82] Michaïe S., Rullière R., Bonjour J. Experimental study of bubble dynamics of isolated bubbles in water pool boiling at subatmospheric pressures. Exp. Therm. Fluid Sci. 87, pp. 117-128 (2017).

[83] S. Michaïe, R. Rullière, J. Bonjour. Towards a more generalized understanding of pool boiling at low pressure: Bubble dynamics for two fluids in states of thermodynamic similarity. Exp. Therm. Fluid Sci. 101, pp. 217-230 (2019).

[84] Mikic B.B. , Rohsenow W.M. A New Correlation of Pool-Boiling Data Including the Effect of Heating Surface Characteristics, J. Heat Transfer. 91 (2), pp. 245-250 (1969).

[85] Mikic B.B., Rohsenow W.M., Griffith P. On bubble growth rates. Int. J. Heat Mass Transf. 13, pp. 657-666 (1970).

[86] Misyura S.Y., Kuznetsov G.V., Feoktistov D.V., Volkov R.V., Morozov V.S., Orlova E.G. The influence of the surface microtexture on wettability properties and drop evaporation. Surf. Coat. Tech. 375, pp. 458-467 (2019).

[87] Moore F.D., Mesler R.B. The measurement of rapid surface temperature fluctuations during nucleate boiling of water. AIChE Journal. 7 (4), pp. 620–624 (1961).

[88] Nukiyama S. Maximum and minimum values of heat flux transmitted from metal to boiling water under atmospheric pressure. J. Soc. Mech. Eng. Japan. 37 (53-54), pp. 367-374 (1934).

[89] Okada J.T., Ishikawa T., Watanabe Y., Paradis P.F. Surface tension and viscosity of molten vanadium measured with an electrostatic levitation furnace. J. Chem. Thermodyn. 42 (7), pp. 856–859 (2010).

[90] Orlande H.R.B., Fudym O., Maillet D., Cotta R.M. Thermal Measurements and Inverse Techniques. CRC Press. 1st Edition, pp. 171-183 (2011).

[91] Parsa M., Harmand S., Sefiane K. Mechanisms of pattern formation from dried sessile drops. Adv. Colloid Interface 254, pp. 22-47 (2018).

[92] Petrovic S., Robinson T., Judd R.L. Marangoni heat transfer in subcooled nucleate pool boiling, Int. J. Heat Mass Transf. 47, pp. 5115–5128 (2004).

[93] Phan H.T., Caney N., Marty P., Colasson S., Gavillet J. How surface wettability influences nucleate boiling? Comptes rendus de l'Académie des sciences. Série IIb, Mécanique. 337, pp. 251–259 (2009).

[94] Picknett R.G., Bexon R. The evaporation of sessile or pendant drops in still air. J. Colloid Interface Sci. 61 (2), pp. 336-350 (1977).

[95] Pioro I.R., Rohsenow W.M., Doerffer S.S. Nucleate pool-boiling heat transfer . I : review of parametric effects of boiling surface. Int. J. Heat Mass Transf. 47, pp. 5033–5044 (2004).

[96] Rainey K., You S., Lee S. Effect of pressure, subcooling and dissolved gas on pool boiling heat transfer from microporous surfaces in FC-72. J. Heat Transf. 125, pp. 75-83 (1998).

[97] Ristenpart W.D., Kim P.G., Domingues C., Wan J., Stone H.A. Influence of substrate conductivity on circulation reversal in evaporating drops. Phys. Rev. Lett. 99 (2007).

[98] Robinson A. J., Judd R. L. The dynamics of spherical bubble growth. Int. J. Heat Mass Transf. 47, pp. 5101-5113 (2004).

[99] Schnabel L., Scherr C., Weber C. Water as refrigerant – experimental evaluation of boiling characteristics at low temperatures and pressures. Proceedings of International Sorption Heat Pump Conference, Seoul, Korea (2008).

[100] Schönfeld F., Graf K.H., Hardt S., Butt H.J. Evaporation dynamics of sessile liquid drops in still air with constant contact radius, Int. J. Heat Mass Transfer. 51 (13), pp. 3696-3699 (2008).

[101] Sefiane K. Patterns from drying drops. Adv. Colloid Interface Sci. 206 (Suppl. C), pp. 372–381 (2014).

[102] Semal S., Blake T.D., Geskin V., de Ruijter M.J., Castelein G., de Coninck J. Influence of surface roughness on wetting dynamics. Langmuir 15 (1999).

[103] Semenov S., Starov V.M., Velarde M.G., Rubio R.G. Droplets evaporation: Problems and solutions. Eur. Phys. J. Spec. Top. 197, pp. 265-278 (2011).

[104] Seo C., Jang D., Chae J., Shin S. Altering the coffee-ring effect by adding a surfactant-like viscous polymer solution. Sci. Rep. 7 (1) (2017).

[105] Shanahan M.E.R., Bourgès C. Effects of evaporation on contact angles on polymer surfaces. Int. J. Adhes. Adhes. 14 (3), pp. 201-205 (1994).

[106] Sharma B., Verma R., Baur C., Bykova J., Mabry J.M., Smith D.W. Ultra low dielectric self-cleansing and highly oleophobic POSS-PFCP aryl ether polymer composites. J. Mater. Chem. 1, pp. 7222-7227 (2013).

[107] Shen B., Suroto B.J., Hirabayashi S., Yamada M., Hidaka S., Kohno M., Takahashi K., Takata Y. Bubble activation from a hydrophobic spot at ”negative” surface superheats in subcooled boiling. Appl. Therm. Eng. 88, pp.230-236 (2015).

[108] Siedel S. Bubble dynamics and boiling heat transfer: a study in the absense and in the presence of electric fields. PhD thesis, Institut National des Sciences Appliquees de Lyon (2012).

[109] Snoeijer J.H., Andreotti B. Moving contact lines scales, regimes and dynamical transitions. Annu. Rev. Fluid Mech. 45, pp. 269–292 (2013).

[110] Sobac B., Brutin D. Thermal effects of the substrate on water droplet evaporation. Phys. Rev. 86 (2012).

[111] Straub J. The role of surface tension for two-phase heat and mass transfer in the absence of gravity. Exp. Therm. Fluid Sci. 9, pp.253-273.(1994).

[112] Summ B. D., Goryunov Y.V. Fiziko-khimicheskie osnovy smachivaniya i rastekaniya (Eng: Physical and chemical basics of wetting and spreading), Moscow: Khimiya (1976).

[113] Sun K., Yanga H., Xue W., He A., Zhu D., Liu W., Adeyemi K., Cao Y. Anti-biofouling superhydrophobic surface fabricated by picosecond laser texturing of stainless steel. Appl. Surf. Sci. 436, pp. 263-267 (2018).

[114] Thome J.R. Heat Transfer Handbook. Chapter 9: Boiling. 1st Edition. Wiley. Editors: Bejan A., Krauss A.D, pp. 635–717 (2003).

[115] Van Stralen S. J. D., Cole R., Sluyter W. M., Sohal M. S. Bubble growth rates in nucleate boiling of water at subatmospheric pressures. Int. J. Heat Mass Transfer. 18, pp. 655-669 (1975).

[116] Van Stralen S. J. D., Sohal M. S., Cole R., Sluyter W. M. Bubble growth rates in pure and binary systems: combined effect of relaxation and evaporation microlayers. Int. J. Heat Mass Transfer. 18, pp. 453-467 (1975).

[117] Wang G., Cheng P. Subcooled flow boiling and microbubble emission boiling phenomena in a partially heated microchannel. Int. J. Heat Mass Transfer. 54, pp. 79-91 (2009).

[118] Wayner P. C. Evaporation from a porous flow control element on a porous heat source. Int. J. Heat Mass Trans. 16, pp. 1919-1929 (1973).

[119] Welty J., Wicks C.E., Wilson R.E., Rorrer G.L. Fundamentals of Momentum, Heat, and Mass Transfer. Wiley, 5th Edition (2007).

[120] Weon B.M,, Je J.H. Capillary force repels coffee-ring effect. Phys. Rev. 82 (2010).

[121] Wojtasik K., Rullière R., Zajaczkowski B., Bonjour J. Some characteristics of bubble dynamics during pressure-induced subcooled pool boiling. In Proceedings of the 10th International Conference of Multiphase Flow ICMF2019, Rio de Janeiro, Brazil (2019)

[122] Xu H., Shirvanyants D., Beers K., Matyjaszewski K., Rubinstein M., Sheiko S.S. Molecular motion in a spreading precursor film. Phys. Rev. Lett. 93 (20) (2004).

[123] Xu X., Luo J. Marangoni flow in an evaporating water droplet. Appl. Phys. Lett. 91 (12) (2007).

[124] Yabuki T., Hamaguchi R., Nakabeppu O. Interferometric measurement of the liquid-phase temperature field around an isolated boiling bubble. J. Therm. Sci. Tech-Jpn. 7 (3), pp. 463-474 (2012).

[125] Yabuki T., Nakabeppu O. Heat transfer mechanisms in isolated bubble boiling of water observed with MEMS sensor. Int. J. Heat Mass Transfer. 76, pp. 286-297 (2014).

[126] Yabuki T., Nakabeppu O. Microscale wall heat transfer and bubble growth in single bubble subcooled boiling of water. Int. J. Heat Mass Transfer. 100, pp. 851-860 (2016).

[127] Yagov V. V., Gorodov A. K., Labuntsov D. A. Experimental study of heat transfer in the boiling of liquids at low pressures under conditions of free motion. J. Eng. Phys. 18, pp. 421–425 (1970).

[128] Yakhno T.A., Sanina O.A., Volovik M.G., Sanin A.G., Yakhno V.G. Thermographic investigation of the temperature field dynamics at the liquid-air interface in drops of water solutions drying on a glass substrate. Tech. Phys. 57 (7), pp. 915-922 (2012).

[129] Yoo H., Kim C. Experimental studies on formation, spreading and drying of inkjet drop of colloidal suspensions. Colloids Surf. 468, pp. 234-245 (2015).

[130] Yunker P.J., Still T., Lohr M.A., Yodh A.G. Suppression of the coffee-ring effect by shape-dependent capillary interactions. Nature 476 (7360), pp. 308-311 (2011).

[131] Zajaczkowski B., Halon T., Krolicki Z. Experimental verification of heat transfer coefficient for nucleate boiling at sub-atmospheric pressure and small heat fluxes. Heat Mass Transfer. 52 (2), pp. 205-215 (2016).

[132] Zang D., Li L., Di W., Zhang Z., Ding C., Chen Z., Shen W., Binks B.P., Geng X. Inducing drop to bubble transformation via resonance in ultrasound. Nature Commun. 9 (1), pp. 35-46 (2018).

[133] Zang D., Tarafdar S., Yu Tarasevich Y., Choudhury M.D., Dutta T. Evaporation of a Droplet: From physics to applications. Physics Reports. 804, pp. 1-56 (2019).

[134] Zang D., Yu Y., Chen Z., Li X., Wu H., Geng X. Acoustic levitation of liquid drops: Dynamics, manipulation and phase transitions. Adv. Colloid. Interface Sci. 243, pp. 77–85 (2017).

[135] Zhang C., Cheng P., Hong F. Mesoscale simulation of heater size and subcooling effects on pool boiling under controlled wall heat flux conditions. Int. J. Heat Mass Transfer. Vol. 101, pp. 1331-1342 (2016).

[136] Zhang H., Kita Y., Zhang D., Nagayama G., Takata Y., Sefiane K., Askounis A. Drop Evaporation on Rough Hot-Spots: Effect of Wetting Modes. Heat Transfer Eng, pp. 1-9 (2019).

[137] Zhao Y. Physical Mechanics of Surfaces and Interfaces. Science Publisher, Beijing (2012).

[138] Zuber N. The dynamics of vapor bubbles in nonuniform temperature fields. Int. J. Heat Mass Transfer. 2, pp. 83-98 (1961).

FOLIO ADMINISTRATIF

THESE DE L'UNIVERSITE DE LYON OPEREE AU SEIN DE L'INSA LYON

NOM : WOJTASIK DATE de SOUTENANCE : 02/07/2021

Prénoms : Karolina

TITRE : Boiling of water at low pressure: the role of subcooling and thermophysical properties on the bubble dynamics and heat transfer

NATURE : Doctorat Numéro d'ordre : 2021LYSEI045

Ecole doctorale : MEGA (Mécanique, Énergétique, Génie Civil, Acoustique)

Spécialité : Thermique et Énergétique

RESUME :

Boiling process is a common heat transfer mode used in various applications, among which air-conditioning and refrigeration. Recently, there has been a sparkling interest in the development of efficient cooling technologies which utilize environmentally-friendly refrigerants. Water could be one of them, but it requires to operate under low pressure. Close to the triple point, the physics of boiling significantly differs from atmospheric pressure. Although the knowledge on subatmospheric boiling is slowly growing, many of its aspects remain unknown.

In order to extend the fundamental knowledge concerning the boiling process, several experimental activities were carried out. Initially, the experiments were conducted on a polished surface with single cavity, and then on a rough surface with multiple nucleation sites. Boiling took place on a heated wall equipped with a novel heat flux sensor, under various vapor pressures. The height of liquid in the experimental reservoir was also varied: the induced static pressure creates a significant liquid subcooling that was shown to strongly affect the boiling behavior. The analysis of the dynamics of isolated bubbles allowed to discover three types of bubbles and explain their associated thermal phenomena. Statistical methods were applied for boiling on a rough surface because of the random character of this process. Along with camera visualization, these methods allowed to distinguish four distinct boiling regimes, whose conditions of occurrence were summarized owing to an original boiling regime map.

To enhance the phase change heat transfer at low pressure, an alternative option to boiling could be to spray multiple droplets on the heated wall. There is lack of knowledge concerning evaporation process at subatmospheric conditions. For that purpose, the last experiments were focused on the evaporation of a drop or a layer of liquid from a horizontal surface. It allowed to describe the various thermal processes occurring during evaporation phenomenon.

MOTS-CLÉS :

Pool boiling, Low pressure, Bubble dynamics, Experimentation, Visualization.

Laboratoire (s) de recherche : CETHIL

Directeur de thèse: BONJOUR Jocelyn, ZAJACZKOWSKI Bartosz

Président de jury : BUTRYMOWICZ Dariusz

Composition du jury : ROBINSON Antony, PIASECKA Magdalena, GIRAUD Florine, CHOROWSKI Maciej, RULLIÈRE Romuald, BONJOUR Jocelyn, ZAJACZKOWSKI Bartosz